OBSERVATION OF IRON ORE PARTICLE FLOW IN A MINERAL SPIRAL CONCENTRATOR BY POSITRON EMISSION PARTICLE TRACKING (PEPT)

Darryel Boucher

Department of Mining and Materials Engineering
McGill University, Montréal

August 12, 2017

A thesis submitted to McGill University
in partial fulfillment of the requirements of the degree of
Doctor of Philosophy

Résumé

Cette thèse présente comment la technique de traçage de particule par émission de positron (*positron emission particle tracking*, PEPT) a été utilisée pour obtenir de l'information détaillée sur le comportement de particules de minerai de fer à l'intérieur d'une spirale de concentration gravimétrique.

Une revue de la littérature a montrée que plusieurs expériences ont ciblées l'écoulement d'eau claire dans une spirale de concentration. Cependant, elle a aussi mis en évidence un manque d'information quantitative sur le comportement des particules à l'intérieur d'une pulpe minérale dense, tel qu'utilisé lors de l'opération de cet équipement. Pour la première fois, l'observation de la séparation des minéraux à l'échelle de l'écoulement de la pulpe a été réalisé et est présenté dans cette thèse.

La description de l'écoulement de particules minérales dans la spiral a été rendue possible par les travaux suivants. Premièrement, des particules de minerai de fer grossières (>1000 µm) ont été activées directement dans un cyclotron MC40 (rayon d'$^3He^+$ de 35 MeV). Deuxièmement, une méthode a été développée pour la fragmentation, la classification et la sélection d'éclats provenant de la surface des particules grossières permettant d'obtenir de petits traceurs activés (≈100 µm). Il s'agit de la première fois que de si petits traceurs représentatifs sont produits et permettent l'observation du comportement des particules dans une pulpe dense et opaque. En considérant le niveau d'activité des petits traceurs, un système de détection de haute performance composé de détecteurs de positron modulaires a été conçu et construit. Ensuite, ce nouvel assemblage de détecteurs a été comparé à un système de détection connu et la précision du traçage a été déterminée pour des particules de différentes compositions minérales, tailles, vitesses et activités. Finalement, ce système de détecteurs modulaires a été utilisé pour observer, pour la première fois, l'écoulement typique de particules d'hématite (5260 kg/m^3) et de quartz (2650 kg/m^3) de dimensions variant entre 90 et 1400 µm à l'intérieur d'une spirale de concentration. Ces mesures ont été réalisées dans une pulpe minérale (minerai de fer) ayant un contenu solide massique de 20%.

Dans cette thèse, les résultats décrivant le flux de particules minérales sont présentés sous la forme de trajectoires, vitesses, accélérations et forces résultantes sur les particules minérales. Un des résultats ayant une très grande importance est le comportement des particules dans l'écoulement secondaire de la pulpe. Pour une particule de quartz d'une taille de 300 à 355 µm, la vitesse radiale à l'intérieur de l'écoulement secondaire a été mesurée entre 0.1 m/s dans la couche inférieure s'écoulant vers le centre de la spirale et jusqu'à 0.2 m/s dans la couche supérieure s'écoulant vers l'extérieure. Cette information est critique pour le développement de spirales de concentrations plus efficaces car la séparation minérale est directement reliée au mouvement des particules dans cette écoulement secondaire.

Les nouvelles informations quantitatives obtenues à partir de ce travail seront utilisées pour l'amélioration et la validation de simulations de l'écoulement de la pulpe, maintenant possibles grâce aux avancées dans la puissance de calcul par ordinateur.

Abstract

This thesis describes how positron emission particle tracking (PEPT) was used to obtain detailed information on ore particle behaviour within a mineral spiral concentrator.

A review of literature has shown a number of experimental measurements of clear water flow in spiral concentrator. However, this review highlighted the lack of quantitative information on the particle behaviour within a dense pulp, used in the operation of this equipment. Thus, for the first time, observations of separation of minerals at the flow scale were undertaken and are reported in this thesis.

The description of mineral particle flow field in the spiral concentrator was made possible by the following work. First, large mineral particles (>1000 µm) were activated via direct activation in a MC40 cyclotron (35 MeV $^{3}He^{+}$ beam). Second, a new procedure was developed for subsequent breakage, sizing and selection of surface fragments of a large particle in order to obtain small activated mineral tracers (≈100 µm). This is the first time such small representative mineral tracers were produced and enabled the observation of particle behaviour in dense and opaque pulp. Considering the low amount of activity carried by these small tracers, a high performance tracking system consisting of modular positron emission detector was designed and built. Subsequently, this new modular detector assembly was compared to an established detection system and tracking error was determined for particles of different mineral composition, size, speed and activity. Finally, the modular detector system was used

to observe, for the first time, the characteristic flow of hematite (5260 kg/m^3) and quartz (2650 kg/m^3) particles with size ranging between 90 and 1400 µm within a spiral concentrator. All measurements were carried out in a mineral (iron ore) pulp consisting of 20% solids by mass.

In this thesis, the results describing mineral particle flow fields are presented in the form of trajectories, velocities, accelerations and resultant forces on the mineral tracer particle. Of key importance is the particle behaviour within the spiral secondary flow. For quartz particle of size 300 to 355 µm, radial velocity magnitude within the secondary flow ranged from 0.1 m/s in the lower inward moving layer of the flow and reached up to 0.2 m/s in the upper outward moving layers. This information is critical for the development of more efficient spiral concentrator since ore separation is a direct result of particle behaviour in this secondary flow.

The new quantitative information obtained from this work will be used for the improvement and validation of particle and fluid flow simulations, now possible thanks to the advances in computational power.

Acknowledgements

Je tiens à remercier mes parents pour m'avoir transmis leurs intérêts pour la nature et les sciences. Pour le temps qu'ils ont dévoué à mon épanouissement. Merci à Cyrille, Mirika, Adrien et Lorianne, l'équipage avec qui j'ai appris la vie! J'ai aussi une pensée pour ma famille plus élargie, des artisants, des intellectuels, des praticiens, des organisateurs. Tous des gens inspirants et nécessaires au succès individuel et commun.

Thorough the course of this project, I had the chance to receive support from many highly qualified persons. I wish to acknowledge Mr. Raymond Langlois, Mr. Joshua M. Sovechles, Dr. Adam Jordens, Dr. Pengbo Chu, Dr. Thomas Leadbeater, Dr. Nima Gharib, Mr. Christopher Marion, Dr. Ozan Kokkilic, Mr. Zhoutong Deng, Mme Vivian Campbell and Mme Marilène Renaud for their help in preparing set-up and conducting parts of experiments as well as reviewing papers, presentations and parts of this thesis. Thanks to you, I will remember our funny experimental and computer days in Montréal and Birmingham for a long time.

I wish to mention the discussions with many of the McGill mineral processing group members which fostered excellent ideas. Among them, Prof. James A. Finch, Mr. Frank Rosenblum, Mr. Ravinder Multani, Mr. Meng Zhou, Mme Jennifer Radman, Dr. Shiva Mohammadi-Jam, Mr. Ronghao Li, Mr. Gilberto Da Silva, Mr. Percy Zambrano, Dr. Jarrett Quinn, Dr. Yue Hua Tan, Dr. Aysan Molaei, Mme Eileen R. Espiritu, Mr. Hao Ma, Prof. Alexandro Navarra, Mme Katherine Aliste, Dr. Amir

Nazari, Mme Jabun Mita, Dr. Azin Zangooi, Dr. Randolph Pax, Mr. Mark Lepage, Mme Nalini Singh, Dr. Cesar Gomez, Mme Koowon Park, Mr. Armando Navarrete, Mr. Xiang Zhou, Mr. Marc Nassif, Dr. Mayeli Alvarez, Mr. Sungjae Moon, Mr. Xiangzhou Ding and Mme Barbara Hanley. YOU make this research group the best mineral processing group in the world!!

Many friendships were developed over the last few years, friendships that will remain wherever future brings us all. I am thinking about Jonathan Tremblay, Lauren McGann, Adam Jordens, Jessica Leal, Pengbo Chu, Xiaoqi Zhang, Martin Lavoie, Jennifer Boudreault, Gabrille Charette-Gagné, Pierre-André Boulay, Camille Charette-Gagné, Joshua Sovechles, Raymond Langlois and Mary Langlois. Montréal was so much fun with you all!

I acknowledge my co-supervisor Prof. Agus P. Sasmito, for his great advices, dedicated time and help. His door was always open up to late hours for unplanned discussion. I am convinced we will work together again some day.

A special acknowledgement goes to my supervisor Prof. Kristian E. Waters, an adviser and a good friend. He taught me how to write in English! I am not the best yet, but now a thousand times better than the first time I showed up in his office. Thank you for your confidence in me to make this project reality and all the freedom of thought and support that you gave me.

В заключение, я хочу выразить отдельную признательность моей жене - моей музе, источнику вдохновения, моей прекрасной Анне. Спасибо тебе за то, что каждый день подтаклкивала меня к успешному завершению данного труда.

McGill University
Montréal, Québec, Canada
August 2017

Preface

This thesis presents the work undertaken over the course of my graduate study at McGill University. It is a traditional format thesis which includes part of the work published by me (Darryel Boucher), as the first author, in different refereed journals [1–5]. After an introduction chapter, the second and third chapters present details of mineral processing basics and a review of the literature related to spiral concentrators, respectively. In chapter four, the technique of positron emission particle tracking (PEPT) is described with the details of how it was used to track mineral particles inside a spiral. Chapter five presents the experimental findings with discussion. Conclusion of the thesis and potential future research directions form chapter six.

The main original contribution to knowledge of the work presented in this thesis is the determination of the typical behaviour of gangue and valuable iron ore particles inside the dense pulp (20% solids by mass) flowing on a spiral concentrator trough. The work completed enabled to obtain, for the first time, the measured particle trajectory, velocity and acceleration during the mineral separation taking place on the spiral. This particle flow field was recovered from real mineral particles of representative densities and sizes taken from a typical iron ore sample (hematite and quartz). The experimental results presented in this thesis provide novel information on particle behaviour on the spiral concentrator.

This was made possible by first completing the successful design, assembly and characterisation of a positron emission particle tracking (PEPT) experimental set-up able to provide information about mineral particle motion in the spiral concentrator. This enabled high resolution tracking within the spiral upper turns. The extension of the direct activation technique to the direct activation and breakage (DAB) procedure enabled to generate representative hematite (5260 kg/m^3) and quartz (2650 kg/m^3) mineral tracers of size between 90 µm to 1400 µm in diameter. This is the first time the lower end of this range is possible for representative mineral tracers. This enabled the observation of small particle behaviour in dense and opaque pulp. Another important development is the preparation of data analysis codes for the treatment of the tracking signal. This enabled representation of the particle flow field by the production of particle trajectory, velocity, acceleration and particle force resultant.

The recovered information made possible the determination of the particle behaviour inside the secondary flow. Motion inside the secondary flow is of key importance for the mineral separation. This is the first time that the secondary flow is measured for particle radial migration and velocity. For quartz particle of size 300 to 355 µm, radial velocity magnitude within the secondary flow (second turn) ranged from 0.1 m/s in the lower inward moving layer of the flow and reached up to 0.2 m/s in the upper outward moving layers. This information is critical for the development of more efficient spiral concentrator since ore separation is a direct result of particle behaviour in this secondary flow.

Finally, the use of an established tracking system (ADAC Forte) in combination with the DAB tracer production technique enabled to follow representative particles during injection of wash water on a longer section of the spiral trough. This enabled the measurement of the wash water effect on the separation at the particle scale. This highlighted the fact that the spiral first and second turns are extremely important in the separation as most of the radial motion was complete before entrance of the particle in the third turn. Addition of wash water disturbed the flow of solids and acted to reject light particle. Wash water enlarged the concentrate band width which has an effect on take off port setting during operation.

Table of Contents

List of Figures

List of Tables

Nomenclature

Symbols

$\boldsymbol{a}$	Acceleration	m/s^2
$\boldsymbol{F}$	Force	N
$\boldsymbol{g}$	Gravitational acceleration	m/s^2
$\boldsymbol{v_f}$	Fluid velocity	m/s
$\boldsymbol{v_p}$	Particle velocity	m/s
$\boldsymbol{v_t}$	Particle terminal velocity	m/s
Γ	Surface tension	N/m
μ_f	Fluid viscosity	Pa s
ρ_f	Fluid density	kg/m^3
ρ_h	Density heavy mineral	kg/m^3
ρ_l	Density light mineral	kg/m^3
ρ_m	Density mixture	kg/m^3
ρ_p	Particle density	kg/m^3
σ	Standard deviation	
A	Cross sectional area	m^2
$a_{x_{p_i}}$	x component of tracer acceleration at point i	m/s^2
C_C	Concentration criterion	

d	Channel characteristic diameter	m
d_p	Particle diameter	µm
d_{50}	Diameter at 50% of cumulative mass	
De	Dean number	
E_s	Separation efficiency	%
f	Fraction of *LoRs* kept for final triangulation	
Fr	Froude number	
Fr_p	Froude number for particle	
G	Grade	%
G_F	Feed grade	%
$G_{C,max}$	Maximum possible grade of concentrate	%
i	Indice	
k	Constant	
L	Characteristic length	m
m	Mass	kg
N	Number of *LoRs* in a triangulation set	
n	Size of a dataset for error analysis	
p_i	Position i of the tracer	mm
R	Recovery	%
r_{cp}	Channel path curvature radius	m
Re	Reynolds number	
Re_p	Reynolds number for particle	
Stk	Stokes number	
t_{p_i}	Time associated with position i of the tracer	s
$v_{x_{p_i}}$	x component of tracer velocity at point i	m/s

W	Free surface width	m
We	Weber number	
Y	Mass yield to concentrate	%

Acronyms

LoR	Line of Response
CAD	Computer Aided Design
CFD	Computational Fluid Dynamics
CMP	Computational Mineral Processing
DAB	Direct Activation and Breakage
DDPM	Dense Discrete Phase Model
DEM	Discrete Element Method
FOV	PEPT Camera Field of View
GRG	Gravity-Recoverbale Gold
MPS	Mineral Processing System
PEPT	Positron Emission Particle Tracking
PIV	Particle Image Velocimetry
RMSE	Root Mean Square Error
RNG	Re-Normalisation Group
S.G.	Specific Gravity
VOF	Volume of Fluid

Chapter 1

Introduction and thesis structure

Today's global population stands at 7.5 billion with 55% living in urban areas. This population is expected to reach 10 billion by 2050 with 65% living in urban areas [6]. Humans already extract billions of tons of minerals resources from the Earth's crust every year to provide supply of metals and others keys elements used in the construction of infrastructure and fabrication of manufactured goods. Considering the increase in population, the share of people living in urban area and the associated economic growth, the amount of mineral resources to be extracted in the following decades is immense [7].

At the same time, most of the high grade ores with high metallic content and easy access are diminishing [8]. Significant improvements are required for mineral resource exploration, extraction and refinement techniques to be able to maintain and increase the number of people living with everyday access to freshwater, food and electricity.

Separation of mined minerals prior to the refinement of metallic and non-metallic elements is essential for the refinement processes. That separation and associated tasks is known as mineral processing. In addition, selecting the desired minerals and discarding the waste ones reduces the amount of energy used in the refinement processes.

Multiple mineral separation techniques are used today, with some dating from many centuries ago, such as gravity based concentration. Over the ages, the equipment used to undertake the separation has evolved, especially with the advances of the industrial revolution and more recently with the advance in computer aided design (CAD). However, every ore and every mineral is different, which still requires intensive testing for the optimisation of a mineral separation equipment to be used effectively on a new ore.

Advances in characterisation, tracking and simulation of particles and fluids flow have the potential to simulate many iterations of new equipment designs, even before manufacturing prototype units. This type of investigation is known as computational mineral processing (CMP) which aims at predicting performance of existing equipment or to foster the design of improved ones [9, 10]. This virtual approach can be replicated for multiple virtual designs with the objective of assessing their performance before running real tests. This has the potential to reduce development and field testing costs (qualified person + equipment set-up + ore sample preparation + time) as long as the computational cost (qualified person + computer set-up + time) is lower. This computational cost is expected to decrease overtime because of the increase in computer power, improvements in software (less user input required) and the reuse of previously built simulations. An important task preceding the wide use of CMP is the experimental production of reference information about the particle and fluid flow behaviour for validation of a simulation. This thesis presents the development of a reference case of particle flow measurements for the processing of iron ore within a gravity spiral concentrator.

1.1 Thesis objectives

The main goal of this research project was to build measured knowledge about mineral particles flow and the separation of high and low density particles in an iron ore spiral concentrator. This was accomplished by completing the following sub-objectives:

1. The first objective was to assemble a positron emission particle tracking (PEPT) experimental set-up able to provide information about real particle motion in the spiral concentrator. This was completed by the characterisation of the particle flow field via the following quantities:
   (a) Particle trajectory
   (b) Particle velocity
   (c) Particle acceleration
2. The second objective was to measure the magnitude of the secondary flow affecting the particle transport.
3. The last objective was to measure the effect of the addition of wash water at the particle scale.

1.2 Thesis scope

To obtain experimental particle motion measurements, the PEPT technique with direct activation of tracers was used to track quartz and hematite particles ranging from 90 µm to 1400 µm in diameter. An established particle tracking algorithm was used [11].

The novelty of this work being in the fact that no previous experimentation measured a particle flow field in a spiral concentrator as presented in this thesis. The experimental results provide novel information on representative mineral particles behaviour in the spiral concentrator, which is a clear improvement in the knowledge of particle separation for this widely used device.

1.3 Thesis structure

The thesis is presented in six chapters with the following content. Two appendices present numerical simulation work and code used for the data analysis.

Chapter 1 - Introduction and thesis structure: The description of the thesis objectives, scope and chapters content is presented.

Chapter 2 - Physical separation of minerals: Key notions of mineral processing and the effects of various forces on particles in a concentration system are presented, with details regarding the main factors influencing gravity concentration. Pertinent particle and fluid flow notions are introduced.

Chapter 3 - The spiral concentrator: A review of the research undertaken on spiral concentrators since their introduction in the early 1900's is presented. In addition, description of the clear water flow in the spiral is provided as well as description of the different modelling approaches used to this date.

Chapter 4 - Positron emission particle tracking: The technique of positron emission particle tracking (PEPT) is described. Details of detector set-ups, production of small tracers (<500 µm) and data analysis is explained.

Chapter 5 - Particle flow within a spiral concentrator: The results of the experimental program are presented. Analysis and discussion of different motion pattern are introduced.

Chapter 6 - Conclusions: The conclusions of the research are presented with the explanation of the contributions to the original knowledge. Additionally, future research directions are suggested.

Appendix A - Preliminary numerical simulation: A preliminary numerical simulation of the particle and fluid flow in the spiral is presented as a starting point for future work.

Appendix B - Particle tracking analysis code: The MATLAB [12] code used to analyse the PEPT data is provided.

Chapter 2

Physical separation of minerals

Minerals occur as natural inorganic substances with different chemical compositions and atomic structures affecting their properties [13]. Harvesting only the technologically and economically useful minerals is the key idea of mineral processing.

2.1 Basics of mineral processing

Rocks are matrices of different mineral grains, some of which are valuable, while others have low to no market value. These low value minerals are known as gangue, and a mixture of valuables and gangue minerals with overall economic value is an ore. Considering that the gangue portion of the ore has little or no value, separation of the valuable minerals is required before transportation and refinement of the component of interest (*e.g.* metallic elements). The separation of the valuable minerals from gangue is mineral processing, the main objective of which is to reduce the amount of low value minerals sent to the refining or smelting process. This is required in order to minimize the handling and energy cost associated with downstream treatment, which may render the process impossible due to process and cost limitations. Mineral processing aims at recovering as much of the valuable mineral while rejecting as much as possible of the gangue. This brings in the concept of metallurgical efficiency which is described by grade and recovery, two important measurements of mineral processing performance [14].

The percent of a component (most commonly by mass) in an ore is grade (G). It represents the ratio of the mass of one of the component (m_1) over the total mass of the ore sample (m_t) being evaluated (Eq. 2.1). Grade is calculated for different process streams as example: feed grade (grade before a unit operation), concentrate grade (grade of the valuable stream), tailings grade (grade of the gangue stream). It is worth mentioning that grade is commonly based on the metal content of an ore (*e.g.* the maximum copper grade of a chalcopyrite ore is 34.6% which represent pure chalcopyrite mineral based on the mineral chemical composition). Typical grade of common metals in their natural ore at today's mining operation are: gold (2 g/t), copper (1%), nickel (2%), zinc (8%), lead (5%), iron (25 to 62%) [8, 15].

$$G(\%) = \frac{m_1}{m_t} \times 100 \tag{2.1}$$

Recovery (R) is linked to the upgrade (or downgrade) taking place in a mineral processing unit operation. It represent the ratio of the final mass of one component (m_{1f}) over its initial mass (m_{1i}) in the feed stream (Eq. 2.2). In other words, it represents the fraction of the component that was kept or discarded during a unit operation or overall process.

$$R(\%) = \frac{m_{1f}}{m_{1i}} \times 100 \tag{2.2}$$

In theory, a recovery of 100% (all the valuable present in the ore) at a valuable mineral concentrate grade of 100% (pure valuable mineral) is the objective of a mining company. In reality, limitations to current large scale mineral separation techniques makes this impossible to attain. Instead, optimisation of the grade and recovery is done based on the market price of the mineral considering the quantity (recovery) and quality (grade) of the products. Obtaining both a higher grade and recovery is the enduring challenge of mineral processors.

To improve grade and recovery, mineral processing consists of two main steps: the first, liberation of the ore component, the second, separation of the ore component.

2.1.1 Liberation

To concentrate single minerals (or native metals) from the interlocked rock matrix containing valuable and gangue, a first stage of liberation is required. This liberation is undertaken by reducing the size of the rocks to the point where most of the small fragments are composed of a single mineral (Figure 2.1). This process of breaking the rocks to achieve minerals liberation is known as comminution [14, 16]. It starts with blasting in the mine, where part of the rock is fragmented to a size (<1000 mm) manageable by earth moving equipment (shovels and trucks). Then crushing takes place to bring the rocks to a size (<300 mm) manageable by continuous material handling systems (apron feeder, conveyor belts, trains). Once crushed in coarse particles, the ore size is further reduced to the liberation size (<2 mm, depending on the ore mineralogy) by grinding in tumbling or stirred mills. Starting at this stage, most of the ore particles handling will be done on a wet basis. A mixture of water and mineral particles is formed by the addition of water to the grinding mills.

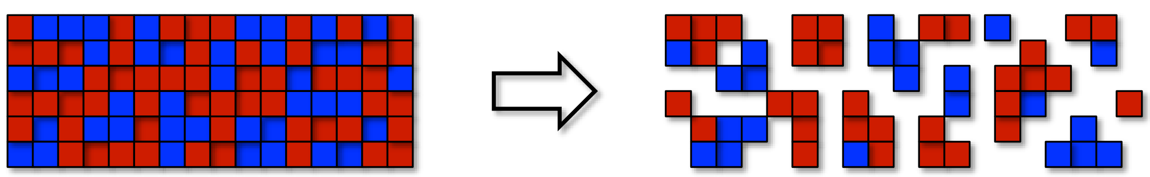

Figure 2.1 – Liberation of the components of a binary ore.

2.1.2 Separation

Once the mineral particles are liberated (or mostly liberated) the second stage of mineral processing can take place: the separation of the different particles based on their mineralogical makeup (Figure 2.2). This separation can be achieved by exploiting the differences in the properties of the minerals present in the ground ore.

Some of the properties are: particle size, shape, surface chemistry, density, magnetic properties and colour. Separation systems rely on the difference of these properties between the different minerals present in the ore. Generally, each separation unit will target a single specific physico-chemical property as the driver of the separation.

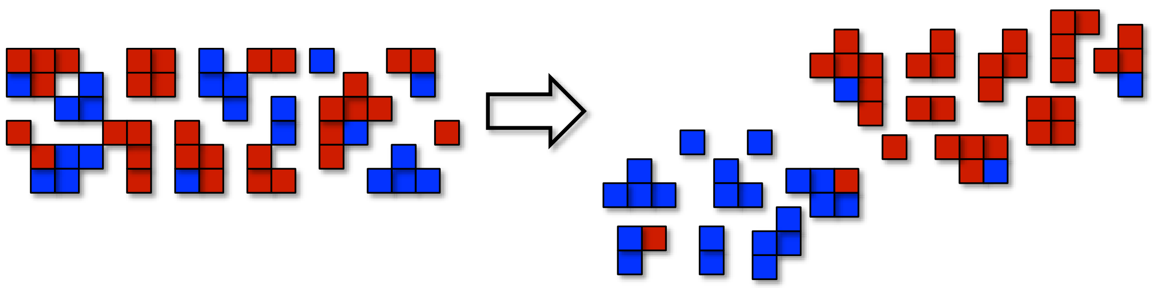

Figure 2.2 – Separation of the components of a binary ore.

Separation brings the idea of a feed stream being separated into product streams (Figure 2.3). It can be conducted under batch type conditions where a set mass of particles is separated into groups of different products. Considering the large volume treated in minerals processing plants (operations treat hundreds of thousand of tonnes of ore per day), the displacement and separation of particles is usually undertaken on a continuous or semi-continuous basis.

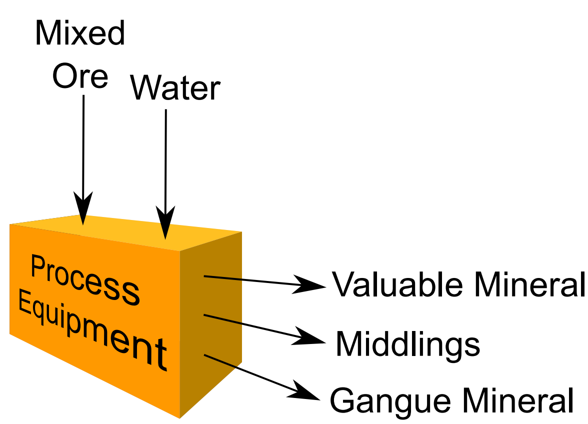

Figure 2.3 – Feed streams separated into product streams.

Handling the ground ore as a wet mixture ensures a smooth continuous flow of mineral particles in the separation equipments. The mixed particles and fluid can be pumped and carried in pipes and launders to reach the different separation steps required to obtain a quality product.

2.2 Separation principles

Mineral separation techniques are commonly divided into the following classes, based on the history of the process equipments used [14, 17]:

1. Screening and classification (separation by size and shape)
2. Dense medium separation (separation by density)
3. Gravity concentration (separation by density and size)
4. Froth flotation (separation through surface chemistry)
5. Magnetic and electrostatic separation (separation based on magnetic and electrostatic properties)

This widely used classification of mineral processing techniques does overlap as certain separation systems rely on a combination of effects. Example such as the hydrosizer, the reflux classifier and the centrifugal fluidized concentrator [18]. A specific example of a separation that is influenced by multiple properties is separation of particles based on size in a classifying hydrocyclone. In this specific case, a secondary separation effect is related to the different centrifugal forces generated on particles of similar size and shape but of different density [19, 20]. Bearing this in mind, it is important to take into consideration the many effects taking place in a separation unit in order to truly understand and improve its performance. These include the forces acting on a particle, and the relevant fluid mechanics.

2.2.1 Forces on ore particles

Considering their size (>1 µm) and velocities (<1000 m/s), the motion of ore particles in a mineral processing equipment follows the rules of classical mechanics. Their trajectories in a defined space (the equipment boundaries) are a function of the particles' initial positions, velocities and accelerations over the time of observation (or processing time). Based on Newton's second law of motion (Eq. 2.3), the acceleration of a particle ($\boldsymbol{a_p}$) is the ratio of the forces ($\boldsymbol{F}$) on this particle to its mass (m_p). Integration over time provides its velocity and second integration provides its displacement in space.

$$\boldsymbol{a_p} = \frac{\sum \boldsymbol{F}}{m_p} \tag{2.3}$$

The following is a list of some of the forces that can be exerted on an ore particle in a mineral processing unit:

1. Weight(caused by gravity)
2. Buoyancy (related to gravity effect within a fluid)
3. Other force by acceleration (inertial, centrifugal)
4. Drag (based on surface and shape)
5. Pressure gradient or lift (related to drag and surface area)
6. Contact (collision, friction, rolling)
7. Magnetic
8. Electrostatic/Electrophoretic
9. Polar interaction
10. Chemical bond
11. van der Waal's forces

The surface chemistry forces become significant for processing of small particles (<150 µm). These fines are related to the small liberation size often required by the mineralogy, or are simply fines generated during grinding. Typically, the surface chemistry forces are more relevant to the case of froth flotation than physical separation.

All mineral separation techniques rely on the different force balances between the valuable and gangue particles. This balance is specific to the properties of each individual particle. Particles with similar properties (*i.e.* same mineral, shape, size, *etc.*) will experience similar force balances, providing them with similar acceleration, velocity and trajectory during their displacement in space. This motion is different from the other mineral particles. The differential motion that occurs in a bulk volume of loose particles will create distinct groups of different mineral particles in different zones of the processing space; this is mineral separation. The differentiated zones can then be funnelled to different output streams by the mean of another transportation flow.

2.2.2 Particle and fluid flow

Two-phase mixtures of ground ore (particles) and water (fluid) are typically used in most mineral processing operations. In the special case of froth flotation, a three phase system is used for separation; composed of ore solids (particles), fluid (water) and gas (air bubbles). One purpose of wet processing is the ease of handling and transportation through pipes, launders, tanks and pumps. Such a mixture is additionally well suited for efficient displacement of particles in grinding mills and sizing screens.

Another important effect of wet processing, is the loosening of the particle bulk. Expansion of the particle bulk is caused by the similar density (in order of magnitude) of the carrier fluid (water, 1000 kg/m^3) and carried particles (minerals, 2000 to 20 000 kg/m^3). In certain case, air will be used as a carrier fluid [21–23]. Considering the much lower density of air relative to minerals (air, 1 kg/m^3), dry processing requires much higher fluid (air) flow velocities or pressures to provide similar forces (and loosening effect) on particles to that of water. Using air as the medium for particle transport and separation can be of interest is specific situations considering the costs (monetary and environmental) of using water.

The wet mineral mixture (also know as a slurry or pulp) is generally composed of 10% to 50% solids by mass. The solids particle size is generally below 2000 µm. The smallest sizes fractions (<150 µm) can be problematic for certain type of mineral separator devices such as spiral concentrator, whereas it is required for others such as flotation cell.

A number of concepts and dimensionless numbers [24] are of interest in the observation of particle flow in mineral concentration systems. The following sections present an introduction to the important ones. It should be noted that due to the many possible pulp viscosity, density and particle size, a wide range of values are possible for each of these.

2.2.2.1 Viscosity

Fluid viscosity (μ_f) is the ratio of the shear stress applied to a fluid to the shear rate produced on the fluid. In the case of a particles and fluid mixture, the viscosity of the fluid phase is not different, but the apparent effect on the mixture depends on the amount of shear stress taken by the particle-fluid interface. Generally, the larger the interfacial surface, the larger the shear stress required to provide the same shear rate. This means that a mixture composed of water and smaller particles (larger surface area) requires more shear stress to obtain the same shear rate as for larger particles in a pulp or suspension. Measuring the apparent viscosity of such mixtures is challenging, especially considering the different settling rates of different particle size and densities [25–30]. Particle shape has a similar effect on the viscosity of the mixture. Porosity and shape of the particle have an effect on viscosity [31]. Elongated and flaked particles have a larger surface area for the same mass as spherical ones and will thus create a mixture with higher viscosity.

This can create difficulties in handling the pulp. A close control of the grinding size (maximum and minimum size) is thus important when considering the mineral liberation size and separation technology to be used. The idea being to keep the liberated particle as coarse as possible. This will help in reducing pulp viscosity while also saving energy at the grinding stage.

2.2.2.2 Reynolds number

The Reynolds number (Re), obtained from Eq. 2.4, is of interest in characterising fluid flow systems [32]. It represents the ratio of inertial forces to viscous forces inside the fluid flow and is a function of ρ_f the fluid density, $\boldsymbol{v_f}$ the fluid velocity, L the characteristic length of the flow and μ_f the fluid viscosity.

$$Re = \frac{\rho_f \boldsymbol{v_f} L}{\mu_f} \tag{2.4}$$

A variant, the particle Reynolds number (Re_p), obtained from Eq. 2.5, is of interest in characterising particle and fluid flow system with $\boldsymbol{v_p}$ being the velocity of the particle and d_p the particle diameter taken as the characteristic length.

$$Re_p = \frac{\rho_f (\boldsymbol{v_p} - \boldsymbol{v_f}) d_p}{\mu_f} \tag{2.5}$$

2.2.2.3 Stokes number

In the case of low particle Reynolds numbers (Re_p<1), the Stokes number (Stk) is obtained from Eq. 2.6 where ρ_p is the particle density and L_o is the dimension of an obstacle in the flow (*e.g.* bend radius, groove in surface). The Stokes number represent the ratio of the particle response time to the flow timescale [33, 34]. In others words, it enables one to determine if the particle motion inside the fluid will be similar to the fluid flow streamline (drag dominated) or not (inertia dominated). A Stokes number below 0.1 means that the particle will closely match the fluid flow behaviour; a Stokes number around unity predict the formation of particles clusters in turbulent vortices and a larger Stokes number predict that a particle will have different trajectory than the fluid flow and eventually settle [35].

$$Stk = \frac{\rho_p {d_p}^2 \boldsymbol{v_f}}{18\mu_f L_o} \tag{2.6}$$

2.2.2.4 Froude number

The Froude number (Fr) is related to open (free surface) channel flow and is obtained from Eq. 2.7 with A being the flow cross sectionnal area and W the free surface width [36]. It represents the ratio of the flow velocity to the free surface wave speed (inertia over gravitationnal forces) [14, 32, 37]. A Froude number greater than unity means that the flow is supercritical (torrential), while subcritical (fluvial) if smaller.

$$Fr = \frac{\boldsymbol{v_f}}{\sqrt[2]{\boldsymbol{g}\frac{A}{W}}} \tag{2.7}$$

The particle Froude number (Fr_p) is obtained from Eq. 2.8 with $\boldsymbol{v_t}$ the particle terminal velocity [14]. A particle Froude number greater than unity means that the particle motion does not disturb the flow ahead of itself [36].

$$Fr_p = \frac{\boldsymbol{v_t}}{\sqrt[2]{\boldsymbol{g} d_p}} \tag{2.8}$$

2.2.2.5 Weber number

The Weber number (We) represents the inertia to surface tension ratio of the flow. It is of interest if in the order of unity or less (*e.g.* thin flowing film with surface ripples of similar size than the flow depth) [32]. It can be obtained with Eq. 2.9 where L_t is the film thickness and Γ the surface tension.

$$We = \frac{\rho_f \boldsymbol{v_f}^2 L_t}{\Gamma} \tag{2.9}$$

2.2.2.6 Dean number

The Dean number (De) is related to the flow within a curved channel. It is a ratio of the square root of the product of centripetal and inertial forces to the viscous forces. It is obtained from Eq. 2.10 with the channel's characteristic diameter d_C (similar to L for Reynolds number), the radius of curvature of the path of the channel r_{cp} and the flow Reynolds number (Re) [38, 39].

$$De = \sqrt{\frac{d_C}{2r_{cp}}} Re \tag{2.10}$$

2.3 Froth flotation

This thesis focuses on gravity concentration and spiral concentrator, however it is important to mention the role of other mineral separation technique widely used, among them, froth flotation [40]. This technique is of critical importance for the separation of finely grained ore or in the case where other separation techniques cannot be used. The principle of this separation technique rely on the hydrophobic or hydrophilic properties of different minerals, by which they can be separated. The process is to create a mixture of fines particles (<150 µm), water and small air bubbles (<2000 µm) in a turbulent vessel. Because of the turbulence, the air bubble enter into contact with the fines particles. The hydrophobic particles will attach to the air bubble penetrating the air/water interface, while the hydrophilic ones will remain fully wetted. As the air bubbles rise, they carry the attached particle to the top of the vessel where a froth layer is formed. Recovering this froth layer loaded with hydrophobic particles enable an important upgrade ratio of the ore. This technique requires understanding of surface and interface chemistry as well as fluid, and gas systems dynamics. More information about froth flotation is available in detail elsewhere [40].

2.4 Magnetic and electric separation

Each mineral has different magnetic property. Minerals can be diamagnetic, which means they are repelled along the lines of magnetic force to a point where magnetic field intensity is smaller, or paramagnetic which means they are attracted along the lines of magnetic force to a point where magnetic field intensity is greater [41]. This property is used for separation in magnetic separator. Such separator can use high or low field intensity depending on the minerals magnetism difference. An important consideration for the design of magnetic separator is the requirement of the presence of a gradient in the magnetic field to ensure particle motion [41].

Electrostatic or electrical separation uses the difference in conductivity between minerals. The two main forces involved in this type of separation are electrophoretic and dielectrophoretic, respectively the force experienced by a charged particle in a electric field and the force experienced by a neutral particle in a fluid subject to a non uniform electric field [41]. Separation based on these forces has limited application considering the magnitude of the forces requiring a carefully controlled environment to ensure the absence of other dominant and non selective forces.

2.5 Gravity concentration

Spiral concentrator is the main topic of this thesis and is part of a family of techniques know as gravity concentration. These techniques utilise the difference in density of minerals contained within an ore [42]. They are some of the oldest separation techniques, as it require only small amount of mechanisation, energy and chemical inputs. These advantages are still extremely important in today's competitive minerals processing industry, especially when processing ores bearing iron, tungsten, tin, gold, industrial minerals and coal to name but a few [18]. Mechanical complexity, use of energy and chemicals are important drivers of cost, especially when it comes to large scale operations such as iron ore, coal or gold mines where millions of tons of ore must be processed each years. Luckily, density of gangue and valuable minerals (or metals) in those operations are very different. They are perfect candidates for gravity concentration as long as the liberation size is in the appropriate range (>50 µm).

The term gravity concentration is used because of the differential effect of gravitational acceleration ($g = 9.81\,\mathrm{m/s^2}$) on minerals of different density. This constant acceleration creates different forces on particles of different densities even if they have the same size (volume). The different forces bring the particles to different velocities and trajectories when they are carried inside a fluid flow (usually water).

The potential for gravity concentration of an ore can be rapidly assessed by determining the concentration criterion (C_C). Equation 2.11 present the calculation to obtain C_C from the heavy and light minerals density (ρ_h and ρ_l) and the density of the fluid (ρ_f). A concentration criterion greater than two suggests a strong potential for gravity concentration [18].

$$C_C = \frac{\rho_h - \rho_f}{\rho_l - \rho_f} \tag{2.11}$$

Gravity concentration relies on the inertial to surface forces differential (*e.g.* weight to drag ratio) for the separation to takes place. Generally, these two forces magnitudes are in the same range for particle of size of 10 µm to 5 mm. The drag force is created by a flow of fluid around the particle. This drag is a function of the flow velocity, fluid viscosity, particle size and particle surface.

Drag to weight differentiation can be achieved among others by means of, a centrifugal action, a settling action, a jigging action, a flowing film action, or by the use of a dense medium.

2.5.1 Centrifugal action

The close range of the density of a specific mineral enable its differentiation from other minerals by its weight as a result of gravitational acceleration. This weight generally represents a significant proportion on the forces balance on the particles.

At lower particle sizes this becomes less important, and drag (among other) forces become predominant.

Applying a large acceleration (5 to 300 $\boldsymbol{g}$) is a technique commonly used to improve the separation by density. It is useful for minerals of close densities and more importantly for the separation of fines particles. The weight of a particle then becomes the "accelerated mass force", having a much larger impact on the force balance around the particle. High speed rotational motion is used in many concentrator devices to produce large accelerations (Falcon concentrator [43], Knelson concentrator [44]). Their general working principle is that the feed slurry enters a rotating bowl, which forces the particle (10 µm<$\oslash$<3 mm) to the wall. In the case of the Knelson concentrator, a system of fluidizing or wash water prevents compaction of the particles on the wall. The water overflow carries the light density particles toward the tailings discharge while the dense particle stay in the groove or on the wall of the bowl. The rotation is then stopped to recover the dense particles remaining in the bowl or a special recovery system is used to remove them during continuous operation.

These concentrators are successful in upgrading ores having very low amounts of high valuable minerals per weight (<0.05%) as gold or platinum group metal ores [18]. The main drawbacks are their mechanical complexity and limited throughput (~150 t/h), plus the large volumes of water required to maintain fluidisation of the particles [18]. This has prevented their use in large scale iron ore, and other low value (per ton of minerals) separation plants.

A curved flow can also provide a centrifugal acceleration on a particle. However, to reach the level of acceleration as high as centrifuge concentrators, high velocity and small curvature are required. An example (real case) would be a particle flowing inside a hydrocyclone of 50 mm in diameter with a slurry feed velocity of 10 m/s providing an acceleration of over 400 $\boldsymbol{g}$ (at the entrance of the cyclone). In this situation, the only particles that do not "centrifuge" to the wall are the very fine ones (<10 µm) having a too great a drag to counteract the "accelerated mass force". This effectively provides an excellent separation by size. Unfortunately, the use of such devices for large scale separation by density has still not been proven viable except in the case of dense medium cyclones used for coal separation [20].

2.5.2 Settling action

Settling is the motion of a particle in a fluid due to gravitational acceleration. Free settling is the situation where the particle is not affected by contact with other particles or surfaces. The particle motion is the result of the forces balance where there are no contact forces. Terminal particle velocity is an important concept in free settling and can be determined by Stokes' Law (Eq. 2.12) at low particle Reynolds number (Re_p<1) while for high particle Reynolds number (Re_p>1000), Newton's Law (Eq. 2.13) should be used [19]. Empirical models can be used for cases in between [45].

$$\boldsymbol{v_t} = \frac{g d_p^2 (\rho_s - \rho_f)}{18 \mu_f} \tag{2.12}$$

$$\boldsymbol{v_t} = \left[\frac{3 g d_p (\rho_s - \rho_f)}{\rho_f} \right]^{1/2} \tag{2.13}$$

Where $\boldsymbol{v_t}$ is the particle terminal velocity, $\boldsymbol{g}$ the gravitational acceleration, d_p the diameter of the particle, ρ_s the density of the particle (solid), ρ_f the density of the fluid and μ_f the fluid viscosity. Hindered settling is the situation where, in addition of the other forces, particle-particle and particle-surface contact forces are present and affect the particle's forces balance. This situation becomes significant when the solids content of the mixture is greater than 15 % by volume. The terminal velocity of a particle in this case can be approximated by the modified Newton's Law (Eq. 2.14) where k is a constant and ρ_m the mixture density [19].

$$v = k[d(\rho_s - \rho_m)]^{1/2} \tag{2.14}$$

Different separators have been developped based on hindered settling action such as: fluidised bed separator [46], crossflow separator [46], reflux classifier [47, 48]. Their general working principle is having a flow of mixed particles (up to 20 t/h/m^2) entering from the top of a water-filled chamber. This chamber is equipped with a device that injects an upward flow of clean water. The upward water velocity is matched to some of the solids settling velocity, usually the fine dense particles. These particles are at equilibrium between upward drag and downward weight. This forms a bed of solids at a certain level of the chamber. The light particles cannot cross this bed and are carried upward (to the overflow) by the flow of water. The dense particles are able to cross the bed and continue to settle in the lower part of the chamber (to the underflow). Operation of such devices require accurate control of water flowrate and particle size (to prevent coarse light particles penetrating the bed and flow down) [18]. This type of separator is of interest for the processing of fine iron ore particles at a high throughput.

Settling is present in most wet mineral separation equipment and should always be considered while designing or optimising such a device. In extreme cases, settling can cause particle accumulation to the point where operation of a device must be stopped (sanding). This can significantly affect the performance of a circuit considering the down time required to stop, clean and restart equipment.

2.5.3 Jigging action

Jigs are a type of device in which mineral particles with different sizes (150 µm$< \oslash <$10 mm) and densities are separated by a moving particle bed (processing of a narrow size class is required) [18]. The bed acts as a density and size filter [20]. The feed slurry is introduced at the top of the bed. The fluidisation level of the bed (expansion-contraction) is controlled by an alternating water flow (upward-downward). In this system, the light particles cannot settle fast enough to pass trough the particle bed and moves on the upward side (carried up and sideways) to the light particles recovery zone. The dense and small particles settle trough the bed and reach the dense particles recovery zone on the underside. The alternating motion (high upward velocity, low downward velocity) of the water in the jig combined with the addition of water from the underside of the bed help the upward motion of the light particle, while it is not sufficient to stop the settling of the dense particles (even if small). Optimisation of the parameters of the alternating motion enables the separation of smaller particles (∼150 µm). The jig separation principle is based on the difference in weight coupled with similitude in drag for particle of a similar size but of different density. Jigs can be used in the beneficiation of iron ore in the size range of 1 to 30 mm [49].

2.5.4 Dense medium separation

Considering its relatively high availability and low cost among many others properties, water is the fluid normally used for mineral processing. Most minerals are of higher density than water. However, in certain situations, a medium of density higher than one of the minerals in the ore enables a change in the concentration criterion (Eq. 2.11) and affects the sink and float behaviour of the ore particles. This enables the use of gravity concentration techniques that would have otherwise not been possible, between minerals with fairly similar densities.

Either heavy liquids (used at lab scale) or mixtures of water and fine dense particles (magnetite or ferrosilicon for industrial scale) are used as dense fluid (medium). Variation of the fine dense particles (media) content enables adjustment in density of the medium, allowing for a precise separation [20].

Combinations of dense medium and centrifugal concentrators enables the separation of a wide range of particle sizes down to 500 µm, but the technique performs better for coarser particles >2000 µm [20, 50]. Fines can be problematic as they increase the viscosity of the medium due to their large surface area. Complexity of the circuit for media recovery and cost of media lost are the two main drawback of using dense medium separation.

Dense medium separation is widely used in coal processing. Some operations use it to upgrade iron ore, with ferrosilicon particles being the media [50, 51]. In the later cases, the iron ore separation is for lump and coarse ore particles (>1 mm). The fines particles being screened out of the ore before the dense medium separation and being treated by spirals concentrators. This size limit is related to the increase in medium viscosity caused by the fines, this makes drag force to be dominant in the fines particles' force balance.

2.5.5 Flowing film action

In the situation where a layer of fluid is flowing on a solid surface, the fluid in direct contact with the solid surface is stationary. The velocity of the fluid increases with distance from the solid surface, to reach a maximum at the fluid layer free surface (laminar flow) [52]. Particles found in the fluid layer are subjected to different magnitudes of fluid drag based on the fluid velocity at the layer in which they are. Particles at the top layer experience higher drag than particles close to the solid surface.

Dense particles settle faster toward the solid surface than the light particles. This means that light particles are carried faster by remaining for a longer time in the upper layer of the flow considering their slower settling velocity.

An oscillating solid surface motion aligned with the flow direction help in the separation of light from dense particles: slow forward (denses and lights go forward), fast backward (denses go backward with the stationary water at the solid surface, lights stay in the forward moving upper layer of fluid).

There are a number of mineral separation devices which are based on this principle. Among them is the traditional pan. Panning is one of the oldest and simplest mineral concentration technique and is still used in artisanal gold mining. For concentrate upgrade, shaking tables offer excellent mineral separation. They are feed with a slurry containing about 25 % by weight of ore particles. The slurry moves along a tilted riffled surface (oscillating in the direction of the riffles). Addition of a fresh water stream perpendicular to the table motion carries the light particles to the tailings side while the table motion carries the dense particles to the concentrate side [18]. Use of a shaking table is not ideal for large tonnage operation considering that they require a large footprint.

Friction between a rolling particle and the solid surface is a source of resistance to motion for the particle at the bottom of the film. In the case of a slurry containing different size classes (full size range of 100 µm< to <3 mm), the small particles tend to accumulate at the solid surface whereas the coarse particles are brought over the small particle by Bagnold forces or interstitial trickling [20]. It is then of importance to process narrow size ranges on flowing film concentrators to truly separate particle by density rather than size. Additionally, maintaining a laminar flow is important to prevent turbulence, which reduces particle separation by density. With the advance of flotation for fines particles separation, flowing film only devices have been phased out completely of industrial plant considering their low throughput per required area.

Chapter 3

The spiral concentrator

The objective of this chapter is to provide a review of the literature available on spiral concentrators and present a summary of spiral development since their introduction to the field of mineral processing in the 1940's. The following sections describe the units and their applications, before providing detailed information about their design, pulp flow properties, operation and simulation.

3.1 General description

A spiral concentrator is a mineral separator composed of a profiled trough wrapped around a central structural post which separates mineral particles based upon difference in density. A pulp of ground liberated minerals and water is fed at the top of the spiral by a pulp feed distributor (Figure 3.1).

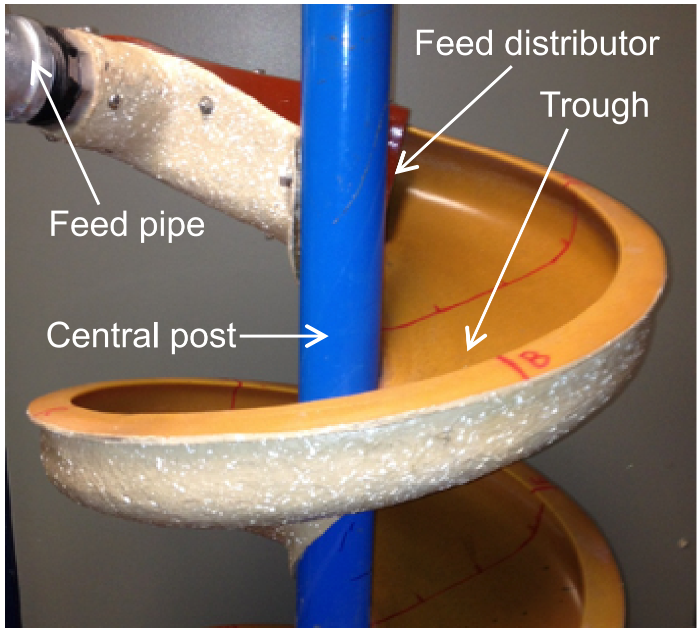

Figure 3.1 – First turn of a Wallaby trough spiral, manufactured by Mineral Technologies.

As the pulp descends along the inclined trough surface under the effect of gravity, the helical design produces a constantly changing flow direction. This causes the accumulation of pulp at the outer radius of the trough. This increases the hydrostatic pressure at the base of the pulp film in the outer region, which in turn, generates an inward flow of the lower pulp layer. As this inward flow reaches the inner radius of the trough, the pulp accumulation and associated hydrostatic pressure effect disappears and the pulp top film layer move outward again.

Sedimentation rates of the mineral particles in this complex flow depends on many factors, among which particle size and density are the most important. The differential sedimentation rate between particles of different densities in combination with the inward and outward flow layer generates the particle separation. The dense particles predominantly report inwards while the light particles move outward. Concentrated dense particles are removed at the inside of the trough while light particles and most of the water from the pulp are recovered from the outer radius.

Considering the low energy requirement (*i.e.* pulp pumping to the top of the spiral) and the low manufacturing cost for the curved channel, spiral concentrators are used in many different mineral separation applications, as described in Section 3.2.

3.2 Applications

The main uses of spiral concentrators have traditionally been in the beneficiation of iron ore, mineral sands and coal. In addition, many other applications were reported considering the low capital and operating costs of this density based separator.

3.2.1 Iron ore

Many fine grained iron ore deposits around the world require removal of different oxide gangue compounds of silicon, aluminium, calcium, phosphorous and sulphur before being used in steel manufacture. These gangue minerals have a lower density ($2.6<\text{S.G.}<3.6$) than the common valuable iron oxides of hematite (S.G.=5.26) and magnetite (S.G.=5.17).

In addition to these deposits, increases in iron ore price, as seen during the 2009-2012 period, leads lump iron ore producers to use spirals as a cost efficient device for processing accumulated "waste" dumps or tailing ponds. These are filled with small sized ($<3000\,\mu\text{m}$) lower grade ore and their reprocessing has proven economical in some cases [53–55]. The same idea applies to the reprocessing of pelletizing plant tailing ponds [56].

Spirals have been used in upgrading iron ore from shortly after their industrial introduction in the 1940's [57]. Iron ore exploitation is a large volume industry with modern producers having sites producing over five millions tons per year of saleable concentrates. The spiral concentrator, being a low capital and operating cost separator, is critical to this industry.

In this application, losses of valuable iron carrier particles are mainly in the size classes smaller than 75 µm and coarser than 600 µm [58]. Additionally, the final spiral concentrate impurities are related to light gangue particles between 75 and 212 µm in size [58]. This highlights the difficulty for spirals to separate particles of size smaller than 300 µm. Unliberated middling and free gangue particle of size of 75 to 300 µm are thought to be recovered by entrapment [59]. This is the main justification for the use of wash water in many iron ore operations, which is described further in Section 3.4.6.

3.2.2 Mineral sands

Spiral concentrators are widely used in mineral sands beneficiation for the production of ilmenite, rutile, zircon and monazite concentrates [18, 60, 61]. They are used in the cleaning of silica sand from iron minerals for use in glass manufacturing which requires excellent purity (<0.1% iron content). This purity level can be achieved using multiple stages of spirals to produce an incremental concentrate [60, 62].

3.2.3 Coal

Cleaning of coal from sulphurous and siliceous minerals is an important application of the spiral concentrator. In this case, the relative density of separation is from 1.5 to 2.0 [63], which means that valuable coal and gangue have a close density. This requires a slightly different design of spiral than for iron ore and mineral sands processing. The coal spirals have a shallower trough and larger diameter, to produce a lower pulp velocity and less turbulence.

The introduction of spirals to coal cleaning plants was initially to divert the small size fraction (<3000 µm) from the shaking table feed, which enabled a larger throughput on the table when treating a coarser feed [63, 64].

3.2.4 Gold

In the gold industry, wash waterless spirals were initially used in alluvial deposits and later in hard rock gold operations for the recovery of coarse gravity-recoverable gold (GRG) [65]. The use in such application is related to the spirals' low cost and low energy intensity for the rejection of large volume of gangue [66]. Preconcentration with spirals reduces the use of environmentally harmful chemicals. For example, spirals can be used before leaching to recover gold particles that would otherwise require large volume of chemicals [67]. Another advantage of spirals in the processing of gold ore is their low weight. They can be easily assembled and transported on modular plants for set-up at the location of small scale alluvial gold deposits [67].

An important aspect to consider in the application of spirals (or other gravity based technique) to the processing of gold, is the effect of particle shape. Gold, being ductile, has tendency to form flaky particles which can have a large drag considering their size and mass. Careful consideration of preprocessing stages or the mineralogy of the deposit itself are important to maximise gold recovery with spirals. For the same reason, wash waterless spirals are much more efficient for gold recovery. Wash water tends to wash the flaky particles to the outer tailings stream.

Development of spirals able to treat small particle size (down to 10 µm) was an important milestone for the processing of previously uneconomical fine alluvial gold deposit [65, 67, 68].

3.2.5 Other minerals

Spiral can be used in the beneficiation of any ore having a difference in density of its component minerals as long as the particle size is in the range of 50 to 3000 µm. They are used in the processing of hard rock ilmenite, a main source of titanium dioxide [57]. They can be found in the recovery of chormite, manganese ore, tin ore, uranothorianite, baddeleyite, diamonds and for oxided copper-lead-zinc ore [69]. Others applications for the upgrade of tantalum ore, vermiculite, barytes, mica and tungsten ore have been reported [57, 60, 70].

3.2.6 Miscellaneous applications

Spirals were quickly seen as inexpensive minerals separation units and were used in the reprocessing of waste materials (mineral sands tailings and coal fines (<6 mm) not worth extracting at the time of disposal [71, 72]). These applications are similar to their use on fresh ore, with the exception that those streams can have small particle size distribution and very low valuables content.

Operation of spirals is possible with the use of sea water, an advantage for areas lacking fresh water [73].

There is a potential of using spirals in the valorisation of slag, construction and demolition waste or for remediation of contaminated soils which require low cost upgrade to have any economical interest [74–76].

Another specialty application is with the use of reagents to change the wetability of some of the mineral particles which render them hydrophobic. These will be carried at the outward stream of the spiral, floating on the bulk of the water flow [57].

3.3 Spiral development

To date, the majority of spiral development has been based on empirical experience. The input of skilled operators and manufacturers is of critical importance for the success of a new spiral design. Furthermore, new ore processing plants are generally built by selecting a spiral design from the manufacturers catalogues. Only in the case of very large order would a special design specific for the ore to be treated be developed. This section describes the general history of the spiral concentrator, the circuit arrangement and recent units used for the treatment of iron ore.

3.3.1 Historical considerations

Spiral concentrators in the early 1900's were used to clean coal ore on a dry basis. They were made from pieces of metal sheet fixed at an angle around a central post forming a spiral of a few turns depending on the coal type to be treated [77]. This design evolved to a helical rectangular channel with a taper from the first turn to the last (from wide to narrow diameter) where the products were split in three groups: concentrate, middling and refuse. These units were still operated on a dry basis (8 to 10 t/h). Operational experience showed that a smooth surface was more beneficial than a corrugated finish for the conditions of this time [78]. They were used to process a relatively coarse particle feed (>10 mm) on steep pitches (700 to 900 mm), sometimes with a small film of water used to help in the material flow [60].

An important revolution in spiral design was the development of the Humphreys unit in the 1940's [79–81]. This design was developed for the separation of heavy minerals from light gangue in minerals sands operations and targetted particle sizes below 2.5 mm. Among others, Humphreys spirals advantages included their high capacity per operator and their low installation, operation and maintenance cost due to the absence of moving parts [57]. These units were quickly tested and used in coal processing. They became the first widely commercialised spiral concentrator being used for both heavy minerals separation and coal processing. Their trough channel of modified semi-circular profile was fed with a fully mixed wet ore pulp rather than a coarse dry bulk. They were made out of moulded cast iron segments (120 deg fraction of turns) with a pitch of 250 to 450 mm. Each segment was equiped with a take off port close to the central column to remove the dense particles concentrating inward [72]. Wash water was added to the inner side of the pulp stream, distributed from the centre of the helix. Spirals of this type were used for iron ore concentration in the late 1940's by Cleveland Cliffs Iron Company at the Hill Trumbull Mine in the United States [31].

Application to iron ore separation expanded in the late 1950's [57, 82]. In 1958, the first large iron ore spiral concentration plant was built in Liberia to produce just over one million tons of iron ore concentrate containing approximately 65% iron with a recovery of 72% from the mined ore [82]. In this case, ore was fed at a size below 850 µm after considering the minerals liberation size [57].

In the early 1960's the Lac Jeannine iron ore concentrator plant was built in the Labrador Trough region of Canada. This plant contained over 2000 Humphreys spirals to concentrate specular hematite [31].

In 1962, the world largest spiral plant was started by the Iron Ore Company of Canada at Carol Lake in Labrador, Canada [83, 84]. In this plant, ore containing hematite, magnetite and quartz was ground below 1410 µm and processed in two size fractions: coarse (80% >105 µm), and fines (66% <105 µm) on dedicated spiral circuits, each circuit being constituted of rougher, cleaner and recleaner spirals stages. The commissioning of this complex assembly of more than 4000 spirals, launders, pipes and pumps showed that careful adjustment of pulp solids content and pulp flow velocity was critical in the operation of the circuit to provide efficient ore distribution and prevent sanding and blockage.

In 1965, a similar concentrator plant was started at the Scully Mine (Cliffs Natural Resources) in Labrador, Canada near to the Carol Lake plant [85]. This plant concentrated hematite from quartz and manganese with a two-stage circuit (rougher, cleaner) of 1152 spirals. The carefully distributed feed of the rougher stage was a pulp of ground ore (<600 µm) at 30% solids content with both rougher and cleaner stages having five-turn spirals [86].

Mount Wright iron ore concentrator (ArcelorMittal Exploitation Miniere), also in the Labrador Trough, started an operation of over 8000 spirals arranged in a double start configuration in 1975. The circuit of this plant comprised three stages (rougher, cleaner, recleaner) with regrinding of cleaner spirals tailings and recirculation of recleaners tailings to the rougher stage.

During the late 1970's, Mineral Technologies (Australia) manufactured spirals with many different trough profile designs, each one having different advantages for different ore types [87]. The steep pitch used for certain applications (>350 mm) enabled two or more troughs to encircle the same central post. This was a huge advantage for reducing plant footprint as capacity was doubled (by doubling the number of troughs) without increasing floor space or launder requirements [87].

During this period, spiral trough roughness (joint misalignment), weight (cast iron) and fabrication complexities (casting) were improved by the use of other materials, such as concrete or polymers and fibreglass composites [87, 88] or even zircon embeded fiberglass for abrasion resistance [60]. Fiberglass quickly proved to be the material of choice as it enabled manufacturing of light multiple-turn troughs in a single piece. These spirals have some structural flexibility which was seen as an advantage for stretching their height to adjust the pitch to specific applications [87]. Fibreglass was used for the helix and as the surface in contact with pulp was prone to wear, the use of polyurethane polymer linings were justified [60]. An important point is the selection of a polyurethane having the right wettability performance [88]. As of today, this is still strategic knowledge for spiral manufacturers.

In the 1980's the low capital and energy cost requirements of high tonnage exploitations made spiral concentrators attractive once more, especially when separating minerals liberated at coarser sizes than required for flotation (>250 µm). This enabled significant savings in the extra grinding and reagent costs required for flotation.

During this time, spiral applications widened to the processing of alluvial cassiterite deposits [67]. In the mineral sands industry, they replaced cones, pinched sluices and trays as more cost effective to manufacture and operate, while providing similar or better performances [88]. During the same period, spirals gradually replaced most shaking tables and allowed for an increase in performance for ore treatment in the size range of 150 (sometimes 75) to 3000 µm. The spirals were fulfilling an important task considering their operating range to be between the optimal size for flotation cells (fine) and jigs (coarse) or dense medium cyclones (coarse).

With emerging air quality regulations in the United States during the 1980's, the use of spirals extended to the removal or pyritic sulfur and ash from coal with flowsheets incorporating multiple stages of Humphreys spirals and flotation cells [60, 89–91].

Some trough designs were specifically made for coal cleaning which required a wider trough and lower pitch as the density difference between minerals is smaller in this case [87, 92, 93]. These coal designs are used for treatment of coal particles between the size required for flotation (<250 µm) and dense medium cyclones (>3000 µm) [94, 95]. Additional interest was linked to the increase in coal fines production due to mechanised mining or exploitation of complex deposits [60, 96]. Investigations were conducted on the use of spirals to treat deslimed coal fines (63 µm to 1000 µm). These studies showed that when considering the small size and required ash content, spirals should be used in combination with flotation or hydraulic classification [97–101]. With the appearance of spiral units specifically designed for the processing of coal fines, retreatment of fine coal dumps where undertaken as now economical [75].

In the late 1980's, spiral development allowed for an increase from typical feed rates of 1 t/h to 4 t/h. This jump was due in part to new trough profiles, and increases in the pulp feed density [60].

Carol Lake concentrator (Iron Ore Company of Canada) achieved recovery of over 92% in the size range 150 to 850 µm in the late 1980's with a flowsheet using spirals (Humphreys' HC-1350) and cones (another flowing film concentrator device). However one of the difficulties in this case was that about 23% of the total iron oxide particles in the size range of 38 to 150 µm were lost to the tailings even if they were highly liberated. This important loss is due to the fact that the spirals in use did not provide the hydrodynamic performance required to recover such fine particles. This fine size fraction represents about 40% of the spiral dry feed mass in this case [102]. This indicates why some flowsheet designs were moving away from spirals in the case of liberation requiring fine particle sizes (<212 µm) [103]. Recovering these fine dense particles in better designed spirals is still seen as an area for significant potential improvements.

In the early 1990's, multiple new spiral designs appeared, with some having a variable profile or pitch [104]. Since this period, different designs were available for specific mineral or ore families, which provides better performance for specific applications

[70]. Recent design improvements are mostly related to capacity increase, with units providing up to 10 t/h, and processing of finer feeds [70].

3.3.2 Circuit architecture

Early plants using many spiral units quickly proved that careful feed preparation was required in order to simplify the operation of the many spirals. Operation of banks (groups of a number of spirals) with the same parameters became common [87]. To obtain a standardised operation of a spiral bank, feed piping required careful layout for optimal distribution [105]. Having an identical feed to each unit greatly reduces the complexity of adjusting each parameters (*e.g.* wash water rate, take off port opening width).

Classification of the feed in different size classes prior to processing through different banks (each optimised for a specific size class) can provide improved recovery and grade [106]. However, considering the particle size involved (<2 mm) this option is generally difficult to implement. Recent installations have shown that the use of hydraulic classification helps in removing the finer size (<38 µm) present in the ore prior to processing, however this remains a complexity for operation and increases costs [107].

An alternative to prior classification is the operation of spirals in a multi-stage circuit. Each stage provides concentrate, middlings and rejects (tails) for further processing or recirculation. Stage processing enables the use of different flowrates and pulp densities which allows for optimal separation of different particle sizes. An example is to have a first stage with high flow rate and dense pulp for coarse particle separation and a second stage with low flowrate and dilute pulp for fine particle separation [108]. Considering multistage processing, different process flowsheet arangement of spiral unit are possible. Different minerals and deposit types can be associated with specific flowsheets [75, 109].

It is possible to use the spiral concentrator to separate particles that would require regrinding based on their liberation rather than size, the fully liberated dense particles being recovered directly, the middlings being reground while the tailings are discarded [20]. This recirculation of middling particles was shown to be beneficial to the separation efficiency [108, 110, 111]. Careful observation of particle mineralogy and adjustment of grinding size (liberation) can thus generate many improvements in a circuit's performance [59]. An operation strategy to maximise recovery while maintaining grade for a three stage spiral circuit is to pull in more middlings at the first stage, and reject (or ideally regrind and recirculate) more middlings in the last two stages [59]. Another strategy can be to treat middlings and fines on dedicated units to prevent their accumulation in the recirculating load [20].

The three stages rougher, cleaner, scavenger configuration is typical of iron ore processing in the Labrador Trough [112]. Operation of this circuit at Mount-Wright (Canada) during the mid 1980's obtained a recovery of the 150 to 1180 µm fraction close to 90% while the 106 to 150 µm and the -75 µm fraction were at 68% and 24% respectively. At the time, a study by Hyma *et al.* [112] assessed the potential of processing the feed in two separate size fractions (finer and coarser than 212 µm). Tests have shown that an improvement from 24% to 37% in recovery for the -75 µm fraction and from 68% to over 90% for the 75 to 106 µm fraction was possible. This was achieved with a lower flowrate (60% of the original) while still maintaining a iron grade of over 66% in the fine concentrate. This shows the possibility of recovering the finer size fraction with spirals while providing pulp flow hydrodynamics tailored to their size. However, the potential negative effect on throughput should be considered.

Optimisation of a multistage spiral circuit is a complex task and should be done accordingly [113–117]. Special attention should be paid to the circulating load [20, 118]. The circuit water balance should include feed solids content control and use of wash water [20]. The use of hydrocyclones between spiral stages can help in adjusting the pulp density to the optimal value. The installation of a surge bin between spiral stages can reduce the effect of feed grade variability and thus provide a more constant feed [119].

3.3.3 Modern iron ore spiral

The HC33 spiral trough (Mineral Technologies, Australia) mounted in twin starts was the rougher spiral of choice in the 2010's for iron ore separation in the Labrador Trough. It was specifically developed for iron ore producers in Brazil and Canada [119]. This spiral can also be mounted in a tighter triple starts assembly with or without the use of an externally mounted wash water distribution system [120, 121]. The wash water system of this model uses multiple static head levels to reduce the complexity of having valves to control the wash water flow [119]. This spiral offer high ore treatment capacity of up to 10 t/h per start [70].

The WW6 spiral trough (Mineral Technologies, Australia) mounted in twin starts and its variant is seen as the cleaner and recleaner spiral of choice. This model is available with seven turns, a diameter of 613 mm, a column diameter of 94 mm and a pitch of 357 mm. The trough includes two concentrate cutters per turn with a wash water system. On such spirals, pulp solids content varies from 55% solids in the inner zone to 5% solids in the outer zone.

Some of the current challenges for iron ore spirals are the ever increasing throughput, the handling of variable feed pulp density and the separation of fines [70]. These are seen as significant challenges for increasing recovery and grade of iron ore processing plants.

3.4 Spiral parameters

Applications of spiral concentrators to different ore mineralogies require selection of different parameters to obtain optimal separation. Recent spiral plant developments suggest that future operations will benefit from custom designed spirals specific to their ore body mineralogy, at least for some stage of a multi-stage spiral circuit [119, 122].

This section first presents the important geometrical features of the spiral. This is followed by a description of the operational parameters affecting performance. The workflow of the design of a spiral concentrator is well described by Holland-Batt [123] and is still relevant today.

3.4.1 Unit geometry

Important geometrical features are: profile, pitch, number of turns, feed box design, construction technologies and number of trough per assembly [20].

3.4.1.1 Profile

The spiral profile is the shape of the trough cross section. It is one of the most important parameters affecting separation.

Three radial sections of the spiral profile are required [75]. The inner section, close to central post, is for handling of the completely separated dense particle stream at high solids content (concentrate band). The second section is the wide transitional area where particle separation and transport occurs, and should enable particle differentiation by density. This is a slightly radially inclined section enabling the formation of the secondary flow. The design of this middle section is the most important and represents a trade-off between particle mobility and particle settling [75]. The third and outer section is for handling and containing the dilute pulp loaded with the light rejected particles. This section gradually becomes a vertical wall and sometime finishes in a inward upper lip to minimise overflow. This outer section affects the volume capability of the spiral rather than the separation [20].

Flat profiles (flat first section and extra low inclination second section) have been developed for separation of minerals having similar densities (*i.e.* a low concentration criterion, Eq. 2.11). This profile type is generally associated with low pitch spirals. This design is beneficial in the separation of finely ground ore (<100 µm) considering the low pulp velocity resulting from a shallow pitch which results in better selectivity

[69, 87].

Profile development with the help of computer assisted design (CAD) was introduced in the early 1980's and enabled more complexity [96]. Compound spiral designs have profile changing along the length of the trough [31, 70]. This enables accomodation of changes in pulp conditions [124]. These compound troughs were initially introduced in the 1980's for coal processing [125]. They are less susceptible to throughput variation, and have higher throughput.

Other profiles include a concentrate channel in the inner section. This can cause some throughput limitations when dealing with high heavy mineral content feed as particle mobility in this channel becomes difficult at increased pulp solids content.

The radial position of take off ports in the profile affect the working surface of the spiral as well as the metallurgical performance considering the width of the material band recovered by the port.

Spiral diameter is function of the profile dimensions. The diameter is generally between 0.6 and 1 m with extreme designs from the 1980's having up to 2 m in certain specific applications [119, 126].

3.4.1.2 Pitch

The pitch is the height of a single turn of the helical spiral trough. This geometrical parameter is the main factor affecting pulp velocity via its influence on the down trough slope [70].

Selection of the pitch depends on the specific gravity of the feed pulp. The dense coarse particles settle first on the spiral trough, and keeping these particles flowing is critical to prevent accumulation, especially at the inner zone of the profile [20]. For ore comprising a greater portion of dense mineral (*i.e.* iron ore), a steep pitch is required to ensure particle displacement down the trough. The optimal pitch should be just enough to ensure particle downward flow at reasonable throughput [75, 127].

A high pitch spiral provides higher capacity, however it can result in lower recovery if operation is not carefully managed [127]. Such spiral can process pulp with higher solids content while requiring less wash water which can have a positive effect on overall performance when compared to similar lower pitch spiral [31].

A small pitch spiral is suitable for ore with small difference in minerals densities or when fine particles content is high [127]. The low pitch spiral are then common in the processing of slow settling coal fines [64, 127]

Composed spiral designs where the pitch varies along the helix were proposed. Plants generally required multiple stages of spiral and using stage specific design (rougher, scavenger, cleaner, recleaner) is sometime less complicated than designing a variable pitch spiral.

3.4.1.3 Number of turns

The number of turns in the spiral helix is related to the pitch and profile. Those three parameters affect the length of the channel and the surface area where the pulp flows. Most recent spirals have between three and seven turns [119].

Determination of the length of a trough was addressed by Holland-Batt *et al.* [128]. The results of this study suggest that particle separation happens up to the sixth turn of the spiral, but at a lower rate after the first two turns. Another study reported a difference in efficiency of up to 15% between three and five turns spirals, favouring the five turns [128].

For certain applications in coarse light particles treatment (*e.g.* coal), short spirals produce sufficient separation as long as there is at least four turns [129, 130].

Multiple spirals of only two or three turns assembled on a single central column were suggested in the 1990's [75, 130]. The main advantage was the regeneration of the feed by remixing the pulp after removal of the spiral concentrate and tailing stream between the multiple short troughs. Different profiles or pitches can then be used on the same column and potentially replace a multiple stages circuit. It is often required to use different numbers of spiral in each stage, considering the change in pulp density caused by the removal of concentrate and tailings. This is the main reason why the multiple small trough concept is not widely used.

The use of many turns is generally required for the recovery of small dense particles. This enables the pulp to stay on the working area of the trough for a longer period of time.

Seven turns is a popular length for roughing spirals considering their performance [88]. This claim is due to the longer residence time on the trough. This advantage is downplayed in the cleaning duty, where the performance is limited by the high heavy mineral content of the pulp [88].

3.4.1.4 Feed box

Experience from manufacturers suggests that the introduction of the pulp in the trough should be parallel to the outer rising wall of the spiral profile [123]. This is thought to help in the establishment of the required flow pattern. The unverified explanation is that solids should be dispersed in the pulp when entering the trough with a low velocity. Feed distribution boxes are thus designed to ensure a homogenous pulp distribution across the width of the trough [70].

3.4.1.5 Construction technologies

Spiral troughs were initially assembled from section of turns made out of cast iron. A negative aspects of this design was the weight which increased building costs as well as the difficulty in fitting the segments together to obtain a smooth trough surface [87].

Because of rapid corrosion and wear, rubber lining protection was developed [87]. Rubber lining was used up to the 1970's, when it was replaced by sprayable urethanes. Ceramic trough spirals can be used in certain specific abrasive applications as chromite, glass sand, metallic slags and in the recovery of scrap materials [75].

The introdution of composite materials such as fibreglass for structural trough material was a revolution. It provides ideal properties for molding and structural strength at low weight and cost. One disadvantage of fibreglass is the low resistance to abrasion and therefore lining protection is still required [75, 124]. Monopolymer troughs made out of reinforced urethane have a durability advantage over urethane lined fibreglass which can cause delamination problems [75]. This option is more expensive considering the special formulation required for the surface urethane and many spirals are still manufactured with fibreglass and resistant urethane coating [119].

Other important characteristics of the materials used for trough fabrication are wettability to ensure a smooth pulp flow and shape consistancy to prevent deformation during transport, installation and operation. Ultraviolet resistance should be considered if the plant is in an open air setting, as is common in areas with a warm climate [75].

Reproducibility of spiral geometry during fabrication is an important factor in the optimisation of a spiral plants. Slight differences in spiral trough geometry can affect their performance. Use of reverse molding and proper fibreglass reinforcment design coupled with proper quality control enable to obtain constant trough geometry [70]. This aspect is still important today considering the increase in manufacturing costs associated with geometrical precision.

All parts in contact with the pulp need to have minimial wear due to abrasion and particle impact. Wear can be reduced by the use of proper geometrical design and improvement of construction materials. Sacrificial wear pieces in impact areas at the feed and outlets of the spiral can ensure a long operational life [88].

3.4.1.6 Multiple starts

Depending on the pitch, it is possible to encircle more than one spiral trough around the same central column. This is known as a multiple starts spiral. An assembly such as this is now very common with two, three or even four starts being the most used. Extreme prototypes have been made with up to ten starts [60, 126]. Assemblies with multiple starts producing throughput of more than 20 t/h are possible [124]. The idea behind the assemblies with multiple starts is the increase of throughput without increase in plant footprint, piping and launder requirements [88].

3.4.1.7 Miscellaneous

The use of magnets afixed to certain areas of the trough of the spiral has been shown to improve recovery for ores comprising magnetic minerals [131]. This is seen as a costly improvement and would probably negate the low cost advantage of the spiral. It should however be kept in mind for the processing of high value magnetic minerals and the recent development of powerful permanent magnets.

Rotating spirals have been reported to be in use, however no clear details about the potential benefit for particles separation have been provided to justify this added complexity [132].

Undocumented cases have been reported about the use of grooves on the trough surface [132]. This feature might be worth looking at in the future considering the potential effect on the displacement of solids on the trough surface.

3.4.2 Ore particle shape

Particle shape affects the separation. Particles tend to group in narrow bands depending on shape factor [133]. In some specific applications (*e.g.* mica ore), the separation is based on the different particle shapes rather than on the mineral densities.

Flaky particles can be subject to floating on top of the fluid film, depending on their hydrophobicity, and preferentially report to the outer stream even if they have a high density [133]. Similarly, elongated particles tend to report to tailings considering their large surface area [134]. This behaviour is related to larger drag force compared to spherical or cubic shaped particles [57]

3.4.3 Ore particle size

Spiral concentrators are efficient for the treatment of particles between 75 and 1000 µm in diameter [18, 126]. This represents an overlap between flotation and dense medium cyclones and can enable a much more cost efficient separation for this size class than flotation [118].

Spiral feed top sizes should be limited to a maximum of approximately 3000 µm and preferably below 1000 µm for optimal performance [87]. This is generally achieved by different stages of screening after grinding.

3.4.3.1 Fine particles

In the case of the spiral, fine particles represents the fraction below 100 µm. This is related to the drop in separation performance below this size which can be observed at sizes up to 300 µm for certain applications such as iron ore. Fine mineral particles can be found in final upgrading after regrind, for tailings re-treatment, or when a fine aluvial deposit needs to be processed [135].

Spiral models specifically designed to process fine ores exist, and provides separation down to about 40 µm [87, 136]. Flatter trough profiles, reduced pitch and a longer trough length are parameters which enables the low turbulence required for the slower particles separation on these spirals.

Having a narrow size range eases the processing of fines particles. For the operation of spirals on feeds containing a large portion of particles under 100 µm, prior feed classification should be conducted [20]. This classification, possible with hydrocyclones, eases the optimisation for each sub-size of particles.

Treatment of fines on standard spirals is possible, however it requires units dedicated to a narrow particle size range (*e.g.* treating only particles below ≈200 µm) [137]. Additionally, a dilute pulp (10 to 15% solids by mass) and a lower feed rate compared to the 200 to 1000 µm size range should be used for such application. In certain cases (mica, feldspar and hematite ore), testwork produced acceptable results for the separation of small size fraction at similar pulp solids content than on a heavy mineral spiral [138].

3.4.3.2 Slimes

For fine particles smaller than 50 µm in diameter, the term slimes is used. Slimes affect the separation efficiency of the spiral [139–141]. Their presence affects the viscosity of the pulp as a result of their large surface area. This increase in viscosity is thought to affect the separation behaviour [142]. Additionally, increases in viscosity affects the concentrate band position which can affect recovery if no splitter adjustment is made accordingly [143].

For the treatment of finely ground ore (d_{50}<80 µm) a drop in efficiency of more than 5% can occurs if the slimes content is greater than 3%. In the case of coarser ground ore (d_{50} ≈300 µm), the presence of a slight amount of slimes might not affect the separation, or can even be beneficial. However, a slimes content of more than 5 to 10% is detrimental [87]. Another problem of slimes is that they tend to follow the bulk of water flow and are weakly affected by the concentrating effect, and simply split with the water [108, 125].

Considering the detrimental effect of slimes, the use of hydrocyclones before spiral separation is a common requirement to remove these slimes [72, 96]. In the case of a spiral circuit having multiple stages, slimes in the feed are reduced after the first stage as they reports to the tailings streams with the bulk of the water fed in this first stage. In this situation, the requirement of hydrocyclones can be negated.

Viscosity of the feed pulp is an important parameter and should be maintained as low as possible not to interfere in the particles separation process [31]. Controlling the amount of slimes recirculated with reclaimed water is thus important as it has a detrimental effect on the spiral performance by increasing the pulp viscosity [31].

Slimes can cause other problems on a longer term basis by the accumulation of scale (hard deposit of slime) in the spiral trough inner and outer limits of the pulp flow. Regular cleaning of the scale is required to maintain a proper surface profile especially in the region near concentrate take off ports [31].

3.4.4 Pulp solids content

The pulp solids content is the amount of ore present in a certain mass of pulp and expressed as a percentage (% solids by mass). It is a critical parameter for the efficient separation on the spiral and for the operation of the pumping and transportation circuit around it.

Typically, the pulp solids content by mass is from 15 to 40%. Higher pulp solids content by mass can be reached in the case of coarse particle of a high density ore. In this case, the solids content by volume can be similar to lower particle density and size pulp. This type of pulp should be processed at high flow rate which prevents particle settling and accumulation. Some spiral designs are tailored toward this type of application as in iron ore processing [119]. They can process up to 50% solids by mass [31, 69, 87, 126]. Higher solids content were reported to prevent the free radial movement of particles [108, 110, 144].

Spirals for fine particle treatment requires a feed pulp density much lower than 35% with a lower feed rate (≈1 t/h) than spirals for larger sizes [136, 145]. The lower feed rate is required to maintain a more laminar flow, which improves the recovery of small dense particles due to lower turbulence.

Feed pulp solids content affects the spiral performance. Generally, concentrate grade decreases with an increase in feed pulp solids content [146, 147].

Another parameter closely related to the pulp solids content is the pulp density which is the mass per unit volume of pulp (kg/m^3). The parameters influencing the pulp density are among others, feed volume of water and ore, mineral density and particle size distribution [31].

3.4.5 Feed rate

The feed rate is the mass of pulp per amount of time (t/h). It affects the pulp film profile in the spiral which influences separation perfomance [148]. A larger feed rate generally provides a lower recovery [134, 140]. However, this larger feed rate can be beneficial in obtaining a better concentrate grade [141]. Experimental studies suggest that the relationship between feed rate and separation efficiency is mostly linear [124].

A spiral operated over its design pulp feed rate tends to lose a larger portion of the fine valuable minerals as they are washed in the tailings stream by the fast flowrate [31]. At higher than designed throughput, some coarse feed material can also bypass the stratification process and end up directly in the tailings stream [125, 149, 150].

At feed rate lower than the design value, solids settle on the trough surface and "sandbars" can form which reduces the efficiency of the separation [31].

The ideal pulp feed rate depends on the mineral size distribution and the content of dense minerals [31]. Determination of the solids tonnage and pulp density of the spiral should be related to its volume feed rate, to ensure a proper loading of the concentrate and middle zones while still providing particle flow in the concentrate zone [20].

For older spiral designs (before the 1990's), feed rates varied from 75 to 125% of the design value without having a large effect on the metallurgical performance. This is not the case for recent models as they are optimised for a single operating point that should be respected [69]. Consistency in feed preparation, distribution and ore properties is important for newer spirals [151].

3.4.6 Wash water addition

In certain situations, the addition of a stream of clear water in the particle packed pulp film can have a beneficial effect. The added water is known as wash water. It is generally introduced in the inner section of the spiral profile from a multiple-orifice distribution system in the spiral central column. Flow rate ranges between 25 and 40 L/min are common for a full spiral [31].

The primary role of wash water is to unlock light and middling particles trapped in the high packing density bed of dense particles. The added stream of water fluidises and cleans the concentrate band, and thus affects the grade of the material taken as concentrate. Wash water assists in the production of very high grade concentrate (final concentrate) where a small amount of wash water can remove fine entrained silica in the case of iron ore processing [88]. This will, however, remove some of the fine dense valuable. An increase in wash water leads to an increase in concentrate grade and a decrease in valuable and gangue recoveries [146].

The secondary role of wash water is the dilution of the thick pulp to ensure mobility of the inner concentrate band. This band has a tendency to settle and move slowly as it contains a reduced amount of water, especially when the spiral feed is at a high solids content, a coarse particle size distribution or a high dense minerals content [20, 88, 152].

The effect of wash water is dominant on coarse dense particles and on light particles of all sizes [146, 153]. It can trigger significant losses of coarse dense particles and this should be taken into acccount when adjusting wash water system parameters [153]. Wash water can cause a loss of small and flaky particles to the outer stream. Stage processing can reduce this loss as cleaner spiral are operated with less wash water addition.

Wash water distribution on a spiral bank and on a spiral itself (between addition points) has a major effect on the spiral metallurgical performance considering the injection flowrate and jet velocity [31]. Too high a wash water flow rate can have a negative impact on the separation as it diverts the dense particles away from the concentrate port or splitter [152]. In extreme cases, it can affect the separation mechanism by disturbing the separation flow pattern, causing remixing [31].

Wash water injection in the inner side of the pulp stream (close to the central post) can be directed either in a tangential or perpendicular direction to the pulp flow [31]. Recent experimental work has shown that a wash water injection stream directed against the downward flow in the trough middle zone (on the outer side of the concentrate band) helps in fluidizing the inner concentrate band for release of trapped light particles, and additionally aids in the recovery of dense minerals found in the middle zone [152].

Wash water should be clean and exempt of any large particle, wood piece, or soft matter. Screening (<1000 µm) of the wash water before distribution is suggested as a way to reduce blockage and maintenance [69]. Wash water produced from reclaimed water should be clean of fine silica (often found in tailing water) as the concentrate band in which the wash water is injected act as a filter keeping the fine silica particle entrapped which reduces metallurgical performance [31].

Wash water systems are rarely used in the mineral sands industry, while most iron ore plants using spirals use such a system [119]. Spirals without wash water have , however, been used on large scale iron ore operations for upgrading ore from ≈55% to 62% iron content [49]. In this case, a deslimed feed (>75 µm) was used to reduce viscosity of the pulp and ensure proper fluidity.

3.4.7 Take off port and splitter

Particle separation is relatively fast on the spiral trough. Dense particles can be found in the inner section of the profile as early as the first and second turns. The use of intermediate concentrate removal orifices known as take off ports (*e.g.* cutter, splitter, spoon) reduces the spiral inner zone loading [63, 123]. This feature is especially important in the processing of pulp with heavy loading of dense minerals as in iron ore plants. Removing a significant mass of the solids as high as possible in the spiral provides improvement in the separation of the middlings band in the lower part of the spiral [20].

In some applications, up to 75% of the concentrate mass can be recovered from the two first spiral turns [31]. This early removed material is generally of the highest grade considering that coarse light particles take more time to migrate inward. Consequently, take off port located in the lower turns have a large influence on the grade of the final concentrate recovered and should be optimised accordingly [31].

Different take off port geometries and trough attachments provide different advantages and difficulties. The main concern in designing a take off port is to minimise the disturbance of the pulp film, which can affect the spiral efficiency by a few percent [123]. A take off port made of a sliding opening on the curved surface enables to remove part of the concentrate stream without disturbing the flow on the trough [70].

The radial location of a concentrate port depends on the amount of valuable present in the spiral feed. A port close to the central column enables a small mass pull and is typically used for ore with a low valuable content (<5%). Ores with larger loading in valuable (such as iron ore) requires larger mass pull and multiple ports reaching a larger radius will be beneficial in increasing the recovery of a single stage of spiral. For applications where both valuable and gangue are heavy minerals, the material band (concentrate and gangue) on the spiral will be closer to the centre of the trough. In this situation, the positioning of the intermediate off take ports closer to the central column provides better selectivity than if situated on a wider radius [69].

A take off port can be installed at the outer vertical section of the profile to remove a low solids content pulp. This provides the possibility of recovering the tailings stream at a much higher density at the end of the trough [70].

Separation of the concentrate band from the middling and tailings band at the end of the trough is accomplished by the use of splitters mounted on vertical pivots on the trough. This enables to use a single adjustment of the pivots on a multiple trough assembly [70].

Once the products discharge from the trough, a products recovery box diverts each stream to different launders under the spiral bank. A products recovery box requires careful design to reduce pulp velocities, especially the tailings stream, while resisting wear and minimising splashes [70].

Variability in the feed requires constant adjustment of the take off ports [57].This optimisation should be based on each individual take off port mineralogical parameters (size, shape and mineral species) [31]. Feed pulp flow rate and solids content, as well as wash water flow rate, should be observed and adjusted before changing take off port and splitter positioning [31]. Image analysis can be used to record concentrate band details (*e.g.* width) and provides meaninful process control information [143, 154, 155]. A solution to changing take off port or splitter position could be to act on the concentrate band position by playing on the operating parameter (feed rate, feed density, volumetric flowrate) [155].

3.4.8 Repulper

The bulk of fluid is centrifuged outward as the pulp flows down the spiral. Capturing and remixing the pulp after a certain point can reinvigorate the particle bed mobility, and provides new chance for the recovery of dense particles captured in the outer turbulent zone.

Considering the higher velocity found in the outer zone, careful positioning of a deflecting bump or edge in the outer zone has the effect of diverting the dilute flow towards the middle and inner zone [70, 123]. This feature is known as a repulper. Self-adjusting repulpers can enable optimal repulping even during volumetric flowrate variation [70].

Revitalising the separation with the use of a repulper after two or three turns offer similar advantage as using multiple shorter spiral trough at a fraction of the complexity of such assembly [128].

3.5 Spiral performance

Feed capacity and separation efficiency are the two most important parameters in the design and selection of a spiral unit[119]. Separation efficiency (E_s (%)) is a macro measurment of the ore particle sorting taking place on the trough [119]. It can be calculated (Eq. 3.1) with the recovery to concentrate (R (%)), the mass yield to concentrate (Y (%)), the feed grade (G_F (%)) and the maximum possible grade of the concentrate ($G_{C,max}$ (%)).

$$E_s = \frac{R - Y}{\frac{1-G_F}{G_{C,max}}} \tag{3.1}$$

3.6 Pulp and particle flow

This section describes different experimental and theoretical considerations related to pulp and clear water flow on spiral concentrator. The important secondary circulation is detailed and known information on particle behaviour in the pulp film is presented.

3.6.1 Pulp profile and flow regime

Pulp exiting the spiral feed distributor spreads radially to form a film on the trough. This film is subject to gravity which provides a velocity high enough to centrifuge the liquid outward to the vertical section of the profile. Figure 3.2 presents an high speed photography of clear water flow in the spiral depicting this behaviour.

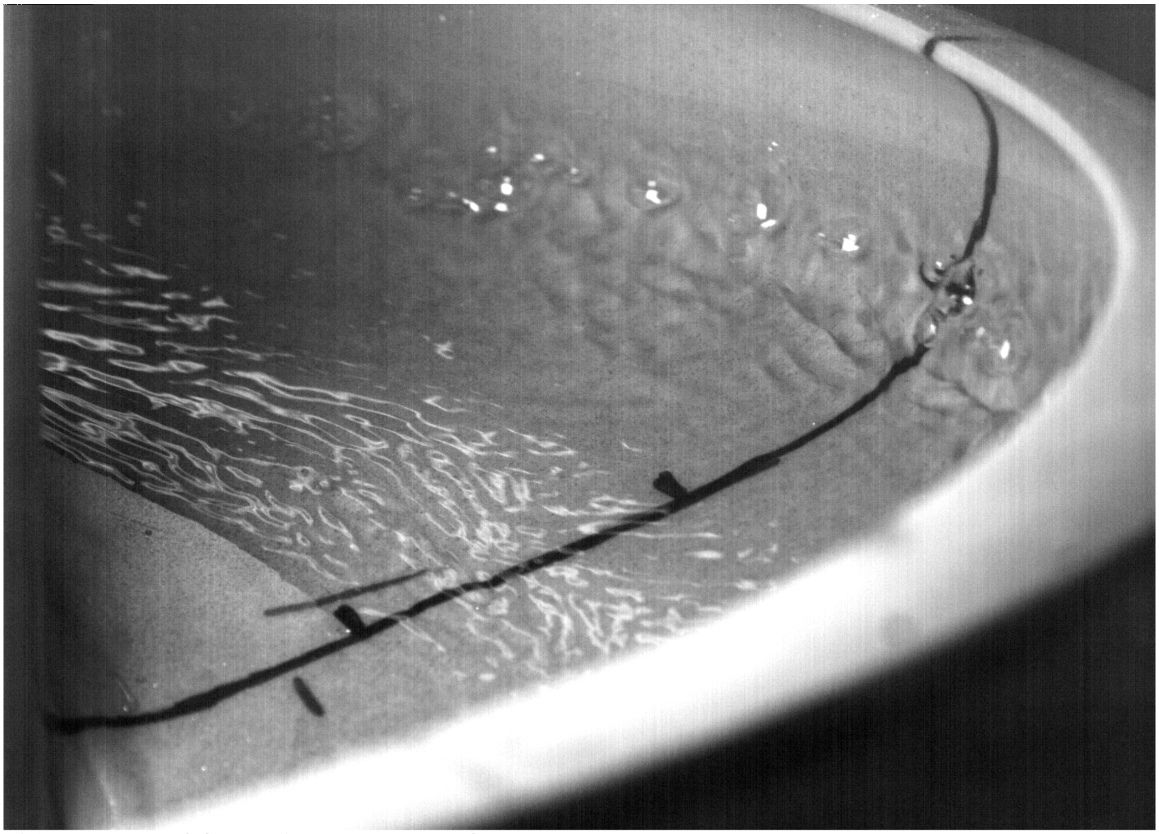

Figure 3.2 – Clear water flow inside the spiral concentrator

Pulp free surface profile is different than water flow free surface profile, mainly because of accumulation of solids in the inner zone, which increases the thickness of the pulp film in this region [156].

Pulp profile measurements initially undertaken by Dallaire *et al.* [147] have shown different pulp depths for different pulp feed rates. Following this work, pulp stream sampling observations were undertaken by different researchers [60, 63, 126]. Detailed measurements of this type were obtained by Holtham *et al.* [60] by using a sampling device which divided the pulp flow into eight radial streams, with each stream being sampled for a certain time with measurement of the pulp thickness at each stream to calculate pulp velocity. Depth measurements were inacurate considering surface waves on the pulp flow, which for this study resulted in an error of around 30% in the value of velocities calculated. This work was undertaken on an open circuit spiral with a trough profile generally used for coal separation with a pulp made of 24% of quartz <1000 µm [60]. Mainstream pulp velocities were reported to be between 0.3 m/s (inner zone) and 1.3 m/s (outer zone) [60].

The Reynolds number (Section 2.2.2.2) can be calculated for the spiral channel flow with the use of the fluid depth as the characteristic length [157]. Transition from the laminar to turbulent regime for an open channel flow is at a Reynolds number between 400 to 2000 [157]. Based on this criterion, the inner zone pulp flow is laminar while the outer section is turbulent [158].

Viscosity has an effect on the value of the Reynolds number; however, the general idea of a laminar inner zone and a turbulent outer zone is valid as the inner zone carries a high solids content pulp (increasing velocity which lowers the Reynolds number) and the outer zone has a very low solids content as most of the water will centrifuge outwards.

3.6.2 Secondary circulation

Cross circulation inside the pulp film is theorised as being the mechanism behind the particle separation taking place on the spiral [81]. This theory originates from river bend sediment flow studies [159].

The flow of pulp is seen to have multiple layers, with each having a different velocity. The top free surface layer experiences extremely low shear with the air interface on the upside and the lower pulp layer on the underside. At the lowest pulp layer, friction (no slip) with the spiral trough surface is present [160].

As the shear on the pulp is relatively small at the free surface, compared to a maximum close to the trough surface, the velocity and centrifugal acceleration acting on each pulp element is much higher at the free surface. This higher centrifugal acceleration brings top pulp film elements in the outer region up to the vertical edge of the profile [161].

As pulp bulges near the vertical wall, hydrostatic pressure builds up at the base of the film. At a certain location in the film thickness, the hydrostatic pressure is greater than the force due to centrifugal acceleration on pulp elements. The lower pulp layer will thus move toward a region of lower pressure as a result of this forces imbalance [161]. This results in an inward fluid motion near the trough surface. As the fluid reaches the inner section of the trough, this hydrostatic pressure diminishes and centrifuging restarts in a rising flow to the top layer.

Figure 3.3 presents a schematic of the primary and secondary circulations present on the spiral. The secondary circulation is thought to take place predominantly in the middle zone of the pulp film. This flow is classified as a Prandtl's secondary flow of the first kind [161].

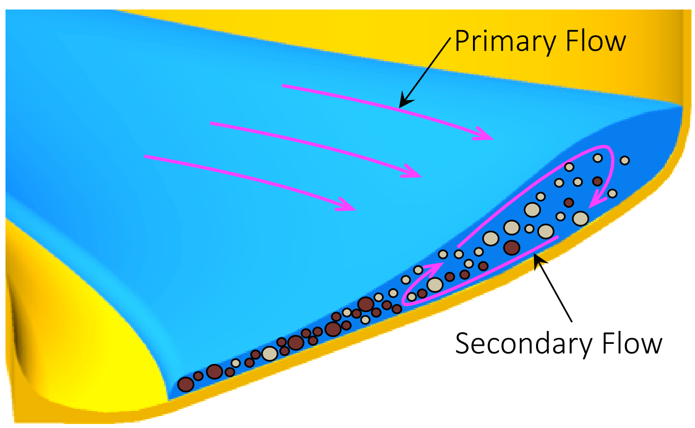

Figure 3.3 – Primary and secondary flow present on the trough

The secondary circulation was observed by the use of dye and fine treads of fabric to track clear water flow on a fine mineral spiral trough [60]. These observations of threads and dye injected at the trough surface have shown deviation of the secondary flow from the trough direction to be between 2°and 5°at the trough surface and between 4°and 8°at the free surface [129, 157, 161, 162]. Measurement error of approximately ±5°was reported on these values.

Based on these deviation angles, an approximation of the secondary circulation velocity (radial velocity) of clean water is below 0.01 m/s at the trough base and between 0.01 and 0.05 m/s at the free surface [157]. Accuracy of those measurement was reported to be within ±30%. The calculations are based on the assumption of a laminar velocity profile in the inner zone, and of a smooth turbulent flow in the outer zone [157]. This assumption might not be valid in the inner zone as the primary flow profile is likely to be distorted by the secondary circulation [157]. However, even if calculated for clear water flow, this gives an order of magnitude of the effect of secondary flow on particle radial motion.

In this case, the largest deviation would have produced a particle inward migration from the outer zone to the inner zone within approximately 1.25 turns for a particle exactly following the flow of water [161]. This somewhat explains why particle separation occurs rapidly on the spiral (*i.e.* 2-3 first turns). However, the magnitude of the secondary flow present in the case of a high density pulp is still unknown, as is the particle velocity in this flow.

Another experiment used particle image velocimetry (PIV) to measure primary and secondary flow velocities in clean water flow on a coal spiral [163]. In this PIV study, light scattering rhodamine particles of <50 µm were mixed in clean water and observed flowing in a specially made clear section of a spiral. Recording of the distance between rhodamine particles light scattering events generated by a timed impulse laser illumination allowed for their velocity to be determined [163]. Considering their size and density, rhodamine particles were expected to closely follow the clean water flow. This provided improved precision on water velocity when compared to stream sampling and film thickness measurements. The nature of the flow without solids is somewhat different than with a high solids content of a full size distribution of different density particles. However, these PIV measurments confirmed the magnitude of the secondary clear water flow velocity with unsteady values between 0.01 and 0.05 m/s [163]. Another observation from these studies is that an increase in feed flow rate increase the magnitude of the secondary circulation [157].

Considering that these measurement were carried out for water only, or very dilute flow (in the case of PIV), it can be difficult to make assumptions regarding the particle motion pattern and velocity in a dense mineral pulp. Observation of particle flow is thus seen as a milestone in the development of a better understanding of the spiral particle concentration process.

3.6.3 Particle flow

The behaviour of particles in the pulp film is affected by different mechanisms. Among them are free and hindered settling, flowing film, stream cross rotation, centrifugal force, stratified bed and interstitial trickling [20, 63, 126, 127, 164].

Settling is thought to be the main process by which the particles separate [128]. Different settling rates for different particle sizes and densities is a major factor in the recovery of particles to the lower pulp layer [160]. This initial separation is followed by transport and particle bed mechanisms in the flowing film which in turn enables recovery of separated particles [128].

In the outer turbulent region, the higher density particles are more likely to settle and thus have a higher chance of being caught by the lower inward moving pulp layer [124]. Considering the reduced velocity of the lower pulp layer, these dense particles are less affected by the centrifugal effect [127]. They are transported in the inner section of the spiral. This results in a concentration of dense mineral particles at the inner zone of the trough. The light mineral particles of similar size are less affected by the lower layer of the pulp film as their settling rate is lower.

Once in the inner zone, the raising component of the secondary flow has the capacity to lift light and small particles [124]. They are carried outward in the upper layer of the secondary flow. Holland-Batt [160] suggested that the spiral inner zone controls grade of the concentrate band by the action of the rising current of the secondary flow, while the outer zone controls the recovery via the difference in settling rates.

For an increase in feed rate, the vortex flow in the outer zone increases. This is due to the larger amount of fluid reaching the outer wall under centrifugal action. This increases turbulence which reduces the settling potential and the recovery of particles in the lower layer of the pulp.

Particle separation and transport in the spiral are mainly related to two processes, suspended-load motion and bed-load motion [129]. The suspended-load motion is where particles are suspended in the upper layers of the fluid. It is expected to be where most of the separation is taking place. The bed-load motion is the case where particles collide with each others to a large extent. It is characteristic of the inner zone where the solids content is much higher.

Francis [165] and Leeder [166] proposed different modes of particle transport inside flow similar to what is found on the spiral trough. These modes can be regrouped in the two load motion processes. The proposed modes, listed in Table 3.1 from Holtham [156], account for inter particle collisions and flow turbulence in a dense pulp. The mode of a particle is function of its density and size as well as the pulp flow around it. These variables result in different transportation modes for different particles, which enables *particle separation*.

Table 3.1 – Particle transport modes, adapted from Holtham [156]

Load process	Transport mode	Description
Suspended-load motion	Uninterrupted saltation	Particle makes ballistic trajectory jump
	Uninterrupted partly suspensive saltation	Particle ballistic trajectory is modified by the effect of fluid turbulence
	Uninterrupted suspension	Particle suspension by the effect of fluid turbulence
Bed-load motion	Rolling	Particle in contact with the bed
	Interrupted partly suspensive saltation	Same as uninterrupted partly suspensive saltation but with addition of upward acceleration due to particle collision
	Interrupted suspension	Particle suspension is maintained by both fluid turbulence and particle collision

On the spiral trough, solids concentration by mass varies from over 70% in the inner zone to less than 3% in the outer edge of the profile [156, 162]. The accumulation of solids in the inner zone brings different effect related to the bed-load process [160]. Interrupted partly suspensive saltation and interrupted suspension are the modes related to the Bagnold normal stress (or Bagnold force) [167].

In a situation of Bagnold normal stress, a particle under shear is subject to a force normal to the shear plane, and proportional to the square of the particle diameter. For a particle bed composed of a size distribution at a given rate of shear, larger particles are subject to an exponentially larger force (*i.e.* square of the diameter). For large particles (>1000 µm) the particle-particle interactions in the high solids content stream are then more significant than settling behaviour [133]. These large particles move up in the bed until equilibrium between the Bagnold normal stress and gravity force is found. This equilibrium arises at the top of the particle bed where shear and thus the Bagnold normal stress is lower [60, 156]. Bagnold normal stress preferentially lifts coarse light particles into the upper layer of the pulp film [127].

Bagnold nomal stress becomes significant only if particle volumetric concentration reaches over 50% (≈70% solids by mass depending on the mineral density) [156]. This suggests that Bagnold normal stress potential effect should be limited to the innermost stream of the spiral trough where this high solids concentration is found. This effect has been suggested as an explanation for pulp dilation and an increase in film thickness at this location on the trough. This dilation and bulging is only present if coarse particle distribution and high solids concentration is locally present on the trough [156].

Experiments with a size distribution of mono density (light) particles showed a finer size distribution in the inner section of the spiral while gradually coarser distribution was found when moving to the outward zone [60, 156]. This was later confirmed for both light and dense particles [158]. This radial size distribution is a factor in the loss of some coarse dense particles to tailings which was shown by size recovery curves from early testwork [108, 134, 168, 169]. Similarly, analysis of size recovery curves in iron ore spirals have shown an systematic decrease in recovery of coarse particle which can lead to significant value losses [170, 171]. Another portion of the large dense particles are lost to tails similarly to the bypass found in other classifiers [60, 172].

Part of the lost is produced by the effect of the Bagnold normal stress which selectively bring coarse particle in the upper layer of the flow at the inner zone of the trough [158]. Once on the upper layer, the coarse particles can be carried by the outward flow up to the tailings take off port if it do not settle back in the inward moving layer. In the case of iron ore, the use of wash water adds to the explaination with the Bagnold normal stress for the loss of dense coarse particles [170, 171].

Many of these remarks are theorised from stream sampling analysis. Obtaining measurments of single particle behaviour is seen as an important next steep to better understand spiral concentrator [133].

3.7 Spiral models and simulations

The principal objective of modelling spiral concentrator is to improve separation performance. This is possible via a reduction of experimental work required to determine the optimal parameters for the design of a unit or its operation. This section describes the different modelling approaches taken to simulate spiral performance.

3.7.1 Experimental measurements

Early models were based on empirical measurements with the brute force approach of testing the full range of each parameters in every possible combination. Considering the many parameters affecting spiral perfomance, obtaining optimum process conditions of a circuit is complex, and could potentially involve thousand different parameter combinations. To overcome the time and cost associated with testing all these combinations, many researchers now use design of experiment techniques [69, 135, 146, 153, 173]. Carefully designed experimental program to minimise the amount of test is, as of today, the most efficient strategy to obtain optimal operating conditions for a fixed spiral design and circuit with a known ore mineralogy and size distribution. Once the optimum parameters are determined, control on ore variability and other parameters is critical to maintain the predicted optimum results.

Many studies found in the literature are a collection of testwork results for a specific ore treated with a specific spiral model at different feed parameters [138, 174–177]. These are useful for general idea about the potential applicability or not of the spiral concentrator to a specific ore type. However, they are extremely specific and because of the lack of mineralogical information (particle size, liberation and shape), it is difficult to use these for fundamental development. Recording of detailed mineralogical information (particle shape, liberation) in addition to particle size distribution is important when reporting on experimental spiral study. These parameters have a large impact on spiral performance [178].

3.7.2 Empirical models

Measurement of the concentrate band radial location can be correlated with other operational parameters with the objective of building a database of potential operation scenarios and their performance which can be used for process control, if similar scenario (or extrapolated scenarios) arise in the future [155]. In this case, equations obtained from linear, polynomial and power law regression are seen as a form of empirical spiral models [155]. This requires a significant amount of experimental work and is highly related to specific spiral design and specific ore properties. This approach is excellent for an established operation where those two variable (spiral design and ore) are known and repeatable.

Multi-spiral empirical models relating particle size, feed rate, solids content, splitter position, mass recovery and product grade exist, mostly for coal spiral unit [91, 96, 117, 148, 179].

Empirical correlations of upgrade ratio or mineral recovery as a function of mass recovery can be used for the comparison of different spiral concentrators in addition of their individual optimisation [180, 181].

Similarly, reduced performance curves or Tromp curve (fraction recovered to concentrate *vs* relative density) can be used to compare different spiral designs or spirals to other gravity spearators [149, 170, 182]. This type of curve was used to show that spirals having multiple take off ports and injection of wash water are more efficient than wash waterless spirals with a single cutter [182]. However, in this type of study, there are many parameters involved and the reduced performance curve needs to be build from many operating points to have a process wide signification.

Empirical size recovery curves have been used to simulate a multistage spiral circuit. In this approach, the model was able to pinpoint optimal operation parameters to improve recovery of coarse dense particles [170].

A semi-empirical and mathematical model of the spiral including the addition of wash water and removal of concentrate via take off port has recently been proposed [183].

It is based on half-turn sub-models for each different effects (feed, wash water, pulp profile, particle motion, concentrate extraction) [183]. This approach requires many hypotheses. However, it was able to reproduce experimental results to a certain degree [183]. Local effects of wash water and particle motion are among the parameters that should be looked upon in detail to improve this recent model.

Empirical models are sufficiently reliable for spiral plant equipment sizing, stage mass balancing and throughput design. Unfortunately, for spiral trough design and operation optimisation, such models do not provide enough precision [172]. Generally, new empirical coefficients are required when one of the conditions used to determine the model is changed [60]. As a result, anyone developing a new spiral trough or spiral circuit should do their own testing unless the ore and spiral design have been tested before.

Most of empirical models are tailored to a close range of pre-established design choice (*e.g.* spiral overall size). They do not enable particle and fluid flow interactions to be the driver of the design. Difficulty in the observation of the particle separation explain the use of whole unit experimental testing (*e.g.* grade and recovery).

3.7.3 Hydrodynamic models

Mathematical relationships describing the flow of fluid down the trough are possible, however they require assumptions related to surface profile, pulp viscosity and pulp profile [127]. These hydrodynamic models are mostly used for determining the fluid film flow field. This flow field can then be used to approximate the particle flow field inside the film by the means of a simple force balance.

A theoretical velocity profile comparison of different flow type and description (laminar, smooth turbulent, rough turbulent, suspension, Manning) made by Holland-Batt [160] suggested than the inner zone velocity profile could be described by the use of the Manning equation with suitable coefficient. The determination of these coefficients are based on assumptions and experimental observation of the mean flow velocity.

This velocity can be determined by the use of pulp film probing and stream sampling on a spiral [160].

A hydrodynamic model which uses the Manning equation to describe the inner trough flow was then proposed [160]. For description of the velocity profile in the outer zone, a free vortex equation was used with a vortex strength based on geometrical and empirical flow profile measurements. This approach enables the prediction of the fluid film profile and downward flow velocity (primary flow). It requires knowledge of the inner and outer wetted limit of the fluid film. This can be obtained experimentally for different feed volumetric flow rate. Similar results to the Manning equation can be obtained by the use of the Suspension equation [162].

This flow description predicting the velocity profile and free surface profile should be taken as an approximation as different from the observed fluid behaviour, especially in the transitional section between the inner and outer zone [160]. However, this model was a step forward in the prediction of fluid velocity, profile and flow rate in the spiral with agreement in consideration of experimental procedure and hypothesis made at the time.

A problem with the Manning flow description is the use of empirical parameters based on spiral experiments without any solids [158]. In the modelling of the laminar portion of the flow, correlation between solids volume content and pulp viscosity can be used [158]. A velocity profile including the effect of Bagnold normal stress was shown to represent pulp flow more accuratelly than with the Manning equation as used by Holland-Batt [160] but less accuratelly than with a laminar flow profile [158]. The profile including Bagnold normal stress is thought to be more realistic under dense particle packing conditions as found at the inner trough zone [158].

Following the work of Loveday [158], Holland-Batt [184] extended the use of its hydrodynamic model to include the flow profile based on Bagnold normal stress. This improved model was used to predict the flow that would arise in large diameter spirals (up to 3 m) of rectangular trough profile. The interest in this type of spiral would be for the separation of fines (<75 µm) mineral particles. The predicted flow produced a lower centrifugal acceleration which could be an advantage as a more tranquil flow can be obtained in this case. Unfortunately, no simulation results or experimental data for the trajectory of small particles is available at the time of writing to validate that the flow conditions predicted on conceptualised large diameter spiral results in efficient mineral separation.

3.7.4 Force based models

With the availability of hydrodynamic models, force equilibrium models can be developed. These models offer certain advantages for the prediction of a particle's radial equilibrium position. This position can then be assumed to represent particle separation [185].

Holland-Batt used this approach with the Manning and free vortex definition of the flow to determine the motion of dense and light particles of different sizes at different locations inside the pulp film. The aim was to predict the particles' equilibrium position between fluid drag, centrifugal and gravitational forces [160]. These equilibrium positions provide information about particles differentiation based on size and density. This work has shown that volumetric feed rate is one of the most important parameters in the particle separation as it governs the intensity of the secondary flow [160]. Improvements suggested to this model are the consideration of higher solids content, and the effect of particle interactions which are significant in the inner section of the trough. Additionally, primary and secondary flows should be treated together rather than separately [160].

The same force equilibirum model has been used to determine the potential of using rotating spirals [186]. This analysis was conducted using assumptions of similarity with the empirical parameters obtained for non rotating spirals. The results have shown a significant effect on the fluid film profile and suggested that improvements in recovery and selectivity of fine particles could be achieved through some degree of negative rotation (*i.e.* opposite to pulp flow), and positive rotation respectively.

Kapur *et al.* [187–189] presented a force equilibrium model to determine the radial position at which a particle would be in static equilibrium. The five forces considered to be of significance in this work were drag, lift, friction, immersed weight and centrifugal. The drag, immersed weight and centrifugal force were estimated to be of the same order of magnitude (10^{-5} to 10^{-4} N) [187–189]. Lift and friction were described as a function of the three others. With a combination of mathematical descriptions of the tangential and longitudinal slope of the spiral trough surface and a hydrodynamic model, an approximation of the fluid depth and velocity was obtained. With this information, the forces were computed to obtain the radial equilibrium position, which can be used to calculate the separation performance. One of the main conclusions from this work was that the important forces on the particles in a spiral are of similar magnitude, and that this is probably the rate of change of those forces with size, density and radial position which affect the separation [187–189].

A detailed force equilibrium model was recently used by Jain *et al.* [190] to physically explain the formation of the secondary flow by mechanistically determining the behaviour of small fluid elements (water or pulp) at different positions on the spiral trough. The approach was subsequently applied to mineral particles and generic motion behaviour depending on the particles location, size and density were presented. This model is simple and efficient, representing only the laminar section of the flow. However, most of the particle recovery is thought to take place in this laminar section which makes this analysis interesting.

Force equilibrium models are of great interest with the only drawback being the complexity required to include detailed spiral geometrical features, particle fluid drag and particle-particle interaction parameters. Improvement in this area would have large potential, but require details on the particle behaviour.

3.7.5 Numerical simulations

Numerical simulations can be used for the prediction of separation performance. Computational mineral processing (CMP) represent the use of different types of numerical simulation to predict the performance of a unit or circuit treating ore [9].

An excellent example of this type of simulation is the JKMRC SimCoal simulator. This simulation tool was built from empirical correlations determined by the use of plastic tracers of different density and size (300 to 2000 µm)) [172], mathematical equations [160] and force equilibria [191]. It is able to predict particle radial equilibrium position and relate it to spiral separation performance. It is built from many experimental tests on specific coal spiral designs (LD2, LD4 and CMI) and consequently offers good agreement if used to predict their separation performance.

The goal of numerical simulation is to remove empirical factor or measurements from the prediction process. This has the power to enable much more freedom in geometrical and operational design of new generations of spiral concentrators. The following sections present different approaches toward this goal.

3.7.5.1 Computational fluid dynamic simulations

Computational fluid dynamics (CFD) is a group of techniques which aim at solving the discretised equations of conservation of mass and momentum numerically [52]. CFD is applied widely to gas and liquid flow problems. However, when it comes to multiphase system, especially including particulate solids, the equations and solutions are more complex and the computational power requirements higher. Nonetheless, CFD is important as it enables a full virtualisation of a fluid flow problem.

Wang *et al.* [192] presented the first CFD simulation of a spiral concentrator. This model represented the flow of a viscous fluid (oil) in an helical rectangular channel. Experimental validation of surface fluid velocity and free surface profile trough in a custom made rectangular spiral validated this simulation approach. Even considering the fluid used and the crude geometry under study, it generated general trends relating spiral pitch and diameter to the fluid velocity. It demonstrated the effect of these parameters on the secondary flow velocity, which increase with an increase in pitch.

A second model was presented by Li *et al.* [172] and Jancar *et al.* [193]. It assumed the fluid as Newtonian with constant physical properties and described its behaviour with laminar steady state Navier-Stokes equations. It included the simulation of the free surface of the spiral fluid film [9, 193]. The simulation domain was half a turn of a LD4 coal spiral trough (Mineral Technologies, Australia) to reduce computational time. To obtain a fully developed solution, the flow properties at the outlet of the half turn were computationally recirculated to the inlet of the half turn up to the point were the solution was in a steady state [9, 193]. An important outcome of this simulation approach is the presence of the secondary circulation loop [9, 193].

This approach was used to simulate clean water and a low particle content (<0.1 %) at moderate Stoke numbers, where the fluid flow is not affected by the particle motion. Performance was shown to be in within 30% agreement in terms of fluid velocity, fluid free surface profile and fluid stream flowrate when compared to experimental measurments[157, 193]. Inclusion of a turbulence model was suggested as a potential improvement for a more accurate description of the outer turbulent zone of the spiral flow [9, 193]. This simulation represents the flow once it is fully developed (*i.e.* fourth turn or more). However, the separation of particle by size and density takes place in the first few turns which a more complete simulation should represent. Introduction of a larger solids content particle phase and its effects on the fluid flow (potentially diminishing the secondary flow magnitude) was reported as being a miletsone in this simulation work [9, 193].

The approach of spiral simulation through CFD was pushed further by Matthews *et al.* [194–197] with the addition of turbulence within the fluid phase and the use of different methods for the addition of dilute particle phases. This work solves the averaged Navier-Stokes equations with the volume of fluid (VOF) method for the representation of the free surface flow and the re-normalisation group $k - \epsilon$ (RNG $k - \epsilon$) formulation for the simulation of the turbulence in the outer zone [195, 196]. This model used a 35° section of the spiral trough with recirculation of the exit to the inlet of the domain to obtain a steady state flow solution. Four walls (*i.e.* trough surface, inner edge, outer edge and top wall) were used to generate a set-up similar to a duct flow partially filled with water and air. Once again, this approach made the assumption that particle separation is happening when the flow and its secondary component has reached a steady state.

Two approaches to the simulation of particles have been used by Matthews *et al.* [194]. The first, the Lagrangian particle description followed a small number of discrete particles (100 in this case) to obtain their detailed trajectories in the water flow [195]. The second, the Eulerian particle description, followed a particle continuum (still diluted at 0.3% by mass) penetrating and interacting with the clear water flow. This second approach is more suitable for a dense particulate content, but it causes difficulty with the description of the free surface (phase diffusion) and the phases interaction. The study with the Eulerian approach used a fixed free surface to partially solve this issue [194]. In this case, the free surface was obtained from a clean water solution modified to account for the bulge created by particle accumulation at the inside on the trough profile.

Characterisation of the performance of these simulations were made by the observation of the particles final radial equilibrium positions as local particle motion experimental measurements were not available. Measurments of this type are seen as a milestone to adequately and locally describe the particle motion on the spiral. The Eulerian simulation of Matthews *et al.* has shown better performance with final radial position within 20-30% of experimental radial cut sampling experiments [194]. Larger variations were found for particles over 1000 µm, and this is expected to be related to the particle-trough surface interaction being more important at this size [196].

Similar work to the simulation by Matthews *et al.* [194] was used on an entire five-turn spiral rather than only section of a turn [164]. This study considered a laminar flow in the trough to simplify the calculations with the assumption that less than 15% of the fluid flow domain was turbulent (*i.e.* the outer zone). Another improvement from this work is the inclusion of terms for the surface tension in the equations governing the fluid flow. Variation with measured water flow depth in a spiral similar to the simulation domain used showed difference of up to 50% in the water depth simulated.

This is most likely related to the laminar flow assumption. The water flow field obtained from this full spiral simulation was used in a Lagrangian particle simulation coupling the fluid to the particles by an inertia and force balance [164]. In the case of the particle flow, the only conclusion presented was that the lighter particle report outward and the heavier inward, without any detailed results [164]. An important point to mention, in regards to this simulation, is that many particles were found to report in an area of the trough where there is no water phase, which means that particles were able to cross the water air interface, which should be addressed in future simulations.

Doheim *et al.* [198] also presented a simulation based on the work of Matthews *et al.* [194]. The improvement here was the consideration of the lift force acting on particles. This work first generated a clean water flow profile from the simulation of the first turn of a spiral. An Eulerian simulation of the pulp was then produced with the fixed free surface profile from the water only simulation. This work compared different turbulence models and finally, the RNG $k-\epsilon$ model was determined to provide the closest results to experimental stream sampling [198]. The particulate phase was 3% solids by mass. Three different size classes (75, 530 and 1400 µm) of different density were used [198]. Particle radial positions were in a good general agreement, with deviation of around 20% from experimental stream sampling in most of the trough. However, differences of up to 30% were reported for the smaller particles, especially in the region near the central post. This could be explained by the difficulty of the simulation to match the behaviour of the high density concentrate stream present in this area. One of the drawback of spiral simulation with dilute particle content is the absence of the dense bed effect at the inner zone of the spiral.

A recent simulation by Mahran *et al.* [199] reused the work of Doheim *et al.* [198]. The main difference here is the use of a higher solid content (15%). However, to obtain a better fit with experimental data, the free surface used in the simulation was set from the one obtained from the experimental study used for comparison of the results. This ensured the exact same free surface as the experiments, thus making a Eulerian simulation of a 15% pulp inside a fixed geometry duct without an air interface.

Numerical and analytical simulations of the free surface and its contact points with the spiral trough surface were compared for a geometry of semi-circular profile [200, 201]. This theoretical work provided a technique to predict the free surface shape and contact point for semi-circular geometry and laminar water flow. These two assumptions limit the complexity of the problem.

A more theoretical solution to the particle flow in a simple rectangular spiral is provided by the model suggested by Lee *et al.* [202]. Their approach of transforming the Navier-Stokes equations is seen as a potential area of interest to build parametric simulation of simple geometry that can be used to analyse general design parameters.

A lot remains to be done on the CFD simulation of the spiral. Among others, the description of the high solid content pulp free surface for complex profile geometries is seen as a milestone. Ideally a simulation approach able to handle a pulp with up to 70% solids by mass would be of interest. The lack of detailed measurements of particle motion seems to limits further development on this front.

3.7.5.2 Discrete element method simulations

Discrete element method (DEM) is a particle simulation technique which allows for the simulation of large number of particles at a low or high packing density. In this technique, the many different forces acting on a discrete particle (including particle-particle and particle-surface contact forces) are computed to obtain the resultant force which affect the particle motion (acceleration, velocity, position) by applying Newton's second law.

A DEM simulation can be combined with a CFD simulation to input the fluid drag force on a particle. It is then possible to determine the trajectory of a large number of particles in the pulp flowing in mineral processing equipment. Many types of coupling between the fluid and particle phases are possible, the simplest being to have a fixed fluid flow field not affected by particle motion used for the determinaton of particle drag force. This approach was used to simulate spherical particles (12 000) of two different densities (2400 and 4800 kg/m^3) in a spiral concentrator [203]. The particles were injected in the DEM simulation using a fixed CFD fluid flow field similar to the one obtained by Matthews *et al.* [195]. Predicted grade based on particle final radial positions were within less than 10% of experimental data for similar density ores. However, it is difficult to assess if the particle separation is taking place at the same rate or in similar pattern to reality. This recent simulation specifically highlights the need to obtain experimental particle trajectory along the trough, rather than just end of trough radial position. This is seen as a milestone for further improvement of particle based simulations.

3.7.5.3 Future simulation trends

Future simulation should conform to fundamentals law of fluid motion with as low empirical input as possible. Among others, future simulation should focus on predicting the free surface multiphase flow from clean water to up to 70% solids by mass. They should additionally be using techniques able to handle a large number (billions) of particles smaller than 100 µm.

Improvements in particle and fluid flow simulation techniques are at the point where a full simulation of the spiral concentrator separation becomes feasible. However, certain experimental informations are still required to enable such simulation to be validated and optimised. Obtaining particle trajectories and particle flow field information is one of the critical informations lacking for the development of spiral simulation. Obtaining such information for the spiral is now possible thanks to recent advances in particle tracking techniques [204].

3.8 Need for particle flow measurements

To bridge the gap between particle scale model of particle interaction and model of a full scale spiral, information on the general particle behaviour in the spiral is required. Fluid flow on the spiral has been observed in detail as mentioned in Section 3.6, however particle flow is mostly theorised rather than measured.

The particle behaviour on the trough as it migrates inward or outward in the secondary circulation has never been characterised experimentally. The extent to which the secondary flow is affecting particles all along the spiral is unknown. The same applies for the effect of wash water on the particle trajectory.

Most simulations are compared to a few experimental study providing the pulp stream flow rate and thickness. Particle trajectory (Langrangian approach) and velocity can be recovered with numerical simulations, however this information is not available from the experimental point of view. The validation of numerical simulation is thus mostly vague and does not reach a level of confidence required for equipment design and optimisation.

An important milestone in the future development of these simulations is the availability of measured representative mineral particle flow field which is the main objective of this thesis. This information can be recovered trough particle tracking, specially trough radioactive particle tracking which enables one to observe particle in dense and opaque medium as the dense pulp on the spiral.

Radio labelled tracer (gold particles) were previously used to investigate spiral concentration, however, the only use was to determine in which one of three stream (concentrate, middlings, tailings) the tracers were reporting at the end of the trough [133]. In this case, gold particles of different sizes (53 to 1400 µm) were added to a sample of mineral sand (silica, garnet, ilmenite and magnetite) for treatment on a recirculating spiral set-up. Unfortunately, the smallest (53 µm) gold tracers were lost due to handling difficulties and no meaningful information were recovered for this size. The result of this work has shown that the 150 and 600 µm gold particles were fully recovered in the concentrate stream which is duly expected considering their density which is much higher than the other mineral particles present in the pulp.

3.9 Experimental spiral set-up

This section describes the experimental pulp and spiral set-up used in the particle tracking experiments undertaken to obtain particle flow information.

3.9.1 Ore and pulp sample

The ore used was an iron ore from ArcelorMittal Exploitation Minière Mount-Wright Mine in Canada's Labrador Trough. The ore comprised mostly of quartz (56.6 % SiO_2) and hematite (43.2 % Fe_2O_3). The fraction coarser than 850 µm (7.3 % of the initial sample mass) was removed to ease the recovery of the activated tracer at the end of the test run when a large particle (1000 to 1180 µm) was tracked and to reduce blockage of the pump. The test sample size distribution is shown in Figure 3.4. Pulp composition and operating parameters are presented in Table 3.2.

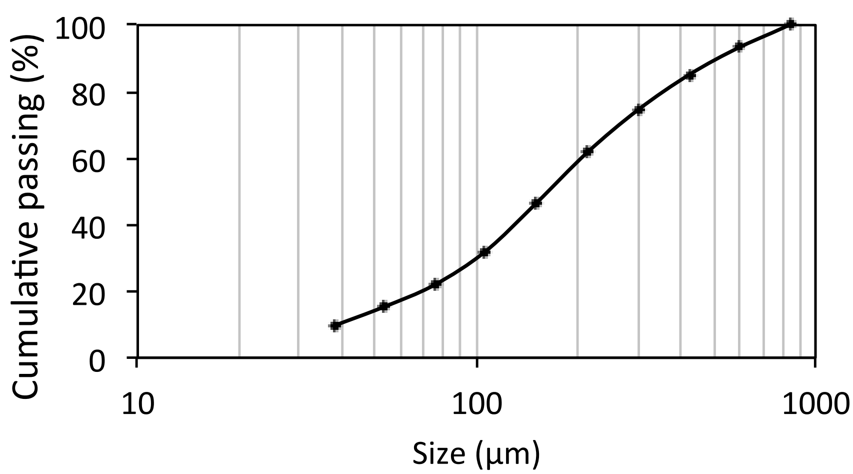

Figure 3.4 – Test ore size distribution.

Table 3.2 – Pulp composition and operating parameters

Parameters	Value
Ore mass	5 kg
Water mass	20 kg
Solids % w/w	20
Pulp feed rate	0.9 t/h

3.9.2 Spiral trough

The spiral used was a Walkabout assembly (Wallaby trough) from Mineral Technologies (Australia) with four turns, a pitch of 208 mm and a trough diameter of 360 mm. The trough profile is shown in Figure 3.5.

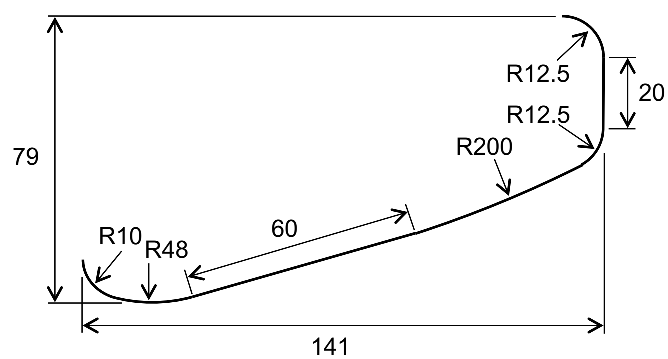

Figure 3.5 – Trough profile with dimensions (mm).

3.9.3 Recirculating spiral set-up

The pulp was contained in a tank equipped with a mixer to prevent sedimentation. A diaphragm pump was used to circulate the pulp to the top of the spiral, which was fitted with a funnel to dampen the flow variations before entering the feed distribution device. At the end of the trough, concentrate and tailings discharged into the tank for remixing and recirculation. Figure 3.6 shows the schematic of the recirculating circuit used to generate many passes of the tracer in the particle tracking detectors field of view. Figure 3.7 show the spiral under operation.

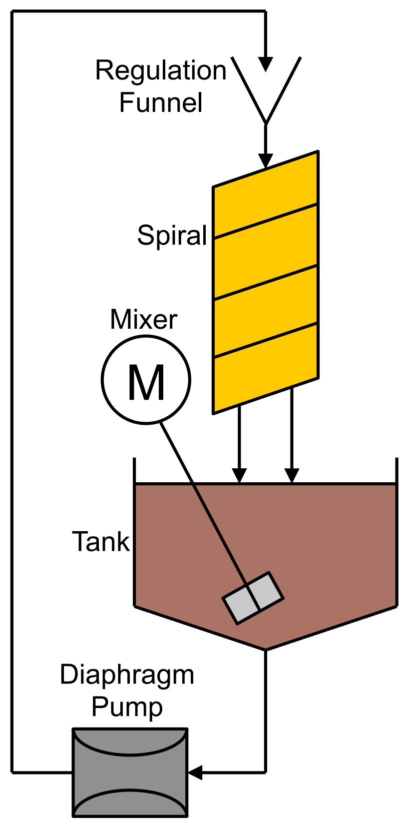

Figure 3.6 – Flow diagram of the recirculating spiral set-up.

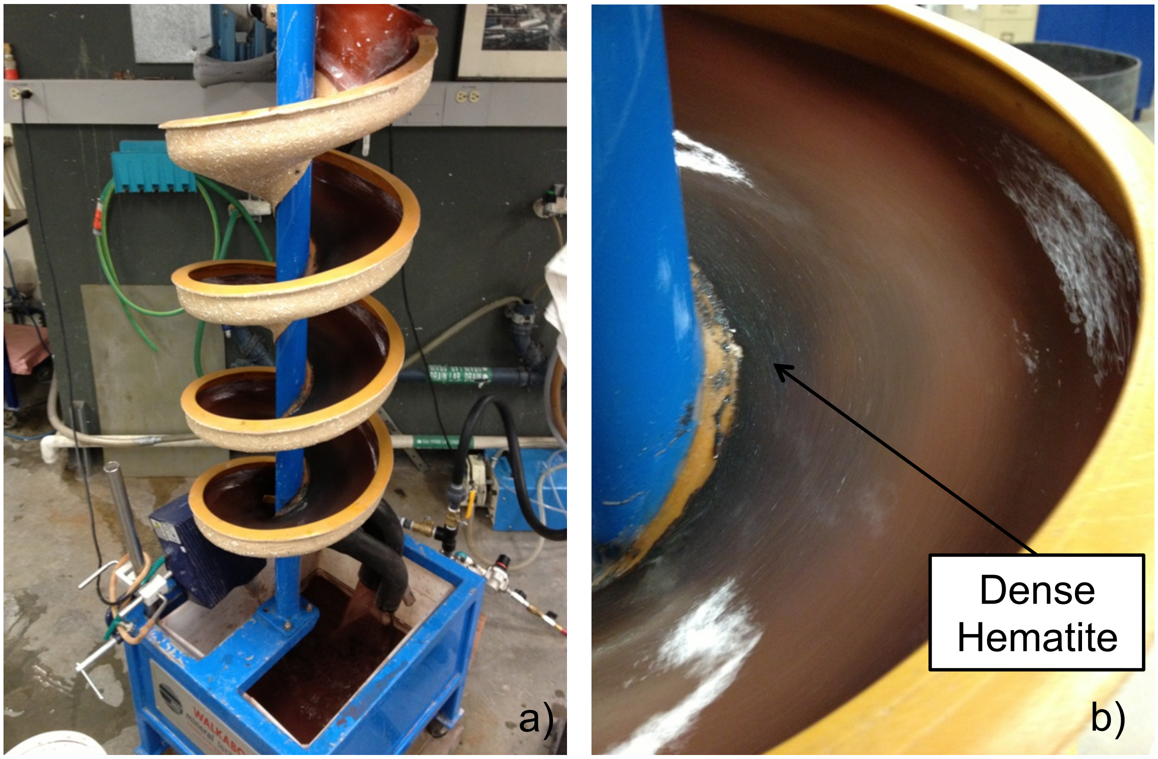

Figure 3.7 – Walkabout test unit treating an iron ore sample a) overview, b) band of concentrated hematite in 3rd turn.

3.9.4 Wash water injection set-up

For the runs where wash water was used, the injection was undertaken via the modified spiral set-up shown in Figure 3.8. A siphon was used to recover water from the surface of the pulp in the tank. This provided water clean enough to be fed to a constant head tank. The injection was performed as shown in Figure 3.9 with a flow rate of 2.3 kg/min provided by the constant head tank.

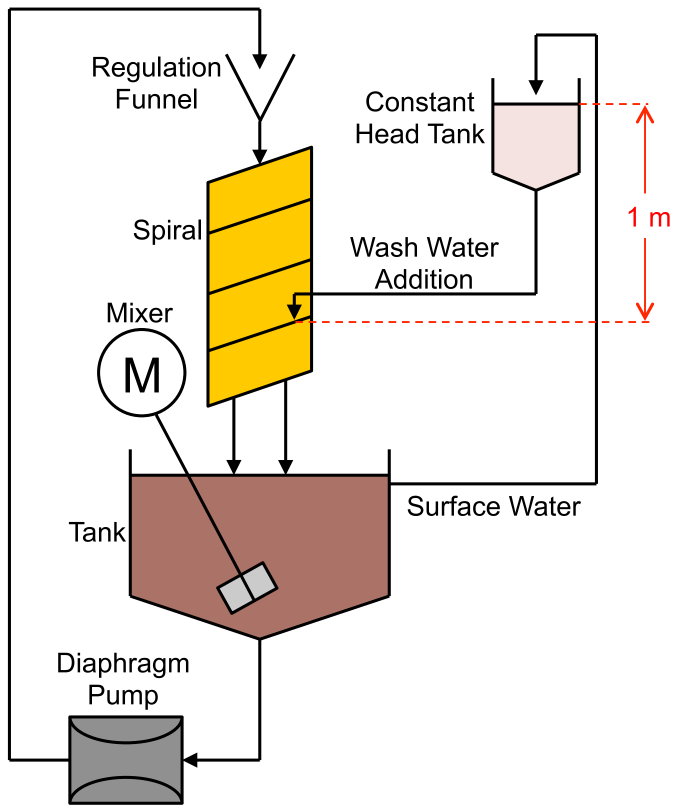

Figure 3.8 – Schematic of the modified spiral set-up to inject wash water in the 3rd turn.

Figure 3.9 – Details of the wash water injection nozzle in the 3^{rd} turn during operation.

Chapter 4

Positron emission particle tracking

Particle motion in dense opaque slurry systems is difficult to observe and measure. In the case of mineral processing applications, such as the spiral concentrator, the displacement of particles within the slurry is central to the operation. Up until recently, only limited quantification of the concentration process was possible, by close observation of the slurry film surface, imaging of dilute particle flow [163], or radial cut sampling [58, 162]. These provide information for high level observations such as recovery and grade in different radial streams with streams pulp velocities or to visually show that particles are moving radially on the trough. However, particle trajectories and velocities in an industrial pulp with a high solids content cannot be determined by these techniques. The trajectories and their derivatives (flow field) are of importance for the simulation of particle flow in the spiral because they are particle scale measurement of the fundamental performance (particle separation: where and how it takes place). Retrieving this information is a milestone to improves spiral simulation which will enable true freedom of profile and geometry design. Along the lines of traditionnal methodologies of particle tracking, such as PIV, require a transluscent system with low solids content. There are limited technologies that can cope with opaque system, one of which is positron emission particle tracking (PEPT). This chapter describes this technique and how it was used for the observation of the motion of mineral tracer that were representative of mineral particles within a dense pulp flowing on a spiral concentrator trough.

4.1 Principle of PEPT

Positron emission particle tracking (PEPT) was developpped at the University of Birmingham (UK), in the early 1990's to track the particle flow in dense and opaque engineering systems [11, 205]. It was recently described in detail by Leadbeater *et al.* [206, 207]. The technique is based on tracking an individual tracer particle which is added to the processed bulk or slurry.

The tracer particle must be labelled with a positron emitting radionuclide (detailed in Section 4.1.1). Once the particle is activated, the radionuclides found in the surface layer of the tracer emit positrons through their decay. Annihilation of these positrons occurs when they come into contact with surrounding electrons. Each annihilation event producing two gamma photons (511 keV each) which are emitted back to back (180°±0.5°).

Coincident detection of these two collinear gamma photons by scintillation crystals in two opposite detectors located around the experimental set-up enables the reconstruction of a line of response (*LoR*) in space as shown in Figure 4.1. The *LoR* is determined by the two scintillation crystal centre points, and it passes very close to the activated particle [207].

The particle location is determined by a group of *LoRs* which are recorded over a short time interval. Among those *LoRs* will be scatter and random coincidence detections. Further processing of the *LoRs* with a tracking algorithm is thus required as explained in Section 4.3.

Tracking a tracer over a long period of time or over many recirculation enables one to average the behaviour of particles similar to the tracer, and show their typical motion in the system as explained in Section 4.5.3.

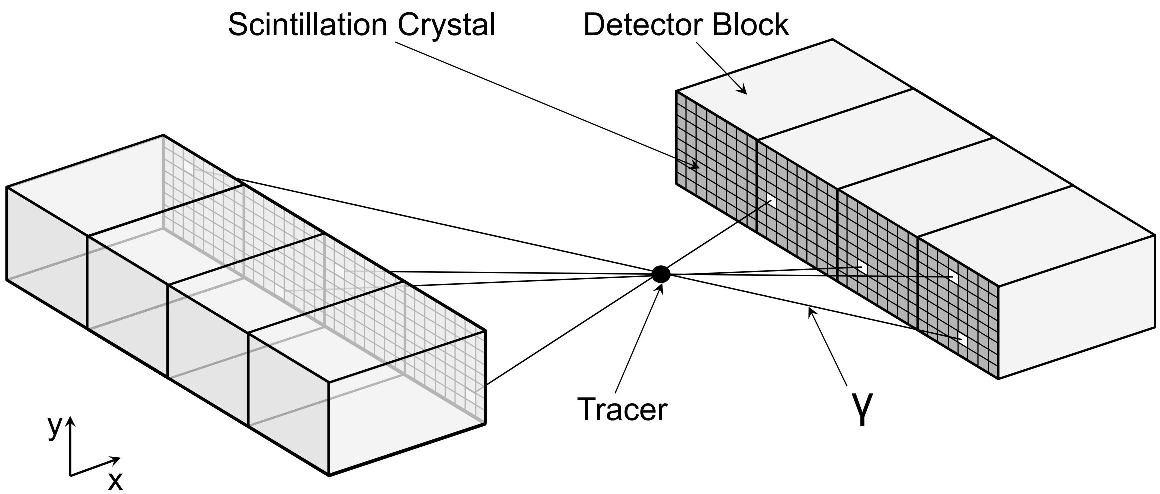

Figure 4.1 – A set of four *LoRs* generated from detection of eight gamma photons emitted by the tracer particle present near two detector buckets made of four detector blocks each containing 64 scintillation crystals.

The advantage of PEPT, over other techniques, is the reliance on the transparency of the experimental system to gamma rays, therefore the trajectory in a slurry with high solids content can be determined.

Two main centres exist in the World where the activation and tracking can be undertaken: the Positron Imaging Centre at The University of Birmingham (UK); and the iThemba LABS in Cape Town (South Africa). In Birmingham, and under optimal conditions, recording rates of a 1 mm tracer moving at 10 m/s are up to 1000 localisations per second with a precision of 0.5 mm (Forte Camera, ADAC Laboratories)[207]. With lower localisation rates, Cole *et al.* [208] showed, in the Cape Town facility, that it is possible to use ion exchange activated tracers to follow trajectories of particles down to 50 µm ± 5 µm, moving at speeds of up to 2 m/s with a location error of approximately 2.6 mm (EXACT3D Camera, Siemens). In this later case, the tracers were made out of specific types of polymers having much lower densities than most minerals. A technique for coating these small light tracer with mineral surface representative material has been tested but it does not provide significant change to the tracer bulk properties [209]. A third PEPT centre is under development at The

University of Tennessee Knoxville (USA) [210, 211]. This recent centre is currently developing new tracking algorithms to be applied to the observation of liquid flow and multiple particle tracking.

4.1.1 Uses of PEPT

PEPT as been previously applied to track particles in mixing vessels with the measurements of different mixing indices [212–216]. Fluidised beds have been observed with the technique [217–220]. Particles behaviour in different mill types was described in details [221–226]. Other mineral processing applications are the observation of flotation cell dynamics [209, 227–229] or measurment of liquid content in foams [230]. Using PEPT in the investigation of hydrocyclone presents an interesting challenge considering the fast flow of particles inside a unit. In this application, some experiments revealed basic information on large particles motion [231, 232].

Development of a tracer having bulk and surface properties representative of the particles under investigation and which can be activated to a sufficient degree for tracking is one of the main challenges of PEPT, especially when dealing with small particle size (<500 µm). In mineral processing the separation size is often below 1000 µm for most deposits and even below 250 µm in the case of most of base metal processing circuits (*i.e.* flotation). This is due to the liberation requirement associated with the general decrease in grain size of the valuable mineral found today. A new technique developed for producing small mineral representative tracers by an extension of the direct activation technique is detailed here. In addition to the production of a new type of tracers, the PEPT technique is applied to the investigation of the particle flow in mineral spiral concentrators.

4.2 Tracer preparation

There are different methods for labelling particles to create tracers: activation via ion exchange [233], ion exchange with surface modification [234] or direct activation (as used in this study) [233]. The purpose of the activation is to transform or transpose atoms present at the particle surface to positron emitting radioisotopes. The most common PEPT radioisotopes include ^{18}F, ^{66}Ga, ^{68}Ga, ^{61}Cu and ^{64}Cu [235, 236]. These radioisotopes decay over time mostly by positron emission from their proton rich nuclei (β^+ decay).

The different minerals used for the tracer production in this study are presented in Table 4.1. They are either isolated from a grounded and liberated ore sample obtained trough mining companies (ArcelorMittal Exploitation Minière (Canada), Unimin (USA)) or from pure mineral sample from collection mineral dealers (Ward's Science, USA).

Table 4.1 – Tracer materials used in this study

Material	General composition†	Specific Gravity (S.G.)
Quartz	SiO_2	2.65
Hematite	Fe_2O_3	5.26

† Other formula possible.

4.2.1 Direct activation

The direct activation technique used in this work allows a particle of the same composition as the bulk to be used as tracer. This is of particular importance in processes where the density of the minerals is the key factor in the particle separation, as in the case of the spiral concentrator, or where surface chemistry plays an important role, such as the separation of minerals through flotation.

The creation of tracers is conducted by the direct activation of 1000 to 1700 µm size particles placed inside a cyclotron beam (the mineral being put directly into the beam) for two to three hours. The Birmingham MC40 cyclotron (35 MeV $^{3}He^{+}$ beam) was used for this work. It activates the oxygen atoms within the mineral particle. During the activation process, ^{16}O atoms from the particle surface layer are converted to ^{18}F via the competing capture reactions [234, 235]. This radioisotope has a half life of 110 min. The amount of activity produced on the tracer is proportional to the size of the particle as the beam activates the exposed surface. The thickness of the activated layer of material is approximately 300 µm [233]. The size of the original particle is currently the lower end limit for practical handling considerations in the target of the cyclotron [234]. Limitations to the activation of the original particle are the heat generated at its surface, and the time required for additional bombardment. A longer time being not significantly beneficial as decay will counteract additional activity produced.

The activation of 3-4 large particles of the same mineral can be performed at the same time in the cyclotron beam target. Activity levels attained by the large original particles were measured with an ionisation chamber (Capintec CRC-25PET). Once activated, one of these particle can be added to the bulk as tracer and the process equipment operated normally or it can be used for the preparation of a smaller tracer. Table 4.2 present the different data acquisition runs realized with information on the tracer; its mineral, size and activity.

Table 4.2 – Details of the tracking runs performed.

Runs	Slice (mm)†	Mineral	Size (µm)	Activity (Bq)	Detector
P31H0106	0 to -100	Hematite	90 to 106	4×10^3 to 1×10^{5}‡	Modular
P31Q0106	0 to -100	Quartz	90 to 106	4×10^3 to 1×10^{5}‡	Modular
P31H0355	0 to -100	Hematite	300 to 355	4×10^3 to 1×10^{5}‡	Modular
P31Q0355	0 to -100	Quartz	300 to 355	2.6×10^6	Modular
P32H0355	-75 to -175	Hematite	300 to 355	7.0×10^6	Modular
P32Q0355	-75 to -175	Quartz	300 to 355	2.1×10^6	Modular
P31H1180	0 to -100	Hematite	1000 to 1180	6.3×10^6	Modular
P31Q1180	0 to -100	Quartz	1000 to 1180	1.5×10^7	Modular
PWWH0355	-300 to -700	Hematite	300 to 355	2.0×10^6	ADAC
PWWQ1180	-300 to -700	Quartz	1000 to 1180	8.8×10^6	ADAC

† Elevation along y axis.
‡ Indicative only as over limit of Tracerco T401 and under limit of Capintech CRC-25PET activity measurement instruments.

4.2.2 Breakage and selection

Certain size fractions to be investigated are under the direct activation lower limit (1000 µm). In consideration, production of the tracers required further steps after activation to reduce their size. The new developed procedure is named direct activation and breakage (DAB) as an extension of the direct activation technique.

In the cases where a submillimetre sized tracer (in this work 50 to 500 µm) is required, the large activated particle with the highest activity is broken into smaller pieces. The breakage is conducted using a brass hammer (100 g) and anvil (500 g) using a gyratory crushing motion.

The fragments were then sized using standard mesh screens to isolate the size fraction to be investigated. From this fraction, an artist's brush with a single remaining hair is used to pick-up the fragments under the field of view of an optical microscope. Measurement of the activity of the small fragments is carried out to select one with the largest activity for use in the spiral system investigation. The idea of this procedure being to obtain a fragment of the original particle surface with a high level of activity as shown in Figure 4.2.

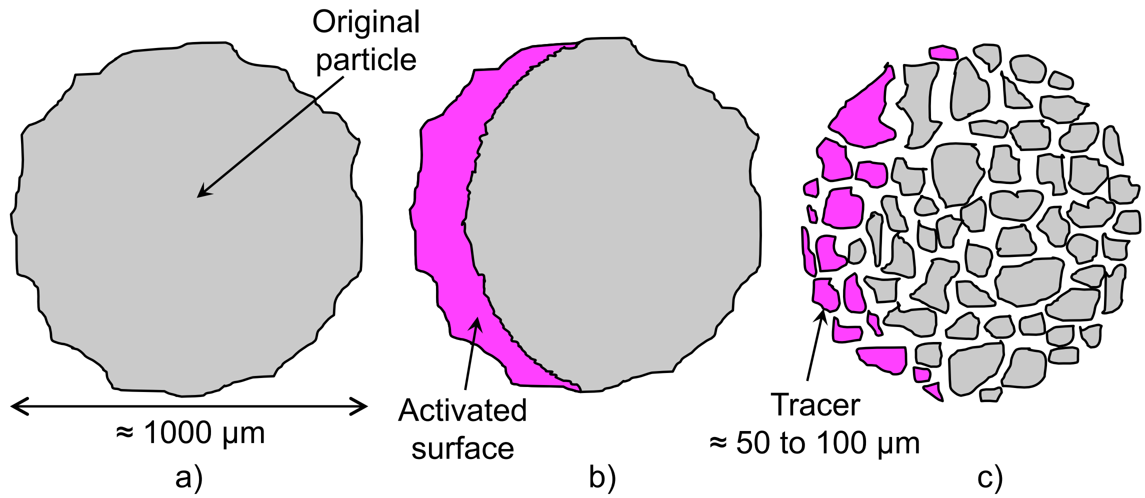

Figure 4.2 – Direct activation of a a) large mineral particle b) surface material and c) breakage.

For the smaller fragment, the activation levels are very low and are measured in counts per second (cps) using a contamination monitor (Tracerco T401). The probe of this device is flat (pancake style), the value measured is thus only based on the gamma rays hitting the probe and not on the whole particle activity and disintegration rate, hence its provides a relative comparison of the activity for the small fragment selection. Activity values for the small tracer shall then be taken relatively as no more efficient way of measuring it was available. Table 4.2 gives the details on the relative activity level of the successful tracers. Figure 4.3 shows example of an original activated particle and a small broken fragment used as tracers.

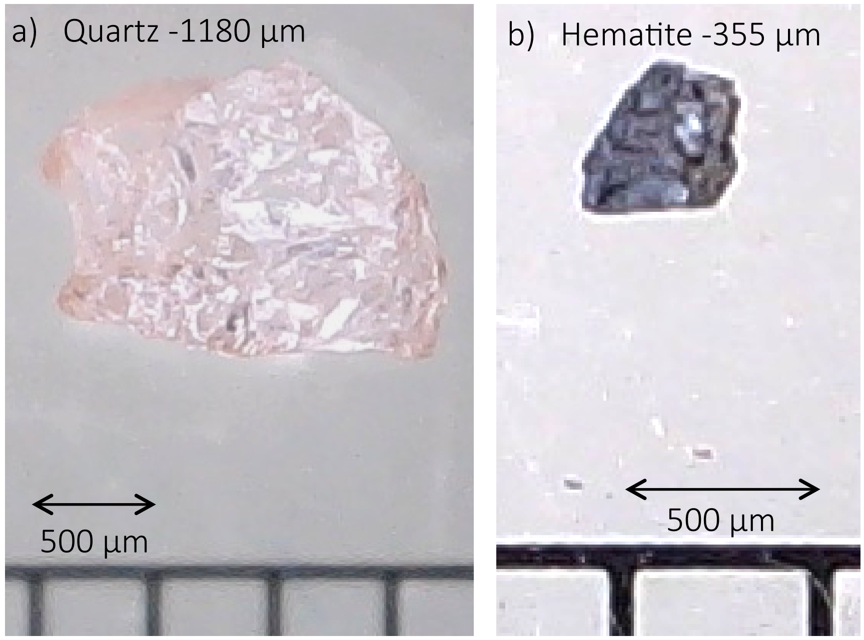

Figure 4.3 – Example of original activated particle and tracer used for tracking a) original quartz (-1180 µm), b) sized hematite (-355 µm).

This method of creating small tracers has some advantages as it provides a particle similar (density, surface properties) to the particles forming the bulk material to be investigated. However, a large number of small fragments are created by the breakage, but only few of them are used, considering that tracking is conducted on one tracer at the time and that the short half-life of ^{18}F limits the number of consecutive experiments possible for each initial activation in the cyclotron. For the smallest size tracers, activity becomes too low for tracking about one hour after activation in the beam stops which can provide about 30 minutes of tracking considering the post activation procedure for size reduction.

4.2.3 Safety and handling

Activation is a complex physical process that additionally generate different isotopes depending on the mineral particle composition and impurities. Examples of isotopes are ^{10}C (half-life 19.3 s), ^{12}N (half-life 11 ms), ^{27}Si (half-life 1.16 s), ^{29}P (half-life 4.1 s), ^{26}Al (half-life 6.4 s). Considering the relatively short half-life, their decay to insignificant level of activity is provided by enabling a *cooling* period (15 min) right after activation by the cyclotron beam. In this study, after this *cooling* period, much of the remaining activity is associated with ^{18}F β^+ decay.

Lead shielding (38 mm) was used as much as possible to keep the activated original particle isolated from the operators during the procedure of breakage and selection, which is the moment of shortest distance to the activated particle. As the breakage is likely to generate many small activated fragments from the original particle, Geiger counters and contamination monitors are used to ensure that work surfaces, tools and any potential contaminated devices are cleaned if contaminated. Dust masks are used to prevent inhalation of small particle fragments.

Unused tracers, redundant fragments and the remaining unbroken activated particles were kept inside lead container until the natural decay lowered their activity. After 24 hours of decay, they were disposed off among other low activity waste (spent towels, gloves and mask) in a specially designated bin for further disposal by the staff as per the lab radioactive waste handling procedure.

Disposal of the slurry which can contains a single tracer or many fragments in case of breakage inside the circuit is done following a 24 hours rest period during which the level of activity returns to the background level.

4.3 Localisation

A single *LoR* generation is called an event, and multiple events are recorded over a short interval of time (of the order of milliseconds). These events can be split to groups of a fixed number (N) of *LoRs*. Some of these *LoRs* are corrupted events caused by scatter or random coincidence. After the removal of these corrupted events by the PEPT iterative triangulation algorithm *TRACK* [11, 207], the remaining fraction (f) of the *LoRs* passes close to one single point (the origin of the gamma rays). This point is assumed to be the tracer particle position for this time interval as shown on Figure 4.4. Recording the tracer positions over time allows a number of parameters to be determined; including (but not limited to) the trajectory, velocity and residence time.

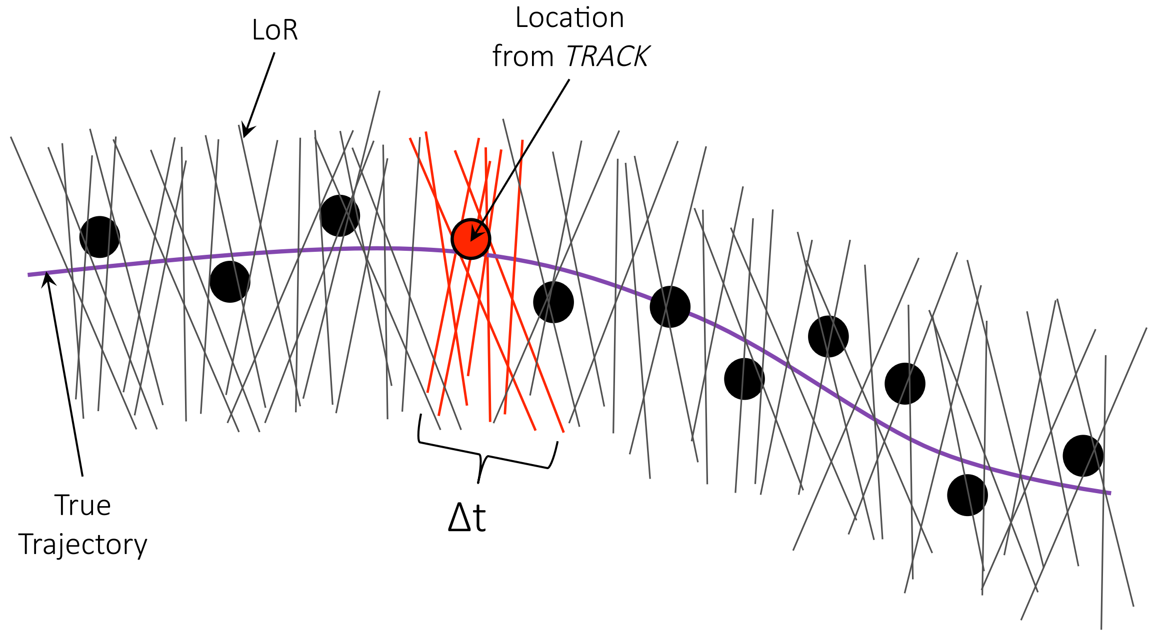

Figure 4.4 – Set of *LoRs* for localisation.

4.4 Detector systems

Gamma photon detection is achieved by the use of scintillation crystals installed close to the experimental set-up. The two arrangements of detectors and acquisition systems used in this study are described in this section. The first is a well characterised system known as the Birmingham ADAC Forte Camera [237]. The second is a custom circular assembly of modular detectors blocks also provided by the University of Birmingham Positron Imaging Center.

4.4.1 ADAC Forte camera

The ADAC Forte camera [237] at the University of Birmingham is used for recording gamma emission events. This system is a standard positron emission tomography camera with two single thallium-doped sodium iodide (NaI(Tl)) crystal scintillator heads (500 by 400 mm) and modified aquisition electronics. The camera (Figure 4.5) is relatively simple to use. However, it has a fixed height which can limit the investigation of tall process equipment. Additionnally, its detection sensitivity limits the observation of tracer with low activity levels ($<3.7 \times 10^6$ Bq depending on tracer velocity) [207].

Figure 4.5 – ADAC Forte camera at Positron Emission Center at The University of Birmingham [235].

4.4.2 Circular ECAT951 modular assembly

PEPT has developed to the point where modular detectors blocks (ECAT 951 detectors, Siemens) can be used in different configurations [206, 207, 238, 239]. This enables the study of systems of different shapes and size operated in a specific environment. Additionally, these bismuth germinate oxide (BGO) scintillation crystal modular detector blocks offer a better sensitivity to gamma photons than the two single crystal heads of the ADAC Forte camera. This is due to a faster scintillation detection electronic coupled with the multiplicity of smaller crystals, each detector block being made of an array of 8 by 8 BGO crystals (Figure 4.1). Considering the height of the spiral and the low amount of activity present on the small tracer surface, such a high sensitivity detector set-up was used for certain experimental runs of this work (see Table 4.2).

In order to determine the best modular detector geometry, simulations of the detection area (Figure 4.6) were created to assess the sensitivity and uniformity of the field of view (FOV) [240]. This type of simulation was used for choosing between different conceptual detector block configurations.

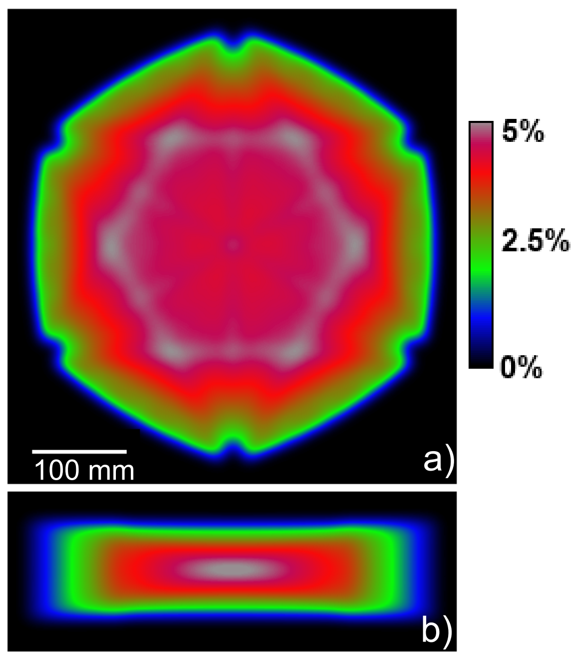

Figure 4.6 – Simulation showing a) xz and b) xy view of a modular ring assembly field of view sensitivity [240].

Finally, twelve modular buckets of four ECAT 951 detector blocks were arranged in a two layer circular pattern (Figure 4.7). For each ring, six buckets are placed every 60° with a clearance diameter of 400 mm (required based on the spiral trough diameter) with a field of view thickness of 100 mm. This specifically designed modular assemblies gives better tracking than the ADAC Forte camera for tracers below 250 µm in diameter, however the characterisation of such a set-up is of great importance.

Figure 4.7 – Double ring assembly of ECAT 951 modular detector blocks.

4.4.3 Tracking performance

Part of this study targeted small particles (<250 µm) which have low activity (<5000 Bq). Assessment of the tracking performance was not available for such a set-up. The two detector systems performance was then assessed for tracking the path of small tracers (≈58 µm) under different conditions:

1. Moving in a known trajectory (circular) and velocity in air.
2. At rest in water.
3. Freely moving in a water-filled, baffled container, stirred by a Rushton turbine.

These conditions were intended to provide a comparison between expected and recorded trajectory as well as the effect of tracer velocity and media attenuation (air or water) on the localisation rate and precision.

4.4.3.1 Circular constrained motion set-up

A planar circular motion is created by fixing a tracer particle to the edge of one of the six paddles of a standard Rushton impeller (Figure 4.8) using carbon tape. Rotation of the impeller is set at the desired speed using a digital mixer (Caframo, BDC 1850, Canada).

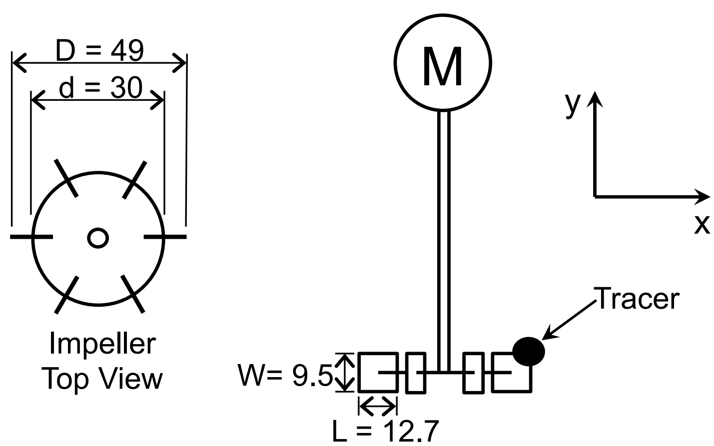

Figure 4.8 – Schematic of the Rushton impeller holding the tracer in a constrained motion with dimension (mm).

With this set-up, the tracer follows a constrained circular trajectory in the xz plane and the expected location over time can be assumed to be a sinusoid in the x axis and another sinusoid in the z axis. In the y axis, the expected location should be constant over time, provided that the plane of rotation is perpendicular to the detector axis. This motion is used for determination of the location error.

4.4.3.2 Water filled vessel set-up

Observation of a tracer initially at rest and then freely moving inside a water filled mixing vessel (Figure 4.9) is undertaken to validate the underwater tracking potential for small tracer carrying low activity. The free tracer is tracked while lying on the bottom of the vessel filled with water, then tracking is conducted while mixing the water with the impeller rotating (Figure 4.10).

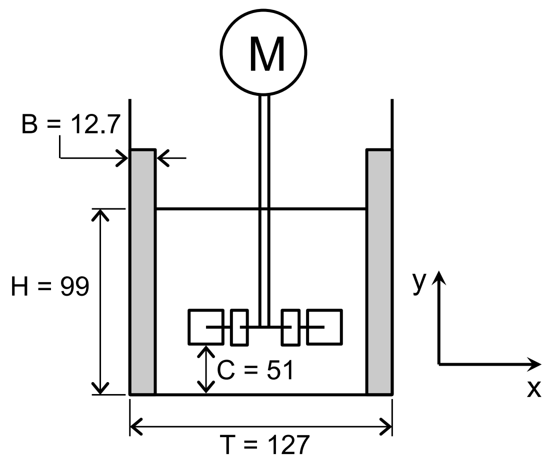

Figure 4.9 – Schematic of the mixing vessel with dimension (mm).

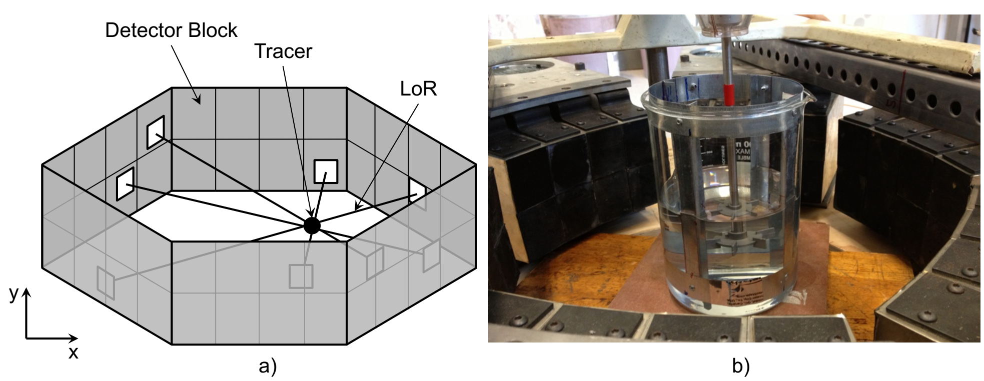

Figure 4.10 – a) Schematic of the tracking and b) image of the mixing vessel inside the modular detector assembly.

4.4.3.3 Location error

With the constrained trajectory set-up, the location error can be determined. For a set of tracked locations, it is calculated using the root mean square error (RMSE) technique with Equation 4.1 (x axis). The error (Δx_i, Δy_i, Δz_i) is the difference between the PEPT axial position and the expected axial position with n being the number of locations in the data sample used. The expected position is determined by fitting the best sinusoid to the located position, starting with a knowledge of some of its parameters based on rotational speed and impeller dimensions. The RMSE was determined by using the MATLAB®Curve Fitting Toolbox™(The MathWorks Inc., USA).

$$RMSE_x = \sqrt{\frac{\sum_{i=1}^{n}(\Delta x_i)^2}{n}} \tag{4.1}$$

The selection of the parameters N and f used in the tracking algorithm can be optimised to reduce the RMSE. To do so, the RMSE values of 30 second samples recorded of the small tracer attached to the impeller while rotating in air (constrained circular trajectory) are calculated with different parameters. Different velocities are tracked for both set-ups. The rotational speed of the impeller carrying a 58 µm diameter tracer is initially set at 150 rpm, then decreased to 75 rpm and finally 15 rpm.

Figure 4.11 presents the different RMSE based on different N and f values for 150 rpm. Figure 4.12 shows the mean location frequency associated with Figure 4.11. This type of graph is used to determine the best parameters. In this case (150 rpm), the tracer velocity is 27.6 cm/s for the ADAC set-up and 37.7 cm/s for the modular assembly. This difference is caused by the tracer being further out on the impeller in the case of the modular set-up. For any case when the location frequency is below three points per rotation (e.g. below 7.5 Hz for 150 rpm), the RMSE is not further analysed. Therefore the errors obtained are of interest for trajectories of a radius of curvature equal to or larger than that of the impeller (≥25 mm). Smaller curvatures will be missed by the low location frequency.

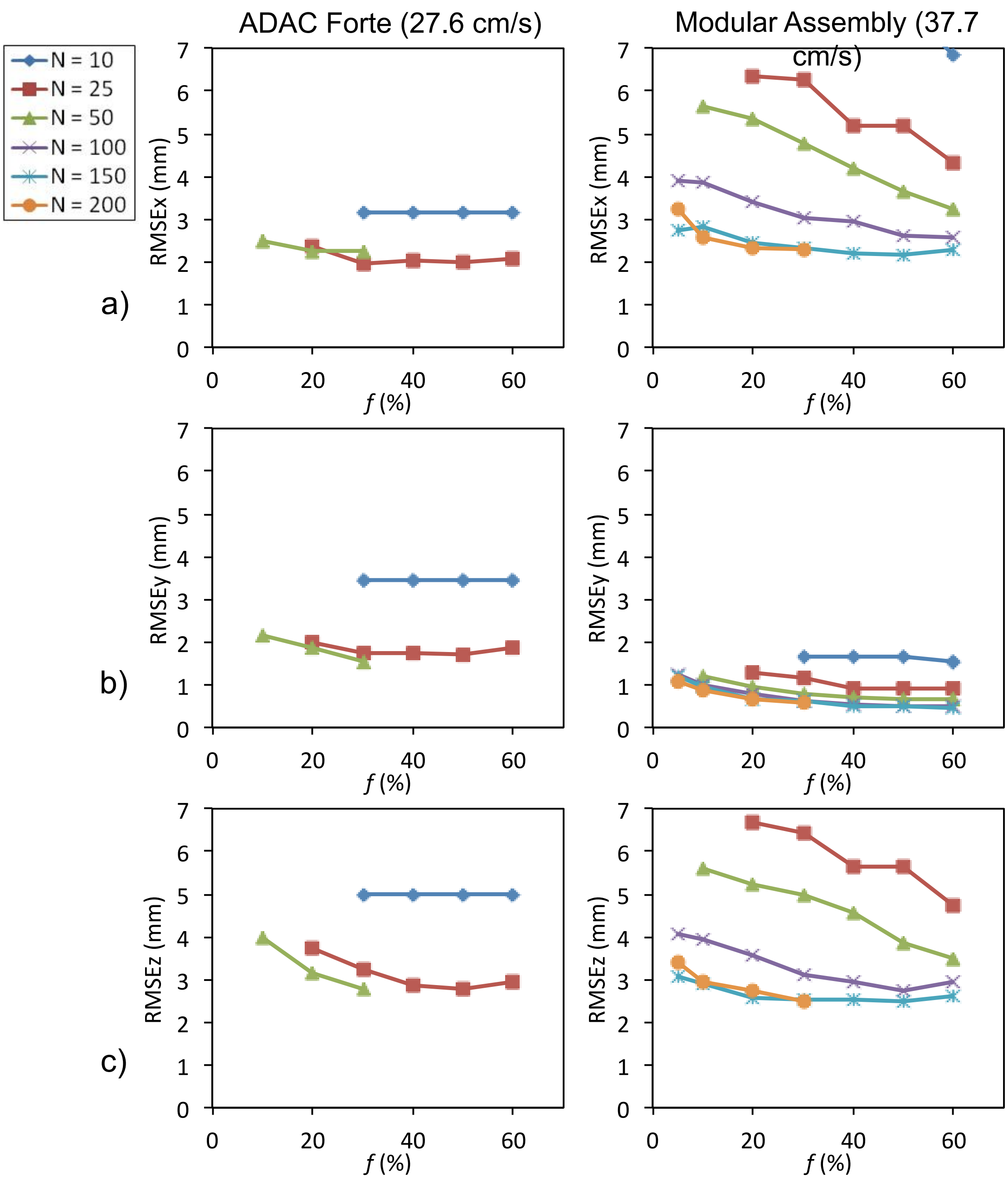

Figure 4.11 – RMSE of the locations for the a) x, b) y and c) z axis.

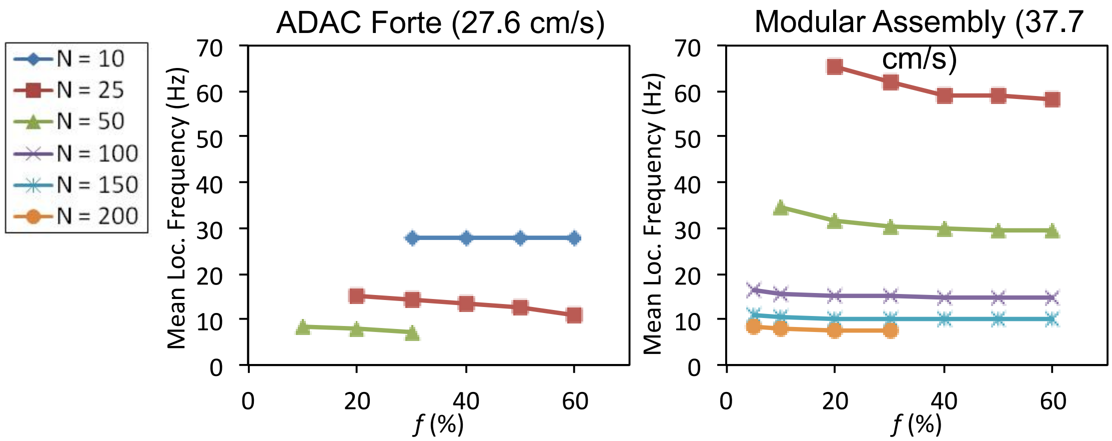

Figure 4.12 – Mean location frequency (Hz) for the ADAC Forte (27.6 cm/s) and the modular assembly (37.7 cm/s).

Table 4.3 provides the N and f values minimising the RMSE for the different cases investigated. For both tracking systems, the final parameters selected are also influenced by the higher location rate provided by a lower value of N, considering the low raw data rate experienced (especially with the ADAC Forte which is 5 to 10 times smaller than the modular assembly). Table 4.4 provides speeds and RMSE for the two detector set-ups for the different rotational speeds.

Table 4.3 – Optimal N and f parameters for the constrained rotational motion of the Ø≈58 µm quartz tracer.

Detector system	Rotational speed (rpm)	Speed (cm/s)	Activity (cps)†	Raw data rate (kHz)	N	f (%)	Mean location frequency (Hz)
ADAC Forte	150	27.6	2600	2	25	50	12.4
ADAC Forte	75	13.8	2300	2	50	40	5.6
ADAC Forte	15	2.8	2100	1	150	30	1.5
Modular Ring	150	37.7	850	10	150	40	10.0
Modular Ring	75	18.9	710	10	150	60	8.6
Modular Ring	15	3.8	620	9	150	60	7.3

† Measured with Tracerco T401.

Table 4.4 – Precision of the localisation for the directly activated quartz tracers of size Ø≈58 µm in a constrained circular trajectory.

Detector system	Rotational speed (rpm)	Speed (cm/s)	$RMSE_x$ (mm)	$RMSE_y$ (mm)	$RMSE_z$ (mm)	$RMSE_{3D}$ (mm)
ADAC Forte	150	27.6	2.0	1.7	2.8	3.8
ADAC Forte	75	13.8	1.6	1.2	2.1	2.9
ADAC Forte	15	2.8	1.2	0.5	1.2	1.8
Modular Ring	150	37.7	2.2	0.5	2.5	3.4
Modular Ring	75	18.9	1.3	0.4	1.3	1.9
Modular Ring	15	3.8	1.2	0.3	1.0	1.6

For each tracking system, the faster that the tracer is moving, the greater the location error (Table 4.4). This is explained by the lower number of *LoRs* recorded for a specific travelled distance. Even at higher speeds, the tracking with the modular assembly is of a better quality and with a higher location frequency. This is mostly due to a greater raw data collection rate (more *LoRs* detected) achievable with the ECAT 951 detector blocks, which have a higher intrinsic efficiency for detecting gamma photons compared to the ADAC Forte detectors. Another point of interest shown in Figure 4.11, is that the $RMSE_z$ is always larger than $RMSE_x$ and $RMSE_y$ for the ADAC Forte. This is caused by the lack of angular sampling in the z axis due to the detectors' configuration (parallel to the xy plane) in the ADAC Forte camera [11].

Figure 4.13 shows the locations of the tracer and the sinusoid representing the expected trajectory for samples of five seconds while the impeller rotates at 75 and 150 rpm. It can be seen that even if the location rate is small (Table 4.3) the locations are sufficient to display a trajectory with a radius similar to that of the impeller.

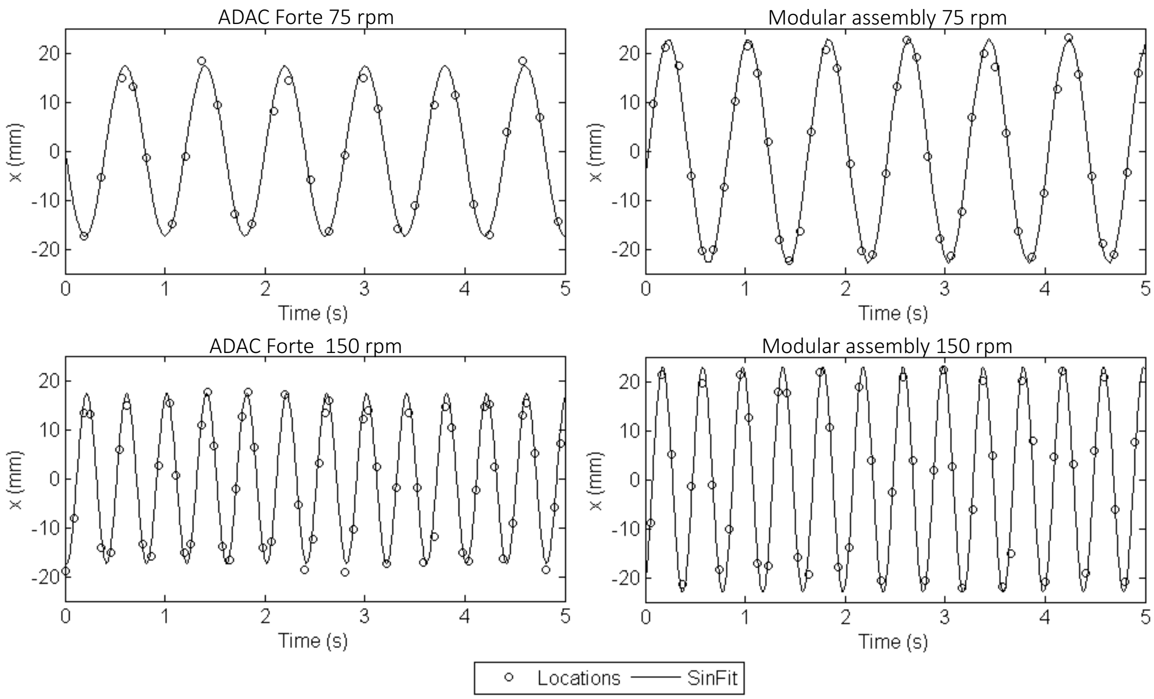

Figure 4.13 – Axial (x) position of the ≈58 µm quartz tracer affixed to the impeller and the sinusoid representing the expected trajectory for the ADAC Forte and the modular detector assembly.

Table 4.5 provides the location rate and RMSE for the tracers lying in the water filled vessel. Figure 4.14 shows an example of the tracers position in time with the expected (least RMSE) position.

Table 4.5 – Precision of the localisation achieved for a directly activated quartz tracer of size Ø≈58 µm at rest in a water filled vessel.

Detector system	Activity (cps)†	Location rate (Hz)	$RMSE_x$ (mm)	$RMSE_y$ (mm)	$RMSE_z$ (mm)	$RMSE_{3D}$ (mm)
ADAC Forte	3200	6.0	1.5	1.6	3.1	3.8
Modular Ring	2400	2.0	1.9	1.5	2.4	3.4

† Measured with Tracerco T401.

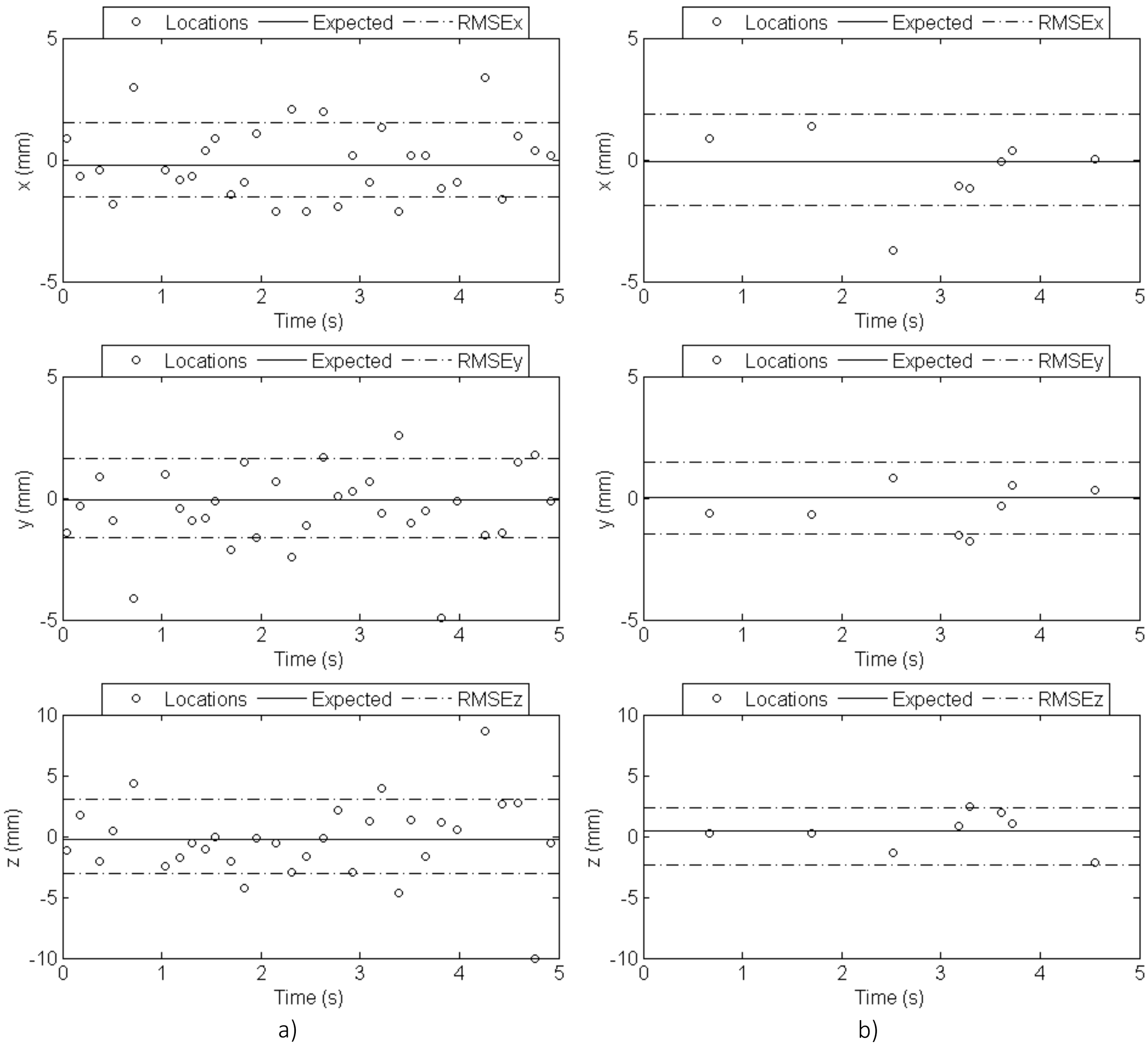

Figure 4.14 – Tracer location while at rest on the bottom of the Rushton turbine with the expected location and RMSE for a) the ADAC Forte and b) the modular assembly.

For this case, the tracking provided by the modular assembly is slightly more accurate than the ADAC Forte with a smaller RMSE, except for the x axis. The location rate was lower for the modular assembly and a better tracking was expected based on the information in Table 4.3. It is worth noting that the activity of the small tracer for the ADAC Forte was originally higher than the one for the modular set-up as seen in Figure 4.5. More importantly, the tracer was lying on the bottom of the vessel hence very close to the lower limit of the detection field of view of the modular set-up where sensitivity is lower (shown in Figure 4.6), which is a potential explanation for this low rate.

4.4.3.4 Freely moving tracer

Figure 4.15 shows the 58 µm tracer motion inside the water filled mixing vessel [2]. The trajectory, here shown as straight lines between the location from *TRACK*, is typical of the loop pattern characteristic of this type of impeller-vessel system. The oscillation in the trajectory display the fact that the locations lay close to the real trajectory rather than exactly on it, which will require further data analysis as described in Section 4.5.

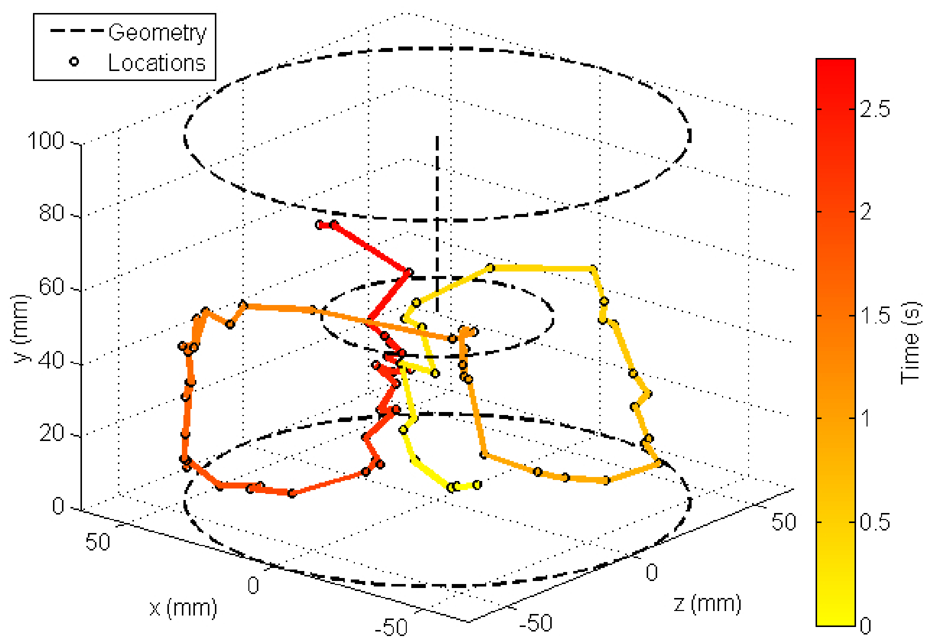

Figure 4.15 – Tracer moving in a loop pattern inside the water filled baffled vessel stirred by the Rushton impeller.

4.5 Data analysis

Once the locations are recovered from the *TRACK* algorithm, further processing of the locations was undertaken with a MATLAB code specifically written for this purpose (Appendix A). The code performs the tasks described in Figure 4.16.

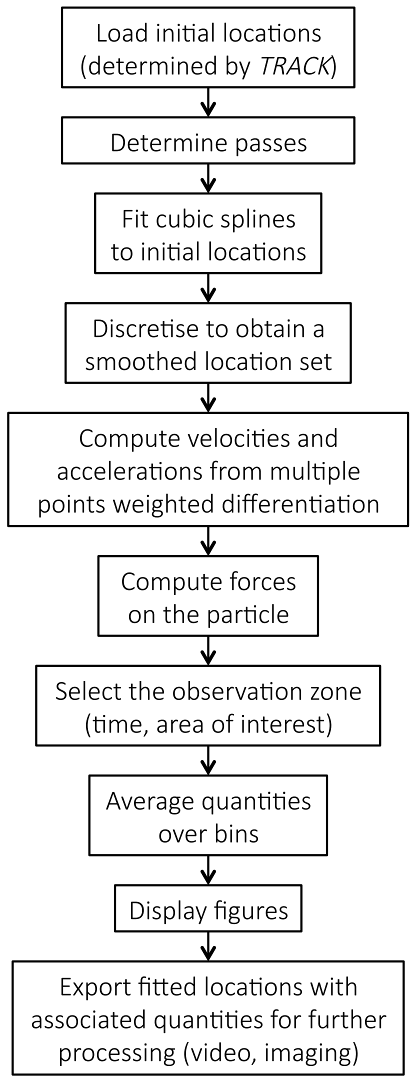

Figure 4.16 – Schematic of the MATLAB code used for analysis of the tracer location.

4.5.1 Data fitting

There is a difference between the true tracer trajectory and the location obtained from the *TRACK* code as shown by the error on each of the location. This error effect is randomly distributed around the true tracer trajectory. This can give the appearance of the tracer quickly shifting from left to right and up and down (Figure 4.17). This effect is expected to be more pronounced for smaller tracer as they carry less activity which emits a lower amount of *LoRs* which provide a limited precision on the location. To smooth this tracked trajectory, a fit inspired by Cole *et al.* [241] is applied on the initial location and is expected to provide a more representative path for the tracer.

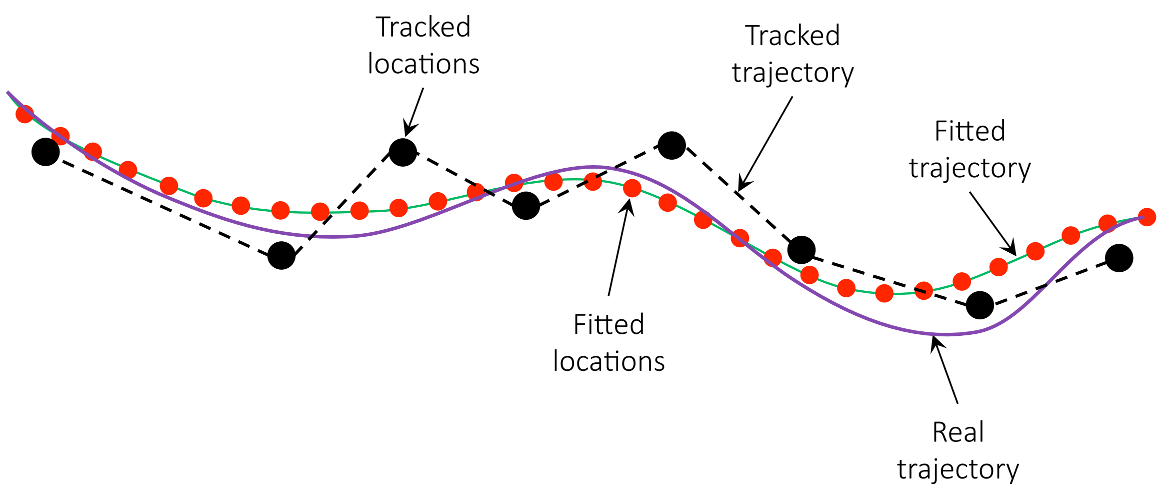

Figure 4.17 – Schematic of the real, tracked and fitted trajectory with locations.

A sliding overlapping interval is used to provide a fit over long datasets (more than a million initial locations). Multiple pieces of cubic spline are used to fit the small time intervals (≈0.5 second) of the axial component of the initial locations. This fit uses the least square spline approximation of the MATLAB `spap2` function. Each section of the fit is discretised (1000 to 2000 Hz) into a *fitted trajectory* locations dataset for further analysis. This simplifies the averaging of different motion parameters. Figure 4.18 presents an example of an initial location set and its fitted trajectory.

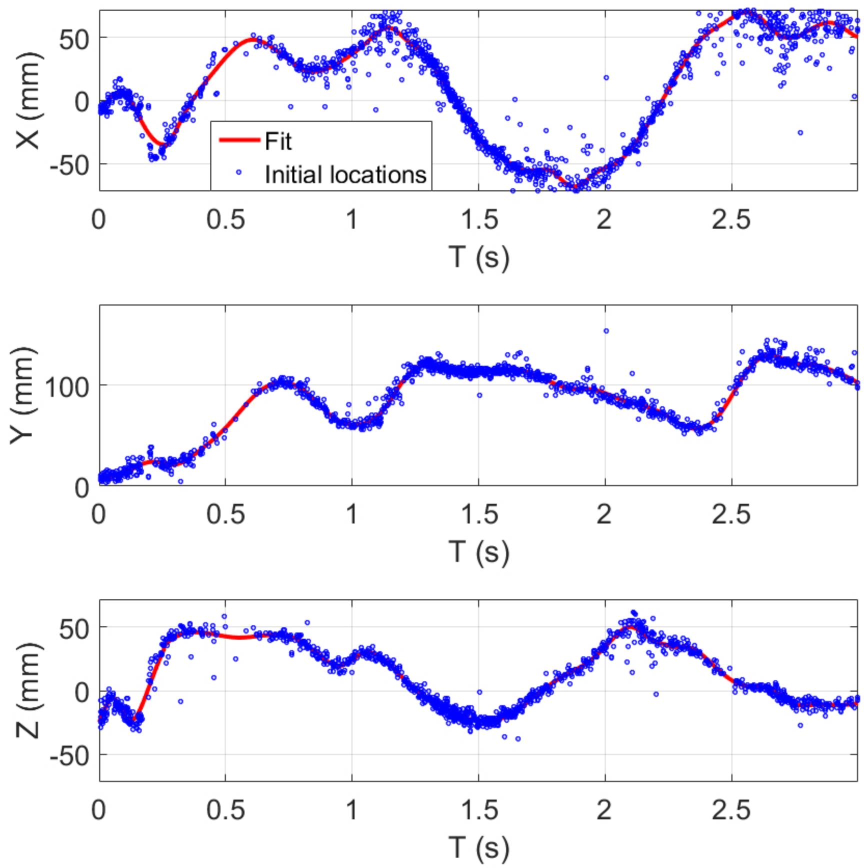

Figure 4.18 – Example of a set of initial location and its cubic spline fit for each axis (100 µm hematite tracer in a mixing vessel).

4.5.2 Determination of tracer velocity and acceleration

Velocity is the time derivative of of the trajectory and acceleration is the time derivative of the velocity or the trajectory second derivative. A discrete approximation of these derivatives is obtained by the following process.

The velocity of the tracer at a fitted location i is calculated by using the five previous, the actual, and the five next locations of the tracer with regards to the time for each of these locations and weighting factors [242]. This method has the effect of smoothing the velocity and reducing the effect of the tracer localisation error [207]. This method must be used carefully when tracking a tracer moving in and out of the field of view of the camera, or at a very low location rates (low tracer activity) as the previous and next locations can be non representative of the tracer motion over a short time interval. Using this method with the fitted trajectory provides a more continuous velocity for the tracer considering that a higher locations rate can be discretised with the fit. Equation 4.2 is used (here for x axis), with positions data (transformed to polar coordinates when required), where $v_{x_{p_i}}$ is the velocity component of interest, p_i is the position of the tracer and t_{p_i} is the time associated with this position.

$$
\begin{aligned}
v_{x_{p_i}} &= 0.10\left(\frac{x_{p_{i+5}} - x_{p_{i-0}}}{t_{p_{i+5}} - t_{p_{i-0}}}\right) + 0.15\left(\frac{x_{p_{i+4}} - x_{p_{i-1}}}{t_{p_{i+4}} - t_{p_{i-1}}}\right) + 0.25\left(\frac{x_{p_{i+3}} - x_{p_{i-2}}}{t_{p_{i+3}} - t_{p_{i-2}}}\right) \\
&+ 0.25\left(\frac{x_{p_{i+2}} - x_{p_{i-3}}}{t_{p_{i+2}} - t_{p_{i-3}}}\right) + 0.15\left(\frac{x_{p_{i+1}} - x_{p_{i-4}}}{t_{p_{i+1}} - t_{p_{i-4}}}\right) + 0.10\left(\frac{x_{p_{i+0}} - x_{p_{i-5}}}{t_{p_{i+0}} - t_{p_{i-5}}}\right) \qquad (4.2)
\end{aligned}
$$

The same treatment is applied to the component of the velocity at each point to obtain the acceleration. In this case, equation 4.3 is used (here for x axis), with velocity data (transformed to polar coordinates when required), where $a_{x_{p_i}}$ is the acceleration component of interest.

$$
\begin{aligned}
a_{x_{p_i}} &= 0.10\left(\frac{v_{x_{p_{i+5}}} - v_{x_{p_{i-0}}}}{t_{p_{i+5}} - t_{p_{i-0}}}\right) + 0.15\left(\frac{v_{x_{p_{i+4}}} - v_{x_{p_{i-1}}}}{t_{p_{i+4}} - t_{p_{i-1}}}\right) + 0.25\left(\frac{v_{x_{p_{i+3}}} - v_{x_{p_{i-2}}}}{t_{p_{i+3}} - t_{p_{i-2}}}\right) \\
&+ 0.25\left(\frac{v_{x_{p_{i+2}}} - v_{x_{p_{i-3}}}}{t_{p_{i+2}} - t_{p_{i-3}}}\right) + 0.15\left(\frac{v_{x_{p_{i+1}}} - v_{x_{p_{i-4}}}}{t_{p_{i+1}} - t_{p_{i-4}}}\right) + 0.10\left(\frac{v_{x_{p_{i+0}}} - v_{x_{p_{i-5}}}}{t_{p_{i+0}} - t_{p_{i-5}}}\right) \qquad (4.3)
\end{aligned}
$$

4.5.3 Averaged quantities

A powerful use of PEPT data is the possibility to group the information obtained from multiple different passes of a tracers in a specific zone of the vessel to determine the average behaviour of the tracer in that zone. Enough passes in each zones can be acquired over long experimental runs, many repeat or multiple tracers tracking.

The analysis of the different zone can be undertaken by splitting the process equipment space into representative bins. Cubic bins are of interest for certain geometry. In the case of the spiral, the cylindrical symmetry enables the use of toroids bins formed by a square grid on the radius-elevation plan (Figure 4.19).

The cross sectional size of the bins in this study is 10 by 10 mm. This is required to have a at least a few locations present in each bin.

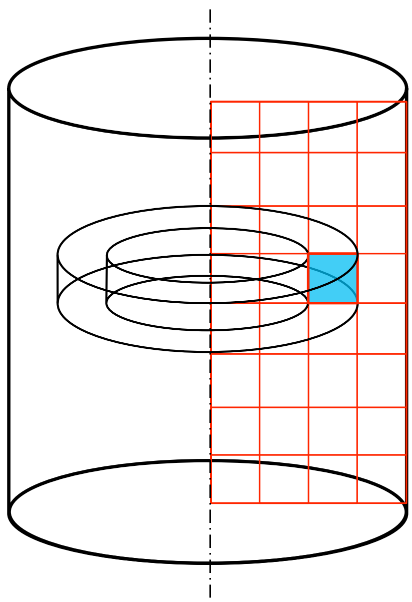

Figure 4.19 – Schematic of the square toroid bins used for averaging quantities.

4.6 Particle tracking on a spiral

Considering the size of the spiral concentrator used (four turns of a pitch of 208 mm), independent runs in the two detectors set-up were used to image the full height. The fixed height ADAC set-up was used for imaging of the lower part of the spiral while the variable height modular ring set-up was used for observation of the upper section.

4.6.1 ADAC Forte tracking set-up

Figure 4.20 present the spiral installed inside the ADAC Forte detectors set-up at the Birmingham Positron Imaging Center. Figure 4.21 details the tracked section of the spiral observed with this set-up. In this configuration, turn 1.5 to 3.5 of the spiral are in the detectors field of view.

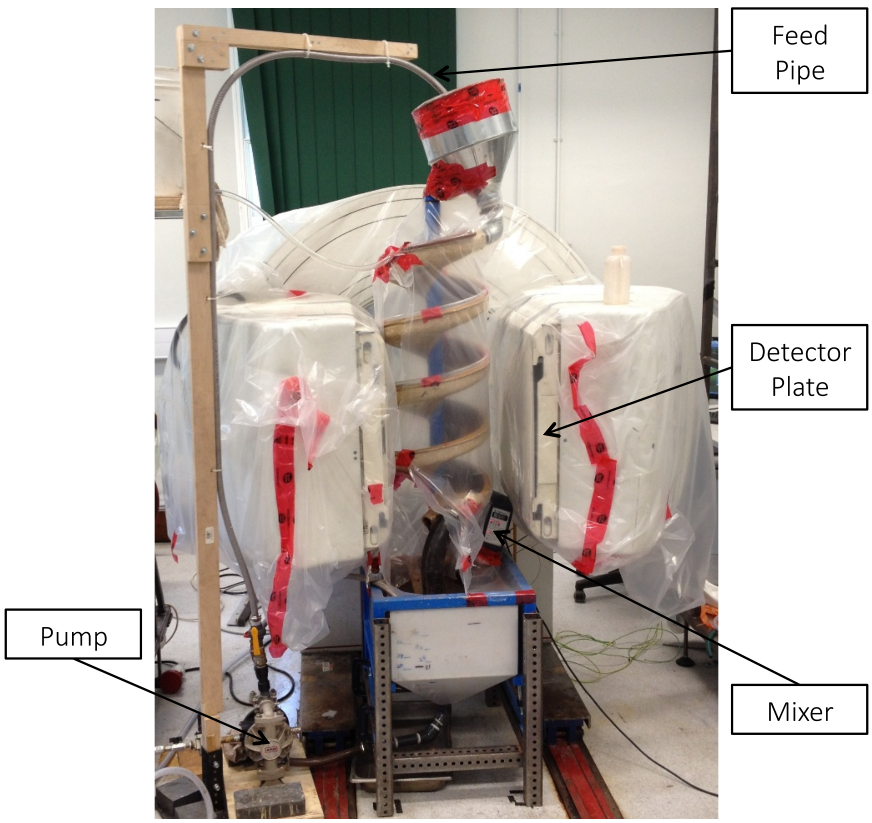

Figure 4.20 – Recirculating spiral inside the ADAC Forte detectors set-up.

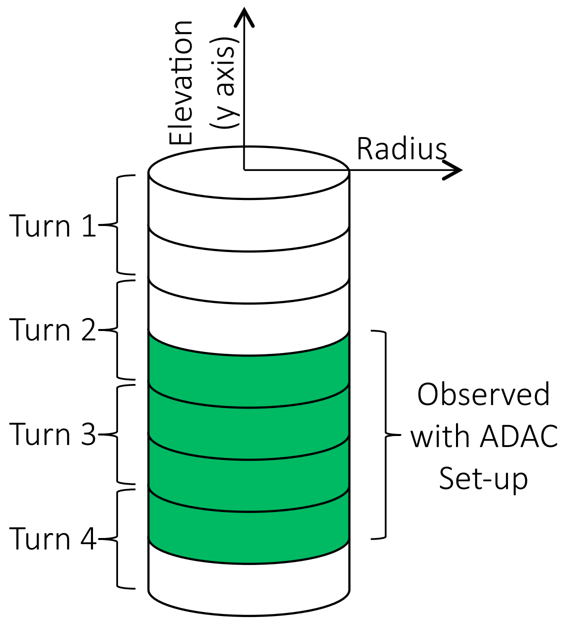

Figure 4.21 – Schematic of the tracked section inside the ADAC Forte detectors set-up.

4.6.2 Modular ring tracking set-up

The modular detector assembly was positioned at different heights around the spiral to track different 100 mm thick slices of the trough. The field of view was set at an angle of 10.5° to match the trough edge angle, and increase the tracked trough length of some slices. An adjustable height support frame enabled the field of view to be easily moved vertically. Tracking runs were carried out for different tracer sizes and minerals at each position before moving the assembly vertically downward to the next slice. This arrangement can be seen on Figure 4.22. The trough sections tracked are presented in Figure 4.23 which cover the first 2.5 turns.

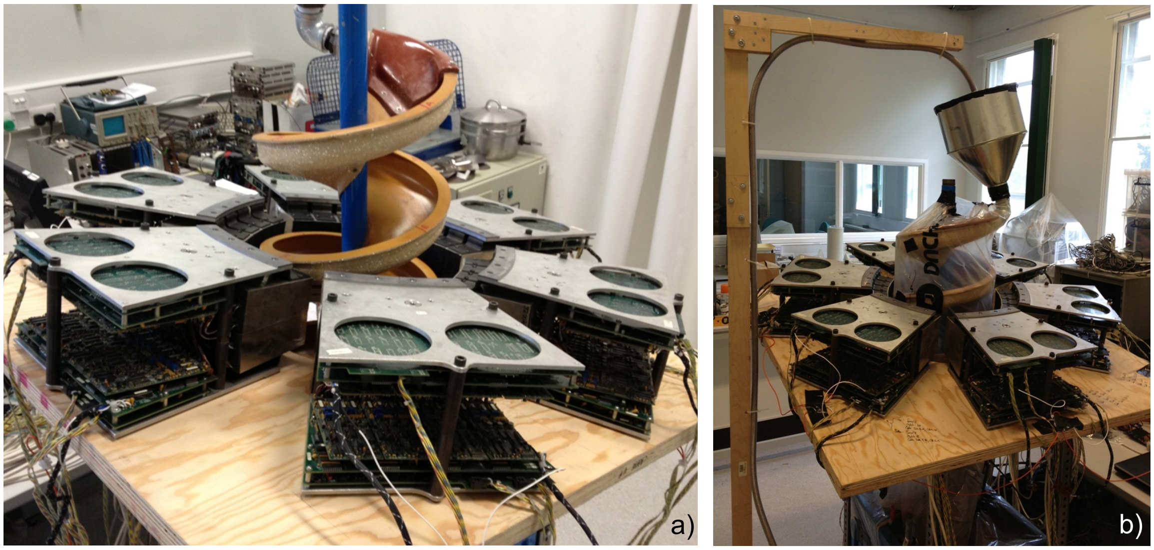

Figure 4.22 – Spiral concentrator inside the modular assembly a) showing the 10.5° inclination following the trough edge and b) in operation.

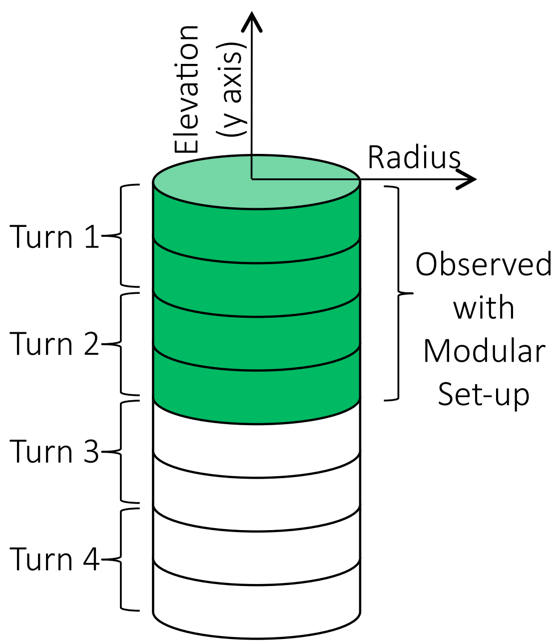

Figure 4.23 – Schematic of the trough slice tracked with the modular detectors set-up.

4.6.3 Tracking runs

During the experiments, 3-4 particles (1000 to 1700 µm) of the same mineral are activated altogether. Breakage and sizing of a smaller tracer is undertaken right after the activation *cooling* period.

Once a sized particle is found to be active enough, considering its size, it is added to the slurry in the first turn of the spiral trough. Data recording is then carried until the particle decay is such that the passes in the FOV cannot be used for data analysis as they would contain too low a number of locations. This is determined by the observation of a live display of the detected coincidence event (*LoR* detection). For the smallest tracers, this is approximately 30 minutes of slurry recirculation on the trough. At this moment, one of the remaining larger activated piece (>450 µm) or one of the original activated particles (>1000 µm) is added to the slurry. This large tracer still have a high activity and can be tracked without any doubt even with the small decayed tracer still present in the slurry.

After about an hour of data recording with this tracer, the slurry is removed from the set-up, the pump is stopped, the large tracer recovered from the slurry for disposal and the spiral set-up cleaned. A new slurry is prepared for each tracer activation run to prevent the use of a contaminated pulp, especially in case of tracer disintegration due to impact in the pump and pulp distribution tube.

Chapter 5

Particle flow within a spiral concentrator

The PEPT technique was used to observe particle flow within a spiral concentrator. It provided particle trajectories, velocities, accelerations and forces that are useful in understanding the particle concentration process [1, 3, 4]. This is the first time that particle motion in a spiral concentrator has been presented as actual particle motion at the scale of the particle rather than a motion hypothesis theorised from pulp stream sampling and film thickness measurements. The latter experimental technique is of interest in determining the performance of a specific spiral design under fixed operation parameters; however, observation of particle trajectories and other motion parameters is an important milestone in the development of future particle-scale models and simulations of the separation that ocurs in a spiral.

This chapter presents the experimental tracking results obtained, as well as a discussion regarding their relevance. First, the conventions used in the presentation of the results are given. Second, the flow of particle in the first turn is described in detail. Third, the particle behaviour in the secondary flow is presented for selected tracers. Finally, the effect of wash water on particle flow is described.

5.1 Conventions

Cartesian coordinates are used for the original locations provided by the PEPT algorithm and *TRACK* code. For the purpose of the analysis, the origin (0,0,0) is set at the top of the spiral with the y axis going upward concentric to the central post and x and z axis defining the horizontal plane. A particle moving down the spiral will thus reduce its elevation (negative y axis). In the case when data are averaged over square toroids bins, as described in Section 4.5.3, the x and z axis coordinates are transformed in cylindrical coordinates (r and θ) while keeping y as the elevation.

Three radial zones are defined for the spiral trough. The inner zone (r<67.5 mm), the middle zone (67.5 mm<r<125 mm) and the outer zone (>125 mm) as shown in Figure 5.1. During operation of the spiral with a dense pulp flow (≥20 % solids), the inner zone is mostly filled by a closely packed dense-particle stream, the outer zone by a dilute light-particle stream and the middle zone is the transitional part of the trough.

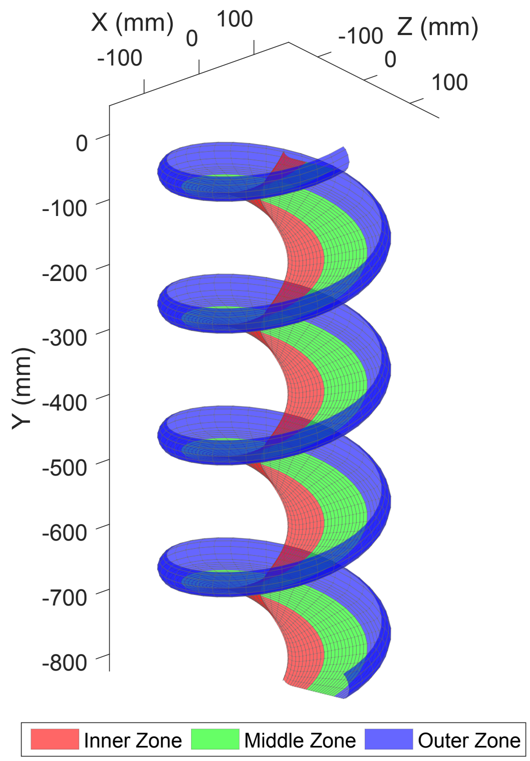

Figure 5.1 – Schematic of the inner, middle and outer zone of the spiral trough used for analysis.

A measure of the concentration or rejection for the particle is the variation in its radial position (radial displacement) between two elevations on the trough (*e.g.* the entrance and exit of the detector FOV). The concentration or rejection of the tracer particle is observed by plotting these entrance and exit radii; as shown in Figure 5.2. Depending on which area of the plot the tracer pass is found, it indicates which behaviour the tracer has for this pass.

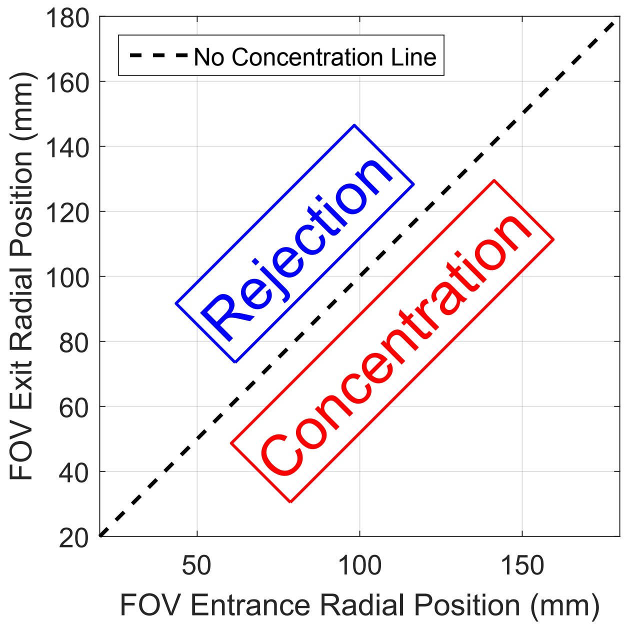

Figure 5.2 – Convention for the radial displacement figures.

The motion is analysed by the use of the three dimensional time recorded locations from which the fit (Section 4.5.1) provides a smooth discrete set of locations used for determination of the particle velocity (Eq. 4.2). From the velocity, the particle acceleration (Eq. 4.3) is determined. With knowledge of the acceleration, the resultant force on the particle is determined (Eq. 2.3) by the approximation of the particle as a sphere of the size observed in the microscope during the tracer preparation (Section 4.6.3) with the mass of the particle being approximated using its mineral density (Table 4.1).

5.2 Particle flow (1st turn)

The first turns of the spiral are of primary importance as separation performance is reaching a steady point within two to three turns if no flow regeneration is used (*e.g.*

material take off port or repulpers) [128]. This section provides information on the measured particle behaviour inside the 1st turn with the details of the flow of small, medium and large particles for both dense (hematite) and light (quartz) minerals.

5.2.1 Small hematite particle (Run P31H0106)

Figure 5.3 presents the radial displacement of a small (90 to 106 µm) hematite tracer for the first slice (3/4 of a turn) of the spiral (Elevation 0 to −100 mm). It shows an overall inward motion for this dense particle with all the passes (except two) moving closer to the centre post even for passes where the particle entered the spiral at the outward extremity of the outer zone.

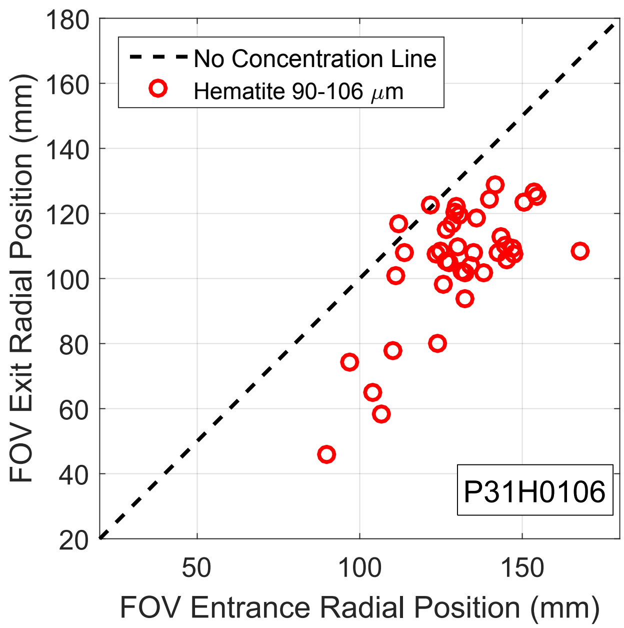

Figure 5.3 – Radial displacement for a small size (90 to 106 µm) hematite tracer (Run P31H0106) in the spiral 1st turn (Elevation 0 to −100 mm).

Figure 5.4 presents the velocities, acceleration and force averages of a small size (90 to 106 µm) hematite tracer. Acceleration values obtained for the outer zone (at the outer edge of the pulp film) give an idea of the turbulence affecting the small hematite particle as the acceleration reaches 12 m/s^2, with a velocity magnitude between 0.8 to 1.2 m/s giving a hint on the rapid change in direction and velocity. The size and density of the particle makes it at the limit of the fluid drag dominated motion. The particle is then expected to partly follow to pulp flow. This is noticeable by observation of the radial velocity, where the particle is following the pulp discharge stream going to the outer vertical section of the profile in the outer zone (shown by outward radial velocity after the feed distribution). After coming into contact with the rising section of the profile, the pulp moves back toward the center.

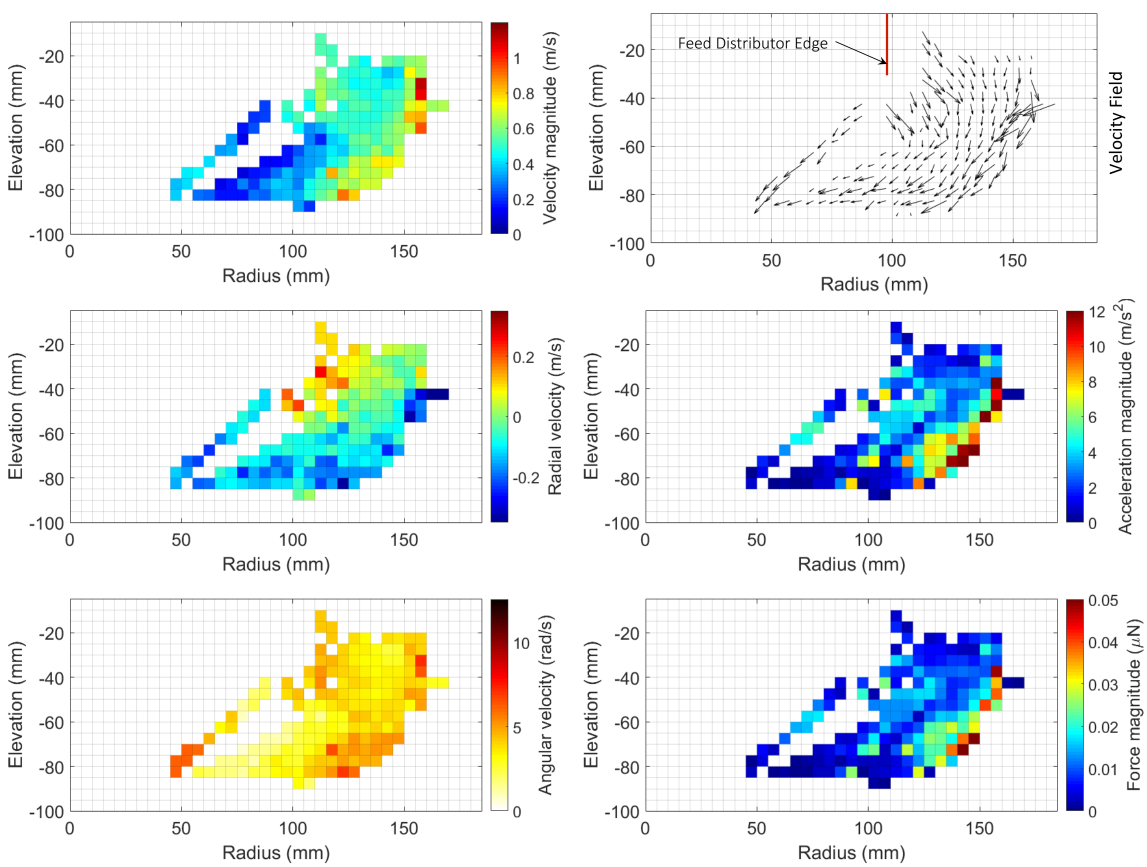

Figure 5.4 – Flow field for a small size (90 to 106 µm) hematite tracer (Run P31H0106) in the spiral 1st turn (Elevation 0 to −100 mm).

5.2.2 Small quartz particle (Run P31Q0106)

Figure 5.5 presents the radial displacement of a small (90 to 106 µm) quartz tracer. As with the hematite tracer of the same size (Figure 5.3), it shows a general inward motion, however, to a smaller extent. Possibly the most likely reason for this inward motion is the overall inward motion of the pulp film after contacting the rising trough edge. A second reason for this inward motion is the nature of the particle being denser than the fluid. This should have a smaller impact than with the hematite tracer due to density difference between hematite and quartz. The differential motion between the small quartz and hematite particles can be observed by the fact that most hematite passes (except two) in Figure 5.3 have inward radial displacement (concentration) compared to most of the quartz passes which show outward radial displacement (rejection) in Figure 5.5.

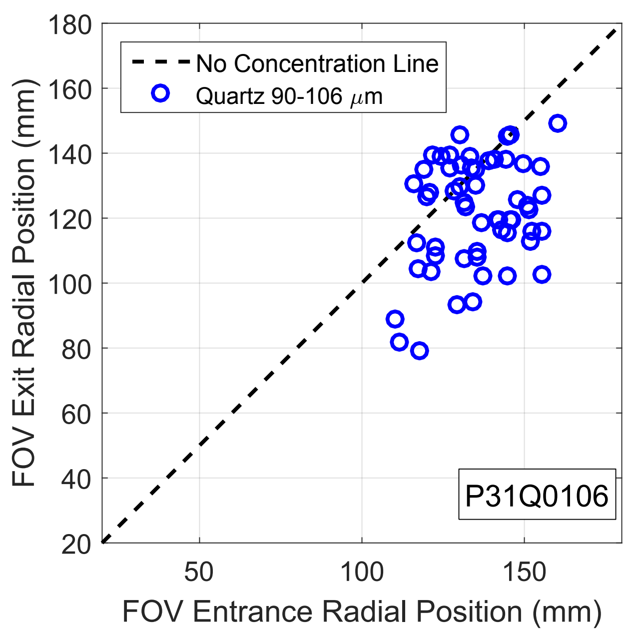

Figure 5.5 – Radial displacement for a small size (90 to 106 µm) quartz tracer (Run P31Q0106) in the spiral 1st turn (Elevation 0 to −100 mm).

Figure 5.6 presents the velocities, acceleration and force averages of a small (90 to 106 µm) quartz tracer. Once again, the turbulence present in the outer zone of the pulp flow provides a large acceleration on the small quartz tracer which results in higher velocity near the end of this slice (FOV limits from 0 to −100 mm in elevation). This effect is more pronounced than for the same sized hematite tracer (Figure 5.4). The size and density of the quartz particle ensures that it is in a fluid drag dominated flow. The particle is expected to follow more closely the pulp flow trubulence which is observed by the general higher velocity for the light quartz tracer than for the same sized heavier hematite one. Another potential contributing factor to the larger velocity magnitude is the feed velocity, which may have been higher. However, the pumping parameters were the same for all runs performed which is expected to provide the same pulp feed velocity. Unfortunately, no pulp velocity control method was used to measure the pulp feed velocity at the discharge point.

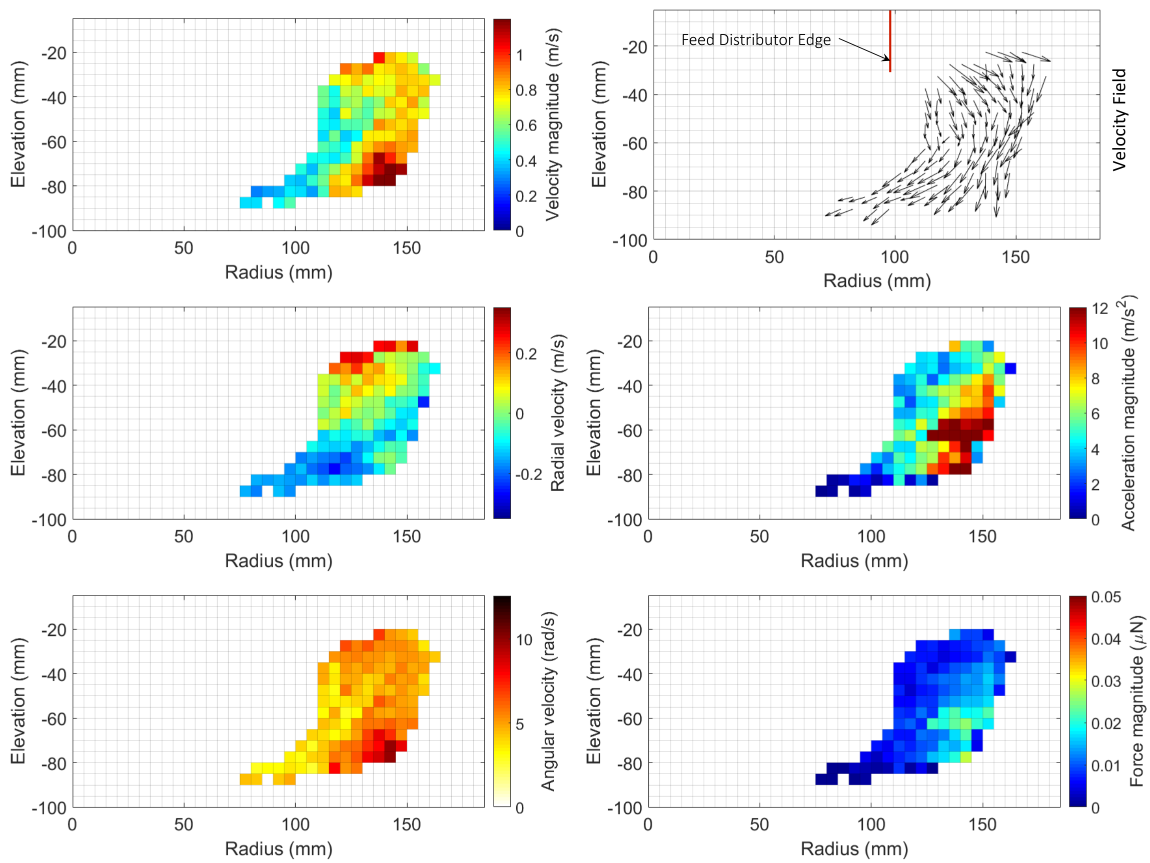

Figure 5.6 – Flow field for a small size (90 to 106 µm) quartz tracer (Run P31Q0106) in the spiral 1st turn (Elevation 0 to −100 mm).

5.2.3 Medium hematite particle (Run P31H0355)

Figure 5.7 presents the trajectory of a medium size (300 to 355 µm) hematite tracer. Passes originating close to the feed distributor inner edge are shown quickly moving inward as a result of the steep decline of the helix in the region close to the central post. Passes fed to the outer region of the trough follow the general direction of the outer section of the trough, but with a slight inward motion.

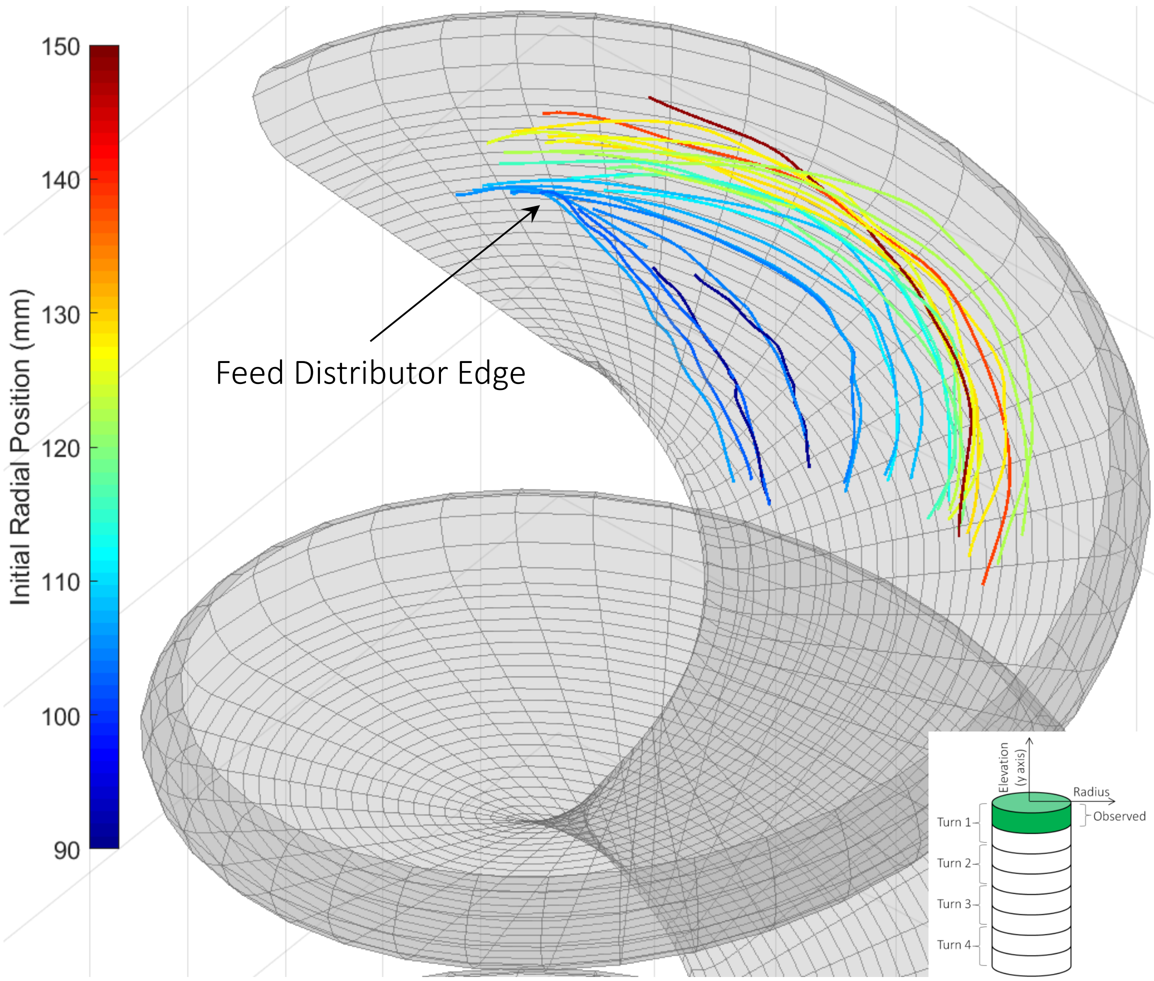

Figure 5.7 – Trajectory for a medium size (300 to 355 µm) hematite tracer (Run P31H0355) in the 1st turn of the spiral (Elevation 0 to −100 mm).

Figure 5.8 presents the radial displacement of a medium size (300 to 355 µm) hematite tracer. Large inward movement of the passes fed at the inner edge of the feed distributors are observable in the region of low initial feed position. These passes are concentrating at a higher rate than the one fed in the outer zone. This can be explained by a lower feed velocity unable to centrifuge the particle outward to the same extend of those passes fed to the outer zone. In addition, the majority of the water is rapidly flowing towards the outer wall immediately after the feed distributor with only a thin film of water remaining in the inner-middle zone to carry the particles.

The dense particle fed in the inner-middle section will thus be less affected by the outward flow, and will follow the steep downward slope of the trough close to the central post.

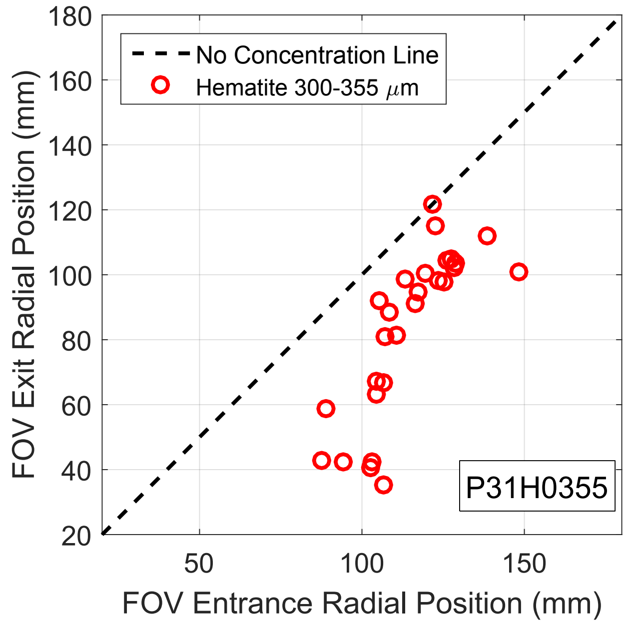

Figure 5.8 – Radial displacement for a medium size (300 to 355 µm) hematite tracer (Run P31H0355) in the spiral 1st turn (Elevation 0 to −100 mm).

Figure 5.9 presents the velocities, acceleration and force averages of a medium size (300 to 355 µm) hematite tracer. The observation of the velocity magnitude for the passes fed at the inner edge of the feed distributor confirm that those passes have a lower initial velocity magnitude and are less affected by the rapid flow of water. The average velocity magnitude in this zone is below 0.4 m/s. Once again, the passes at the outer edge of the profile appear to be affected by the turbulence in the outer zone, but to a lesser extent than the small tracer, as the acceleration magnitude is much lower in the case of the medium particle ($\approx$6 m/s^2) compared to the acceleration on the small tracers ($\approx$12 m/s^2). A component of this overall acceleration is related to the general curved motion of the pulp in the helix.

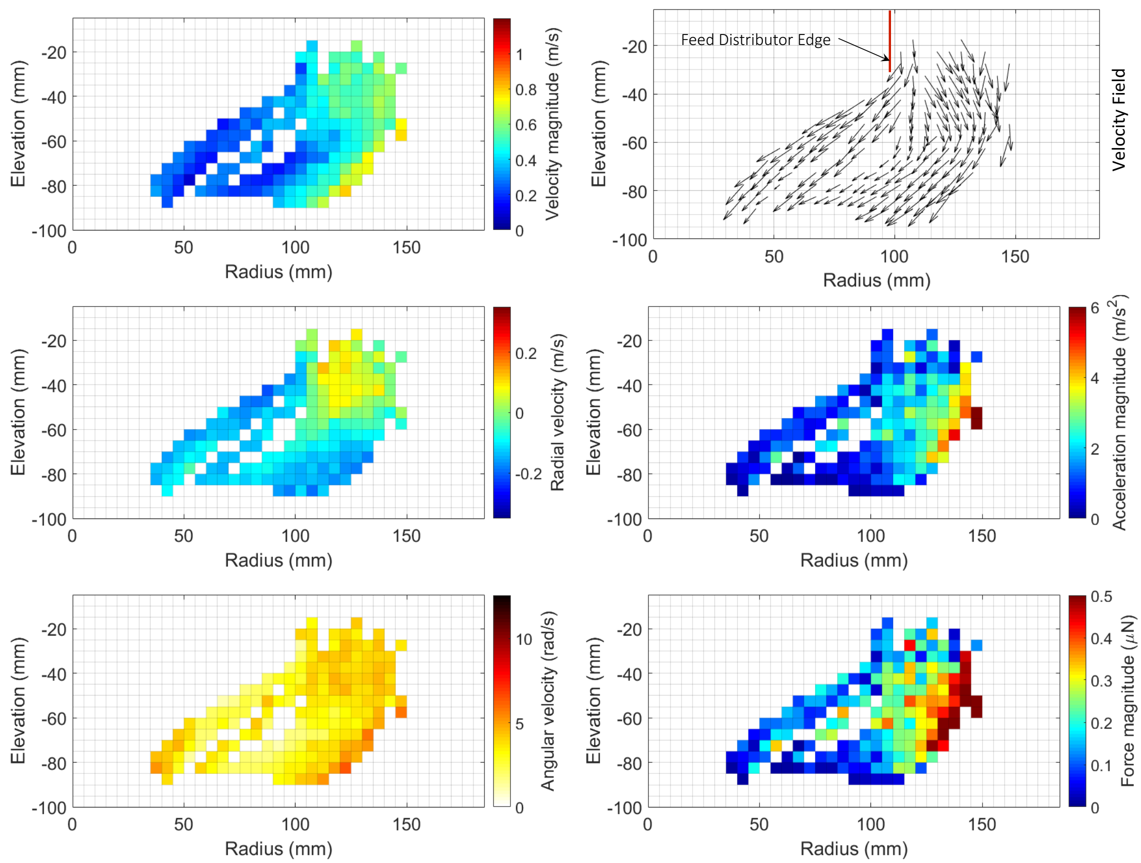

Figure 5.9 – Flow field for a medium size (300 to 355 µm) hematite tracer (Run P31H0355) in the spiral 1^{st} turn (Elevation 0 to -100 mm).

5.2.4 Medium quartz particle (Run P31Q0355)

Figure 5.10 presents the trajectory of a medium size (300 to 355 µm) quartz tracer. The same effect than for the similar size hematite tracer is seen at the inner side of the feed discharge for some passes of the tracer flowing down to the inner zone in the step section of the helix. However, this behaviour is not observed in many passes. The vast majority of the passes are found to be fed in the middle-outer zone as per the design of the feed distributor. Once on the trough, some passes will stay in the inner side of the slurry film while others will stay completely outward. A large portion of the passes are found to be interchanging places within the middle-outer zone region of the trough. Some of the passes originating in the middle zone are even seen flowing over other passes originating in the outer zone. This is an excellent visualisation of the particle motion happening due to the secondary motion of the fluid. This outward-inward motion is localised in a band at the inner side of the outer zone.

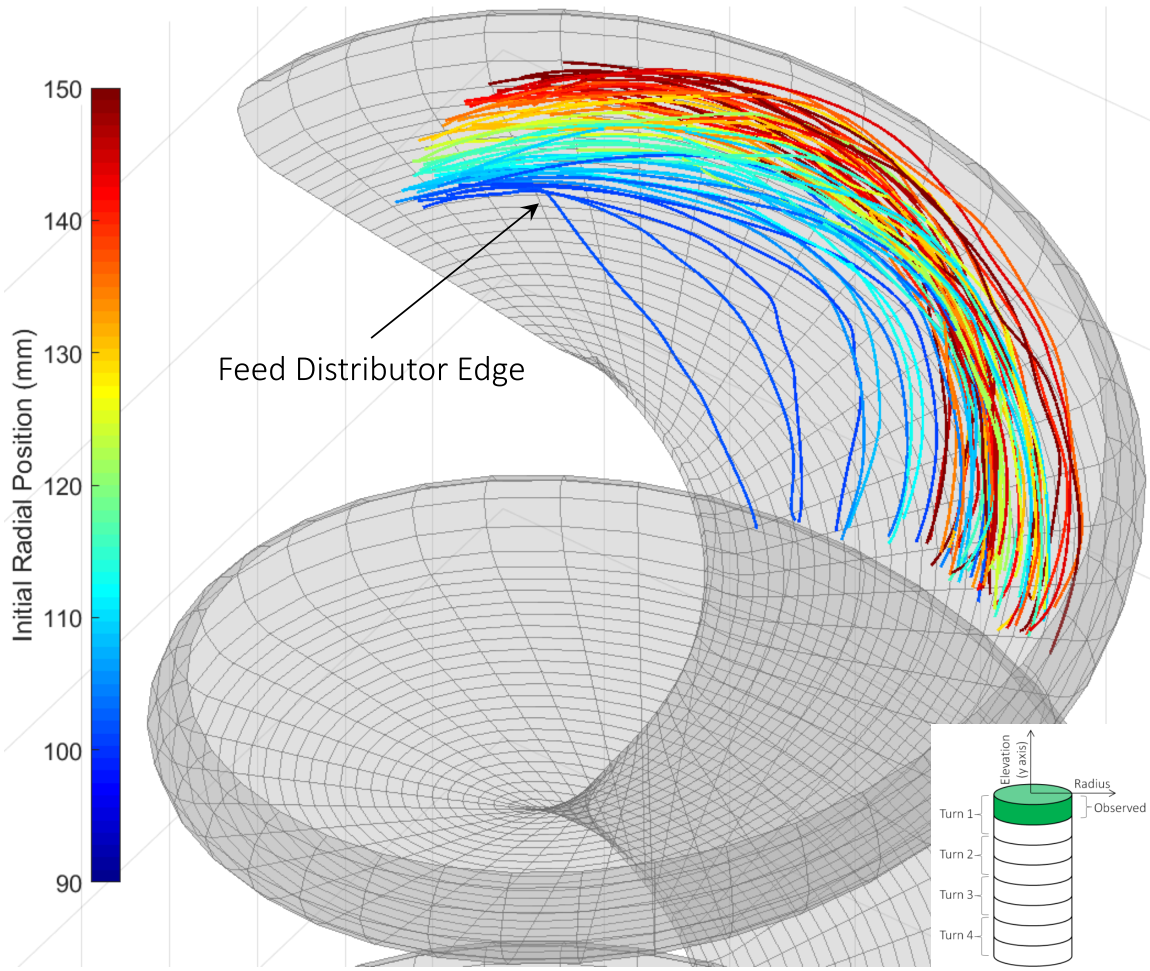

Figure 5.10 – Trajectory for a medium size (300 to 355 µm) quartz tracer (Run P31Q0355) in the spiral 1st turn (Elevation 0 to −100 mm).

Figure 5.11 presents the radial displacement of a medium size (300 to 355 µm) quartz tracer. The few passes moving inside the step section of the helix are present on the region just above 100 mm in radial feed position. In the region of 120 mm (radial feed position), the passes show an outward motion while in the region of 145 mm they exhibit an inward motion. This is potentially related to the secondary flow which, in this case, would happen in the band situated between 115 and 155 mm (radial position).

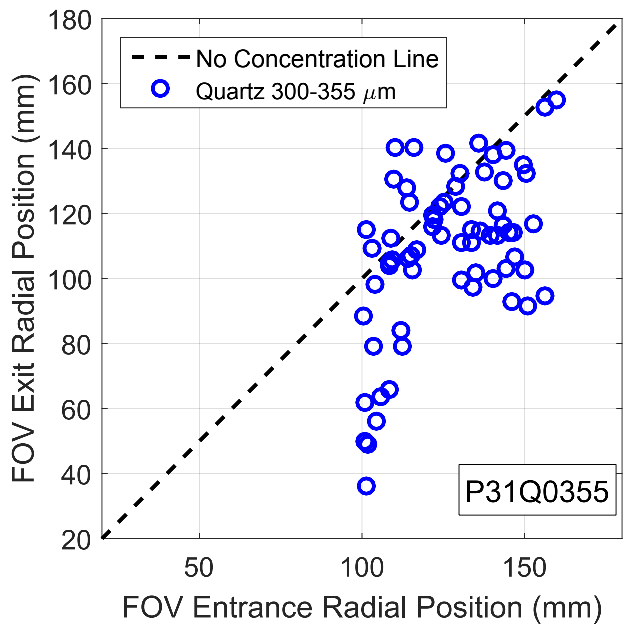

Figure 5.11 – Radial displacement for a medium size (300 to 355 µm) quartz tracer (Run P31Q0355) in the spiral 1st turn (Elevation 0 to −100 mm).

Figure 5.12 presents the velocities, acceleration and force averages of the medium quartz tracer. The particles initially fed at a velocity magnitude of about 0.7 m/s were observed to quickly separate in two patterns; the first one of velocity below 0.4 m/s in the inner section of the trough; while the second one in the outer zone exhibit particle velocity up to 1 m/s. Once again, the higher acceleration is found on the particles found at the outer edge of the pulp film. The outward-inward general motion of the pulp film can be observed through radial velocity (Figure 5.12).

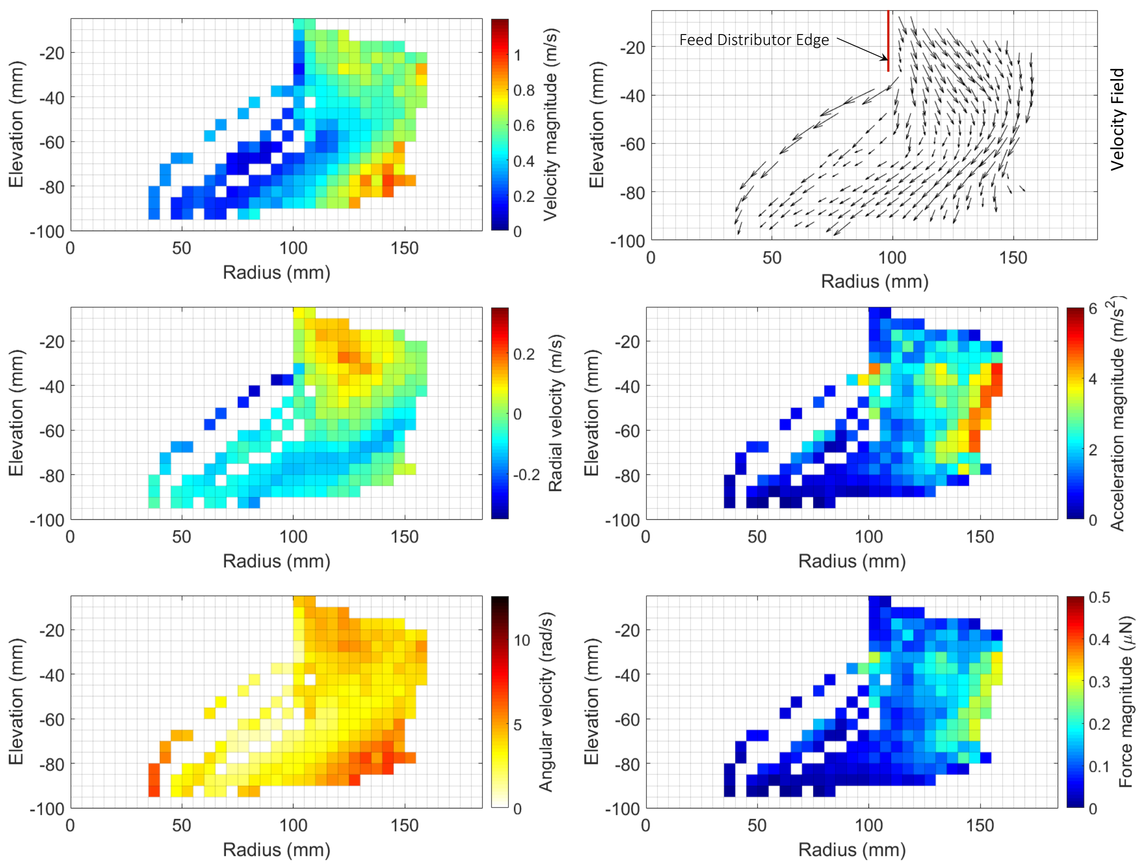

Figure 5.12 – Flow field for a medium size (300 to 355 µm) quartz tracer (Run P31Q0355) in the spiral 1st turn (Elevation 0 to −100 mm).

5.2.5 Medium hematite particle (Run P32H0355)

Figure 5.13 presents the trajectory of a medium size (300 to 355 µm) hematite tracer for the second slice of the first turn of the spiral (Elevation -75 to −175 mm). The passes recorded in this slice clearly show how the first turn is important in the separation. From the first slice (Figure 5.7) where most of the medium hematite tracer passes ended up in the inner side of the outer zone to the end of this second slice, the hematite passes are mostly grouped in a band towards the inner side of the middle zone. A few passes are the exception, and are in the outer zone. The band of material is forming the concentrate band, which will slowly move inward in the later turns. An interesting observation is the increase in velocity magnitude of the band as it reaches the last tier of the slice (from 0.3 to 0.5 m/s). This likely is due to the outward-inward flow of pulp originating from the feed distributor. This outward-inward pattern disappears in the later turns as the pulp flow becomes helical, and seems to play an important role in the formation of this concentrate band.

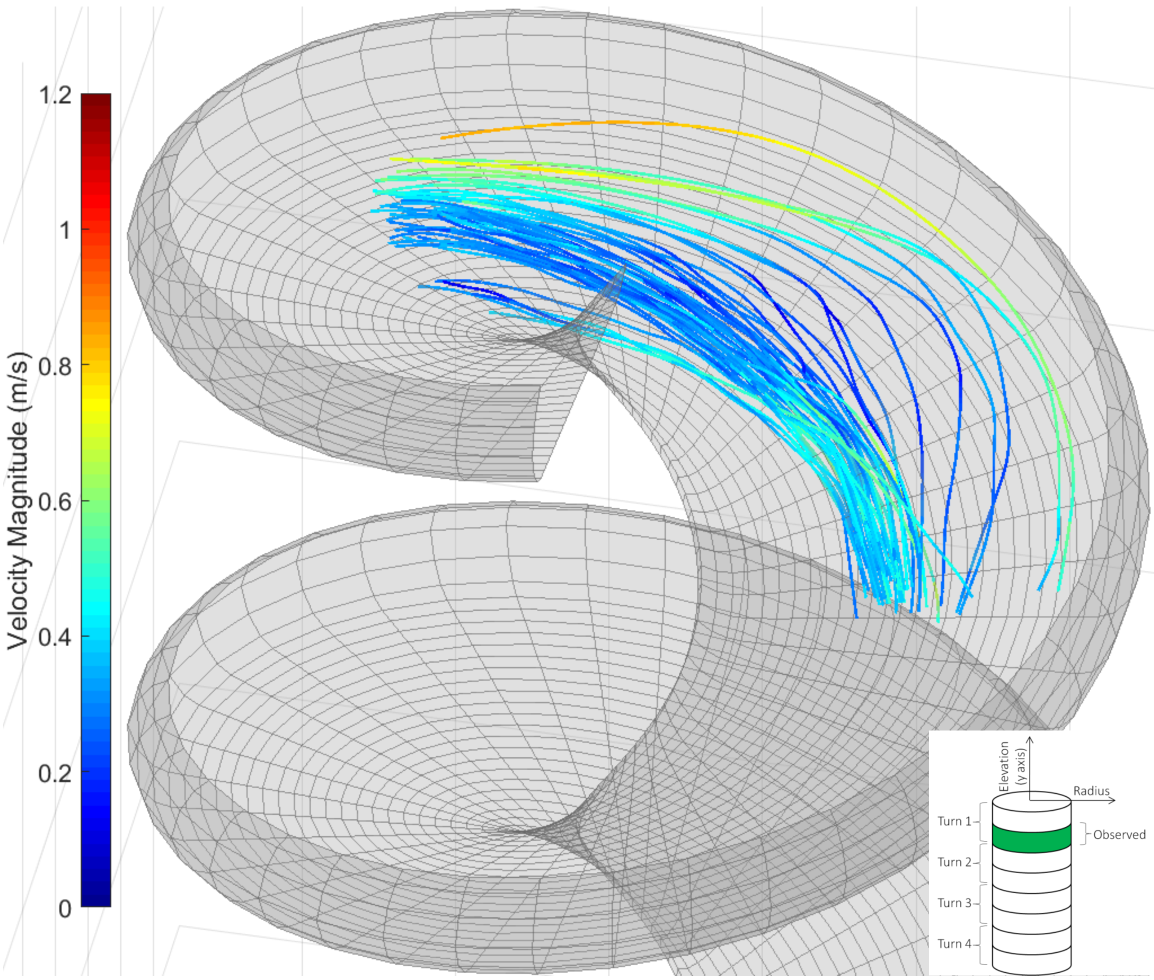

Figure 5.13 – Trajectory for a medium size (300 to 355 µm) hematite tracer (Run P32H0355) in the spiral 1st turn (Elevation -75 to −175 mm).

Figure 5.14 presents the radial displacement of a medium size (300 to 355 µm) hematite tracer in the second slice of the 1st turn. The consolidation toward a concentrated band of dense particle is shown by the closely pack group of passes in the region from 100 to 125 mm in initial radial position. This group of passes generally moves further inwards.

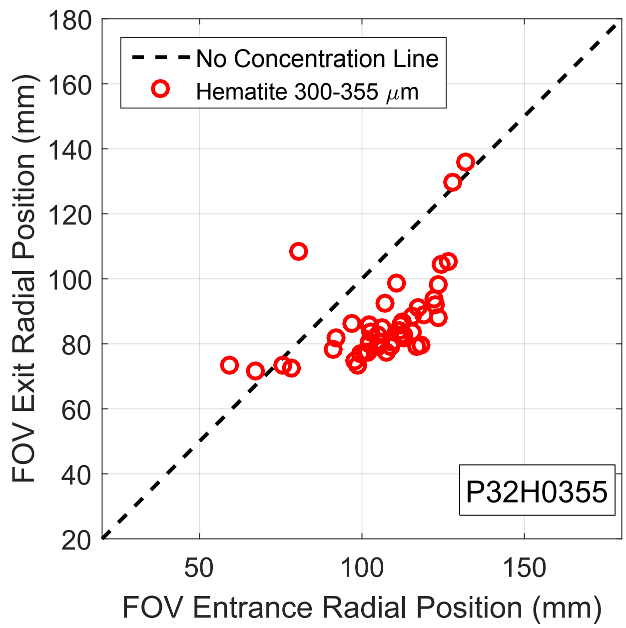

Figure 5.14 – Radial displacement for a medium size (300 to 355 µm) hematite tracer (Run P32H0355) in the spiral 1st turn (Elevation -75 to −175 mm).

Figure 5.15 presents the velocities, acceleration and average force acting on a medium size (300 to 355 µm) hematite tracer. The velocity field indicates a difference between the passes forming the concentrate band and those nearer to the outer zone. The latter ones appear to take longer to regroup towards the inner zone. The higher angular velocity in the inner zone is explained by the fact that at a similar particle velocity magnitude, the particles at the inner radial position are travelling through a larger angular section of the helix for the same absolute displacement. Another observation is the straightening of the overall particle flow, which becomes radially more stable with a radial velocity closer to 0 m/s at the end of this slice.

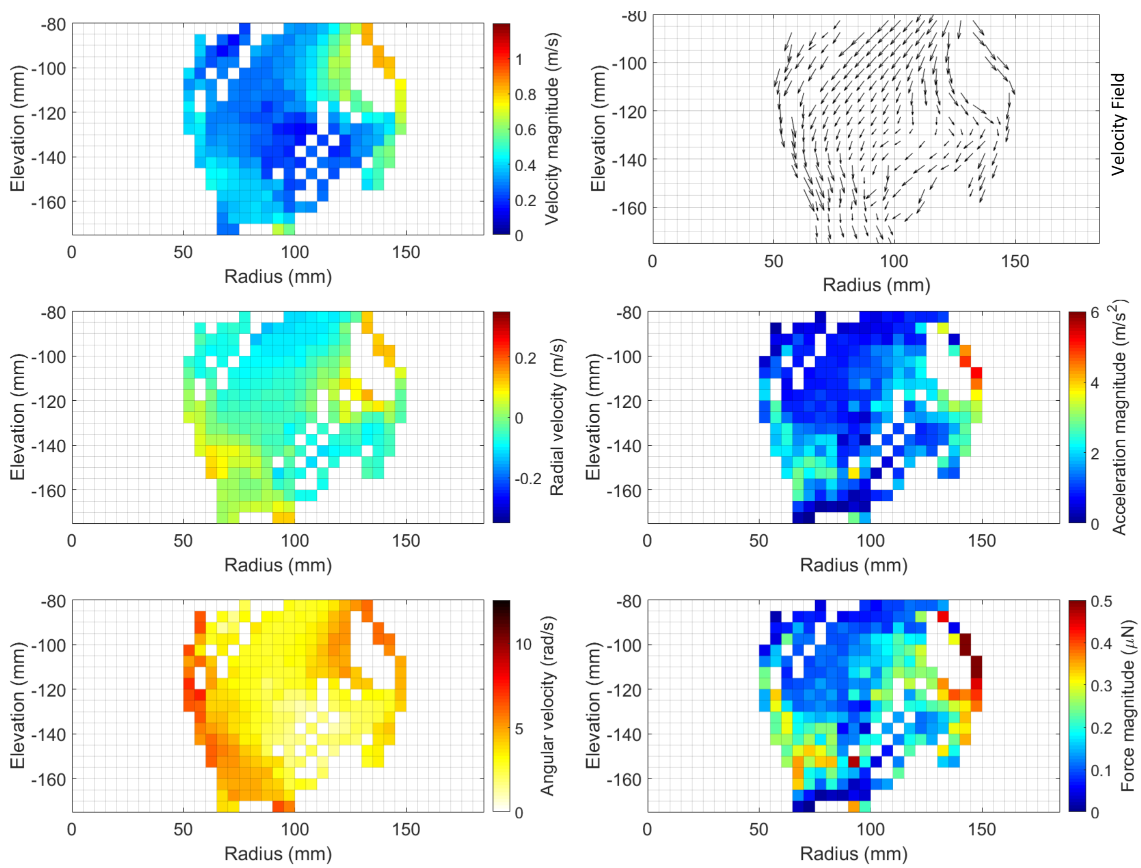

Figure 5.15 – Flow field for a medium size (300 to 355 µm) hematite tracer (Run P32H0355) in the spiral 1st turn (Elevation -75 to −175 mm).

5.2.6 Medium quartz particle (Run P32Q0355)

Figure 5.16 presents the trajectory of a medium size (300 to 355 µm) quartz tracer. The quartz passes show significant radial motion, with passes starting in the outer zone moving to the inner zone and passes starting in the inner zone moving toward the outer zone. However, compared with the hematite tracer of the same size (Figure 5.13), the passes of the medium quartz tracer do not regroup toward the inner zone of the spiral trough. This is where the separation happens between the hematite and quartz particle for this size class. This observation is in good agreement with the presence of the secondary flow. In this specific case, the secondary flow appears to prevent the quartz particle from moving radially inward, which was observed for the hematite particle of the same size.

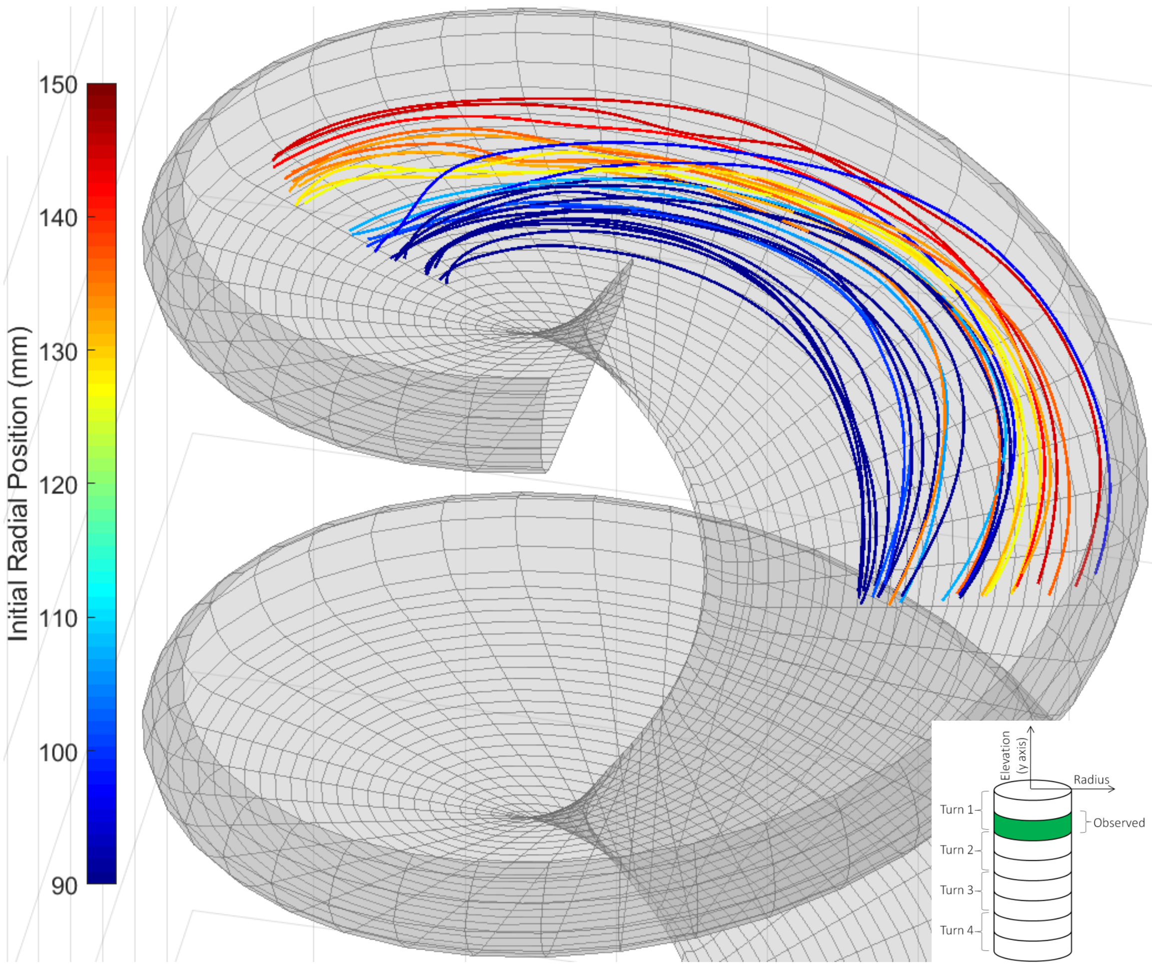

Figure 5.16 – Trajectory for a medium size (300 to 355 µm) quartz tracer (Run P32Q0355) in the spiral 1st turn (Elevation -75 to −175 mm).

Figure 5.17 presents the radial displacement of a medium size (300 to 355 µm) quartz tracer. It shows that the light particle has a lower inward motion than the hematite particle of the same size (Figure 5.14). There is no consolidation of the passes, even if there is no clear rejection of this low density particle.

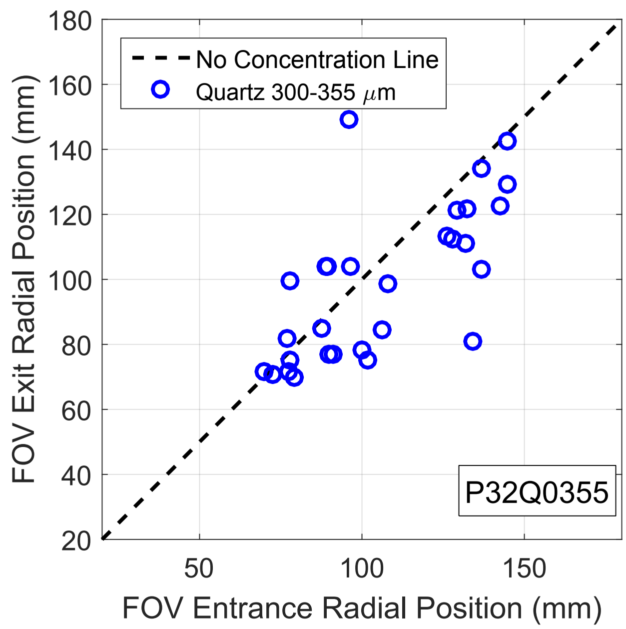

Figure 5.17 – Radial displacement for a medium size (300 to 355 µm) quartz tracer (Run P32Q0355) in the spiral 1st turn (Elevation -75 to -175 mm).

Figure 5.18 presents the velocities, acceleration and force averages of a medium size (300 to 355 µm) quartz tracer. Compared with the hematite tracer (Figure 5.15), there is no particle with high angular velocity as less quartz particles are found in the inner zone. Similarly to the hematite tracer of the same size, the particle flow is establishing itself toward a steady state.

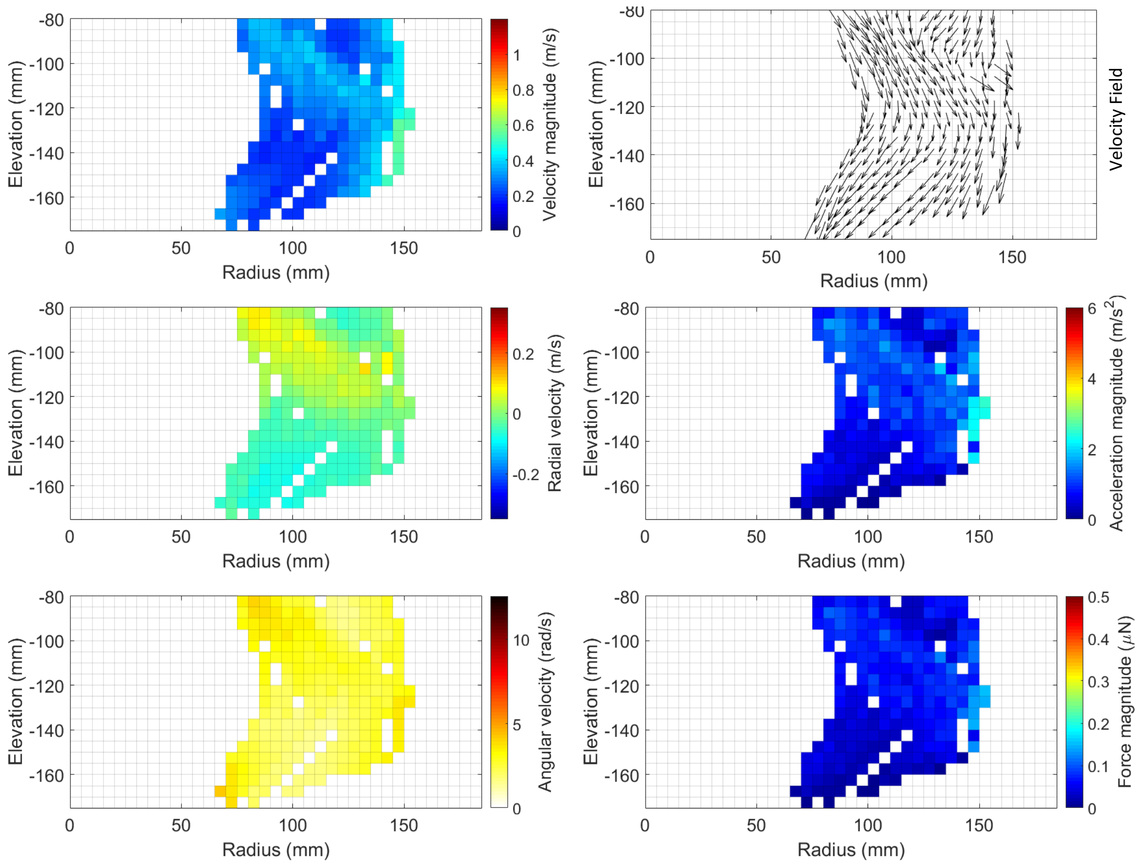

Figure 5.18 – Flow field for a medium size (300 to 355 µm) quartz tracer (Run P32Q0355) in the spiral 1st turn (Elevation -75 to −175 mm).

5.2.7 Coarse hematite particle (Run P31H1180)

Figure 5.19 presents the trajectory of a coarse (1000 to 1180 µm) hematite tracer. The majority of the passes were fed at a constant velocity of 0.7 m/s. The outer zone passes are seen to accelerate to a velocity just under 0.8 m/s while the inner-middle zone passes quickly move radially inward, while reducing their velocity.

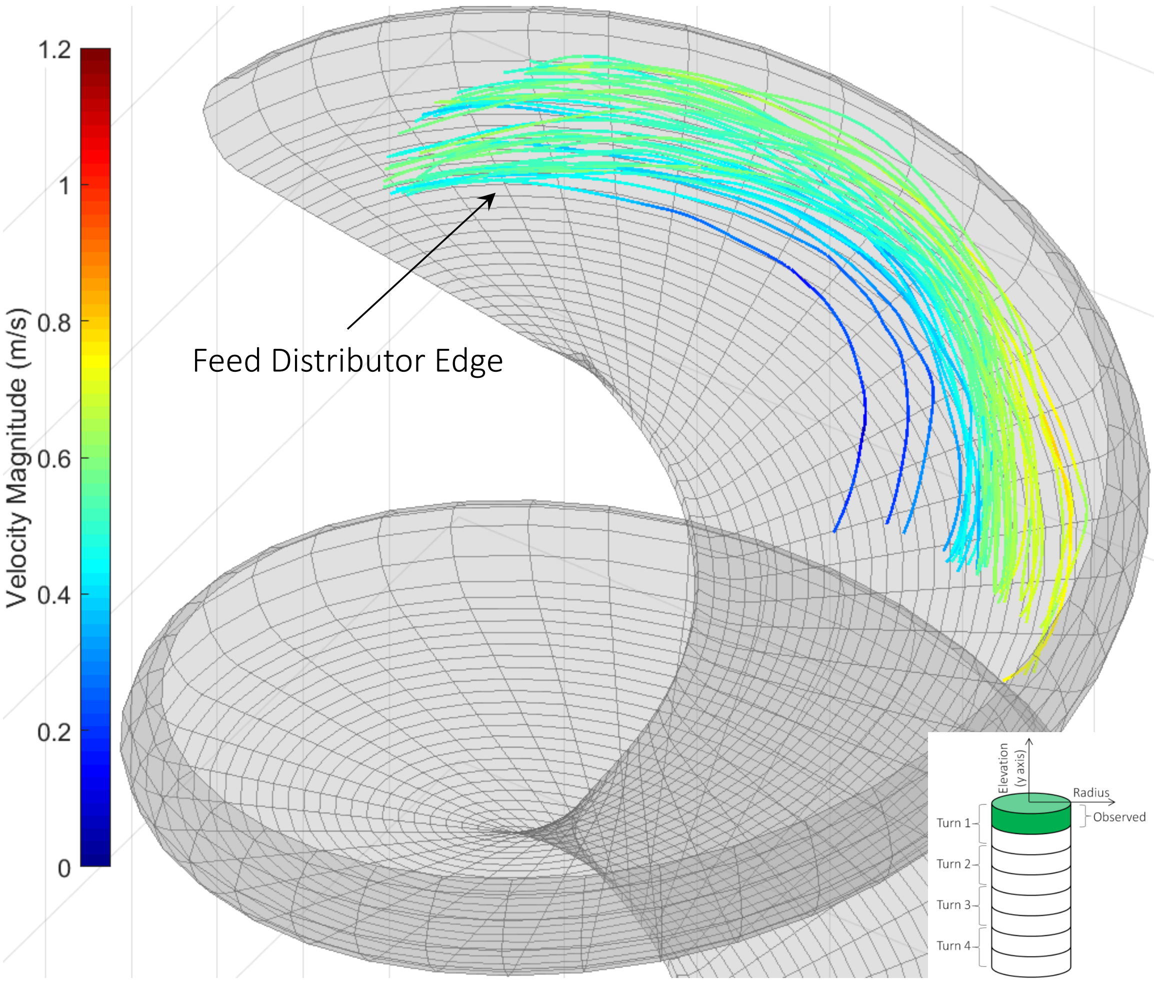

Figure 5.19 – Trajectory for a coarse size (1000 to 1180 µm) hematite tracer (Run P31H1180) in the spiral 1st turn (Elevation 0 to −100 mm).

Figure 5.20 presents the radial displacement of the coarse (1000 to 1180 µm) hematite tracer. The low velocity of the passes moving inward are observed close to the 100 mm initial radial position. Many passes are seen to have no significant radial motion when originating from an initial radial position of 110 mm. This contrasts with the outward-fed passes (having an initial radial position greater than 125 mm), which are observed to move inwards. This is potentially related with the secondary flow behaviour where the dense particle settle at the trough surface of the outer zone and are carried inward. In this case, the tracer seems to be too heavy to be lifted and carried outward by the top fluid layer when in the middle zone, which could explain why it does not exhibit significant outward motion. This is a detail of the concentration mechanism.

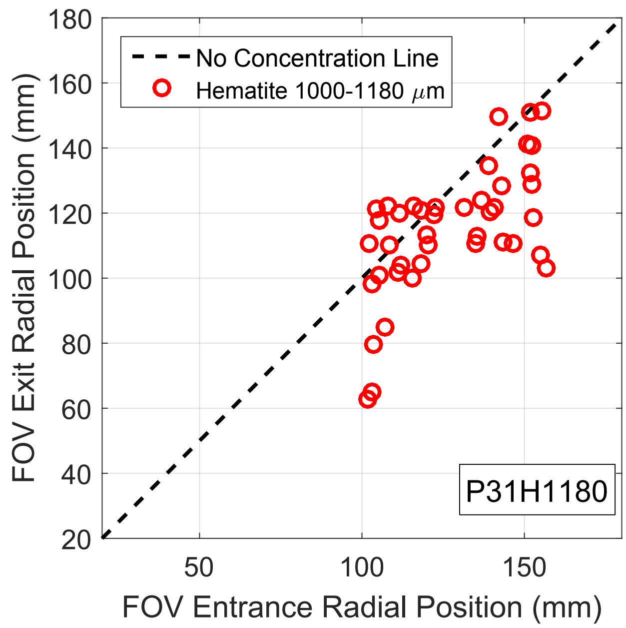

Figure 5.20 – Radial displacement for a coarse size (1000 to 1180 µm) hematite tracer (Run P31H1180) in the spiral 1st turn (Elevation 0 to −100 mm).

Figure 5.21 presents the velocities, acceleration and force averages of a coarse (1000 to 1180 µm) hematite tracer. In the outer zone, average accelerations are observed to be of lower magnitude than smaller tracers in the same slice, which is to be expected considering the mass, surface area and drag on this particle size. Considering the same parameters, the total force magnitude is much higher for this large dense particle with values reaching 20 µN in the fast flowing outer zone. The velocity magnitude shows that the flow is moving at low velocity in the inner-middle zone or at a larger velocity in the outer zone.

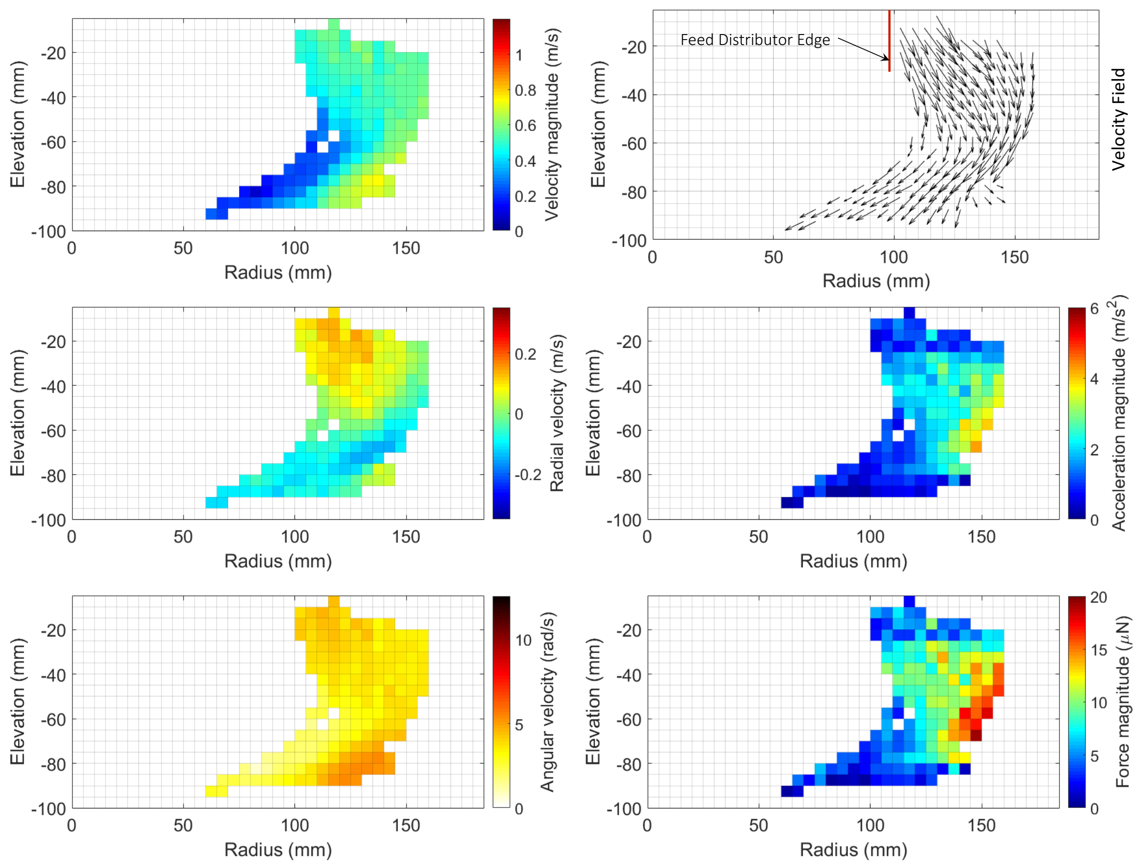

Figure 5.21 – Flow field for a coarse size (1000 to 1180 µm) hematite tracer (Run P31H1180) in the spiral 1^{st} turn (Elevation 0 to -100 mm).

5.2.8 Coarse quartz particle (Run P31Q1180)

Figure 5.22 presents the trajectory of a coarse (1000 to 1180 µm) quartz tracer. A very similar behaviour to that of the the coarse hematite tracer (Figure 5.19) is observed, with similar velocities. The only difference being that the passes are slightly more outward at the end of this slice. An interesting observation is the deceleration of a few passes on the inner side of the group of passes. This deceleration is most likely due to the settling of the tracer at the trough surface, while most of the water in the pulp flows outward.

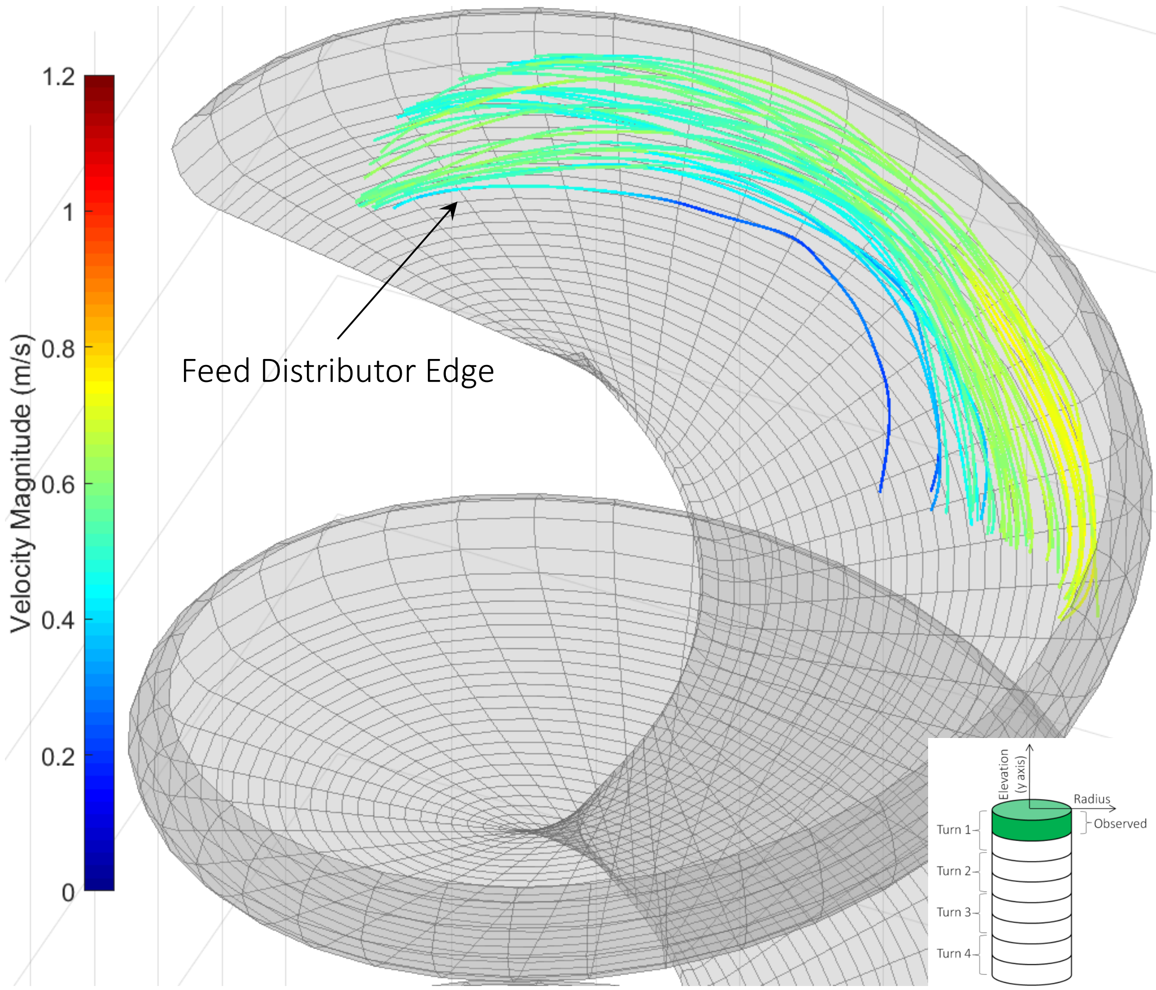

Figure 5.22 – Trajectory for a coarse size (1000 to 1180 µm) quartz tracer (Run P31Q1180) in the spiral 1st turn (Elevation 0 to −100 mm).

Figure 5.23 presents the radial displacement of a coarse quartz tracer. Similar behaviour to the hematite tracer of the same size (Figure 5.20) is observed, with the exception being that a few passes show an outward motion when originating close to 115 mm. This potentially shows a small rejection of the large quartz tracer caused by the outward moving fluid top layer in this band. Another difference is that the inward motion is of a lower extent.

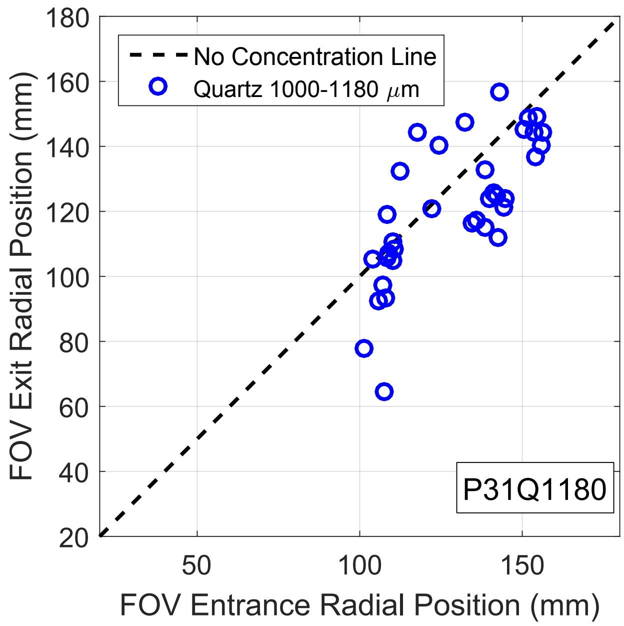

Figure 5.23 – Radial displacement for a coarse size (1000 to 1180 µm) quartz tracer (Run P31Q1180) in the spiral 1st turn (Elevation 0 to −100 mm).

Figure 5.24 presents the velocities, acceleration and force averages of the coarse quartz tracer. A difference with the coarse hematite tracer (Figure 5.21) is observed by the smaller region of low velocity magnitude at the end of the slice. This shows that most of the passes of the quartz tracer stay outside of the low velocity flow in the inner-middle zone section of the trough. The passes are affected by the general outward/inward motion of the pulp, as can be observed by the radial velocity. The force on the coarse quartz tracer are of smaller magnitude than for the hematite tracer. This is to be expected, considering the density difference and the fact that acceleration magnitude is similar than for the hematite tracer.

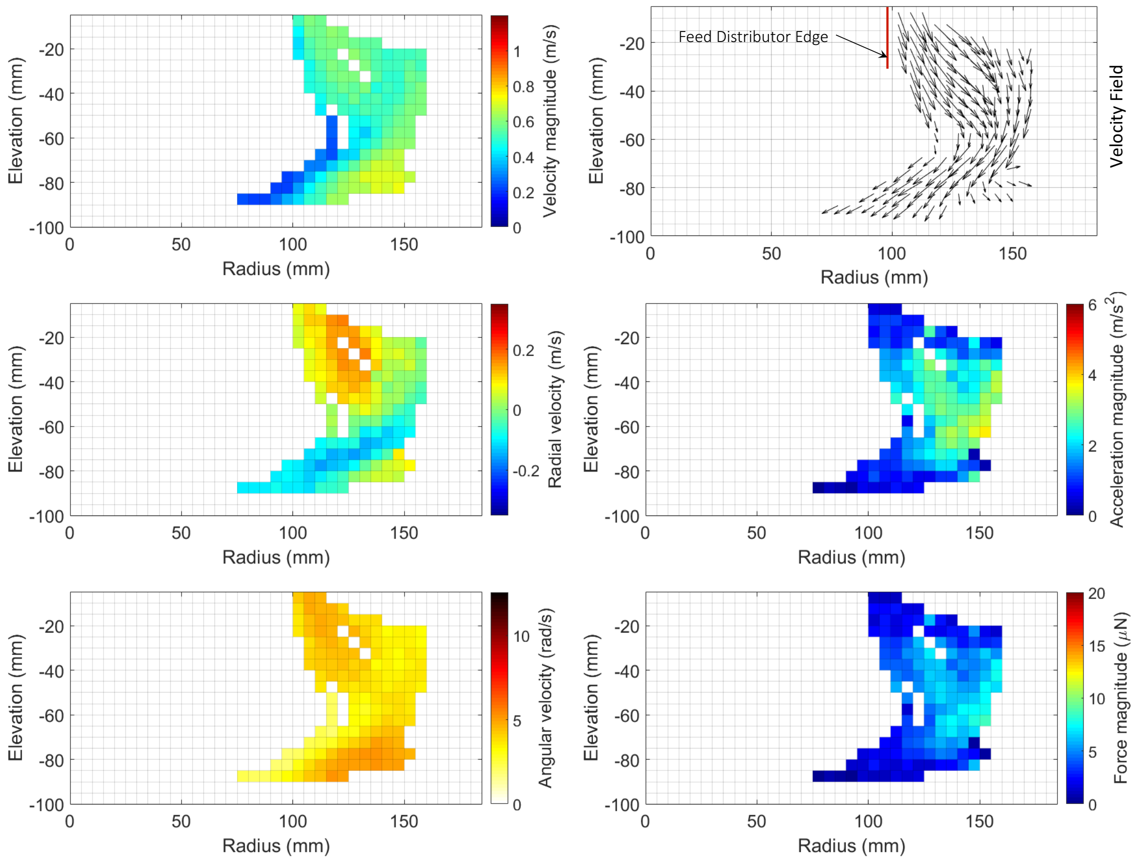

Figure 5.24 – Flow field for a coarse size (1000 to 1180 µm) quartz tracer (Run P31Q1180) in the spiral 1st turn (Elevation 0 to −100 mm).

5.2.9 1st turn combined radial motion

Figure 5.25 presents the values of radial displacement for the different tracers tracked in the top slice (Elevation 0 to −100 mm) of the 1st turn. It shows a better separation (largest differential displacement) for the 300 to 355 µm tracers. In this specific case, the difference between the mean radial displacements is 14 mm, meaning that the group of hematite passes averages an inward displacement 14 mm more pronounced than a quartz tracer of the same size. This is a measure of the separation due to density difference happening in this 100 mm horizontal slice of the spiral 1st turn. Interestingly, the 1000 to 1180 µm tracers are observed to have a similar behaviour in this section with only a slight difference in radial displacement (4 mm).

Figure 5.25 shows that the quartz particles are moving inward, but to a lesser extent when compared to the hematite particles. This inward radial motion of light particles shows that the spiral is not yet “rejecting” the light particles outward, it is rather “recovering” them at a lower rate than the dense particles. It should be mentioned that the spiral feed is in the outer zone which provide a situation in which the particles starts in this outer zone, and will tend to slide inward based on the inward inclination of the profile. This inward sliding is reduced by the outward flow of pulp, as discussed in Section 5.3, which has a greater effect on light density particles.

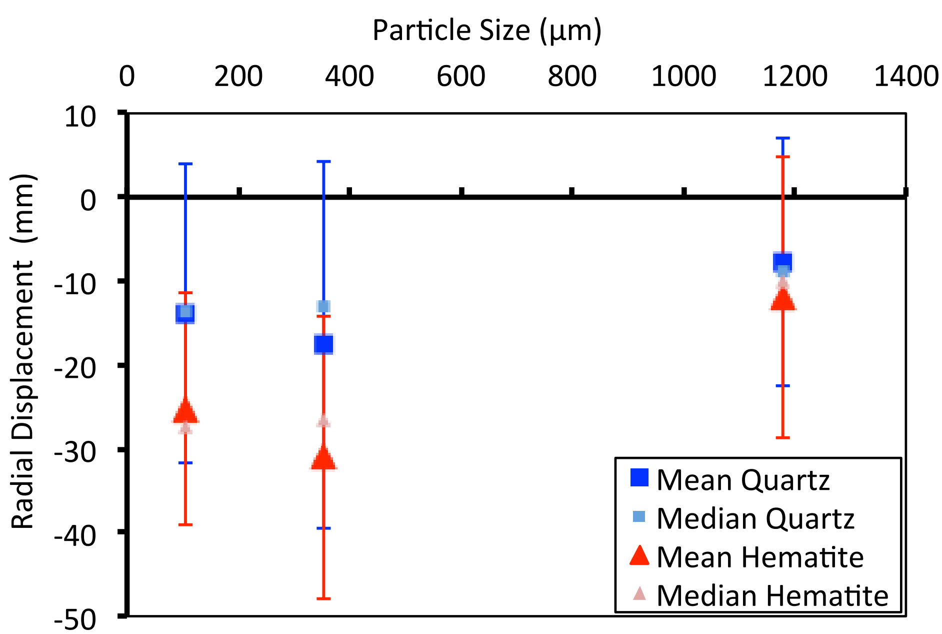

Figure 5.25 – Radial displacement (negative value representing inward motion) for the different tracers in a 100 mm horizontal slice (Elevation 0 to −100 mm) of the spiral 1st turn with error bars representing the standard deviation of each group of passes.

5.3 Particle secondary flow

Previous secondary flow observation were obtained for fluid only systems [161, 162]. For the first time, the effect of the fluid secondary flow on the motion of particle in a dense pulp (20% solids) can be quantified. This observation was possible with the performance achieved with the new set-up of modular detectors (Section 4.4.2) coupled with the new DAB mineral tracer production method (Section 4.2.2).

With a combination of both trajectory and velocity observation, it is possible to display and quantify particle motion inside the secondary flow. The result is a measurement of the radial velocity of the mineral tracer particle, which depends on its vertical distance from the trough profile. Figure 5.26 shows the particle velocity in the secondary flow in a radial cut of first turn for a quartz tracer of 300-355 µm in diameter. The passes in which the mineral tracer was in the upper layer of the pulp film (further away from the profile surface) show a positive radial velocity signifying an outward motion. On the other passes, in which the tracer is found in the lower layer of the pulp film (close to the profile surface), the radial velocity is negative which signifies an inward motion. In this latter case, the radial velocity is of lower magnitude, meaning that the inward particle flow is slower than the outward particle flow. This measurement is in agreement with clear-water velocity measurements [161, 162], and the theoretical basis of film flow in which the layer in contact with the solid surface is at rest, with increasing velocity further away from the solid surface. In the case of the helical flow of the spiral, the layer of pulp eventually reaches a point where the radial velocity is null, and then becomes positive (outward-moving top layer).

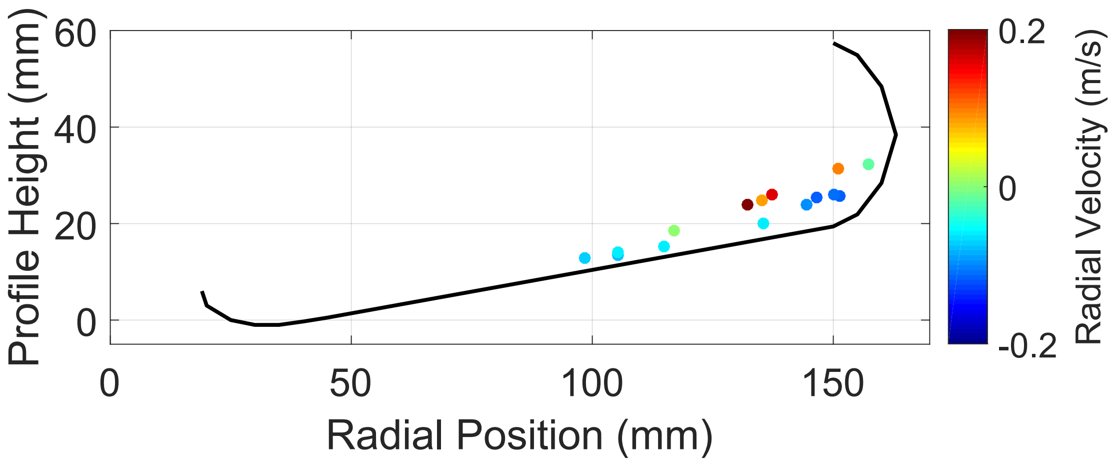

Figure 5.26 – Particle location coloured by radial velocity showing the secondary circulation (top outward, bottom inward) for many passes of a quartz tracer of 300 to 355 µm in the first turn of the spiral.

The particle secondary flow was not observed for all tracers and across the entire length of the spiral. The situation presented in Figure 5.26 occurs in the specific case in which the pulp film reaches the vertical rising section of the profile during the general inward outward pulp motion. In other situations, the superposed inward and outward moving layer of particle have not been observed to the same extent.

5.4 Wash water injection

The aim of this section is to detail the particle behaviour around a wash water injection point situated in the 3rd turn of the spiral. The modified spiral set-up presented in Section 3.9.4 was used with the ADAC detector set-up described in Section 4.6.1.

5.4.1 Effect of wash water on trajectories

Figure 5.27 presents the passes of a 300-355 µm hematite tracer in the 2nd, 3rd and 4th turns. Both cases (wash water on and wash water off) behave the same in the 2nd turn. The difference in trajectory for the passes with wash water is revealed in the 3rd turn where the passes exhibit an outward shift. The concentrate band, well established by the end of the 2nd turn, is larger with wash water injection. On the 4th turn, the passes with wash water move inward again, without being as packed as the concentrate band shown by the passes without wash water.

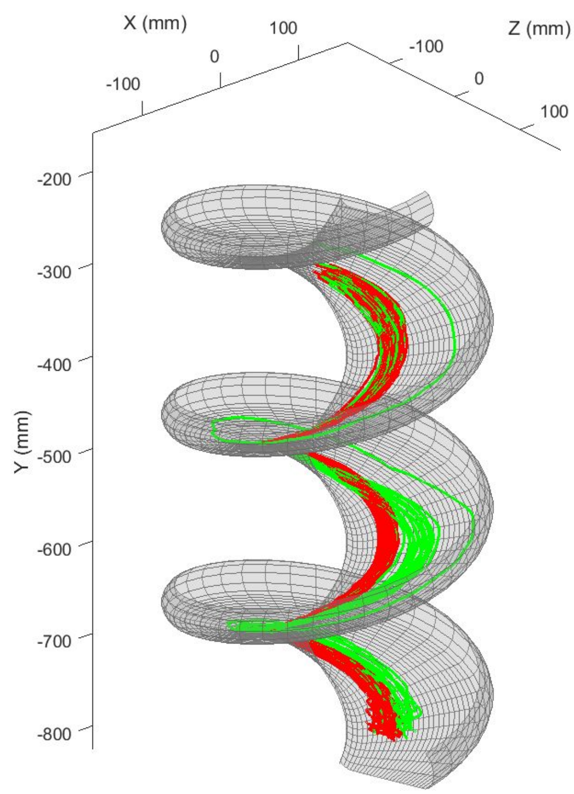

Figure 5.27 – Trajectory for the hematite tracer of size 300 to 355 µm while wash water is ON (green) and OFF (red) (view of turn 2, 3 and 4).

Figure 5.28 presents the passes of a 1000 to 1180 µm quartz tracer in the 2nd, 3rd and 4th turns. The passes without wash water are found to be spread from the middle zone to the outer zone on the three last turns of the spiral. In the case of the passes with wash water, the large quartz tracer is diverted in the 3rd turn to move outward in the outer zone. Once the pulp area affected by wash water is passed, certain passes move back inward, but to a lower extent than their outward motion thus the inner zone is effectively cleaned from the coarse quartz tracer.

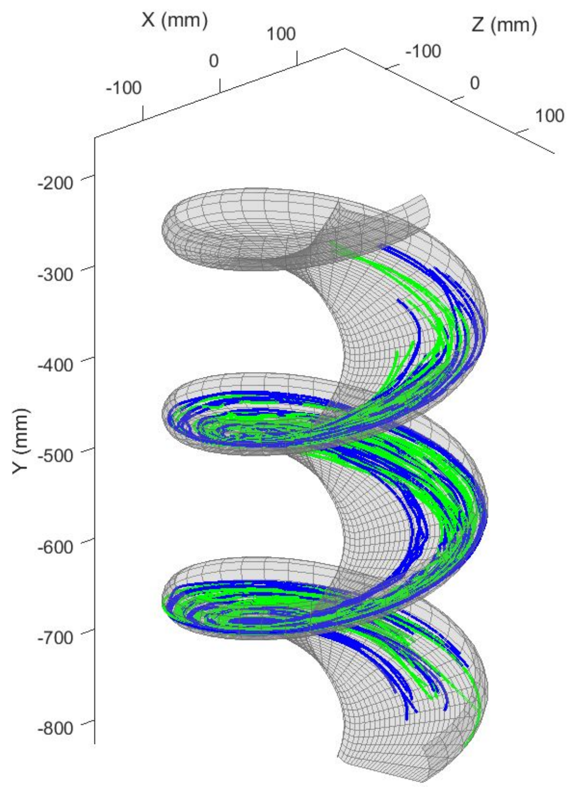

Figure 5.28 – Trajectory for the quartz tracer of size 1000 to 1180 µm while wash water is ON (green) and OFF (blue) (view of turn 2, 3 and 4).

5.4.2 Effect of wash water on separation

Figure 5.29 presents the radial displacement of the passes of the hematite tracer of size 300 to 355 µm without wash water. The group of passes is tightly packed in the inner zone as most of the radial displacement for this dense medium particle happened in the first turn and a half of the trough. There is only a slight inward motion of the concentrate band.

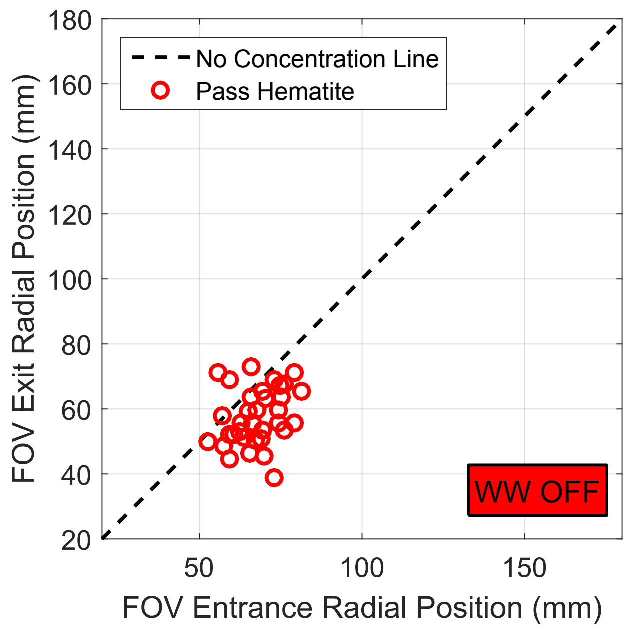

Figure 5.29 – Radial displacement for the hematite tracer of size 300 to 355 µm while wash water is OFF.

Figure 5.30 presents the radial displacement of the passes of the hematite tracer of size 300 to 355 µm with wash water. In comparison to the case where there is no wash water (Figure 5.29), the passes radial motion is more disperse, but centered on the no concentration line. The slight inward motion is thus prevented by the wash water injection in the 3rd turn.

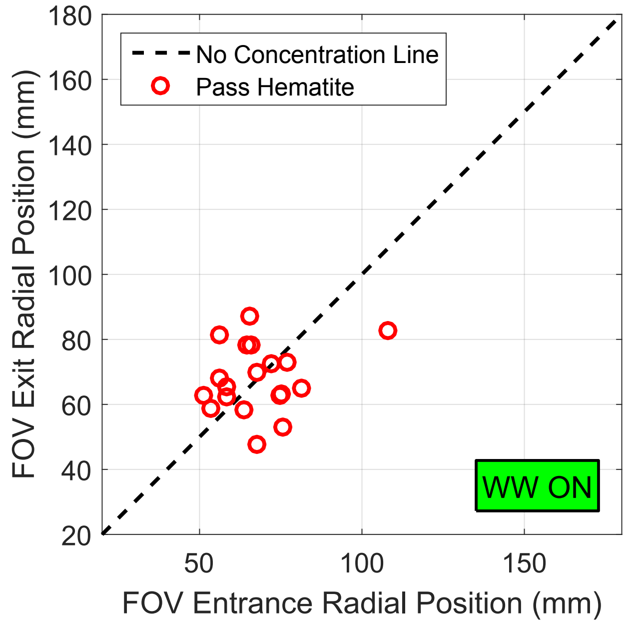

Figure 5.30 – Radial displacement for the hematite tracer of size 300 to 355 µm while wash water is ON.

Figure 5.31 presents the radial displacement of the passes of the quartz tracer of size 1000 to 1180 µm without wash water. The passes are mostly aligned on the no concentration line and situated in the middle-outer zone. There is a slight inward motion for the passes in the region of 120 mm, but the general behaviour is a stable radial position.

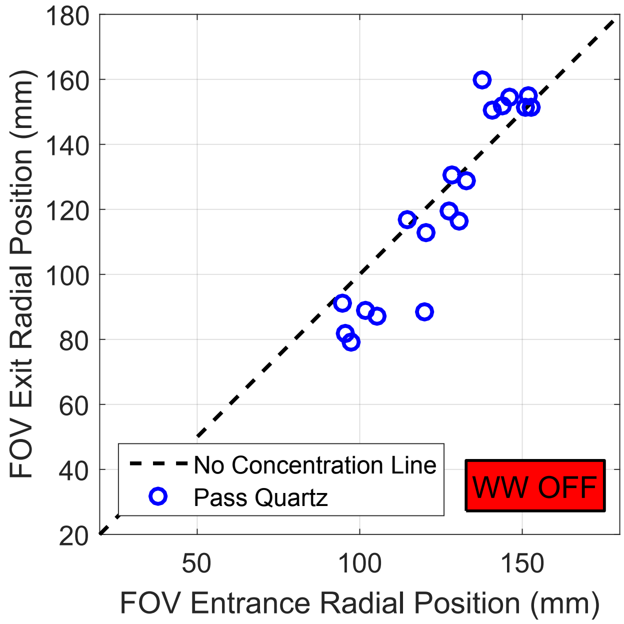

Figure 5.31 – Radial displacement for the quartz tracer of size 1000 to 1180 µm while wash water is OFF.

Figure 5.32 presents the radial displacement of the passes of the quartz tracer of size 1000 to 1180 µm with wash water. A clear rejection is observed for this tracer size and density. In the first turns, most of the pulp initial water content is moving radially outward to the outer zone. The addition of wash water at the 3rd turn inner zone dilute the high solids content pulp film remaining in the inner and middle zone. The wash water is moving radially outward and unlock the large light particle motion. This effect is happening up to the outer zone as even particle with an FOV entrance radial position of around 120 mm are moving outward.

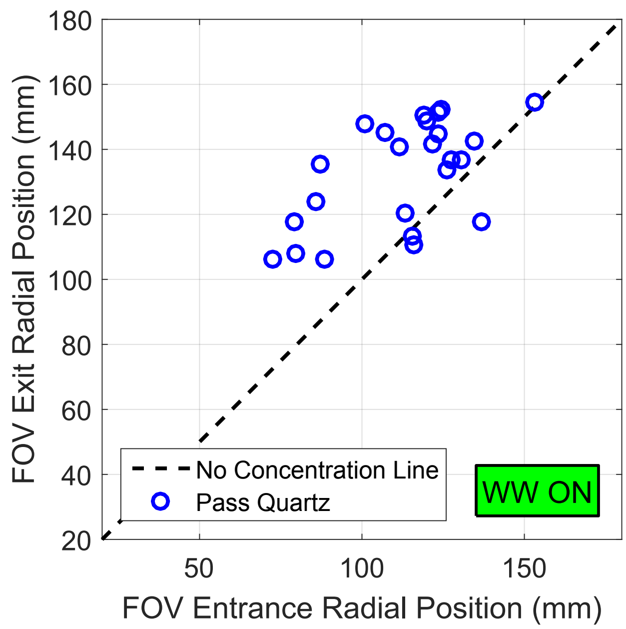

Figure 5.32 – Radial displacement for the quartz tracer of size 1000 to 1180 µm while wash water is ON.

The average wash water influence on the mineral tracers radial displacement is presented in Table 5.1. As described, the medium hematite tracer's slight inward motion (−10 mm) is reduced to a very low amount (−0.1 mm) by the addition of wash water. The larger dispersion of the passes is observed by the larger standard deviation for the passes with wash water. In the case of the large quartz tracer, radial motion is much more affected by the wash water addition (from -4.0 to 20.4 mm). Once again, the standard deviation is higher with wash water and shows a more disperse radial motion.

Table 5.1 – Effect of wash water on the particle radial displacement in the FOV.

Tracer mineral	Size (µm)	Wash water	$\overline{\Delta r}$ (mm)	σ (mm)	$\tilde{\Delta r}$ (mm)
Hematite	300 to 355	OFF	-10.0	10.0	-8.6
Hematite	300 to 355	ON	-0.1	14.9	2.5
Quartz	1000 to 1180	OFF	-4.0	12.4	-3.3
Quartz	1000 to 1180	ON	20.4	17.4	24.6

5.4.3 Effect of wash water on particle flow field

In this section, the effect of wash water on the particle flow field is presented in detail with the square toroid bins averaged values for the tracer particles velocities (magnitude, radial and angular).

5.4.3.1 Wash water effect on medium hematite

The particle radial displacement in the spiral is associated with establishing a flow parallel to the helical trough surface. Once this flow is established and most of the water has reached the rising section of the profile, only a small amount of radial displacement occurs if no flow disturbance is induced.

The flow of an hematite tracer of size 300 to 355 µm in the 2nd, 3rd and 4th turn is an excellent example of this situation. Figure 5.33 presents the flow of this medium-sized tracer without wash water addition or any other disturbance. The observation is clear about the particle radial motion already completed as all the passes recorded are forming a narrow band in the inner zone of the trough. The average radial velocity of the bins in this band is close to 0 m/s. The angular velocity shows a minimal decrease in the 4th turn in comparison to the 2nd turn. This is likely to be related to the movement of water to the outer zone, which results in a higher solids content in the inner concentrate band moving down the trough at a gradually slower pace.

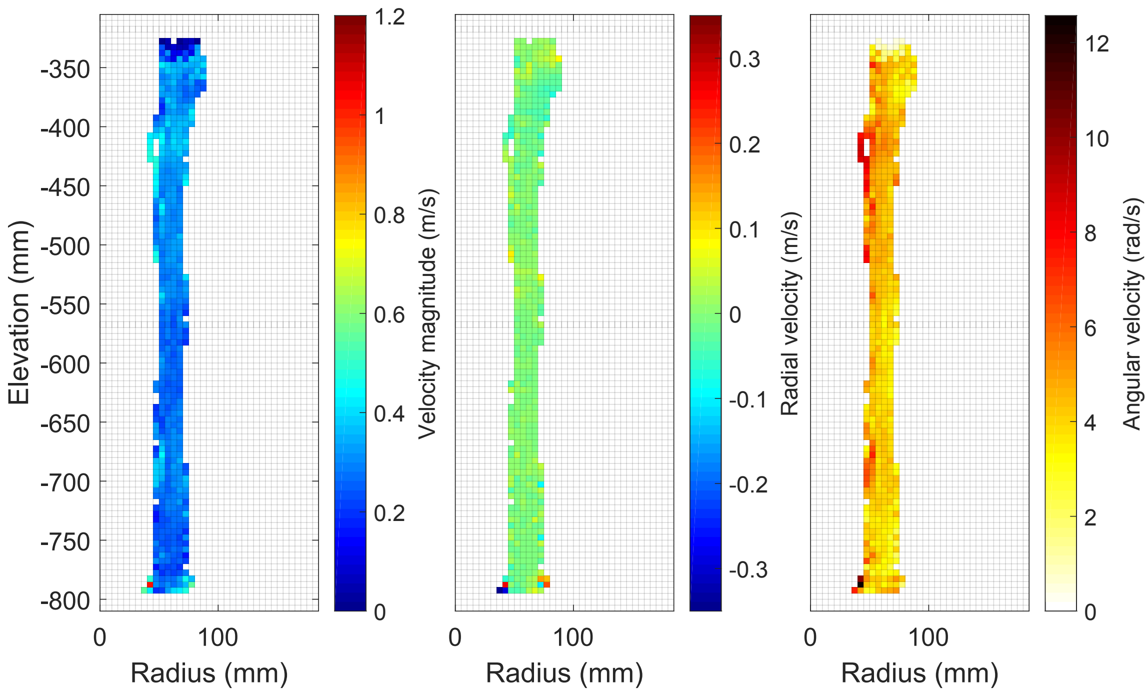

Figure 5.33 – Velocity for the hematite tracer of size 300 to 355 µm while wash water is OFF.

The constant flow field of Figure 5.33 was disturbed by the injection of wash water to obtain the flow field presented in Figure 5.34.

Just before reaching the wash water injection point, an increase in the hematite tracer velocity magnitude is observed. This might seem counter intuitive as it happens before the injection, but can be explained by the later fast flowing dilute pulp locally generated by the wash water. The diluted pulp is quickly moving outward which frees some space on the trough for the dense pulp ahead of the injection point to increase in velocity magnitude. The angular velocity increase at this position supports this argument as it does not include the change in radial velocity.

After the wash water disturbance, the medium hematite particle moves slightly inward. However, the width of the concentrate band remains wider for the 4^{th} turn.

One pass originated in the middle zone (end of 1st turn), and showed an inward/outward motion, potentially related to the secondary flow in the middle zone. An interesting behaviour is the velocity magnitude of this pass which resemble the secondary flow (faster outward on top of the film, slower inward at the trough surface). Once this pass reaches the disturbance created by the wash water injection, it migrates inward to integrate with the now wider concentrate band. In this particular situation, the particle was captured in the concentrate band due to the addition of wash water. However, considering that the radial motion happening in the 1st turn already brought most of the passes in the inner concentrate band, it is possible to say that wash water effect on the medium dense particle recovery could be mitigated by a wider opening of the bottom cutter to capture the wider concentrate band.

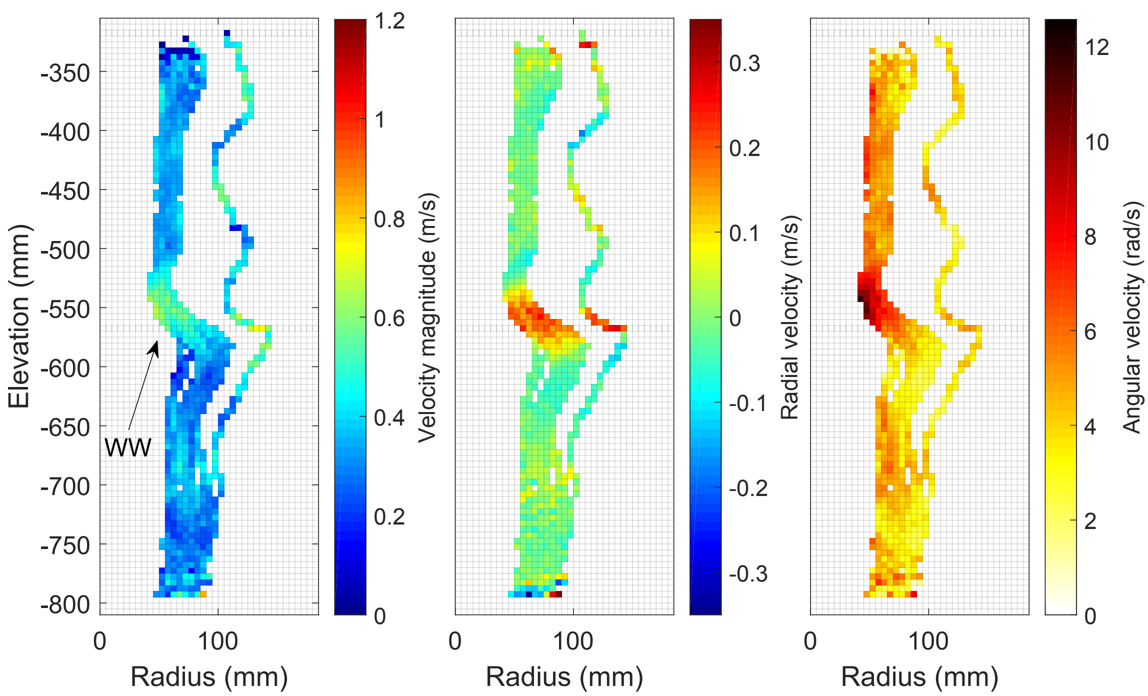

Figure 5.34 – Velocity for the hematite tracer of size 300 to 355 µm while wash water (WW) is ON.

5.4.3.2 Wash water effect on coarse quartz

Figure 5.35 presents the flow field of the large quartz tracer in the last three turn of the spiral without wash water. The velocity magnitude in this case is a excellent example showing the lower flow velocity in the inner zone increasing up to the outer zone. Once again here, radial displacement of the tracer is limited, with only slight radial motion in the middle zone. An hypothesis for this can be the secondary flow as it appears that the outward motion has higher velocity.

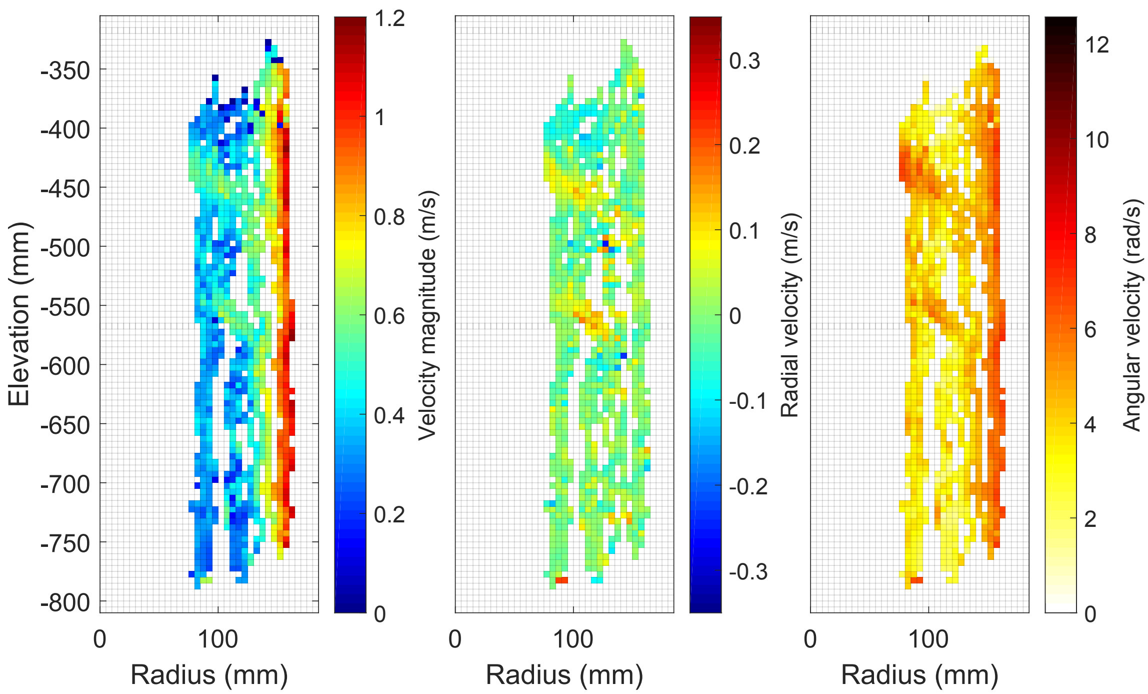

Figure 5.35 – Velocity for the quartz tracer of size 1000 to 1180 µm while wash water is OFF.

In comparison to Figure 5.35, Figure 5.36 presents the particle velocities while injecting wash water. A clear radial displacement is observed up to the outer side of the middle zone. The injection send a wave of clean water which pushes the large quartz tracer further outward. When the wave is passed by, quickly, some passes come back inward, but without reaching the previous radial position. The inner-middle zone is effectively cleaned out of the large quartz. The injection of wash water is then positively affecting the grade of the concentrate band by rejecting the coarse quartz particles. Finally, the passes at the outer section of the profile seems to slightly increase in velocity, however, it is difficult to confirm if it is due to the extra a mount of water added by the injection.

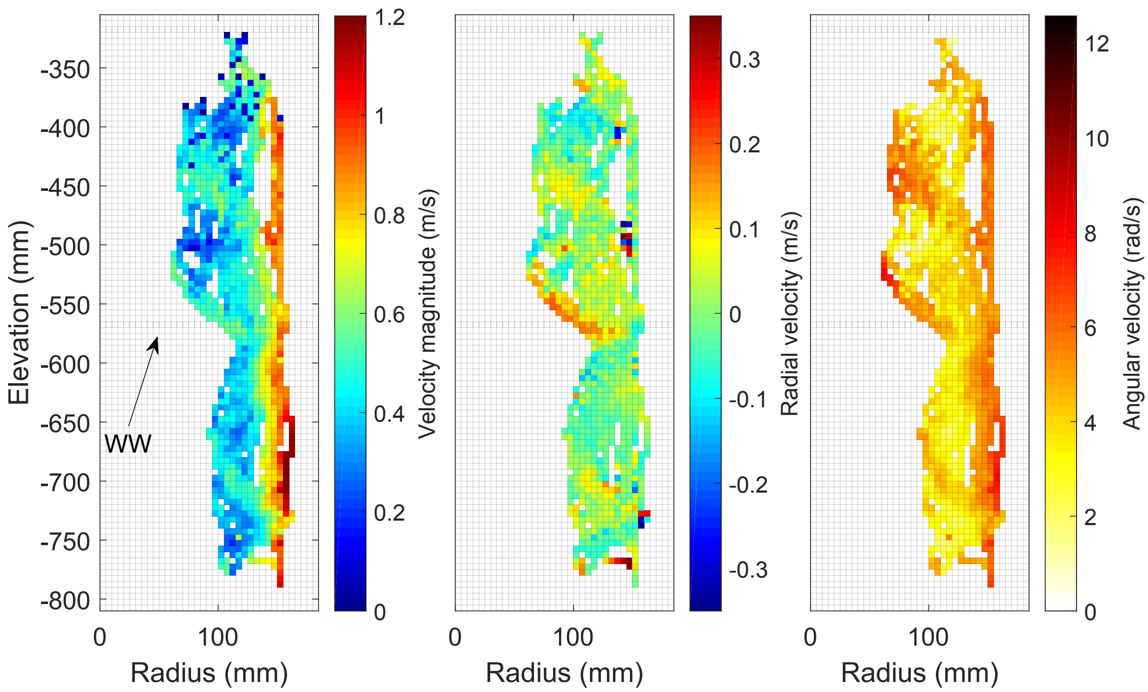

Figure 5.36 – Velocity for the quartz tracer of size 1000 to 1180 µm while wash water (WW) is ON.

Chapter 6

Conclusions

This chapter summarises the important outcomes of the experimental program and describes the scientific advancements made during this project. In addition, directions and ideas for future work are presented.

6.1 Conclusions

After discussing the key notions of mineral processing and gravity concentration (Chapter 2), an extensive review of the published literature focussing on the spiral concentrator was presented (Chapter 3). This review has shown a recent trend toward numerical particle flow simulations of the spiral concentrator operation. In addition, it highlighted a lack of information on the measured behaviour of dense and light mineral particles within the pulp flow. This information has now become critical to further advances in numerical spiral simulation. Accordingly, the work presented in this thesis focussed on measuring detailed particle flow field within a spiral concentrator. The achievement of the three objectives stated in the introduction (Chapter 1) enabled the particle flow field information to be retrieved.

The first objective completed was the successful design, assembly and characterisation of a positron emission particle tracking (PEPT) experimental set-up able to provide information about mineral particle motion in the spiral concentrator. The development of this system (Chapter 4) enabled the high resolution tracking of the spiral's upper turn.

In addition, the extension of the direct activation technique to the direct activation and breakage (DAB) procedure enabled the generation of representative hematite (5260 kg/m^3) and quartz (2650 kg/m^3) mineral tracers between 90 µm to 1400 µm in diameter. The lower end of this range represents a substancial decrease in size for mineral PEPT tracers. This is the first time such small representative mineral tracers were produced and enabled the observation of particle behaviour in dense and opaque pulp. This advance is already in use for other studies investigating other important techniques of mineral processing such as flotation [5].

Another important component of the first objective was the development of data analysis codes for the treatment of the tracking signal. This enabled production of quality data representing particle trajectory, velocity, acceleration and particle force resultant. This made reporting the particle flow field (Chapter 5) possible.

Thanks to the tracking performance achieved in the first objective, the completion of the second objective was possible. This second objective was the determination of the particle behaviour inside the secondary flow. Motion inside the secondary flow is of key importance for the mineral separation. This is the first time that the secondary flow has been measured for particle radial migration and velocity. For quartz particles of size 300 to 355 µm, the radial velocity magnitude within the secondary flow (second turn) ranged from 0.1 m/s in the lower inward moving layer of the flow and reached up to 0.2 m/s in the upper outward moving layers. This information is critical for the development of more efficient spiral concentrators, since ore separation is a direct result of particle behaviour in this secondary flow.

The use of an established tracking system (ADAC Forte) in combination with the DAB tracer production technique enabled representative particles to be tracked during injection of wash water on a longer section of the spiral trough. This fulfilled the third objective of measuring the wash water effect on the separation at the particle scale. The particle flow field is now available for representative iron ore mineral particles in different trough locations and under different conditions of wash water. This flow field highlighted the fact that the spiral first and second turns are extremely important in the separation as most of the radial motion was complete before entrance of the particle in the third turn. Addition of wash water disturbed the flow of solids and acted to reject light particle. Wash water enlarged the concentrate band width which has an effect on the take off port setting during operation.

6.2 Contributions to original knowledge

The main original contribution of this research project is the direct observation of the typical behaviour of gangue and valuable mineral particles inside a dense pulp (20% solids by mass) flowing on a spiral trough. The work allowed, for the first time, measured particle trajectory, velocity and acceleration to be determined during the separation occurring on the spiral. This particle flow field was recovered from real mineral particles of representative densities and sizes taken from a typical iron ore sample. These experimental results provide new information on particle behaviour in the spiral concentrator. A reference flow field is now known and can be used to advance particle flow simulations of the spiral.

6.3 Future work

More and better tracking could improve knowledge about smaller particle flow or other minerals' behaviour in other spiral geometries. This information is of importance in the optimisation of actual spiral concentrator. However, in consideration of the work presented in this thesis, the next logical step should be one of simulation, either by means of fundamental particle-fluid flow mechanics or numerical simulation. This thesis presents a reference case for the development of these simulations as they require detailed flow field information as particle trajectories, velocities, and accelerations for assessing their performance.

The presented data are of interest for validation of simulations depicting smaller scale models as single first turn or wash water injection point, with only a few particle sizes present. These could form a interesting starting point and could then be integrated in a larger multiscale simulation. The later step would be a complete simulation of a full spiral with a full size and mineral distribution present on the trough. Different approaches towards these simulations have been discussed in the litterature review (Chapter 3) and use of other methods of simulation should also be considered. Interesting cases for inspiration are present in recent literature [243].

The development of numerical simulations in the field of mineral processing has the potential to truly revolutionise the separator of the future. The fact that design ideas can be tested virtually before any physical prototyping or experimental work is undertaken is a significant advantage. An interesting task to be completed to help in the development of new separator concept is the development of an extensive framework for dimensional analysis of mineral pulp system. This framework should focus on the particle and pulp properties typically found in the field of mineral processing. This could enable detailed correlation of separation efficiency with system geometry and feed composition.

On the tracking technique side, the activity level of tracer and the amount of gamma rays recovered by the detectors is still a challenge for applications with small tracers carrying low activity and moving at high speed. Considering the breakage and division of the activity in the DAB technique, a relatively small sized tracer ($<$100 µm carry lower activity. This creates a tracking of lower resolution both in frequency and location precision. Better ways to directly activate small particles could improve this aspect. This requires review and design improvements of the cyclotron beam and target system. Detecting a larger portion of the emitted radiation could additionally lead to a better tracking performance, but this would require new detectors or even more packed detector setup. Evaluation of the effect of tracer activity on location error can be pushed further than presented here. In addition, new tracking algorithms are now being developed [211] with a focus on multiple particle tracking. This has the potential to provide much more refined flow fields.

On the spiral experimental side, measurement of the variation of the spiral performance in relation to a variation in the feed pulp injection direction and velocity (not just flow rate) would be an interesting avenue to pursue. The dispersion of the pulp across the profile is seen as a important factor in the particle separation which occurs in the first few turns. The dispersion pattern is affected by the feed direction and velocity.

Spiral surface roughness or micro pattern can have an effect on the pulp film velocity profile and particle motion on the trough. This should be investigated thoroughly as the wear life of spiral concentrator is debatable, and no comprehensive studies are available as to which surface finish is acceptable or not. Increased precision in moulding techniques now allows for specific patterns to be imprinted on the polymer trough surface, and this may be beneficial in channelling particles or water on the trough.

6.4 Concluding remarks

Improving metallurgical efficiency and reducing water and energy requirements of mineral processing devices and circuits is key to a successful and sustainable mineral processing industry. Observation and understanding of the fundamentals of such devices and circuits is an important step towards improvement in their performance.

A suggested work flow for the optimization of a mineral processing system (MPS) should contains the following items:

1. Geometallurgy to provide ore characteristics associated with different zones of the ore body;

2. Comminution test and mineral liberation analysis to provide representative particle shape, size and composition of the ground ore to be processed;

3. Particle fluid flow simulation based on representative ore characteristics to be used to optimize the design of a MPS;

4. Particle fluid flow simulation based on representative ore characteristics to provide simulated operating dataset on the MPS (covering a range of operational parameters and ore variability);

5. Generalized relationship obtained from the simulated dataset to represent the process performance and for process control;

6. Real operational process records which can be added to the simulated dataset to further improve the generalized relationship representing the process performance.

The last item is important in the optimisation of currently existing mineral processing systems. At a plant scale, mineralogical understanding of grain size, distribution and liberation of valuable and gangue minerals in the ore feed, concentrate and tailings is fundamental in the selection of processing parameters. This information should be made available on a continuous basis. Integrating all the observed and simulated mineral parameters (particle size, shape, composition, feed rate, pulp density, equipment parameters, recovery, feed and product grade) inside a database can enable instantaneous automated optimisation of process parameters in response to fresh mineralogical data from the plant feed and products.

References

[1] D. Boucher, Z. Deng, T. W. Leadbeater, R. Langlois, M. Renaud, and K. E. Waters. Pept studies of heavy particle flow within a spiral concentrator. *Minerals Engineering*, 62:120–128, 2014.

[2] D. Boucher, N. Gharib, Z. Deng, T. W. Leadbeater, R. Langlois, and K. E. Waters. Pept validation of a cfd-dem model of a fine quartz particle (60 um) behaviour in stirred water. *Procedia Engineering*, 102(0):1305–1315, 2015.

[3] D. Boucher, Z. Deng, T. W. Leadbeater, R. Langlois, and K. E. Waters. Observation of iron ore beneficiation within a spiral concentrator by positron emission particle tracking of large (1440 um) and small (58 um) hematite and quartz tracers. *Chemical Engineering Science*, 140:217 – 232, 2016.

[4] D. Boucher, Z. Deng, T.W. Leadbeater, R. Langlois, and K.E. Waters. Speed analysis of quartz and hematite particles in a spiral concentrator by pept. *Minerals Engineering*, 91:86 – 91, 2016. Physical Separation.

[5] D. Boucher, A. Jordens, J. Sovechles, R. Langlois, T. W. Leadbeater, N. A. Rowson, J. J. Cilliers, and K. E. Waters. Direct mineral tracer activation in positron emission particle tracking of a flotation cell. *Minerals Engineering*, 100:155 – 165, 2017.

[6] Department of Economic and Social Affairs. World population 2015. Technical

report, United Nations, Population Division, 2015. OPTISBN 978-92-1-151540-4.

[7] K. Van der Elst and N. Davis. The future availability of natural resources - a new paradigm for global resource availability. Technical report, World Economic Forum, 91–93 route de la Capite, CH-1223 Cologny/Geneva, Switzerland, 2014.

[8] E. van der Voet. Environmental risks and challenges of anthropogenic metals flows and cycles. Technical report, United Nations Environment Programme, 2013.

[9] C. A. J. Fletcher, T. Jancar, B. Matthews, M. M. Guzman, and J. Y. Tu. Computational simulation for mineral processing, 1995.

[10] H. Safikhani and P. Mehrabian. Numerical study of flow field in new cyclone separators. *Advanced Powder Technology*, 27(2):379 – 387, 2016.

[11] D. J. Parker, C. J. Broadbent, P. Fowles, M. R. Hawkesworth, and P. McNeil. Positron emission particle tracking - a technique for studying flow within engineering equipment. *Nuclear Instruments and Methods in Physics Research Section A: Accelerators, Spectrometers, Detectors and Associated Equipment*, 326(3):592–607, 1993.

[12] The MathWorks, Inc. Matlab.

[13] Barry A. Wills and James A. Finch. Chapter 1 - introduction. In Barry A. Wills Finch, James A., editor, *Wills' Mineral Processing Technology (Eighth Edition)*, pages 1 – 27. Butterworth-Heinemann, Boston, eighth edition edition, 2016.

[14] M. C. Fuerstenau and K. N. Han. *Principles of Mineral Processing*. Society for Mining, Metallurgy, and Exploration, 2003.

[15] G. M. Mudd. The sustainability of mining in australia: Key production trends and their environmental implications for the future. Technical report, Department of Civil Engineering, Monash University and Mineral Policy Institute, 2009.

[16] Barry A. Wills and James A. Finch. Chapter 5 - comminution. In Barry A. Wills Finch, James A., editor, *Wills' Mineral Processing Technology (Eighth Edition)*, pages 109 – 122. Butterworth-Heinemann, Boston, eighth edition edition, 2016.

[17] Barry A. Wills and James A. Finch. *Wills' Mineral Processing Technology (Eighth Edition)*, pages 1 – 462. Butterworth-Heinemann, Boston, eighth edition edition, 2016.

[18] Barry A. Wills and James A. Finch. Chapter 10 - gravity concentration. In Barry A. Wills Finch, James A., editor, *Wills' Mineral Processing Technology (Eighth Edition)*, pages 223 – 244. Butterworth-Heinemann, Boston, eighth edition edition, 2016.

[19] Barry A. Wills and James A. Finch. Chapter 9 - classification. In Barry A. Wills Finch, James A., editor, *Wills' Mineral Processing Technology (Eighth Edition)*, pages 199 – 221. Butterworth-Heinemann, Boston, eighth edition edition, 2016.

[20] R. H. Goodman, C. A. Brown, and I.C. Ritchie. Advanced gravity concentrators for improving metallurgical performance. In metallurgy Society for mining and Exploration, editors, *AIME Annual Meeting*, volume 84-149, pages 1–17. PREPRINTS.

[21] O. Kökkılıç, R. Langlois, and K. E. Waters. A design of experiments investigation into dry separation using a knelson concentrator. *Minerals Engineering*, 72:73 – 86, 2015.

[22] M. Greenwood, R. Langlois, and K. E. Waters. The potential for dry processing using a knelson concentrator. *Minerals Engineering*, 45(0):44–46, 2013.

[23] A. J. ALynch and C. A. Rowland. *The History of Grinding*. Society for Mining, Metallurgy, and Exploration, Inc., Littleton, Colorado, USA 80127, electronic edition edition, 2005.

[24] Josef Kuneš. 3 - fluid mechanics. In J. Kuneš, editor, *Dimensionless Physical Quantities in Science and Engineering*, pages 53 – 133. Elsevier, Oxford, 2012.

[25] Q. D. Nguyen. Yield Stress Measurement for Concentrated Suspensions. *Journal of Rheology*, 27:321, 1983.

[26] Q. D. Nguyen and D. V. Boger. Direct Yield Stress Measurement with the Vane Method. *Journal of Rheology*, 29:335–347, June 1985.

[27] R.T Jacobsen. The determination of the flow curve of a plastic medium in a wide gap rotational viscometer. *Journal of Colloid and Interface Science*, 48 (3):437 – 441, 1974.

[28] D. Fisher, S. Clayton, D. Boger, and P. Scales. The bucket rheometer for shear stress-shear rate measurement of industrial suspensions. *Journal of Rheology*, 51(5):821 – 831, 2007.

[29] S. Mueller, E. W. LLewellin, and H. M. Mader. The rheology of suspensions of solid particles. *Proceedings of the Royal Society A*, 466:1201–1228, 2010.

[30] M. P. Deosarkar and V. S. Sathe. Predicting effective viscosity of magnetite ore slurries by using artificial neural network. *Powder Technology*, 219(0):264–270, 2012.

[31] T. J. Ferree. Spirals and reichert cone circuits. In *Operation and Maintenance in Mineral Processing Plants*, pages 219–238, 1989.

[32] F. M. White. *Fluid Mechanics*. McGraw-Hill series in mechanical engineering. McGraw-Hill, 2008.

[33] N. Raju and E. Meiburg. The accumulation and dispersion of heavy particles in forced two-dimensional mixing layers. part 2: The effect of gravity. *Physics of Fluids*, 7:1241–1264, June 1995.

[34] Shinichi O., David S., and Kohei O. A numerical study on a macroscopic stokes number based on shear-induced interparticle collisions in a micro-separator/classifier. *Chemical Engineering Journal*, 135, Supplement 1:S21 – S29, 2008. Microreaction Technology 9: Proceedings of the Ninth International Conference on Microreaction Technology IMRET9 Special Issue.

[35] M. Guala, A. Liberzon, K. Hoyer, A. Tsinober, and W. Kinzelbach. Simultaneous measurements of the fluid and the solid phases in homogeneous turbulence: preliminary results at re = 250. In B. J. Geurts, H. Clercx, and W. Uijttewaal, editors, *Particle Laden FLow: From Geophysical to Kolmogorov Scales*, volume 11 of *ERCOFTAC*, pages 271–283. Springer, 2007.

[36] H. Chanson. *Hydraulics of Open Channel Flow*. Elsevier Science, 2004.

[37] J. Davilla and J. C. R. Hunt. Settling of small particles near vortices and in turbulence. *Journal of Fluid Mechanics*, 440:117–145, 8 2001.

[38] W.R. Dean M.A. Lxxii. the stream-line motion of fluid in a curved pipe (second paper). *The London, Edinburgh, and Dublin Philosophical Magazine and Journal of Science*, 5(30):673–695, 1928.

[39] S. A. Berger, L. Talbot, and L. S. Yao. Flow in curved pipes. *Annual Review of Fluid Mechanics*, 15(1):461–512, 1983.

[40] Barry A. Wills and James A. Finch. Chapter 12 - froth flotation. In Barry A. Wills Finch, James A., editor, *Wills' Mineral Processing Technology (Eighth Edition)*, pages 265 – 380. Butterworth-Heinemann, Boston, eighth edition edition, 2016.

[41] Barry A. Wills and James A. Finch. Chapter 13 - magnetic and electrical separation. In Barry A. Wills Finch, James A., editor, *Wills' Mineral Processing Technology (Eighth Edition)*, pages 381 – 407. Butterworth-Heinemann, Boston, eighth edition edition, 2016.

[42] R. O. Burt. *Gravity Concentration*. Wiley-VCH Verlag GmbH and Co. KGaA, 2000.

[43] F.F. Lins, M.M. Veiga, J.A. Stewart, A. Papalia, and R. Papalia. Performance of a new centrifuge (falcon) in concentrating a gold ore from texada island, b.c., canada. *Minerals Engineering*, 5(10):1113 – 1121, 1992.

[44] B. Knelson. The knelson concentrator. metamorphosis from crude beginning to sophisticated world wide acceptance. *Minerals Engineering*, 5(10–12):1091–1097, 1992.

[45] K. Heiskanen. *Particle Classification (Particle Technology Series)*, pages 1 – 336. Springer, 1993 edition edition, 1993.

[46] C. G. Anderson, R. C. Dunne, and J. L. Uhrie. *Mineral Processing and Extractive Metallurgy: 100 Years of Innovation*. Society for Mining Metallurgy & Exploration, 2014.

[47] K.P. Galvin, J. Zhou, A.J. Price, P. Agrwal, and S.M. Iveson. Single-stage recovery and concentration of mineral sands using a reflux™ classifier. *Minerals Engineering*, 93:32 – 40, 2016.

[48] D. Amariei, D. Michaud, G. Paquet, and M. Lindsay. The use of a reflux classifier for iron ores: Assessment of fine particles recovery at pilot scale. *Minerals Engineering*, 62:66 – 73, 2014. SI: Physical Separation.

[49] D.J. Miller. Design and operating experience with the goldsworthy mining limited batac jig and spiral separator iron ore beneficiation plant. *Minerals Engineering*, 4(3–4):411 – 435, 1991.

[50] Barry A. Wills and James A. Finch. Chapter 11 - dense medium separation (dms). In Barry A. Wills Finch, James A., editor, *Wills' Mineral Processing Technology (Eighth Edition)*, pages 245 – 264. Butterworth-Heinemann, Boston, eighth edition edition, 2016.

[51] E. Maré, B. Beven, and C. Crisafio. *10 - Developments in nonmagnetic physical separation technologies for hematitic/goethitic iron ore*, pages 309–338. Woodhead Publishing, 2015.

[52] H. Versteeg and W. Malalasekera. *An Introduction to Computational Fluid Dynamics - The Finite Volume Method*. 2/e edition, 2007.

[53] M. P. Srivastava, S. K. Pan, N. Prasad, and B. K. Mishra. Characterization and processing of iron ore fines of kiriburu deposit of india. *International Journal of Mineral Processing*, 61(2):93–107, 2001.

[54] C. Stanton and M. Bannear. Arrium's iron baron hematite beneficiation plant - a success from start to finish. In *Iron Ore Conference 2013*, pages 547–552, August 2013.

[55] E. Selvapandian and R. Barr. Managing challenges faced in the brownfield commissioning of an ultra-fine hematite processing circuit at arrium's iron duke ore beneficiation plant. In *Iron Ore Conference 2013*, pages 533–538, August 2013.

[56] G. Chevalier. Improved iron recovery at qcm pellet plant. In *Montreal Energy and Mines*, pages 355–373. Canadian Institute of Mining, Metallurgy and Petroleum, April 2007.

[57] J. V. Thompson. The humphreys spiral concentrator its place in ore dressing. *Mining Engineering*, (January):84–87, 1958.

[58] M. Sadeghi, C. Bazin, and M. Renaud. Radial distribution of iron oxide and silica particles in the reject flow of a spiral concentrator. *International Journal of Mineral Processing*, 153:51–59, June 2016.

[59] J. M. D. Wilson, W. Petruk, and C. Cote. A mineralogical evaluation of the spiral circuit at mount wright concentrator by image analysis. *CIM Bulletin*, 83(943):76–83, November 1990.

[60] P. N. Holtham and P. H. Stitt. Development in australian spiral separator technology. In *Minerals and Exploration at the Crossroads*, pages 165–173. The AusIMM Sydney Branch, July 1988.

[61] M.H. Staia, E.S. Puchi, F. Fernandes, and E. Hernandez. Recovery of ilmenite from venezuelan black sand. In *Proceedings of Process Mineralogy XIII*, pages 71–78. The Minerals, Metals and Materials Society, 1995.

[62] H. Haghi, M. Noaparast, A. Shabani, Farrokhrouz M., A. Ghadyani, A. Ghorbani, M. Shevrini, and M. Tayebi. Reduction of iron content from silical by gravitational processes. In *XXV International Mineral Processing Congress*, pages 767–780. International Mineral Processing Congress, September 2010.

[63] L. E. Apodaca. *Industrial Practice of Fine Coal Processing*, chapter 12 - Application of Spiral Concentrators, pages 87–96. 1988.

[64] M. G. Ayat and B. C. Scott. Spiral separator versus concentrating tables - a comparison for the coal preparation industry. In *Fall Meeting Preprint*, number 86-320, pages 1–6. Society for Mining Engineers, September 1986.

[65] R. G. Richards and P. J. Bangerter. Gravity concentrator systems in gold ore processing. In *Regional Conference on Gold Mining, Metallurgy and Geology*, pages 89–100. The Aus. I.M.M. Perth and Kalgoorlie Branches, October 1984.

[66] R. Abela and D. Denysschen. Recovering gold from sand dumps using gravity concentration. In *DMS and Gravity Concentration Operation and Technology in South Africa*, pages 49–60. The South African Institute of Mining and Metallurgy, 2006.

[67] B. J. Reaveley. Recovery of fine free gold. Society for Mining Engineers, 1986.

[68] R.G. Richards and M.K. Palmer. Currents trends in gravity separation technology for fine gold recovery. Norgold 88, pages 1–7. Mineral Deposits Limited, August 1988.

[69] A. B. Holland-Batt, G. F. Balderson, and M. S. Cross. The application and design of wet-gravity circuits in the south african minerals industry. *Journal of the South African Institue of Mining and Metallurgy*, pages 53–70, March 1982.

[70] D. M. MacHunter, R. G. Richards, and M. K. Palmer. Improved gravity separation systems utilizing spiral separators incorporating new design parameters and features. In *Heavy Minerals 2003*, pages 131–138. South African Institue of Mining and Metallurgy, 2003.

[71] R. B. Adair and J. O. Crabtree. Recovery of mica from silt deposits in the nolichucky reservoir, tennessee. Technical Report TN23.U7, no. 7488, 622.06173, Bureau of Mines, United States Department of Interior, 1971.

[72] J. S. Browning. Recovering fine-size coal from alabama washer wastes unsing humphreys spiral. In *Falls Meeting Preprint 77-B-318*, pages 1–17. Society of Mining Engineers, 1977.

[73] C. Pena. Eco-efficient gravity separation solutions in india. In *XXV International Mineral Processing Congress*, pages 1123–1131. International Mineral Processing Congress, September 2010.

[74] C. Ulsen, H. Kahn, G. Hawlitschek, and E.A. Masini. Mineral processing on the production of recycled sand from construction and demolition waste. In *XXVI International Mineral Processing Congress*, pages 5567–5580. International Mineral Processing Congress, September 2012.

[75] P. O. J. Davies, R. H. Goodman, and J. A. Deschamps. Recent developments in spiral design, construction and application. *Minerals Engineering*, 4(3–4): 437–456, 1991.

[76] J. H. van Reenen, H. Thiele, and C. Bergman. The recovery of chorme and manganese alloy fines from slag. In *Tenth International Ferroalloys Congress*, pages 548–554. International Ferroalloys Congress, February 2004.

[77] F. Pardee. Separator for ore, coal and c., 1898.

[78] A. Murphy. Spiralizing plant spring canyon coal company. In *Proceeding Rocky Mountain*, pages 12–16. Society for Mining, Metallurgy and Exploration, 1926.

[79] I. B. Humphreys. Helical chute concentrator and the method of concentration practiced thereby, 1943.

[80] I. B. Humphreys. Wash water pickup for spiral concentrator, 1952.

[81] G.W. Gleeson. Why the humphreys spiral works. *Engineering and Mining Journal*, 146:85–86, 1945.

[82] D.F. Boyd. Liberia mining company ltd. operates iron ore beneficiation plant. In *Annual Meeting Preprint 62B1*, pages 1–9. American Institute of Mining, Metallurgical and Petroleum Engineer, 1962.

[83] A.P. Giambra. Start-up of the iron ore company of canada's carol concentrator. In *The Canadian Mining and Metallurgical Bulletin*, pages 377–380, Montreal, May 1963.

[84] W. Taciuk and T. C. Murphy. Recovery of magnetite in spiral tailings at labrador city. *CIM Bulletin*, pages 41–45, January 1972.

[85] L. Lewczuk. Mineralogical and liberation study of the iron ore mill products from the scully concentrator. In D. J. T. Carson and A. H. Vassiliou, editors, *Process Mineralogy VIII*, pages 227–234. The Minerals, Metal and Materials Society, 1988.

[86] A. M. McKim and J. S. Ambler. Ore dressing at scully mine. *CIM Bulletin*, pages 942–947, 1969.

[87] G. F. Balderson. Recent developments and applications of spiral concentrators. In *Proceedings of The Aus.I.M.M North-West Queensland Branch Mill Operators' Conference*, pages 57–73. The Australasian Institute of Mining and Metallurgy, September 1982.

[88] B. J. Reaveley and I. C. Ritchie. The development of high efficiency spiral separators. In *A World Source of IImenite, Rutile, Monazite and Zircon, Conference*, pages 87–97. The Aus. I.M.M. Perth Branch, Australia, September 1986.

[89] J. S. Browning. Removal of sulfur from coal by a combination of gravity and flotation methods. pages 1222–1224, 1982.

[90] D.T. Hornsby, S.J. Watson, and C.J. Clarkson. Fine coal cleaning by spiral and water washing cyclone. *Coal Preparation*, 12:122–161, 1993.

[91] L.M. Tavares and C.H. Sampiao. Spiral concentrator for cleaning fines from major brazilian coalfields. In *High Efficiency Coal Separation: An International Symposium*, pages 129–138, 1995.

[92] R. G. Richards, J. L. Hunter, and A. B. Holland-Batt. Spiral concentrators for fine coal treatment. *Coal Preparation*, 1(2):207–229, 1985.

[93] E. R. Palowitch, A. W. Deurbrouck, and T. H. Parsons. *Section 2: Hydraulic Concentration*, pages 414–449. 1991.

[94] L.F. Delgato. Spiral applications in mexico - industrial sands and coal. In *SME Annual Meeting Preprint 94-193*, number 94-193, pages 1–5. Society for Mining Metallurgy and Exploration, Inc., February 1994.

[95] G. Atesok, I. Yildirim, and M. S. Celik. Applicability of the reichert spiral for cleaning bituminous and lignitic coals: a pilot scale study. *International Journal of Mineral Processing*, 40(1–2):33–44, 1993.

[96] A. B. Holland-Batt, J. L. Hunter, and J. H. Turner. The separation of coal fines using flowing-film gravity concentration. *Powder Technology*, 40(1–3):129–145, 1984.

[97] C. N. Bensley and R. Keast-Jones. A comparison of froth flotation and spiral concentrators for the treatment of fine coal in the hunter valley, n.s.w. In *Procedings of the Australasian Institute of Mining and Metallurgy*, volume 289, pages 181–188, June 1984.

[98] D.M. Riley, Firth B.A., and C.L. Neville. Enhanced gravity separation. In *High Efficiency Coal Preparation: An international Symposium*, pages 79–88, 1995.

[99] M. J. Mankosa, F. L. Stanley, and R. Q. Honaker. Combining hydraulic classification and spiral concentration for improved efficiency in fine coal recovery

circuits. In *High Efficiency Coal Preparation: An international Symposium*, pages 99–107, 1995.

[100] B. K. Parekh, W. R. Carson, B. J. Arnold, and C. E. Raleigh Jr. Coal pond fines cleaning with classifying cyclones, spirals and column flotation. In *SME Annual Meeting Preprint 98-97*, pages 1–7. Society for Mining, Metallurgy and Exploration, Inc., March 1998.

[101] T. A. Toney, L. R. Fish, and P. J. Bethell. Increase your plant recovery: More efficient spiral circuits. *Mining Engineering*, pages 61–64, March 1999.

[102] W. Petruk. Evaluation of concentrator of iron ore company of canada by image analysis and materials balancing techniques. In *Process Mineralogy IX*, pages 111–118. The Minerals, Metals and Materials society, 1989.

[103] W. R. McDonald, J. L. Johnson, J. N. Greaves, and N. Wetzel. Chromite recovery from northern california ores using a physical concentration process. Technical Report RI9300, United States Department of the Interior, Bureau of Mines, 1990.

[104] T. J. Ferree. Applciation of mdl reichert cone and spiral concentrators for the separation of heavy minerals. *CIM Bulletin*, 86(975):35–39, December 1993.

[105] R. Abela. Solutions to common design and operating problems in spiral circuits. In *Heavy Minerals 2003*, pages 9–12. South African Institue of Mining and Metallurgy, 2003.

[106] M. R. Geer, H. F. Yancey, C. L. Allyn, and R. H. Eckhouse. Laboratory performance tests of the humphreys spiral as a cleaner of fine coal - discussion. In *Mining Engineering Transaction AIME*, volume 187, pages 1160–1162. American Institute of Mining and Metalurgical Engineers, November 1950.

[107] J. M. F. Clout. Beneficiation of iron ores using the desand process. In *Iron Ore Conference 2013*, pages 337–347, August 2013.

[108] W. E. Brown and L. J. Erck. Humphreys spiral concentration on mesabi range ores. In *Mining Transactions*, volume 184, pages 187–193. American Institute of Mining and Metalurgical Engineers, June 1949.

[109] D. Wright, R. G. Richards, and M. S. Cross. The development of mineral sands separation technology. pages 107–121. AusIMM, Australia: A World Source of Ilmenite, Rutile, Monazite and Zircon, October 1986.

[110] W.L. Dennen and V.H. Wilson. Cleaning anthracite silt for boiler fuel with humphreys spiral separator. In *Coal Technology*, pages 357–371. Society for Mining, Metallurgy and Exploration, 1948.

[111] M. R. Geer, H. F. Yancey, C. L. Allyn, and R. H. Eckhouse. Laboratory performance tests of the humphreys spiral as a cleaner of fine coal. In *Mining Engineering Transaction AIME*, volume 187, pages 1057–1067. American Institute of Mining and Metalurgical Engineers, October 1950.

[112] D. B. Hyma and J. A. Meech. Preliminary tests to improve the iron recovery from the -212 micron fraction of new spiral feed at quebec cartier mining company. *Minerals Engineering*, 2(4):481–488, 1989.

[113] G.H. Luttrell, J.N. Kohmuench, F.L. Stanley, and G.D. Trump. Improving spiral performance using circuit analysis. *Minerals and Metallurgical Processing*, 15(4):16–21, November 1998.

[114] T. McKeon and G. H. Luttrell. Application of linear circuit analysis in gravity separator circuit design. In *Heavy Minerals 2005*, pages 179–184. South African Institue of Mining and Metallurgy, 2005.

[115] G. Luttrell, T. McKeon, and J. Kohmuench. Design criteria for multistage spiral circuits. In *SME Annual Meeting Preprint 07-126*, pages 1–4. Society for Mining, Metallurgy and Exploration Inc., February 2007.

[116] T. J. McKeon and G. H. Luttrell. Optimization of multistage circuits for gravity concentration of heavy mineral sands. *Minerals and Metallurgical Processing*, 29(1):1–5, February 2012.

[117] P. Tucker. An approach to modelling industrial unit processes: application to a spiral concentrator for minerals. *Applied Mathematical Modelling*, 9(5):375–379, 1985.

[118] P. J. Bethell, F. L. Stanley, and S. Horton. Benefits associated with two stage spiral cleaning at mcclure river preparation plant. *Minerals and Metallurgical Processing*, pages 215–219, November 1991.

[119] M. Palmer and C. Vadeikis. New developments in spirals and spiral plant operations. In *XXV International Mineral Processing Congress*, pages 1099–1108. International Mineral Processing Congress, September 2010.

[120] Mineral Technologies. Unlocking value for onesteel. In *Gravity Tales*, number 20, pages 1–2. January 2012.

[121] Mineral Technologies. Innovative spiral technology and new washwater design delivers 50 percent production increase in same footprint. In *Gravity Tales*, number 21, pages 1–2. May 2012.

[122] P.L. Dunn, R. Rose, and D. Settles. Development of the sii 'mission' mineral sands project. In Canadian Mineral Processors, editor, *47th Annual Canadian Mineral Processors Operators Conference*, pages 106–116, 2015.

[123] A. B. Holland-Batt. Some design considerations for spiral separators. *Minerals Engineering*, 8(11):1381–1395, 1995.

[124] R. G. Richards and M. K. Palmer. High capacity gravity separators a review of current status. *Minerals Engineering*, 10(9):973–982, 1997.

[125] E. G. Kelly, D. J. Spottiswood, D. E. Spiller, and C. N. Robinson. Gravity cleaning fo fine coal. In *19th Annual Conference of the New Zealand Branch*

of the Australasian Institute of Mining and Metallurgy, number 10, pages 1–11. Aus. I.M.M., August 1985.

[126] R.O. Burt. *Mineral Processing Design*, volume 122 of *NATO ASI Series*, chapter Gravity Concentration Methods, pages 106–137. Springer, 1987.

[127] R. Sivamohan and E. Forssberg. Principles of spiral concentration. *International Journal of Mineral Processing*, 15(3):173–181, 1985.

[128] A. B. Holland-Batt. The dynamics of sluice and spiral separations. *Minerals Engineering*, 8(1–2):3–21, 1995.

[129] Y. Atasoy and D. J. Spottiswood. A study of particle separation in a spiral concentrator. *Minerals Engineering*, 8(10):1197–1208, 1995.

[130] W. S. Weldon and R. M. G. MacHunter. Recent advances in coal spiral development. In *SME Annual Meeting Preprint 97-82*, pages 1–15. Society for Mining, Metallurgy and Exploration, Inc., February 1997.

[131] E. Martinez. Recovery of non-magnetic minerals with a gravity magnetic separator. In *SMe Annual Meeting Preprint 92-65*, pages 1–6. Society for Mining, Metallurgy and Exploration, February 1992.

[132] R. Burt. The role of gravity concentration in modern processing plants. *Minerals Engineering*, 12(11):1291–1300, 1999.

[133] D. E. Walsh and E. G. Kelly. An investigation of the performance of a spiral using radioactive gold tracers. *Minerals and Metallurgical processing*, pages 105–109, August 1992.

[134] T. J. Napier-Munn and R. A. Alford. The causes of heavy mineral loss from mineral sands wet concentrators. In *The AusIMM Proceedings*, pages 19–30. The AusIMM, 1991.

[135] S. K. Tripathy and Y. Rama Murthy. Modeling and optimization of spiral concentrator for separation of ultrafine chromite. *Powder Technology*, 221:387–394, 2012.

[136] R. G. Richards, D. M. MacHunter, P. J. Gates, and M. K. Palmer. Gravity separation of ultrafine (less than 0.1mm) minerals using spiral separators. *Minerals Engineering*, 13(1):65–77, 2000.

[137] R. Q. Honaker, M. Jain, B. K. Parekh, and M. Saracoglu. Ultrafine coal cleaning using spiral concentrators. *Minerals Engineering*, 20(14):1315–1319, 2007.

[138] O. Y. Gulsoy and M. Kademli. Effects of operational parameters of spiral concentrator on mica-feldspar separation. *Mineral Processing and Extractive Metallurgy*, 115(2), 2006.

[139] R.M.G. MacHunter. The effect of ultrafine particles on the separation performance of wet gravity processing equipment and flowsheet design implications for their treatment. In *Heavy Minerals 2005*, pages 185–187. South African Institue of Mining and Metallurgy, 2005.

[140] P. Ramsaywok, M. K. G. Vermaak, and R. Viljoen. Case study: high capacity spiral concentrators. *The Journal of The Southern African Institute of Mining and Metallurgy*, 110:637–642, 2010.

[141] C. Kari, G. Kapure, and S. M. Rao. Effect of operating parameters on the performance of spiral concentrator. In *International Seminar on Mineral Processing Technology*, pages 316–319, 2006.

[142] R. Abela. The effect of slimes content on the rougher spiral circuit in a heavy mineral sands operation. In *Heavy Minerals 2003*, pages 1–8. South African Institue of Mining and Metallurgy, 2003.

[143] M. K. G. Vermaak, H. J. Visser, J. B. Bosman, and G. Krebs. A simple process control model for spiral concentrators. *The Journal of The Southern African Institute of Mining and Metallurgy*, 108, 2008.

[144] W.R. Hudspeth. Spiral recover heavy mineral by-product - kings mountain, n.c. *Mining Engineering*, page 767, August 1952.

[145] D.K. Henderson and D.M. MacHunter. A review of spiral technology for fine gravity beneficiation. pages 1–6. MD Mineral Technologies, 2000.

[146] M. Sadeghi, C. Bazin, and M. Renaud. Effect of wash water on the mineral size recovery curves in a spiral concentrator used for iron ore processing. *International Journal of Mineral Processing*, 129:22–26, 2014.

[147] R. Dallaire, A. Laplante, and E. Jorgen. Humphrey's spiral tolerance to feed variations. *CIM Bulletin*, pages 128–134, August 1978.

[148] A.B. Holland-Batt. The effect of feed rate on the performance of coal spirals. pages 1–20. Mineral Technologies, 1994.

[149] E. G. Kelly. Performance of modern spirals cleaning fine coal. In *Annual Meeting Preprint*, number 84-48, pages 1–12. Society for Mining Engineer of AIME, February 1984.

[150] B. J. Zhang, F. Yang, P. Sahoo, M. K. Mohanty, and X. X. Zhang. Optimization of a compound spiral for cleaning high sulfur fine and ultrafine coal. pages 653–662, 2014.

[151] T. W. West and L. E. Apodaca. Cost effective btu recovery by fine coal washing spirals. In *Preprint*, number Preprint 88-82, pages 1–10. Society of Mining Engineers, 1988.

[152] C. M. Ramotsabi, W. Erasmus, and F. Bornman. Wash water optimization on an iron ore spiral. In Canadian Mineral Processors, editor, *47th Annual Canadian Mineral Processors Operators Conference*, 2015.

[153] Q. Dehaine and L.O. Filippov. Modelling heavy and gangue mineral size recovery curves using the spiral concentration of heavy minerals from kaolin residues. *Powder Technology*, (292):331–341, February 2016.

[154] L. Auret, A. Haasbroek, P. Holtzhausen, and B. Linder. Online concentrate band position detection for a spiral concentrator using a raspberry pi. In *XXVII International Mineral Processing Congress*, pages 1–10. International Mineral Processing Congress, September 2014.

[155] A. Steinmuller. Development and application of simple process models for spiral concentrators. In *Heavy Minerals 2005*, pages 167–172. South African Institue of Mining and Metallurgy, 2005.

[156] P. N. Holtham. Particle transport in gravity concentrators and the bagnold effect. *Minerals Engineering*, 5(2):205–221, 1992.

[157] P. N. Holtham. Primary and secondary fluid velocities on spiral separators. *Minerals Engineering*, 5(1):79–91, 1992.

[158] G. K. Loveday and J. J. Cilliers. Fluid flow modelling on spiral concentrators. *Minerals Engineering*, 7(2–3):223–237, 1994.

[159] J. Thomson. On the origin of windings of rivers in alluvial plains, with remarks on the flow of water round bends in pipes. *Proceedings of the Royal Society of London*, 25(171-178):5–8, 1876.

[160] A. B. Holland-Batt. Spiral separation: theory and simulation. In *African Mining*, pages 46–60. Institution of Mining and Metallurgy, July 1987.

[161] P. N. Holtham. Flow visualisation of secondary currents on spiral separators. *Minerals Engineering*, 3(3–4):279–286, 1990.

[162] A. B. Holland-Batt and P. N. Holtham. Particle and fluid motion on spiral separators. *Minerals Engineering*, 4(3–4):457–482, 1991.

[163] K.J. Golab, P.N. Holtham, and W. Jie. Measurment of water velocities on the spiral separator by particle image velocimetry. In *Chemeca '96: 24th Australian and New Zealand chemical engineering conference*, pages 3–8, 1996.

[164] S. Mohanty and B.K. Mishra. Cfd simulation of flow on a spiral concentrator. In *XXVI International Mineral Processing Congress*, pages 3478–3487. International Mineral Processing Congress, September 2012.

[165] J. R. D. Francis. Experiments on the motion of solitary grains along the bed of a water-stream. *Proceedings of the Royal Society of London A: Mathematical, Physical and Engineering Sciences*, 332(1591):443–471, 1973.

[166] M. R. Leeder. Bedload dynamics: Grain-grain interactions in water flows. *Earth Surface Processes*, 4(3):229–240, 1979.

[167] R. A. Bagnold. Experiments on a gravity-free dispersion of large solid spheres in a newtonian fluid under shear. *Proceedings of the Royal Society of London A: Mathematical, Physical and Engineering Sciences*, 225(1160):49–63, 1954.

[168] W. M. Bertholf. Cleaning table middlings from a coal washery with the humphreys spiral concentrator. In *Mining Technology, Class B, Milling and Concentration*, pages 1–8. American Institute of Mining and Metalurgical Engineers, 1946.

[169] B.R. Brits. Effect of particle size in gravity separation processes at palabora south africa. pages 159–167. SME, 1991.

[170] C. Bazin, M. Sadeghi, P. Roy, M. Bourassa, D. Cataford, F. Lavoie, C. Rochefort, C. Gosselin, M. Renaud, and G. Mahieu. Simulation of an iron ore concentration circuit using mineral size recovery curves of industrial spirals. In *46th Annual Canadian Mineral Processors Operators Conference*, pages 387–402. Canadian Mineral Processors, January 2014.

[171] C. Bazin, M. Sadeghi, M. Bourassa, P. Roy, F. Lavoie, D. Cataford, C. Rochefort, and C. Gosselin. Size recovery curves of minerals in industrial spirals for processing iron oxide ores. *Minerals Engineering*, 65:115–123, 2014.

[172] M. Li, T. Jancar, P. N. Holtham, J. J. Davis, and C. A. J. Fletcher. Approaches to development of coal spiral models. In *High Efficiency Coal Preparation: An International Symposium*, pages 335–345, 1995.

[173] P. Dixit, R. Tiwari, A. K. Mukherjee, and P. K. Banerjee. Application of response surface methodology for modeling and optimization of spiral separator for processing of iron ore slime. *Powder Technology*, 275:105–112, 2015.

[174] M.N. Rao and F. Rondon. Comparative analysis of hydrogravimetric separation of friable minerals of district piar between spirals hc1870 and hg8/7. In *EPD Congress 1999*, pages 1009–1018. The Minerals, Metals and Materials Society, 1999.

[175] R.P. Killmeyer, P.H. Zandhuis, M.V. Ciocco, W. Weldon, T. West, and D. Petrunak. Fine anthracite coal washing using spirals. Technical Report DOE/NETL-2001/1149, U.S. Department of Energy - National energy Technology Laboratory, May 2001.

[176] D. Gucbilmez and S.L. Ergun. A comparison of performances of spiral concentrators having different geometries. In *XXVI International Mineral Processing Congress*, pages 1733–1739. International Mineral Processing Congress, September 2012.

[177] G. E. Sreedhar, D. R. Venkatesulu, and N. K. Nanda. Evaluation of gravity spirals for beneficiation of banded haematite jasper iron ore of india. In *Iron Ore Conference*, pages 323–326, July 2009.

[178] C. Philander and A. Rozendaal. A process mineralogy approach to geometallurgical model refinement for the namakwa sands heavy minerals operations, west coast of south africa. *Minerals Engineering*, 65(0):9–16, 2014.

[179] R. P. King, A. H. Juckes, and P. A. Stirling. A quantitative model for the prediction of fine coal cleaning in a spiral concentrator. *Coal Preparation*, 11 (1-2):51–66, 1992.

[180] A. B. Holland-Batt. Interpretation of spiral and sluice tests. In *African Mining '91*, pages C11–C20. Institution of Mining and Metallurgy, June 1991.

[181] J.D. Grobler, N. Naude, and J.H. Zietsman. Enhanced holland-batt spline for describing spiral concentrator performance. *Minerals Engineering*, (92):189–195, March 2016.

[182] R. N. Guest and R. C. Dunne. An evaluation of gravity separators by use of a synthetic ore. *Journal of the South African Institute of Mine and Metallurgy*, 85(6):187–195, June 1985.

[183] C. Bazin, M. Sadeghi, and M. Renaud. An operational model for a spiral classifier. *Minerals Engineering*, 2016.

[184] A. B. Holland-Batt. A method for the prediction of the primary flow on large diameter spiral troughs. *Minerals Engineering*, 22(4):352–356, 2009.

[185] S. K. Das, K. M. Godiwalla, Lopamudra Panda, K. K. Bhattacharya, Ratnakar Singh, and S. P. Mehrotra. Mathematical modeling of separation characteristics of a coal-washing spiral. *International Journal of Mineral Processing*, 84(1–4): 118–132, 2007.

[186] A. B. Holland-Batt. A study of the potential for improved separation of fine particles by use of rotating spirals. *Minerals Engineering*, 5(10–12):1099–1112, 1992.

[187] P. C. Kapur, H. I. Bilgesu, and T. P. Meloy. Spirals unveiled, part 1: Geometric description and physical processes. In metallurgy Society for mining and Exploration, editors, *Annual Meeting Proceedings*, 1996.

[188] P. C. Kapur and T. P. Meloy. Spirals observed. *International Journal of Mineral Processing*, 53(1–2):15–28, 1998.

[189] P. C. Kapur and T. P. Meloy. Industrial modeling of spirals for optimal configuration and design: spiral geometry, fluid flow and forces on particles. *Powder Technology*, 102(3):244–252, 1999.

[190] P. K. Jain and V. Rayasam. An analytical approach to explain the generation of secondary circulation in spiral concentrators. *Powder Technology*, 308:165–177, 2017.

[191] M. Li, C. J. Wood, and J. J. Davis. A study of coal washing spirals. In *5th Australian Coal Preparation Conference*, pages 82–97, 1991.

[192] J. Wang and J. R. G. Andrews. Numerical simulations of liquid flow on spiral concentrators. *Minerals Engineering*, 7(11):1363–1385, 1994.

[193] T. Jancar, A. J. Fletcher, P. N. Holtham, and J. A. Reizes. Computational and experimental investigation of spiral separator hydrodynamics. In *Proceedings of the XIX IMPC*, pages 147–151. International Mineral Processing Congres, 1995.

[194] B. W. Matthews, P. N. Holtham, C. A. Fletcher, K. Golab, and A. C. Partridge. Computational and experimental investigation of spiral concentrator flows. *Coal Operators' Conference*, 1998.

[195] B. W. Matthews, C. A. J. Fletcher, and A. C. Partridge. Computational simulation of fluid and dilute particulate flows on spiral concentrators. *Applied Mathematical Modelling*, 22(12):965–979, 1998.

[196] B. W. Matthews, C. Fletcher, A. Partridge, and S. Vasquez. Computations of curved free surface water flow on spiral concentrators. *Journal of Hydraulic Engineering*, 125(11):1126–1139, 1999.

[197] B. W. Matthews, C. A. J. Fletcher, and T. C. Partridge. Particle flow modelling on spiral concentrators: Benefits of dense media for coal processing. *Second International Conference on CFD in the Minerals and Process Industries*, 1999.

[198] M. A. Doheim, A. F. Abdel Gawad, G. M. A. Mahran, M. H. Abu-Ali, and A. M. Rizk. Numerical simulation of particulate-flow in spiral separators: Part i. low solids concentration (0.3 *Applied Mathematical Modelling*, 37(1–2):198–215, 2013.

[199] G. M. A. Mahran, M. A. Doheim, A. F. AbdelGawad, M. H. Abu-Ali, and A. M. Rizk. Numerical simulation of particulate flow in a spiral separator (15 percent solids). In *AFINIDAD LXXII*, number 571, pages 223–229, Septembre 2015.

[200] Y. M. Stokes. Computing flow in a spiral particle separator. *14th Australasian Fluid Mechanics Conference*, 2001.

[201] Y. M. Stokes. *Flow in Spiral Channels of Small Curvature and Torsion*, volume 62 of *Fluid Mechanics and Its Applications*, chapter 35, pages 289–296. Springer Netherlands, 2001.

[202] S. Lee, Y. Stokes, and A.L. Bertozzi. A model for particle laden flow in a spiral concentrator. In *XXIII ICTAM*, pages 1–2, August 2012.

[203] B. K. Mishra and A. Tripathy. A preliminary study of particle separation in spiral concentrators using dem. *International Journal of Mineral Processing*, 94 (3–4):192–195, 2010.

[204] K. E. Waters, R. Langlois, and T. W. Leadbeater. Using positron emission particle tracking to understand spiral concentrators. In *9th International Mineral Processing Conference*, pages 530–538. Procemin2012, 2012.

[205] M. R. Hawkesworth, M. A. O'Dwyer, J. Walker, P. Fowles, J. Heritage, P. A. E. Stewart, R. C. Witcomb, J. E. Bateman, J. F. Connolly, and R. Stephenson. A positron camera for industrial application. *Nuclear Instruments and Methods in Physics Research Section A: Accelerators, Spectrometers, Detectors and Associated Equipment*, 253(1):145–157, 1986.

[206] T. W. Leadbeater. *The Development of Positron Imaging Systems for Applications in Industrial Process Tomography, Ph.D. Thesis*. Ph.d. thesis, 2009.

[207] T. W. Leadbeater, D. J. Parker, and J. Gargiuli. Positron imaging systems for studying particulate, granular and multiphase flows. *Particuology*, 10(2): 146–153, 2012.

[208] K. E. Cole, A. Buffler, N. P. van der Meulen, J. J. Cilliers, J. P. Franzidis, I. Govender, C. Liu, and M. R. van Heerden. Positron emission particle tracking measurements with 50 micron tracers. *Chemical Engineering Science*, 75(0): 235–242, 2012.

[209] K. Cole, A. Buffler, J. J. Cilliers, I. Govender, J. Y. Y. Heng, C. Liu, D. J. Parker, U. V. Shah, M. van Heerden, and X. Fan. A surface coating method to modify tracers for positron emission particle tracking (pept) measurements of froth flotation. *Powder Technology*, 263(0):26–30, 2014.

[210] S. Langford, C. Wiggins, D. Tenpennya, and A. Ruggles. Positron emission particle tracking (pept) for fluid flow measurements. *Nuclear Engineering and Design*, 302:81–89, 2016.

[211] C. Wiggins, R. Santos, and A. Ruggles. A novel clustering approach to positron emission particle tracking. *Nuclear Instruments and Methods in Physics Research A*, 811:18–24, March 2016.

[212] F. Chiti, S. Bakalis, W. Bujalski, M. Barigou, A. Eaglesham, and A. W. Nienow. Using positron emission particle tracking (pept) to study the turbulent flow in a baffled vessel agitated by a rushton turbine: Improving data treatment and validation. *Chemical Engineering Research and Design*, 89(10):1947–1960, 2011.

[213] A. Guida, X. Fan, D. J. Parker, A. W. Nienow, and M. Barigou. Positron emission particle tracking in a mechanically agitated solid–liquid suspension of coarse particles. *Chemical Engineering Research and Design*, 87(4):421–429, 2009.

[214] A. Guida, A. W. Nienow, and M. Barigou. Mixing of dense binary suspensions: Multi-component hydrodynamics and spatial phase distribution by pept. *AIChE Journal*, 57(9):2302–2315, 2011.

[215] A. Guida, A. W. Nienow, and M. Barigou. Pept measurements of solid–liquid flow field and spatial phase distribution in concentrated monodisperse stirred suspensions. *Chemical Engineering Science*, 65(6):1905–1914, 2010.

[216] A. Guida, A. W. Nienow, and M. Barigou. Shannon entropy for local and global description of mixing by lagrangian particle tracking. *Chemical Engineering Science*, 65(10):2865–2883, 2010.

[217] M. Van de Velden, J. Baeyens, J.P.K. Seville, and X. Fan. The solids flow in the riser of a circulating fluidised bed (cfb) viewed by positron emission particle tracking (pept). *Powder Technology*, 183(2):290 – 296, 2008.

[218] F. Depypere, J.G. Pieters, and K. Dewettinck. Pept visualisation of particle motion in a tapered fluidised bed coater. *Journal of Food Engineering*, 93(3): 324 – 336, 2009.

[219] J. A. Laverman, X. Fan, A. Ingram, M. van Sint Annaland, D. J. Parker, J. P. K. Seville, and J. A. M. Kuipers. Experimental study on the influence of bed material on the scaling of solids circulation patterns in 3d bubbling gas–solid fluidized beds of glass and polyethylene using positron emission particle tracking. *Powder Technology*, 224(0):297–305, 2012.

[220] T. Hensler, M. Tupy, T. Strer, T. Pöschel, and K. E. Wirth. Positron emission particle tracking in fluidized beds with secondary gas injection. *Powder Technology*, 279:113 – 122, 2015.

[221] C. T. Jayasundara, R. Y. Yang, B. Y. Guo, A. B. Yu, I. Govender, A. Mainza, A. van der Westhuizen, and J. Rubenstein. Cfd–dem modelling of particle flow in isamills – comparison between simulations and pept measurements. *Minerals Engineering*, 24(3–4):181–187, 2011.

[222] L. S. Bbosa, I. Govender, A. N. Mainza, and M. S. Powell. Power draw estimations in experimental tumbling mills using pept. *Minerals Engineering*, 24 (3–4):319 – 324, 2011. Special issue: Comminution.

[223] A.P. van der Westhuizen, I. Govender, A.N. Mainza, and J. Rubenstein. Tracking the motion of media particles inside an isamill™ using pept. *Minerals Engineering*, 24(3–4):195 – 204, 2011. Special issue: Comminution.

[224] T. S. Volkwyn, A. Buffler, I. Govender, J. P. Franzidis, A. J. Morrison, A. Odo, N. P. van der Meulen, and C. Vermeulen. Studies of the effect of tracer activity on time-averaged positron emission particle tracking measurements on tumbling mills at pept cape town. *Minerals Engineering*, 24(3–4):261–266, 2011.

[225] I. Govender, P. W. Cleary, and A. N. Mainza. Comparisons of pept derived charge features in wet milling environments with a friction-adjusted dem model. *Chemical Engineering Science*, 97(0):162–175, 2013.

[226] A. J. Morrison, I. Govender, A. N. Mainza, and D. J. Parker. The shape and behaviour of a granular bed in a rotating drum using eulerian flow fields obtained from pept. *Chemical Engineering Science*, 152:186 – 198, 2016.

[227] K. E. Waters, N. A. Rowson, X. Fan, and J. J. Cilliers. Following the path of hydrophobic and hydrophilic particles in a denver cell using positron emission particle tracking. *Asia-Pacific Journal of Chemical Engineering*, 4(2):218–225, 2009.

[228] K. E. Waters, N. A. Rowson, X. Fan, D. J. Parker, and J. J. Cilliers. Positron emission particle tracking as a method to map the movement of particles in the pulp and froth phases. *Minerals Engineering*, 21(12–14):877–882, 2008.

[229] K. E. Cole, K. E. Waters, X. Fan, S. J. Neethling, and J. J. Cilliers. Combining positron emission particle tracking and image analysis to interpret particle motion in froths. *Minerals Engineering*, 23(11–13):1036–1044, 2010.

[230] K. Cole, P. R. Brito-Parada, A. Morrison, I. Govender, A. Buffler, K. Hadler, and J. J. Cilliers. Using positron emission tomography (pet) to determine liquid content in overflowing foam. *Chemical Engineering Research and Design*, 94: 721–725, 2015.

[231] Y. F. Chang, C. G. Ilea, Ø L. Aasen, and A. C. Hoffmann. Particle flow in a hydrocyclone investigated by positron emission particle tracking. *Chemical Engineering Science*, 66(18):4203–4211, 2011.

[232] J. R. Radman, R. Langlois, T. W. Leadbeater, J. A. Finch, N. Rowson, and K. E. Waters. Particle flow visualization in quartz slurry inside a hydrocyclone using the positron emission particle tracking technique. *Minerals Engineering*, 62:142 – 145, 2014. SI: Physical Separation.

[233] X. Fan, D. J. Parker, and M. D. Smith. Labelling a single particle for positron emission particle tracking using direct activation and ion-exchange techniques. *Nuclear Instruments and Methods in Physics Research Section A: Accelerators, Spectrometers, Detectors and Associated Equipment*, 562(1):345–350, 2006.

[234] X. Fan, D. J. Parker, and M. D. Smith. Enhancing 18f uptake in a single particle for positron emission particle tracking through modification of solid surface chemistry. *Nuclear Instruments and Methods in Physics Research Section A: Accelerators, Spectrometers, Detectors and Associated Equipment*, 558(2):542–546, 2006.

[235] A. Buffler, I. Govender, J. J. Cilliers, D. J. Parker, J. P. Franzidis, A. Mainza, R.T. Newman, M. Powell, and A. van der Westhuizen. Pept cape town: a new positron emission particle tracking facility at ithemba labs, 2010.

[236] D. J. Parker and X. Fan. Positron emission particle tracking—application and labelling techniques. *Particuology*, 6(1):16–23, 2008.

[237] D. J. Parker, R. N. Forster, P. Fowles, and P. S. Takhar. Positron emission particle tracking using the new birmingham positron camera. *Nuclear Instruments and Methods in Physics Research Section A: Accelerators, Spectrometers, Detectors and Associated Equipment*, 477(1–3):540–545, 2002.

[238] T. W. Leadbeater and D. J. Parker. A modular positron camera for the study of industrial processes. *Nuclear Instruments and Methods in Physics Research Section A: Accelerators, Spectrometers, Detectors and Associated Equipment*, 652(1):646–649, 2011.

[239] D. J. Parker, T. W. Leadbeater, X. Fan, M. N. Hausard, A. Ingram, and Z. Yang. Positron emission particle tracking using a modular positron camera.

Nuclear Instruments and Methods in Physics Research Section A: Accelerators, Spectrometers, Detectors and Associated Equipment, 604(1–2):339–342, 2009.

[240] T.W. Leadbeater and D. J. Parker. Current trends in positron emission particle tracking. In *7th World Congress on Industrial Process Tomography*. Elsevier Ltd., 2013.

[241] K. E. Cole, K. E. Waters, D. J. Parker, S. J. Neethling, and J. J. Cilliers. Pept combined with high speed digital imaging for particle tracking in dynamic foams. *Chemical Engineering Science*, 65(5):1887–1890, 2010.

[242] R. L. Stewart, J. Bridgwater, and D. J. Parker. Granular flow over a flat-bladed stirrer. *Chemical Engineering Science*, 56(14):4257–4271, 2001.

[243] E. Onate and R. Owen, editors. *Particle Based Methods Fundamentals and Applications*. Computational Methods in Applied Sciences. springer Netherlands, 1 edition, 2011.

[244] D. Boucher, J. Sovechles, A. P. Sasmito, and K. E. Waters. A eulerian-dense discrete phase model (ddpm) for simulation of a 8.4 percent solids mass of iron ore particles (500 micrometers, hematite and quartz) in a spiral concentrator - a preliminary study. In *Proceedings of MEI Computational Modelling '15*, pages 1–13. Mineral Enginering International, June 2015.

[245] X. Chen and J. Wang. A comparison of two-fluid model, dense discrete particle model and cfd-dem method for modeling impinging gas–solid flows. *Powder Technology*, 254(0):94–102, 2014.

[246] Z. Y. Zhou, S. B. Kuang, K. W. Chu, and A. B. Yu. Discrete particle simulation of particle-fluid flow: model formulations and their applicability. *J. Fluid Mech.*, 661:482–510, 2010.

[247] D. Hryb, M. Cardozo, S. Ferro, and M. Goldschmit. Particle transport in turbulent flow using both lagrangian and eulerian formulations. *International Communications in Heat and Mass Transfer*, 36(5):451–457, 2009.

[248] S. Elghobashi. On predicting particle-laden turbulents flows. *Applied Scientific Research*, 52:309–329, 1994.

[249] X. Zhang and G. Ahmadi. Eulerian–lagrangian simulations of liquid–gas–solid flows in three-phase slurry reactors. *Chemical Engineering Science*, 60(18): 5089–5104, 2005.

[250] L. Schiller and Z. Naumann. *Z. Ver. Deutsch. Ing.*, 77(318), 1935.

[251] M. Syamlal, W. Rogers, and T. J. O'Brien. *Computer simulation of bubbles in a fluidized bed*. 1989.

[252] A. Haider and O. Levenspiel. Drag coefficient and terminal velocity of spherical and nonspherical particles. *Powder Technology*, 58(1):63–70, 1989.

[253] P. A. Cundall and O. D. L. Strack. A discrete numerical model for granular assemblies. *Géotechnique*, 29(1):47–65, 1979.

Appendices

Appendix A

Preliminary numerical simulation

This appendix presents a preliminary simulation of particle and fluid flow in the spiral concentrator. The material presented here formed a paper presented at the *Mineral Engineering International - Computational Modelling Conference* held in Falmouth, UK in 2015 [244].

A.1 Information

Title: A Eulerian-dense discrete phase model (DDPM) for simulation of a 8.4 % solids mass of iron ore particles (500 µm, hematite and quartz) in a spiral concentrator - A preliminary study

Authors and affiliations: D. Boucher[a], J. Sovechles[a], A. Sasmito[a], K. Waters[a]

[a]Department of Mining and Materials Engineering, McGill University, 3610 University Street, Montreal, Quebec, H3A 0C5, Canada

A.1.1 Highlights

1. Eulerian fluid description and Lagrangian particle tracking are coupled together.

2. Discrete element method was used in the Lagrangian particle tracking.
3. Particle content in the spiral slurry flow was 8.4 % by mass of hematite and quartz.
4. Water flow velocity and patterns are similar to experimental values.
5. Momentum exchange between phase requires further development.

A.1.2 Abstract

A multi-fluid Eulerian model combined with a dense discrete phase model (DDPM) was used to simulate water and iron ore particles (hematite and quartz) flowing in a spiral concentrator. The particles' diameter was set to 500 µm and the slurry mass solid concentration at 8.4 %. The model solves for sets of conservation equations of mass and momentum for each continuous phase (air, water) in the Eulerian domain, coupled with a source term in the momentum equation to track the solid particle forces calculated in the Lagrangian domain by the discrete element method. This technique highlights the potential to simulate high particle concentrations. Flow behaviour, particle velocities and particles migration are discussed. This research demonstrates the potential of the Eulerian-DDPM modelling approach for the simulation of spiral concentrators, and other density-based concentrators.

A.1.3 Keywords

Computational fluid dynamics; Dense discrete particle model; Gravity concentration; Spiral concentrators.

A.2 Introduction

The spiral concentrator is a gravity concentration device used to separate minerals of different densities. This separator is important in the iron ore industry, considering the large quantity of ore treated annually. For some operations, yearly tonnage can range up to tens of millions of tons. These ores are mostly composed of quartz (specific gravity of 2.65) and iron bearing minerals, such as hematite and magnetite (specific gravity of 5.26 and 5.18 respectively). The difference in densities of the valuable and gangue minerals make these types of ore good candidates for gravity separation. The interest in the use of the spiral concentrator to achieve separation relies on the simplicity and low cost of a unit per throughput mass, which ranges from 4 to 8 tons per hour per spiral start [119, 124].

Spiral concentrators are composed of a rubber-lined trough forming a helix around a central post, as shown in Figure A.1. The ground ore (75 to 3000 μm) is mixed with water to form a slurry (15 to 45 % solids by mass) which is fed at the top of the helix [17]. The slurry forms a thin film on the trough as it flows down. The top layer of the film is under the influence of a lower shear (air-slurry interface) than the lower layer of the film (slurry-trough interface). This low shear coupled with the ever changing direction of the flow caused by the helical trajectory makes the top layer of the film divert towards the outside radius of the trough. An accumulation of fluid at the trough's outer, vertical, edge creates a higher pressure region near the lower slurry-trough interface causing the lower layer of the film to move radially inward [81, 161]. This pattern, present in the primary downward circulation, will preferentially bring dense particles inwards, as settling will cause them to be closer to the slurry-trough interface. In the case of the low density particles settling at a slower rate, they will be affected by the top layer of the film to a greater extent, thus moving outwards. The trough geometry (profile, pitch and diameter) and operating parameters (feed rate, slurry solid content and particle size) are of importance in the separation as they enable this specific flow pattern to occur.

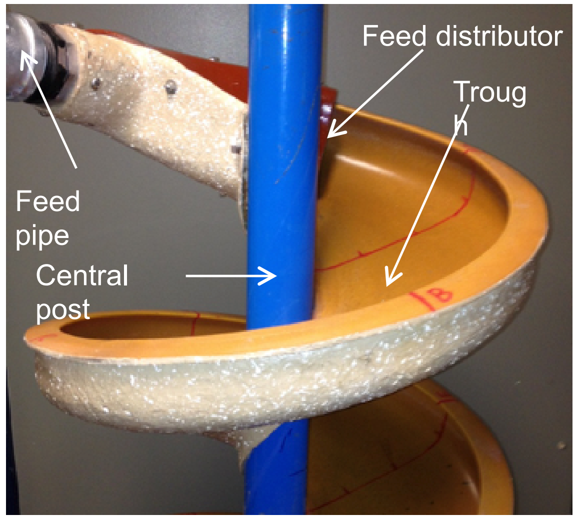

Figure A.1 – General view of the first turn of a spiral concentrator (Wallaby trough from Mineral Technologies).

When the dense particles are found at the inner radius, a cutter is positioned to divert them into a recovery channel, or into the central hollow post holding the trough. The lighter particle stream is then discarded to the tailings or to retreatment. Reported main flow velocities range from 0.4 to 2.1 m/s at the inner and outer radius respectively [157, 162]. Flow velocities are dependent upon operating and trough parameters and require careful testing to optimise process conditions for specific ore and spiral designs. Currently, most spiral development is carried out by laboratory and pilot scale testing [119, 152]. Having fundamental simulation techniques using geometrical and feed properties is of interest to foster advances in the design and operation of spiral concentrators. The main objective is to predict the macroscopic interactions which occur in the mixture of liquid (water), solids (ore particles) and gas (air) based on fluid mechanics and particle motion. This paper describes how a new computational fluid dynamic (CFD) approach, a Eulerian-dense discrete phase model, is applied to the simulation of particle-fluid flow on a spiral trough.

A.3 CFD model of the spiral

A.3.1 Available models

Preliminary CFD models of the spiral were aimed at the prediction of the liquid flow in a helical channel (with a rectangular cross section) without including any particles [9, 192]. These models were able to show and quantify the secondary circulation present in the primary downward flow. Since then, a few researchers have provided computational models which include particulate flow.

The volume of fluid (VOF) method has been used in a CFD model by Matthews *et al.* to predict free surface, flow depth and mainstream velocity for water flow [195]. In this model, 100 spherical particles were simulated by a Lagrangian method and provided similar migration behaviour to those obtained experimentally [162] considering their size and densities.

A combination of CFD and discrete element method (DEM) with Matthews *et al.*'s model for the water velocity profile [195] was used to create a one way coupled (particles affected by fluid drag) model with 12,000 spherical particles of two different densities [203]. This model predicted particle separation and a concentrate grade within 11 % of experimental results from literature.

These models are only accurate below a solids concentration of approximately 10 % by volume. This limitation is due to the fact that the particle-particle interactions and the effect of the particle volume fraction on the continuous (fluid) phase are considered negligible and, as such, are not accounted for. For a high particle content, the effect of the particles on the fluid should be taken into consideration. This is a limitation for the simulation of real spiral operations.

To overcome this limitation, Matthews *et al.* presented a two-fluids (Eulerian) model with approximately 0.3 % solids by mass [197]. A similar model by Doheim *et al.* had a content of up to 3 % solids by mass [198]. These simulations first determined the free surface of water flowing on the trough by the VOF method. This free surface was then fixed as a domain boundary for the computation of the particle-fluid flow using the two-fluids model. A drawback of this technique is the description of the free surface as it is normally influenced by the slurry viscosity which is unaccounted for when retrieving the water only free surface. These two models presented realistic particle behaviour (radial mass distribution) for small particles (which closely follow water flow), while larger particles were highly affected by the description of the contact with the trough surface and gravity.

The extent by which a particle will follow the flow of a moving fluid is represented by the Stokes number. A Stokes number greater than one means there is slip between particles and fluid and that it will have a different trajectory. For the spiral slurry flow, the particle's Stokes number (Eq. A.1) ranged from around zero to 10 for hematite particles of 10 to 1500 µm in diameter (d_p) respectively. This is for a flow velocity (u_0) of 2 m/s using the trough outer radius (166 mm) as the characteristic length (l_0). The particle density (ρ_p) is 5260 kg/m^3 for hematite and water viscosity (μ_l) is 0.001 Pa s. Considering these Stokes number values, the particles trajectories are then expected to be different of the flow field, at least for the larger particles. Therefore, the particles' trajectories should be described in a realistic model.

$$St = \frac{\rho_p d_p^2 u_0}{18 \mu_l l_0} \tag{A.1}$$

A.3.2 High particle content

Typically, for spirals processing iron ore, the feed slurry is approximately 35 % solids by mass (13 % solids by volume). However, during operation, most of the water from the mixture will report outwards creating a dilute slurry with as low as 10 % solids by mass (3 % solids by volume) at the outer section of the trough. Conversely, a dense slurry containing up to 70 % solids by mass (39 % solids by volume) will be found close to the central post [156]. The spiral case should then be considered as a dense particle-fluid flow where particle motion is controlled by particle-particle and particle-trough collisions in addition to the drag force created by the water. Furthermore, considering this high solids volume content, it is thought that the water motion close to the central post will be affected by the particles' motion. It is of interest to model the free surface and the liquid spread across the trough in conjunction with the particles' motion. In this paper, the set-up will include two fluid phases (water and air) and two particle phases (hematite and quartz).

Two approaches to include particles in a CFD model are commonly used: the Lagrangian; and the Eulerian approaches [245, 246]. The Lagrangian approach treats the solids as they are, many discrete particles moving inside the flow. The coupling between the liquid and solid particles is completed by the addition of source terms (representing fluid drag, particle-geometry contact forces, *etc.*) in the equations of each cell where particles are present [9]. This approach retrieves each particle's speed and trajectory using Newton's equation of motion [247]. This information is of prime importance in the case of a spiral separator, as the goal is to produce different trajectories for the gangue and valuable particles, such that they can be separated. This approach can be computationally intensive considering the amount of particles and information for each one. This is a drawback when looking at flow fields with a high particle content, local solids concentration or mean particle velocities.

The Eulerian approach can easily provide local solids concentration and mean particle velocities as it simulates the many particles as a continuum interpenetrating the other phases in the model [246]. The simulation is then one of many fluids (phases) of which one or more represents the particles, with each phase having its own governing equations and rheological properties. The coupling between the phases takes place as source terms in the governing equations of the interacting phases. The extent of this coupling is dependent on the amount of particles [248]. For high particle concentrations, as found in the spiral, a multi-way coupling is required; this means that particle phases and liquid phase will both have source terms in their momentum equations [9]. The Eulerian approach can provide this multi-way coupling and it is generally better suited for high solid concentrations. However, some of the granular phase rheological properties are difficult to obtain as they are difficult to measure experimentally.

A.3.3 Mixed approach

To resolve the dense particle fluid flow of the spiral, the use of a multi-fluid (Eulerian) model coupled with a dense discrete phase model (DDPM) was investigated. In this arrangement, each of the fluid phases (water, air) and particulate phases (hematite, quartz) are described as Eulerian phases. This treatment enables a greater particle volume content while the effect of the non negligible volume fraction of solids is accounted for [245]. Additional to the Eulerian phase description, a Lagrangian tracking is performed on the solid particles and enable the addition of source terms in the equations of each phases [249]. The value of those sources terms are determined by the DDPM model which uses the discrete element method (DEM) to balance the forces and contact acting on the particles. Those forces and their balanced reaction from the fluid are thus included in the multiphase Eulerian momentum equations solution.

A.3.4 Governing equations and coupling

All phases (water, air, hematite, and quartz) have independent mass and momentum conservation equations (Eq. A.2 and A.3). There is no mass transfer between phases as the ore is inert and the ambient temperature is constant. The model solves the mass and momentum conservation equations only for the continuous phases (water and air). The particle velocity field and amount of particles in the cell for each discrete phases (hematite and quartz) is taken from the Lagrangian tracking solution.

$$\frac{\partial}{\partial t}(\epsilon_i \rho_i) + \nabla \cdot (\epsilon_i \rho_i \boldsymbol{u}_i) = 0 \tag{A.2}$$

$$\frac{\partial}{\partial t}(\epsilon_i \rho_i \boldsymbol{u}_i) + \nabla(\epsilon_i \rho_i \boldsymbol{u}_i \boldsymbol{u}_i) = -\epsilon_i \nabla p_i + \nabla \boldsymbol{\tau}_i + \epsilon_i \rho_i \boldsymbol{g} + \sum_{j=1}^{n} \Big(\boldsymbol{K}_{ji}(\boldsymbol{u}_j - \boldsymbol{u}_i)\Big) + S_{DDPM} \tag{A.3}$$

In Eq. A.3, ϵ_i represents the volume fraction, ρ_i is the density and $\boldsymbol{u}_i$ is the velocity vector all of phase i. $\boldsymbol{\tau}_i$ is the stress-strain tensor described by Eq. A.4 for a fluid phase. The pressure is p_i and $\boldsymbol{g}$ is the gravitational acceleration. $\boldsymbol{K}_{ij}$ is the interphase momentum exchange coefficient as defined by Eq. A.5 for fluid-fluid exchange (phase i and j) and Eq. A.6 for fluid-solid exchange (phase f and s). S_{DDPM} is the source term associated with the forces retrieved by the dense discrete phase model.

$$\boldsymbol{\tau}_f = \epsilon_f \mu_f \left(\nabla \boldsymbol{u}_f + \nabla \boldsymbol{u}_f^T\right) - \epsilon_f \frac{2}{3} \mu_f \nabla \boldsymbol{u}_f \boldsymbol{I} \tag{A.4}$$

$$\boldsymbol{K}_{ji} = \frac{\epsilon_j \epsilon_i \rho_j f_i}{T_i} \tag{A.5}$$

$$\boldsymbol{K}_{sf} = \frac{\epsilon_s \rho_s f_f}{T_s} \tag{A.6}$$

In Eq. A.5 and A.6, T is the fluid or solid particle relaxation time and f_i are described by Schiller *et al.* [250] and Syamlal *et al.* [251] respectively.

The Lagrangian tracking uses Newton's second law of motion as the particle force summation (Eq. A.7) to determine each particle displacement in the domain over the particle motion time step.

$$m_p \frac{d\boldsymbol{u}_p}{dt} = \boldsymbol{F}_g + \boldsymbol{F}_D + \boldsymbol{F}_{VM} + \boldsymbol{F}_C + \boldsymbol{F}_P \tag{A.7}$$

In Eq. A.7, m_p is the discrete particle's mass and $\boldsymbol{u}_p$ is its velocity. $\boldsymbol{F}_g$ is the gravity related force, $\boldsymbol{F}_D$ is the drag force, $\boldsymbol{F}_{VM}$ is a virtual mass force, $\boldsymbol{F}_C$ is the forces related to the particle contact with other particles and the geometry and $\boldsymbol{F}_P$ is the force related to the pressure.

The gravity related force $\boldsymbol{F}_g$ is given by Eq. A.8 which includes the effect of buoyancy.

$$\boldsymbol{F}_g = \frac{\pi d_p^3}{6}(\rho_f - \rho_p)\boldsymbol{g} \tag{A.8}$$

The drag force $\boldsymbol{F}_D$ is calculated using Eq. A.9, which represents the drag for a non-spherical particle with a drag coefficient C_D given by Eq. A.10. In this equation, the coefficients b_{1-4} are a function of the shape factor (chosen to be 0.5) representing the ratio of the surfaces of a sphere to a particle of non-spherical shape with the same mass [252].

$$\boldsymbol{F}_D = \frac{3\mu_f C_D Re}{4\rho_p d_p^2}(\boldsymbol{u}_f - \boldsymbol{u}_p) \tag{A.9}$$

$$C_D = \frac{24}{Re_{sph}}\left(1 + b_1 Re_{sph}^{b_2}\right) + \frac{b_3 Re_{sph}}{b_4 + Re_{sph}} \tag{A.10}$$

The virtual mass force $\boldsymbol{F}_{VM}$ represents the effect of the inertia from a fluid phase when the particle is moving and is provided by Eq. A.11.

$$\boldsymbol{F}_{VM} = \frac{1}{2}\frac{\rho_f}{\rho_s}\frac{d}{dt}(\boldsymbol{u}_f - \boldsymbol{u}_p) \tag{A.11}$$

$\boldsymbol{F}_C$ is the force resultant of particle-particle and particle-geometry contact (Eq. A.12). This force is based on particle deformation as by the soft sphere overlap approach of the discrete element method (DEM) [253]. The spring-dashpot force (Eq. A.13) and the friction force (Eq. A.14) are the two contact forces accounted for. In Eq. A.13, k is the spring constant, δ is the particles overlap, $\boldsymbol{v}_{12}$ is the velocity difference between colliding particle 1 and 2 and $\boldsymbol{e}_{12}$ is a unit vector in the direction between colliding particle 1 and 2. In Eq. A.14, μ_F is the friction coefficient and $\boldsymbol{F}_N$ is the normal force based on $\boldsymbol{F}_{SD}$.

$$\boldsymbol{F}_C = \boldsymbol{F}_{SD} + \boldsymbol{F}_F \tag{A.12}$$

$$\boldsymbol{F}_{SD} = \big(k\delta + \gamma(\boldsymbol{v}_{12}\boldsymbol{e}_{12})\big)\boldsymbol{e}_{12} \tag{A.13}$$

$$\boldsymbol{F}_F = \mu_F \boldsymbol{F}_N \tag{A.14}$$

$\boldsymbol{F}_P$ is given by Eq. A.15.

$$\boldsymbol{F}_P = -\frac{1}{\rho_p}(p_f - p_p) \tag{A.15}$$

A.3.5 Turbulence model

The flow regime is mostly laminar close to the centre post (Reynolds number for open channel flow: Re<400) and transforms into a turbulent regime as velocity increases toward the edge of the trough (Re ≈30000). In the model here, the RNG $k-\epsilon$ turbulence description is used based on the work conducted by Doheim *et al.* [198].

A.4 Simulation set-up

This section describe the simulation set-up used. The simulation is carried on with ANSYS FLUENT V14.0 (2014).

A.4.1 Geometry and meshing

The simulation domain used represents the first 1.125 turn of a Walkabout Wallaby Trough spiral manufactured by Mineral Technologies. The volume domain is represented by a layer of thickness of 15 mm over the trough surface, this geometry was created using SolidWorks (2015). A cut view of the mesh used is shown in Figure A.2. It is composed mostly of elongated quadrilateral prisms with a maximum end face edge of 1.5 mm and Table A.1 presents the key values of this mesh created with ANSYS Meshing.

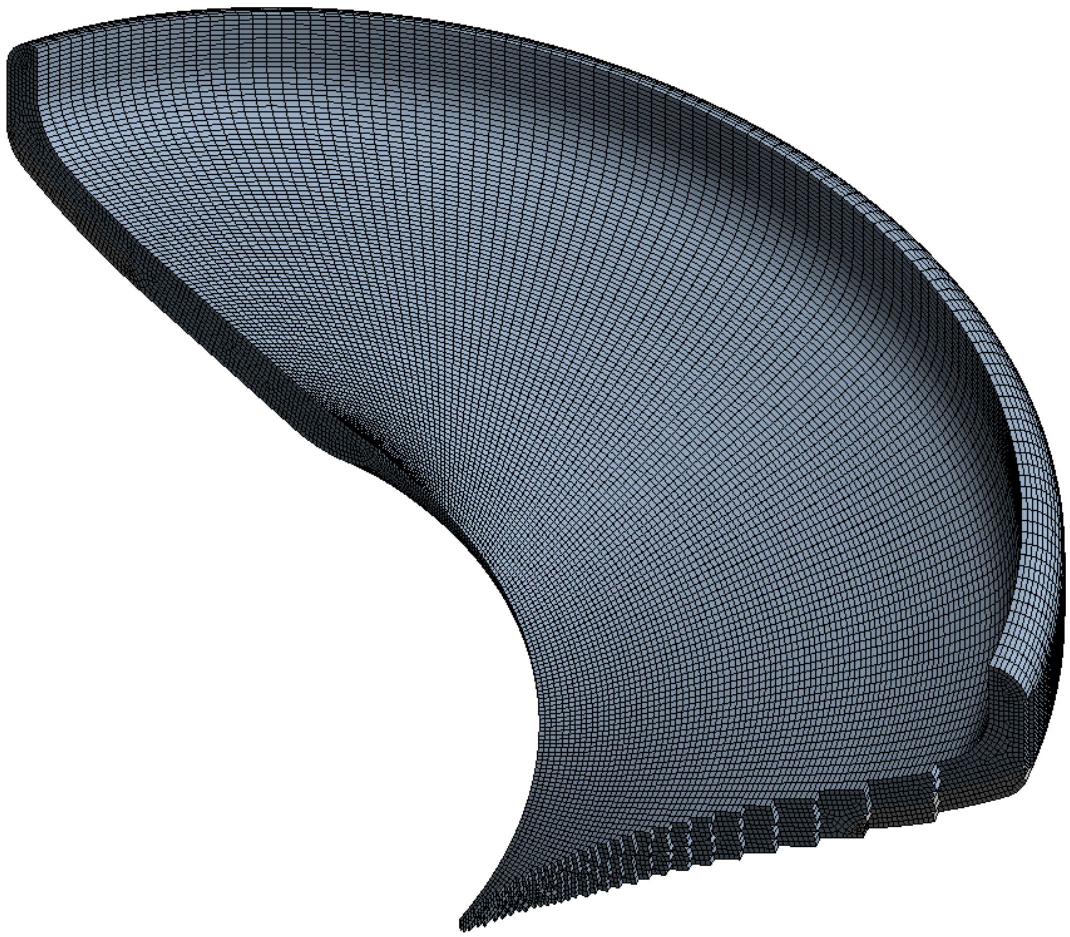

Figure A.2 – Cut view of the mesh used for the simulation.

Table A.1 – Mesh properties

Elements type	Hexahedral
Number of elements	286 470
Element minimum volume (mm^3)	1.1
Element maximum volume (mm^3)	13.2

The average mesh element size is smaller (≈30 %) than other models found in literature [9, 195, 198]. In the present case, a mesh with larger elements created problems with the free surface.

A.4.2 Conditions and materials properties

Table A.2, Table A.3 and Table A.4 details the properties of the materials used. Some are based on initial assumptions.

Table A.2 – Properties of the solid materials used.

Parameter	Quartz	Hematite	Rubber
Density kg/m^3	2650	5260	860
Coefficient of restitution	0.5	0.5	0.5

Table A.3 – Properties of the fluid materials used.

Parameter	Water	Air
Density kg/m^3	998.2	1.225
Viscosity kg/m s	0.001003	0.00001789

Table A.4 – DEM contact model parameters for the solid materials.

Parameter	Quartz	Hematite	Rubber
Spring constant k	0.0001	0.0001	0.0001
Damping coefficient γ	0.8	0.8	0.8
Friction coefficient μ_{stick}	0.5	0.5	0.5

A feed surface was defined for the addition of water and particles. This surface had a velocity inlet boundary condition. The water volume fraction at this boundary was set to unity, with a velocity of 0.6 m/s (derived from a one ton per hour feed rate). The turbulence specification of this inlet was defined by a hydraulic diameter (0.075 m) and a turbulence intensity (5 %). The trough surface acts as a wall boundary condition with a roughness constant of 0.5. The material of this surface was defined as rubber for the purpose of the DEM collision calculations. The top of the domain was also defined to be a wall, and considering the thickness 15 mm of the domain, no contact with water was expected by this surface as an air layer was to be superposed on the water-particles mixture. Surface tension coefficient between air and water is 0.0728 N/m. The outlet of the spiral was an atmospheric pressure outlet boundary condition. Backflow of air was allowed, and the turbulence defined with a hydraulic diameter (0.075 m) and a turbulence intensity (5 %).

The coefficient used in the RNG $k - \epsilon$ turbulence model are given in Table A.5.

Table A.5 – Turbulence model coefficients.

C_μ	0.0845
$C_{1\epsilon}$	1.42
$C_{2\epsilon}$	1.68
Prandtl Number	0.75

Spherical particles of hematite and quartz were added at the same surface as the water inlet boundary condition, with the domain initially filled with air. The time step for computing the fluid phase was 0.005 s and the particles' motion computed with a time step of 0.001 s. Table A.6 presents the under-relaxation factor used for the simulation.

Table A.6 – Under-relaxation factors

Factor	Value
Pressure	0.3
Density	1.0
Momentum	0.2
Volume fraction	0.2
Turbulent kinetic energy	0.4
Turbulent dissipation rate	0.4
Turbulent viscosity	1.0
Discrete phase source	1.0

The pressure velocity coupling scheme used is phase coupled SIMPLE. The spatial discretisation was performed by the QUICK method for the momentum, volume fraction, turbulent kinetic energy and dissipation rate. Residual values used to trigger convergence were all set at 0.0001. Additionally, the amount of fluid and solid present on the domain and the outlet velocity was monitored to ensure a steady state was attained.

A.5 Results and discussion

A.5.1 Simulated water pattern

The general slurry shape is presented in Figure A.3, where the colour indicates water velocity. The maximum velocity (1.81 m/s) is found at the end of the first turn close to the upper layer of the outer side of the slurry film. This maximum velocity is similar to values reported by Holtham *et al.* [157].

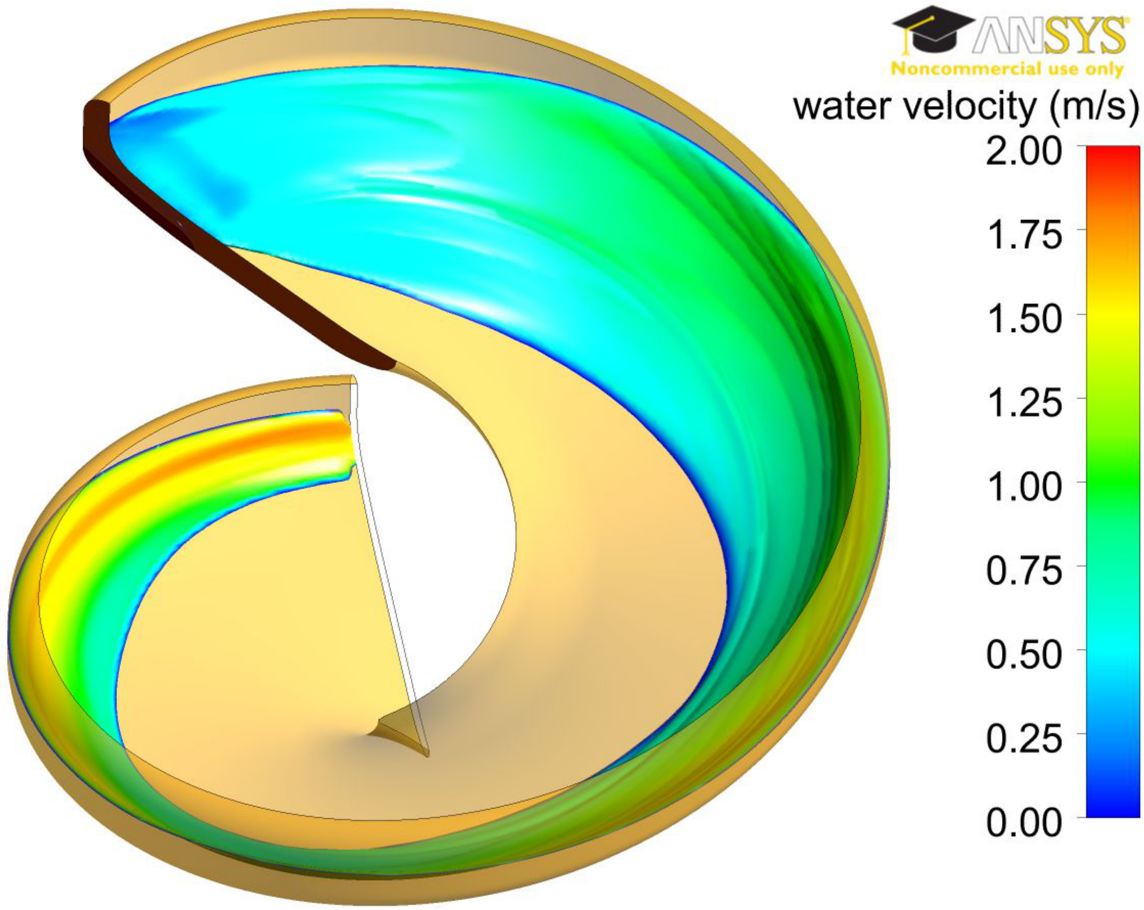

Figure A.3 – General shape of the water on the trough.

Figure A.4 and A.5 present the radial velocity contour magnitude for a cut view of the 0.5 and 0.75 turn points respectively. In both cases, the top layer of the slurry film is seen to be moving outwards as expected by literature [161]. More importantly, the velocity values are in the same range as those reported [157]. In the case of the 0.75 turn, the inward motion is much lower than in the case of the 0.5 turn. This is important to note as the free surface profile is also showing more slurry close to the vertical edge of the trough. The slurry is not in a complete circular motion, as it is found in the first turn of a real spiral. This behaviour seems to have an effect on the secondary circulation pattern. The free surface shown here is situated at a 0.05 volume fraction of water. The water air surface tension coefficient and the mesh size affects the accuracy of this free surface, and further testing is required to validate the surface profile obtained.

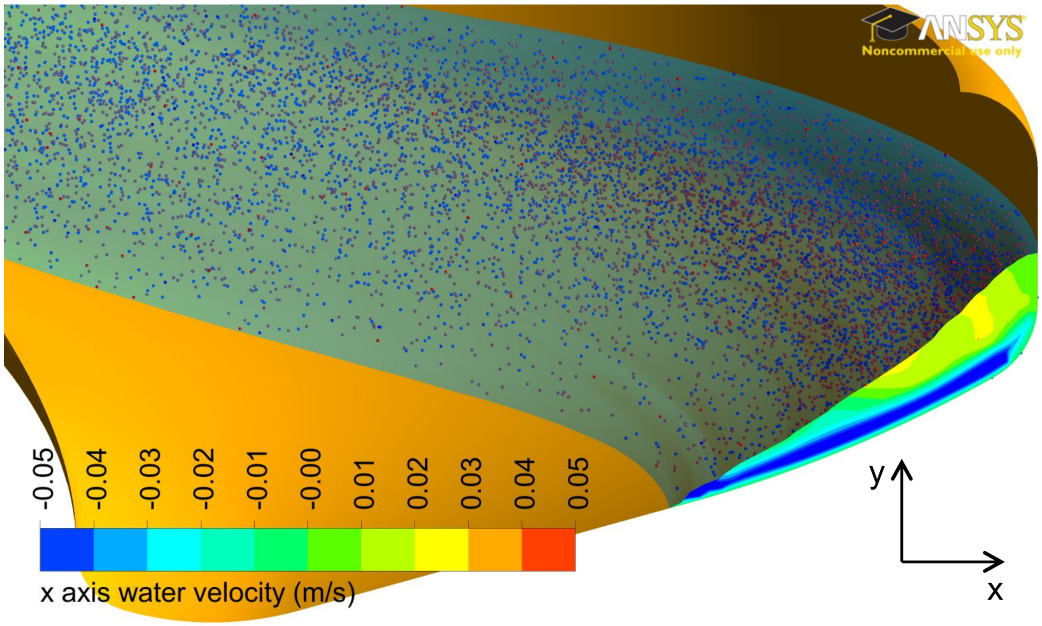

Figure A.4 – Secondary flow (here as x axis velocity) at 0.5 turn (particle content reduced by a factor of 10 for clarity, red dot is hematite, blue dot is quartz).

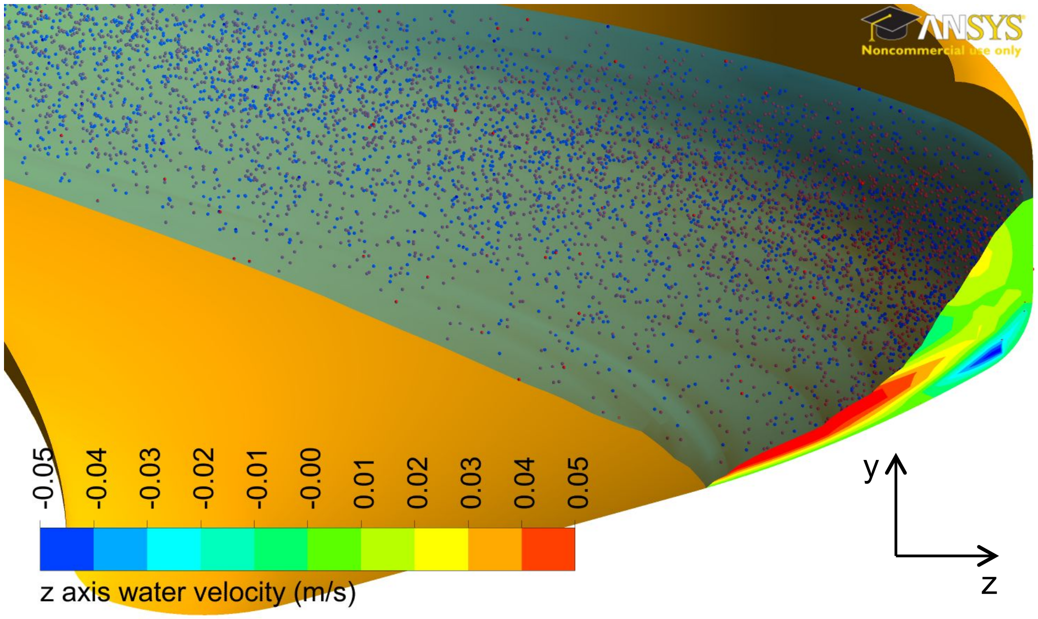

Figure A.5 – Secondary flow (here as z axis velocity) at 0.75 turn (particle content reduced by a factor of 10 for clarity, red dot is hematite, blue dot is quartz).

A.5.2 Simulated particles pattern

Once a steady trough loading state was reached (approximately one second of simulation), the amount of 500 µm particles was approximately 466 000, representing a solid mass of 0.121 kg. Considering the water loading of 1.322 kg, the solids content by mass was 8.4 %. The particles composition was of 50 % quartz and 50 % hematite by volume (similar amount of particle). Figure A.6 and Figure A.7, respectively, present the particles radial position and radial velocity. The data is compiled over height horizontal slice each representing 1/8 of a turn, with "Slice 1" being the top part of the computational domain (*i.e.* the slice where particles and water addition takes place).

Based on Figure 6, which shows the mean radial position for each slice, there is no clear separation of the hematite from the quartz particles. This is surprising even if the simulation represents the first turn of the spiral. The radial particle velocity shown in Figure 7 is in accordance with this as there is no clear difference between the hematite and quartz radial separation. This behaviour shows that the particles do not separate in different layers of the slurry film to being carried inwards or outwards. The high value of the drag caused by the shape factor of the particle is thought to be in cause here.

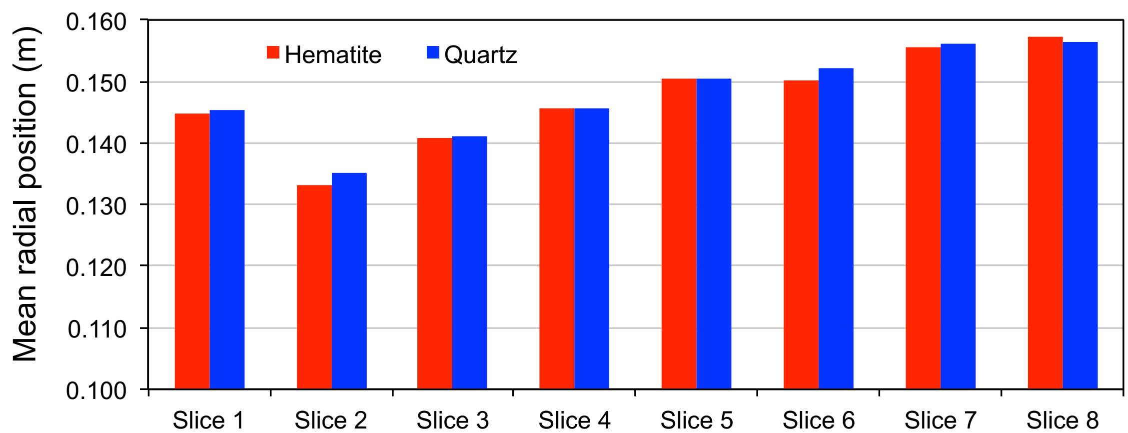

Figure A.6 – Simulated particle mean radial position.

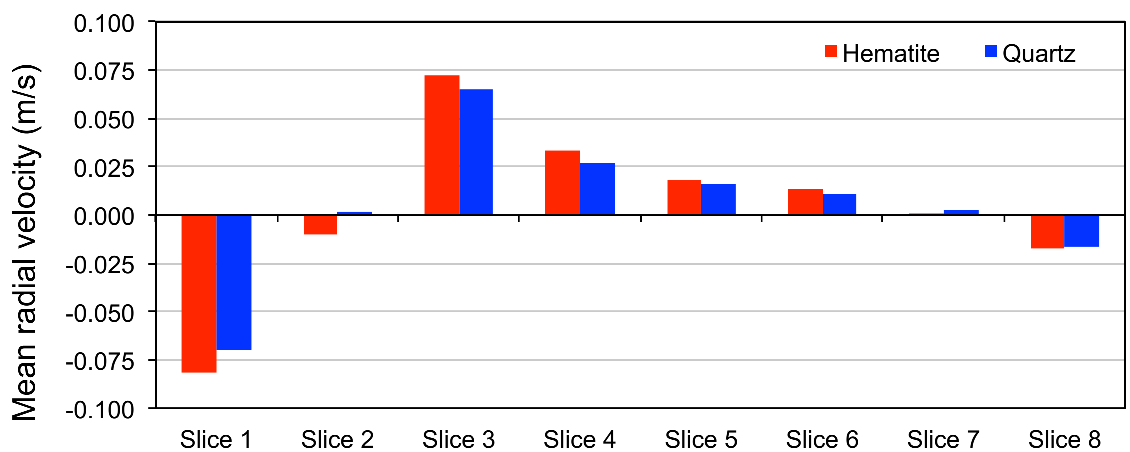

Figure A.7 – Simulated particle mean radial velocity.

A.6 Conclusions

A preliminary Eulerian dense discrete phase model of particle-fluid flow in the spiral separator has been presented. This model includes a larger mass solids concentration (8.4 %) than previous models. This is made possible by the accounting of each phases volume fraction in the Eulerian description while the particles trajectories are computed by a Lagrangian method. The solids comprised of 500 µm diameter particles representing a quartz and hematite mixed ore. The fluid velocity magnitude is of similar values than what is found within the literature on spiral concentrator. In the case of particle separation, the variations in the radial position of the two different density particles is not significant enough to conclude in separation. The particles simply follow the flow of water which gives an indication that a better interphase exchange relationship (between particle and water) should be developed. Additionally, the free surface definition will be improved, and once again the interphase exchange relationship (between air and water) requires further work.

A.7 Acknowledgements

The authors are grateful for the financial support of COREM and The Natural Sciences and Engineering Research Council of Canada (NSERC) through the Collaborative Research and Development Project Grant (CRDPG 437324-12). The McGill Engineering Doctoral Award (MEDA) from the Faculty of Engineering at McGill University is also duly acknowledged (funding for D. Boucher).

Appendix B

Particle tracking analysis code

MATLAB code

```
%Copyright Darryel Boucher, 2016

%INITIALIZATION
%----------------------------------------------------------%
clear all; clc; close all;

%Load location data set (file provided by TRACK.EXE)
%------------------------------------------%
[T, X, Y, Z, Error, Nbevent] = textread('
    S_06_AM_002_N050_L050_f040.a01','%f %f %f %f %f %f'
    ,2000000,'headerlines',16); %2 000 000 is max number of
    row to be read.
%T: Time (ms) X: X axis coordinate (mm) Y: Y axis coordinate
    (mm) Z: Z axis coordinate (mm)

```

```

%DATA PREPARATION
%------------------------------------------------------------%
Z=-Z;
T=T/1000; %From (ms) to (s).
id=find(T);

%Rotate locations to align x, y, z axis to geometry
thetaX=5.5/180*pi(); %Rotation angle on X axis (deg/180*pi()=
    rad)
thetaY=0/180*pi();
thetaZ=9.5/180*pi();

RX = [1,0,0;0,cos(thetaX),sin(thetaX);0,-sin(thetaX),cos(
    thetaX)]; % Rotation matrix on X
RY = [cos(thetaY),0,-sin(thetaY);0,1,0;sin(thetaY),0,cos(
    thetaY)];
RZ = [cos(thetaZ),sin(thetaZ),0;-sin(thetaZ),cos(thetaZ)
    ,0;0,0,1];

Locations=[X Y Z]; %Creation of a matrix to be rotated
Locations=Locations*RX; %Applying the rotation around X axis
Locations=Locations*RY;
Locations=Locations*RZ;

X=Locations (:,1); %Replacing with the new rotated
    coordinates
Y=Locations (:,2);
Z=Locations (:,3);

```

```
%Center view on geometry
 Xtranslation=12;% %Translation on X axis (mm)
 Ytranslation=-40;
 Ztranslation=-5;
X=X+Xtranslation;
Y=Y+Ytranslation;
Z=Z+Ztranslation;

%PASSES SPLIT
%------------------------------------------------------------%
maxlength=500000; %Max number of location in a pass
pcount=0; %initialise pass count

pTadd=zeros(maxlength,1); pTadd(:)=NaN; %Creating an array
    for the first passes with every array value to Not a
    Number marker
pTaddreset=pTadd; %Creating an array for the pass time
    reseted to 0 at the begining of the pass
pXadd=pTadd; %Array for the X value of each location of the
    pass
pYadd=pTadd;
pZadd=pTadd;
pidadd=pTadd;

aTi=0;
Treset=T(1); %used to make pass time starting at 0.
minlocpass=5000; %min number of location per pass

%Check all location to see in which pass it is
for i=1:length(T)-1
```

```
    if T(i+1)-T(i)<0.0017 %checking time interval between
       point i and i+1 and detecting end of pass if time too
       long
        aTi=aTi+1; %Counting the location rank in the pass
        pTadd(aTi)=T(i); %attributin the T value to the pass
        pTaddreset(aTi)=T(i)-Treset; %attributing the reseted
            time value to the pass
        pXadd(aTi)=X(i); %attributin the X value to the pass
        pYadd(aTi)=Y(i);
        pZadd(aTi)=Z(i);
        pidadd(aTi)=id(i);

    else %time between location is too long, means end of
       pass
        if pcount==0 %if it is the first pass
            if aTi>minlocpass %Check how many location in the
                pass
                pcount=pcount+1; %a new pass has been
                   completed
                pT=pTadd; %attributing the pass to the T
                   matrix of pass
                pTreset=pTaddreset;
                pX=pXadd;
                pY=pYadd;
                pZ=pZadd;
                pid=pidadd;
            else % do not keep the pass if not enough
               location
            end
            pTadd(:)=NaN; %Reseting the pass array
```

```
            pTaddreset=pTadd;
            pXadd=pTadd;
            pYadd=pTadd;
            pZadd=pTadd;
            pidadd=pTadd;

            aTi=0; %reseting the location rank in the pass
            Treset=T(i+1); %getting the time of the first
               location of the next pass as the reset time

        else %if not first pass
            if aTi>minlocpass %Check how many location in the
                pass
                pcount=pcount+1; %a new pass has been
                   completed

                pT=[pT pTadd]; %addng the pass to the T
                   matrix of passes
                pTreset=[pTreset pTaddreset];
                pX=[pX pXadd];
                pY=[pY pYadd];
                pZ=[pZ pZadd];
                pid=[pid pidadd];
            else % do not keep the one with not enough
               location
            end

            pTadd(:)=NaN; %Reseting the pass array
            pTaddreset=pTadd;
            pXadd=pTadd;
```

```
            pYadd=pTadd;
            pZadd=pTadd;
            pidadd=pTadd;

            aTi=0; %reseting the location rank in the pass
            Treset=T(i+1); %getting the time of the first
               location of the next pass as the reset time
        end
    end
end

% Write the last pass if it has enough locations
if aTi>minlocpass %Check how many location in the pass
    pcount=pcount+1; %a new pass has been completed

    pT=[pT pTadd]; %addng the pass to the T matrix of passes
    pTreset=[pTreset pTaddreset];
    pX=[pX pXadd];
    pY=[pY pYadd];
    pZ=[pZ pZadd];
    pid=[pid pidadd];
else % do not keep the one with not enough location
end

%Reconstruct the dataset with only the good pass
[m,n]=size(pT);

T2=[]; %T2 is used to store the data of kept passes
X2=[];
Y2=[];
```

```
Z2=[];
id2=[];

for i=1:n;
    T2=cat(1,T2,pT(:,i)); %concatenate all the passes T value
        into 1 array
    X2=cat(1,X2,pX(:,i));
    Y2=cat(1,Y2,pY(:,i));
    Z2=cat(1,Z2,pZ(:,i));
    id2=cat(1,id2,pid(:,i));
end

T2(isnan(T2))=[]; %remove the NaN from the array
X2(isnan(X2))=[];
Y2(isnan(Y2))=[];
Z2(isnan(Z2))=[];
id2(isnan(id2))=[];
%T2, X2, Y2, and Z2 are now arrays containing only good
   passes original locations (identified by indice 2).

%FIT AND INTERPOLATION PASS BY PASS AND VELOCITIES
   CALCULATIONS
%------------------------------------------------------------%
for f=1:n %for all the pass in pT, this has the effect of
   using only the good passes
    Inter=1; %Interval length for fitting (s)
    Overlap=0.05; %Interval overlap at both end of interval
    TStart=min(pT(:,f)); %Begining time of a pass
    TEnd=max(pT(:,f)); %End time of a pass
    WantedRate=100; %location rate wanted (Hz)
```

```
    InterFit=1/WantedRate; %interval time for fitted location
        (s)

    Tfit=(TStart:InterFit:TEnd)'; %Generating time data for
       generating fitted locations
    Tresetfit=Tfit-min(Tfit);
    nblocfit=length(Tfit);
    Xfit=NaN(nblocfit,1);
    Yfit=NaN(nblocfit,1);
    Zfit=NaN(nblocfit,1);
    XRes=NaN(length(pT(:,f)),1);
    YRes=NaN(length(pT(:,f)),1);
    ZRes=NaN(length(pT(:,f)),1);
    NRes=NaN(length(pT(:,f)),1);

    TinterS=TStart; %set first time interval start time
    TinterE=TinterS+Inter; %set first time interval end time

    while TinterS<TEnd %Not at the end of the data yet

        %Select data in time interval
        Tsel=T(T>TinterS & T<TinterE);
        Xsel=X(T>TinterS & T<TinterE);
        Ysel=Y(T>TinterS & T<TinterE);
        Zsel=Z(T>TinterS & T<TinterE);
        idsel=id(T>TinterS & T<TinterE);

        nblocint=length(Tsel); %number of location in the
           selected interval

```

```
        %Fit data in time interval
        L=10; %Number of polynomial piece
        K=4; %Order of the spline 4=cubic spline , 2=linear

        if length(Tsel)<=L
        else

            sp1X=spap2(L,K,Tsel,Xsel); %Least square spline
               approximation
            sp1Y=spap2(L,K,Tsel,Ysel);
            sp1Z=spap2(L,K,Tsel,Zsel);

            %extrapolate data with new time and rate
            idTfit=find(Tfit); %get id from makeup time
            idfit=idTfit(Tfit>=(TinterS+(Overlap*Inter)) &
               Tfit<(TinterE-(Overlap*Inter))); %select ID in
                the 0.25-0.75 of the interval
            Xfit(idfit)=fnval(sp1X,Tfit(idfit)); %Generating
               the fitted locations
            Yfit(idfit)=fnval(sp1Y,Tfit(idfit));
            Zfit(idfit)=fnval(sp1Z,Tfit(idfit));

            XRes(idsel)=fnval(sp1X,T(idsel))-X(idsel); %
               Calcul and store residual for each initial
               location point
            YRes(idsel)=fnval(sp1Y,T(idsel))-Y(idsel);
            ZRes(idsel)=fnval(sp1Z,T(idsel))-Z(idsel);

```

```
                % for i=1:length(idsel) %Find shortest distance between initial location and fit position
                % A=Xfit(Tfit>TinterS & Tfit<TinterE)-X(idsel(i));
                % B=Yfit(Tfit>TinterS & Tfit<TinterE)-Y(idsel(i));
                % C=Zfit(Tfit>TinterS & Tfit<TinterE)-Z(idsel(i));
                % distVect=sqrt((A).^2+(B).^2+(C).^2);
                % NRes(idsel(i))=min(distVect); %Store the shortest distance for each initial location
                % end

                clc;
                percent=max(Tsel)/max(T)*100

            end
            %Go to next time interval
            TinterS=TinterE-2*Overlap*Inter; %Overlap interval
            TinterE=TinterS+Inter;
        end

        idstart=find(Tfit(Tfit<=(TStart+Overlap*Inter)));
        Xfit(idstart)=Xfit(max(idstart)+1);
        Yfit(idstart)=Yfit(max(idstart)+1);
        Zfit(idstart)=Zfit(max(idstart)+1);

        Rfit=(Xfit.^2+Zfit.^2).^(1/2); %Radius around y axis

```

```
    Afit=Tfit; %Angle from first position on xz plan
    vect1=[0 0 1];
    vect2=[Xfit(1) 0 Zfit(1)];
    Afitprev=atan2(norm(cross(vect1,vect2)),dot(vect1,vect2))
        ;
    Afit(1)=Afitprev;

    for i=2:length(Tfit)
        vect1=[Xfit(i-1) 0 Zfit(i-1)];
        vect2=[Xfit(i) 0 Zfit(i)];
        Afit(i)=Afitprev+atan2(norm(cross(vect1,vect2)),dot(
            vect1,vect2));
        Afitprev=Afit(i);
    end


    vRfit=Tfit; %Radial velocity
    endi=0;
    starti=0;
    for i=1:length(Tfit)
        j=i;
        if i<6 %if you are at the begining of the pass, use
            the later points
            starti=1;
            i=i+6;
        end
        if i>=(length(Tfit)-6) %if you are at the end of the
            pass, use the previous pooints
            endi=1; i=i-6;
        end
```

```
        vRfit(j)=...
            0.10*((Rfit(i+5)-Rfit(i-0))/(Tfit(i+5)-Tfit(i-0))
               )+...
            0.15*((Rfit(i+4)-Rfit(i-1))/(Tfit(i+4)-Tfit(i-1))
               )+...
            0.25*((Rfit(i+3)-Rfit(i-2))/(Tfit(i+3)-Tfit(i-2))
               )+...
            0.25*((Rfit(i+2)-Rfit(i-3))/(Tfit(i+2)-Tfit(i-3))
               )+...
            0.15*((Rfit(i+1)-Rfit(i-4))/(Tfit(i+1)-Tfit(i-4))
               )+...
            0.10*((Rfit(i+0)-Rfit(i-5))/(Tfit(i+0)-Tfit(i-5))
               );
        if starti==1 %reset i to its original value
            i=i-6;
        end
        if endi==1 %reset i to its original value
            i=i+6;
        end
        starti=0;
        endi=0;
    end
    vRfit=vRfit/1000; %from mm/s to m/s

    aRfit=Tfit; %Radial acceleration
    endi=0;
    starti=0;
    for i=1:length(Tfit)
        j=i;
```

```
        if i<6 %if you are at the begining of the pass, use
            the later points
            starti=1; i=i+6;
        end
        if i>=(length(Tfit)-6) %if you are at the end of the
            pass, use the previous pooints
            endi=1; i=i-6;
        end
        aRfit(j)=...
            0.10*((vRfit(i+5)-vRfit(i-0))/(Tfit(i+5)-Tfit(i
                -0)))+...
            0.15*((vRfit(i+4)-vRfit(i-1))/(Tfit(i+4)-Tfit(i
                -1)))+...
            0.25*((vRfit(i+3)-vRfit(i-2))/(Tfit(i+3)-Tfit(i
                -2)))+...
            0.25*((vRfit(i+2)-vRfit(i-3))/(Tfit(i+2)-Tfit(i
                -3)))+...
            0.15*((vRfit(i+1)-vRfit(i-4))/(Tfit(i+1)-Tfit(i
                -4)))+...
            0.10*((vRfit(i+0)-vRfit(i-5))/(Tfit(i+0)-Tfit(i
                -5)));
        if starti==1 %reset i to its original value
            i=i-6;
        end
        if endi==1 %reset i to its original value
            i=i+6;
        end
        starti=0; endi=0;
    end
    aRfit=aRfit; %from m/s to m/s
```

```
    vAfit=Tfit; %Angular velocity
    endi=0;
    starti=0;
    for i=1:length(Tfit)
        j=i;
        if i<6 %if you are at the begining of the pass, use
            the later points
            starti=1; i=i+6;
        end
        if i>=(length(Tfit)-6) %if you are at the end of the
            pass, use the previous pooints
            endi=1; i=i-6;
        end
        vAfit(j)=...
            0.5*((Afit(i+1)-Afit(i-0))/(Tfit(i+1)-Tfit(i-0)))
                +...
            0.5*((Afit(i+0)-Afit(i-1))/(Tfit(i+0)-Tfit(i-1)))
                ;
        %           0.10*((Afit(i+5)-Afit(i-0))/(Tfit(i+5)-Tfit
            (i-0)))+...
        %           0.15*((Afit(i+4)-Afit(i-1))/(Tfit(i+4)-Tfit
            (i-1)))+...
        %           0.25*((Afit(i+3)-Afit(i-2))/(Tfit(i+3)-Tfit
            (i-2)))+...
        %           0.25*((Afit(i+2)-Afit(i-3))/(Tfit(i+2)-Tfit
            (i-3)))+...
        %           0.15*((Afit(i+1)-Afit(i-4))/(Tfit(i+1)-Tfit
            (i-4)))+...
```

```
        %           0.10*((Afit(i+0)-Afit(i-5))/(Tfit(i+0)-Tfit(i-5)));
        if starti==1 %reset i to its original value
            i=i-6;
        end
        if endi==1 %reset i to its original value
            i=i+6;
        end
        starti=0; endi=0;
    end

    aAfit=Tfit; %Angular acceleration
    endi=0;
    starti=0;
    for i=1:length(Tfit)
        j=i;
        if i<6 %if you are at the begining of the pass, use the later points
            starti=1; i=i+6;
        end
        if i>=(length(Tfit)-6) %if you are at the end of the pass, use the previous pooints
            endi=1; i=i-6;
        end
        aAfit(j)=...
            0.5*((vAfit(i+1)-vAfit(i-0))/(Tfit(i+1)-Tfit(i-0)))+...
            0.5*((vAfit(i+0)-vAfit(i-1))/(Tfit(i+0)-Tfit(i-1)));
```

```
        %           0.10*((vAfit(i+5)-vAfit(i-0))/(Tfit(i+5)-
            Tfit(i-0)))+...
        %           0.15*((vAfit(i+4)-vAfit(i-1))/(Tfit(i+4)-
            Tfit(i-1)))+...
        %           0.25*((vAfit(i+3)-vAfit(i-2))/(Tfit(i+3)-
            Tfit(i-2)))+...
        %           0.25*((vAfit(i+2)-vAfit(i-3))/(Tfit(i+2)-
            Tfit(i-3)))+...
        %           0.15*((vAfit(i+1)-vAfit(i-4))/(Tfit(i+1)-
            Tfit(i-4)))+...
        %           0.10*((vAfit(i+0)-vAfit(i-5))/(Tfit(i+0)-
            Tfit(i-5)));
        if starti==1 %reset i to its original value
            i=i-6;
        end
        if endi==1 %reset i to its original value
            i=i+6;
        end
        starti=0; endi=0;
    end


    vXfit=Tfit; %X velocity
    endi=0;
    starti=0;
    for i=1:length(Tfit)
        j=i;
        if i<6 %if you are at the begining of the pass, use
            the later points
            starti=1; i=i+6;
```

```
        end
        if i>=(length(Tfit)-6) %if you are at the end of the
           pass, use the previous pooints
            endi=1; i=i-6;
        end
        vXfit(j)=...
            0.10*((Xfit(i+5)-Xfit(i-0))/(Tfit(i+5)-Tfit(i-0))
               )+...
            0.15*((Xfit(i+4)-Xfit(i-1))/(Tfit(i+4)-Tfit(i-1))
               )+...
            0.25*((Xfit(i+3)-Xfit(i-2))/(Tfit(i+3)-Tfit(i-2))
               )+...
            0.25*((Xfit(i+2)-Xfit(i-3))/(Tfit(i+2)-Tfit(i-3))
               )+...
            0.15*((Xfit(i+1)-Xfit(i-4))/(Tfit(i+1)-Tfit(i-4))
               )+...
            0.10*((Xfit(i+0)-Xfit(i-5))/(Tfit(i+0)-Tfit(i-5))
               );
        if starti==1 %reset i to its original value
            i=i-6;
        end
        if endi==1 %reset i to its original value
            i=i+6;
        end
        starti=0; endi=0;
    end
    vXfit=vXfit/1000; %from mm/s to m/s

    aXfit=Tfit; %X acceleration
    endi=0;
```

```
    starti=0;
    for i=1:length(Tfit)
        j=i;
        if i<6 %if you are at the begining of the pass, use
           the later points
            starti=1; i=i+6;
        end
        if i>=(length(Tfit)-6) %if you are at the end of the
           pass, use the previous pooints
            endi=1; i=i-6;
        end
        aXfit(j)=...
            0.10*((vXfit(i+5)-vXfit(i-0))/(Tfit(i+5)-Tfit(i
               -0)))+...
            0.15*((vXfit(i+4)-vXfit(i-1))/(Tfit(i+4)-Tfit(i
               -1)))+...
            0.25*((vXfit(i+3)-vXfit(i-2))/(Tfit(i+3)-Tfit(i
               -2)))+...
            0.25*((vXfit(i+2)-vXfit(i-3))/(Tfit(i+2)-Tfit(i
               -3)))+...
            0.15*((vXfit(i+1)-vXfit(i-4))/(Tfit(i+1)-Tfit(i
               -4)))+...
            0.10*((vXfit(i+0)-vXfit(i-5))/(Tfit(i+0)-Tfit(i
               -5)));
        if starti==1 %reset i to its original value
            i=i-6;
        end
        if endi==1 %reset i to its original value
            i=i+6;
        end
```

```
        starti=0; endi=0;
    end
    aXfit=aXfit; %from m/s to m/s


    vYfit=Tfit; %Y velocity
    endi=0;
    starti=0;
    for i=1:length(Tfit)
        j=i;
        if i<6 %if you are at the begining of the pass, use
           the later points
            starti=1; i=i+6;
        end
        if i>=(length(Tfit)-6) %if you are at the end of the
           pass, use the previous pooints
            endi=1; i=i-6;
        end
        vYfit(j)=...
            0.10*((Yfit(i+5)-Yfit(i-0))/(Tfit(i+5)-Tfit(i-0))
               )+...
            0.15*((Yfit(i+4)-Yfit(i-1))/(Tfit(i+4)-Tfit(i-1))
               )+...
            0.25*((Yfit(i+3)-Yfit(i-2))/(Tfit(i+3)-Tfit(i-2))
               )+...
            0.25*((Yfit(i+2)-Yfit(i-3))/(Tfit(i+2)-Tfit(i-3))
               )+...
            0.15*((Yfit(i+1)-Yfit(i-4))/(Tfit(i+1)-Tfit(i-4))
               )+...
```

```
            0.10*((Yfit(i+0)-Yfit(i-5))/(Tfit(i+0)-Tfit(i-5))
                );
        if starti==1 %reset i to its original value
            i=i-6;
        end
        if endi==1 %reset i to its original value
            i=i+6;
        end
        starti=0; endi=0;
    end
    vYfit=vYfit/1000; %from mm/s to m/s

    aYfit=Tfit; %Y acceleration
    endi=0;
    starti=0;
    for i=1:length(Tfit)
        j=i;
        if i<6 %if you are at the begining of the pass, use
            the later points
            starti=1; i=i+6;
        end
        if i>=(length(Tfit)-6) %if you are at the end of the
            pass, use the previous pooints
            endi=1; i=i-6;
        end
        aYfit(j)=...
            0.10*((vYfit(i+5)-vYfit(i-0))/(Tfit(i+5)-Tfit(i
                -0)))+...
            0.15*((vYfit(i+4)-vYfit(i-1))/(Tfit(i+4)-Tfit(i
                -1)))+...
```

```
            0.25*((vYfit(i+3)-vYfit(i-2))/(Tfit(i+3)-Tfit(i
                -2)))+...
            0.25*((vYfit(i+2)-vYfit(i-3))/(Tfit(i+2)-Tfit(i
                -3)))+...
            0.15*((vYfit(i+1)-vYfit(i-4))/(Tfit(i+1)-Tfit(i
                -4)))+...
            0.10*((vYfit(i+0)-vYfit(i-5))/(Tfit(i+0)-Tfit(i
                -5)));
        if starti==1 %reset i to its original value
            i=i-6;
        end
        if endi==1 %reset i to its original value
            i=i+6;
        end
        starti=0; endi=0;
    end
    aYfit=aYfit; %from m/s to m/s


    vZfit=Tfit; %Z velocity
    endi=0;
    starti=0;
    for i=1:length(Tfit)
        j=i;
        if i<6 %if you are at the begining of the pass, use
            the later points
            starti=1; i=i+6;
        end
        if i>=(length(Tfit)-6) %if you are at the end of the
            pass, use the previous pooints
```

```
            endi=1; i=i-6;
        end
        vZfit(j)=...
            0.10*((Zfit(i+5)-Zfit(i-0))/(Tfit(i+5)-Tfit(i-0))
               )+...
            0.15*((Zfit(i+4)-Zfit(i-1))/(Tfit(i+4)-Tfit(i-1))
               )+...
            0.25*((Zfit(i+3)-Zfit(i-2))/(Tfit(i+3)-Tfit(i-2))
               )+...
            0.25*((Zfit(i+2)-Zfit(i-3))/(Tfit(i+2)-Tfit(i-3))
               )+...
            0.15*((Zfit(i+1)-Zfit(i-4))/(Tfit(i+1)-Tfit(i-4))
               )+...
            0.10*((Zfit(i+0)-Zfit(i-5))/(Tfit(i+0)-Tfit(i-5))
               );
        if starti==1 %reset i to its original value
            i=i-6;
        end
        if endi==1 %reset i to its original value
            i=i+6;
        end
        starti=0; endi=0;
    end
    vZfit=vZfit/1000; %from mm/s to m/s

    aZfit=Tfit; %Z acceleration
    endi=0;
    starti=0;
    for i=1:length(Tfit)
        j=i;
```

```
        if i<6 %if you are at the begining of the pass, use
           the later points
            starti=1; i=i+6;
        end
        if i>=(length(Tfit)-6) %if you are at the end of the
           pass, use the previous pooints
            endi=1; i=i-6;
        end
        aZfit(j)=...
            0.10*((vZfit(i+5)-vZfit(i-0))/(Tfit(i+5)-Tfit(i
               -0)))+...
            0.15*((vZfit(i+4)-vZfit(i-1))/(Tfit(i+4)-Tfit(i
               -1)))+...
            0.25*((vZfit(i+3)-vZfit(i-2))/(Tfit(i+3)-Tfit(i
               -2)))+...
            0.25*((vZfit(i+2)-vZfit(i-3))/(Tfit(i+2)-Tfit(i
               -3)))+...
            0.15*((vZfit(i+1)-vZfit(i-4))/(Tfit(i+1)-Tfit(i
               -4)))+...
            0.10*((vZfit(i+0)-vZfit(i-5))/(Tfit(i+0)-Tfit(i
               -5)));
        if starti==1 %reset i to its original value
            i=i-6;
        end
        if endi==1 %reset i to its original value
            i=i+6;
        end
        starti=0; endi=0;
    end
    aZfit=aZfit; %from m/s to m/s
```

```
    vMfit=(vXfit.^2+vYfit.^2+vZfit.^2).^(1/2); %3D velocity
       magnitude as the sqrt of the sum of square of each
       axis speed
    aMfit=(aXfit.^2+aYfit.^2+aZfit.^2).^(1/2); %3D
       acceleration magnitude as the sqrt of the sum of
       square of each axis acceleration

    %Adding the fitted pass to the cell array of fitted
       passes
    pTfit{1,f}=Tfit;
    pTresetfit{1,f}=Tresetfit;
    pXfit{1,f}=Xfit;
    pYfit{1,f}=Yfit;
    pZfit{1,f}=Zfit;
    pidfit{1,f}=idfit;
    pRfit{1,f}=Rfit;
    pAfit{1,f}=Afit;
    pvRfit{1,f}=vRfit;
    pvAfit{1,f}=vAfit;
    pvXfit{1,f}=vXfit;
    pvYfit{1,f}=vYfit;
    pvZfit{1,f}=vZfit;
    pvMfit{1,f}=vMfit;
    paRfit{1,f}=aRfit;
    paAfit{1,f}=aAfit;
    paXfit{1,f}=aXfit;
    paYfit{1,f}=aYfit;
    paZfit{1,f}=aZfit;
    paMfit{1,f}=aMfit;
```

```
end

%Assemble the fitted passes in a single array (indice 3 is
    for identification as fitted locations).
T3=vertcat(pTfit{:}); %Vertical concatenation of the cell
    array
X3=vertcat(pXfit{:});
Y3=vertcat(pYfit{:});
Z3=vertcat(pZfit{:});
id3=vertcat(pidfit{:});
R3=vertcat(pRfit{:});
A3=vertcat(pAfit{:});
vR3=vertcat(pvRfit{:});
vA3=vertcat(pvAfit{:});
vX3=vertcat(pvXfit{:});
vY3=vertcat(pvYfit{:});
vZ3=vertcat(pvZfit{:});
vM3=vertcat(pvMfit{:});
aR3=vertcat(paRfit{:});
aA3=vertcat(paAfit{:});
aX3=vertcat(paXfit{:});
aY3=vertcat(paYfit{:});
aZ3=vertcat(paZfit{:});
aM3=vertcat(paMfit{:});

%FORCES CALCULATIONS BASED ON PARTICLE SIZE, DENSITY AND
    ACCELERATION
%---------------------------------------------------------%

Dp=1180; %Particle diameter (um)
```

```
Rp=Dp/2/1000000;%Particle radius (m)
Vp=4/3*pi()*Rp^3; %Particle volume (m^3)
rhop=2650; %Particle density (kg/m^3)
Mp=Vp*rhop; %Particle mass (kg)

FpR3=Mp*aR3; %Force in R axis (combination of x and z)
FpX3=Mp*aX3; %Force in x axis equal particle mass time
    acceleration in x axis
FpY3=Mp*aY3;
FpZ3=Mp*aZ3;
FpM3=Mp*aM3; %Force Magnitude
Fpcheck=FpM3-(FpX3.^2+FpY3.^2+FpZ3.^2).^(1/2); %Should be
    zero or really close to 0

%FIELD OF VIEW BOUNDARIES
%------------------------------------------------------------%
Tmin=50; %Remove value with T value lower than (s)
Tmax=10000; %Remove value with T value higher than (s)
tT3=(T3>=Tmin & T3<Tmax);
tT=(T>=Tmin & T<Tmax);

Xmin=-190; %Remove points with X value lower than (mm)
Xmax=190; %Remove points with X value higher than (mm)
tX3=(X3>=Xmin & X3<Xmax);
tX=(X>=Xmin & X<Xmax);

Ymin=-100;
Ymax=0;
tY3=(Y3>=Ymin & Y3<Ymax);
tY=(Y>=Ymin & Y<Ymax);
```

```

Zmin=-190;
Zmax=190;
tZ3=(Z3>=Zmin & Z3<Zmax);
tZ=(Z>=Zmin & Z<Zmax);

% Keep only fitted points inside the boundaries
Select=ones(size(T3)); %Creating a array with true (1) for
    each existing locations
Select=Select.*tT3.*tX3.*tY3.*tZ3; %Applying the condition to
     convert from true (1) to false (0) if locations to be
    rejected
Select=Select>0;

SelectIni=ones(size(T)); %Creating a array with true (1) for
    each existing locations
SelectIni=SelectIni.*tT.*tX.*tY.*tZ; %Applying the condition
    to convert from true (1) to false (0) if locations to be
    rejected
SelectIni=SelectIni>0;

T3=T3(Select); %T (or T1) is kept as unfiltered data
id3=find(T3);
X3=X3(Select);
Y3=Y3(Select);
Z3=Z3(Select);
R3=R3(Select);
A3=A3(Select);
vR3=vR3(Select);
vA3=vA3(Select);
```

```
vX3=vX3(Select);
vY3=vY3(Select);
vZ3=vZ3(Select);
vM3=vM3(Select);
aR3=aR3(Select);
aA3=aA3(Select);
aX3=aX3(Select);
aY3=aY3(Select);
aZ3=aZ3(Select);
aM3=aM3(Select);
FpR3=FpR3(Select);
FpX3=FpX3(Select);
FpY3=FpY3(Select);
FpZ3=FpZ3(Select);
FpM3=FpM3(Select);

T=T(SelectIni); %Keep only the initial data corresponding to
    boundaries (for comparison)
X=X(SelectIni);
Y=Y(SelectIni);
Z=Z(SelectIni);
XRes=XRes(SelectIni);
YRes=YRes(SelectIni);
ZRes=ZRes(SelectIni);



%DATA SET BASICS INFORMATION
%------------------------------------------------------------%
nbLocini=length(T);
```

```
nbLocFit=length(T3);
sampleT=max(T3)-min(T3);
locrate=nbLocini/sampleT;  %Location frequency calculation
locrateFit=nbLocFit/sampleT;

T1=[T;mean(T)];
T2=[mean(T);T];
Tdelta=T2-T1;
MeanTdelta=mean(Tdelta);
StdTdelta=std(Tdelta);

T1fit=[T3;mean(T3)];
T2fit=[mean(T3);T3];
Tdeltafit=T2fit-T1fit;
MeanTdeltaFit=mean(Tdeltafit);
StdTdeltaFit=std(Tdeltafit);

X1=[X;mean(X)];
X2=[mean(X);X];
Xdelta=X2-X1;
MeanXdelta=mean(Xdelta);
StdXdelta=std(Xdelta);

X1fit=[X3;mean(X3)];
X2fit=[mean(X3);X3];
Xdeltafit=X2fit-X1fit;
MeanXdeltaFit=mean(Xdeltafit);
StdXdeltaFit=std(Xdeltafit);

Y1=[Y;mean(Y)];
```

```
Y2=[mean(Y);Y];
Ydelta=Y2-Y1;
MeanYdelta=mean(Ydelta);
StdYdelta=std(Ydelta);

Y1fit=[Y3;mean(Y3)];
Y2fit=[mean(Y3);Y3];
Ydeltafit=Y2fit-Y1fit;
MeanYdeltaFit=mean(Ydeltafit);
StdYdeltaFit=std(Ydeltafit);

Z1=[Z;mean(Z)];
Z2=[mean(Z);Z];
Zdelta=Z2-Z1;
MeanZdelta=mean(Zdelta);
StdZdelta=std(Zdelta);

Z1fit=[Z3;mean(Z3)];
Z2fit=[mean(Z3);Z3];
Zdeltafit=Z2fit-Z1fit;
MeanZdeltaFit=mean(Zdeltafit);
StdZdeltaFit=std(Zdeltafit);

XYZdelta=(Xdelta.^2.+Ydelta.^2.+Zdelta.^2).^(1/2);
MeanXYZdelta=mean(XYZdelta); %Average distance between
    subsequent locations
StdXYZdelta=std(XYZdelta);

XYZdeltafit=(Xdeltafit.^2.+Ydeltafit.^2.+Zdeltafit.^2).^(1/2)
    ;
```

```
MeanXYZdeltaFit=mean(XYZdeltafit); %Average distance between subsequent locations (fit)
StdXYZdeltaFit=std(XYZdeltafit);

%Display info
disp(['Particle diameter (um): ',num2str(Dp)])
disp(['Particle density (kg/m^3): ',num2str(rhop)])
disp(['Number of locations: ',num2str(nbLocini)])
disp(['Number of locations (fit): ',num2str(nbLocFit)])
disp(['Sample time (s): ',num2str(sampleT)])
disp(['Location rate (Hz): ',num2str(locrate)])
disp(['Location rate (fit) (Hz): ',num2str(locrateFit)])
disp(['Mean delta subsequent locations (mm): ',num2str(MeanXYZdelta)])
disp(['Mean delta subsequent locations (fit) (mm): ',num2str(MeanXYZdeltaFit)])
disp(['Std dev delta subsequent locations (mm): ',num2str(StdXYZdelta)])
disp(['Std dev delta subsequent locations (fit) (mm): ',num2str(StdXYZdeltaFit)])
disp(['Number of passes: ',num2str(pcount)])


%DISPLAY LOCATIONS VALUES X, Y, Z, T
%---------------------------------------------------------------%
figure(01)

subplot(3,1,1)
plot(T3-min(T3),X3,'ro','LineWidth',2,'MarkerSize',5);
hold on
```

```
plot(T-min(T3),X,'bo','LineWidth',1,'MarkerSize',3);
axis([Tmin-min(T3) Tmax-min(T3) Xmin Xmax])
xlabel('T (s)','FontSize',20);
ylabel('X (mm)','FontSize',20);
grid on
legend('Fit', 'Initial locations')
set(gca,'FontSize',20)

subplot(3,1,2)
plot(T3-min(T3),Y3,'ro','LineWidth',2,'MarkerSize',5);
hold on
plot(T-min(T3),Y,'bo','LineWidth',1,'MarkerSize',3);
axis([Tmin-min(T3) Tmax-min(T3) Ymin Ymax])
xlabel('T (s)','FontSize',20);
ylabel('Y (mm)','FontSize',20);
grid on
set(gca,'FontSize',20)

subplot(3,1,3)
plot(T3-min(T3),Z3,'ro','LineWidth',2,'MarkerSize',5);
hold on
plot(T-min(T3),Z,'bo','LineWidth',1,'MarkerSize',3);
axis([Tmin-min(T3) Tmax-min(T3) Zmin Zmax])
xlabel('T (s)','FontSize',20);
ylabel('Z (mm)','FontSize',20);
grid on
set(gca,'FontSize',20)


%DISPLAY VELOCITIES VALUES vX, vY, vZ, T
```

```
%--------------------------------------------------------------%
figure(02)

subplot(4,1,1)
plot(T3,vX3,'mo','LineWidth',2,'MarkerSize',2);
axis([Tmin Tmax min(vX3) max(vX3)])
xlabel('T (s)','FontSize',20);
ylabel('vX (mm)','FontSize',20);
grid on
set(gca,'FontSize',20)

subplot(4,1,2)
plot(T3,vY3,'mo','LineWidth',2,'MarkerSize',2);
axis([Tmin Tmax min(vY3) max(vY3)])
xlabel('T (s)','FontSize',20);
ylabel('vY (mm)','FontSize',20);
grid on
set(gca,'FontSize',20)

subplot(4,1,3)
plot(T3,vZ3,'mo','LineWidth',2,'MarkerSize',2);
axis([Tmin Tmax min(vZ3) max(vZ3)])
xlabel('T (s)','FontSize',20);
ylabel('vZ (mm)','FontSize',20);
grid on
set(gca,'FontSize',20)

subplot(4,1,4)
plot(T3,vM3,'mo','LineWidth',2,'MarkerSize',2);
axis([Tmin Tmax min(vM3) max(vM3)])
```

```
xlabel('T (s)','FontSize',20);
ylabel('vM (mm)','FontSize',20);
grid on
set(gca,'FontSize',20)


%RADIUS STATS
%----------------------------------------------------------%
StatR=zeros(pcount,3);
for i=1:pcount
    rad=cell2mat(pRfit(:,i));
    %rad(isnan(rad))=[];
    radini=rad(1);
    radfin=rad(length(rad));
    delrad=radfin-radini;
    StatR(i,:)=[radini radfin delrad];
end
meanDelRad=mean(StatR(:,3))
stdDelRad=std(StatR(:,3))
medianDelRad=median(StatR(:,3))

%DISPLAY PASSES CONCENTRATION
%----------------------------------------------------------%
figure(03)

line=[0 0;200 200];
plot(line(:,1),line(:,2),'--k','LineWidth',2,'MarkerSize',5);
hold on
plot(StatR(:,1),StatR(:,2),'ro','LineWidth',2,'MarkerSize',8)
    ;
```

```
hold off
xlabel('Entrance FOV radial position (mm)','FontSize',20);
ylabel('Exit FOV radial position (mm)','FontSize',20);
axis([20 180 20 180])
grid on
axis square
set(gca,'FontSize',20)
legend('No Concentration Line','Pass','Location','northwest')
% legend1='No Concentration Line';
% legend2='Pass';
% legend3=sprintf('Mean radial change = %.1f',meanDelRad);
% legend4=sprintf('Mean radial change = %.1f',stdDelRad);
% legend({legend1, legend2, legend3, legend4},'FontSize',18);

% %Print image in pdf
% h1=figure('position', [5, 5, 495, 495]);
%
% line=[0 0;200 200];
% plot(line(:,1),line(:,2),'--k','LineWidth',2,'MarkerSize
    ',5);
% hold on
% plot(StatR(:,1),StatR(:,2),'bo','LineWidth',2,'MarkerSize
    ',8);
% hold off
%
% xlim=get(gca,'XLim');
% ylim=get(gca,'YLim');
```

```
% ht = text(0.65*xlim(1)+0.77*xlim(2),0.1*ylim(1)+0.175*ylim(2),'P31Q1180','Color','black','EdgeColor','black','BackgroundColor','white','LineWidth',0.5,'HorizontalAlignment','center','VerticalAlignment','middle');
% %set(ht,'Rotation',45);
% set(ht,'FontSize',16);
%
% xlabel('FOV Entrance Radial Position (mm)');
% ylabel('FOV Exit Radial Position (mm)');
% axis([20 180 20 180]);
% grid on
% axis square
% set(gca,'FontSize',14);
% legend('No Concentration Line','Quartz 1000-1180 \mum','Location','northwest')
%
% set(h1,'PaperUnits','inches');
% set(h1,'papersize',[5 5]);
% set(h1,'PaperPosition', [0.05 0.05 4.95 4.95]);
% print(h1, '1000_1180_P31_Quartz_Concentration', '-dpdf');


%CREATE GEOMETRY FOR DISPLAY (circles and straight lines)
%-------------------------------------------------------%
pitch=203; %pitch in mm
nbt=4; %number of turn
ppt=40; %point per turn
maxZ=nbt*pitch;
maxA=nbt*2*pi;
```

```
nbp=ppt*nbt; %number of point total
Zzero=-28;%Offset of the geometry to height of origin (0,0,0)
Zbase=Zzero:-maxZ/nbp:Zzero-maxZ;
Rin=38/2;
% Rout=141;
nbh=22;
% R=linspace(Rin,Rout,nbh);
% P=linspace(0,50,nbh);
% for n=1:length(P)
%       P(n)=P(n)*n/length(P)*n/length(P)*n/length(P);
% end
P0=0;
R=[19 20 25 30 35 40 45 50 55 60 65 70 75 80 85 90 95 100 105
    110 115 120 125 130 135 140 145 150 155 160 163 160 155
    150];
P=[6 3 0 -1 -1 -0.3 0.5 1.4 2.3 3.2 4.1 5.0 5.9 6.8 7.7 8.6
    9.5 10.4 11.3 12.2 13.1 14.0 14.9 15.8 16.7 17.6 18.5 19.4
    21.9 28.4 38.4 48.4 54.9 57.4];
Zbase=Zbase';
Zfull=Zbase;
for n=1:length(R)-1
    Zfull=[Zfull Zbase+P(n+1)];
end


%DISPLAY 3D LOCATIONS COLORED BY PASS TIME
%-------------------------------------------------------%
figure(04)

for n=1:length(R)-1
```

```
    [x1 z1 y1]=pol2cart((0+pi/2:maxA/nbp:maxA+pi/2),R(n),
        Zfull(:,n)');
    [x2 z2 y2]=pol2cart((0+pi/2:maxA/nbp:maxA+pi/2),R(n+1),
        Zfull(:,n+1)');
    surface([x1;x2],[y1;y2],[z1;z2],'FaceColor','[0.6 0.6
        0.6]','FaceAlpha',0.3,'EdgeColor','[0.4 0.4 0.4]','
        EdgeAlpha',0.7);
end
for i=1:pcount
    hold on
    h = surface([pXfit{1,i}, pXfit{1,i}], [pYfit{1,i}, pYfit
        {1,i}], [pZfit{1,i}, pZfit{1,i}],[pTresetfit{1,i},
        pTresetfit{1,i}],'LineWidth',2,'EdgeColor','flat', '
        FaceColor','none');
end
hold off
col = colorbar;
colormap jet
ylabel(col,'Pass Time (s)','FontSize',18);
caxis([0,5])
xlabel('X (mm)','FontSize',18);
ylabel('Y (mm)','FontSize',18);
zlabel('Z (mm)','FontSize',18);
axis equal
axis([Xmin Xmax Ymin Ymax Zmin Zmax])
grid on
set(gca,'FontSize',18)
AZ=0;
EL=90;
view(AZ,EL);
```

```
camorbit(225,22.5,'camera')


%DISPLAY 3D LOCATIONS COLORED BY VELOCITY MAGNITUDE
%----------------------------------------------------------------%
figure(05)

for n=1:length(R)-1
    [x1 z1 y1]=pol2cart((0+pi/2:maxA/nbp:maxA+pi/2),R(n),
        Zfull(:,n)');
    [x2 z2 y2]=pol2cart((0+pi/2:maxA/nbp:maxA+pi/2),R(n+1),
        Zfull(:,n+1)');
    surface([x1;x2],[y1;y2],[z1;z2],'FaceColor','[0.6 0.6
        0.6]','FaceAlpha',0.3,'EdgeColor','[0.4 0.4 0.4]','
        EdgeAlpha',0.7);
end
for i=1:pcount
    hold on
    h = surface([pXfit{1,i}, pXfit{1,i}], [pYfit{1,i}, pYfit
        {1,i}], [pZfit{1,i}, pZfit{1,i}],[pvMfit{1,i}, pvMfit
        {1,i}],'LineWidth',2,'EdgeColor','flat', 'FaceColor','
        none');
end
hold off
col = colorbar;
colormap jet
ylabel(col,'Velocity Magnitude (m/s)','FontSize',18);
caxis([0,1.2])
xlabel('X (mm)','FontSize',18);
ylabel('Y (mm)','FontSize',18);
```

```
zlabel('Z (mm)','FontSize',18);
axis equal
axis([Xmin Xmax Ymin Ymax Zmin Zmax])
grid on
set(gca,'FontSize',18)
AZ=0;
EL=90;
view(AZ,EL);
camorbit(225,22.5,'camera')


%DISPLAY 3D LOCATIONS COLORED BY RADIAL VELOCITY MAGNITUDE
%----------------------------------------------------------------%
figure(051)

for n=1:length(R)-1
    [x1 z1 y1]=pol2cart((0+pi/2:maxA/nbp:maxA+pi/2),R(n),
        Zfull(:,n)');
    [x2 z2 y2]=pol2cart((0+pi/2:maxA/nbp:maxA+pi/2),R(n+1),
        Zfull(:,n+1)');
    surface([x1;x2],[y1;y2],[z1;z2],'FaceColor','[0.6 0.6
        0.6]','FaceAlpha',0.3,'EdgeColor','[0.4 0.4 0.4]','
        EdgeAlpha',0.7);
end
for i=1:pcount
    hold on
    h = surface([pXfit{1,i}, pXfit{1,i}], [pYfit{1,i}, pYfit
        {1,i}], [pZfit{1,i}, pZfit{1,i}],[pvRfit{1,i}, pvRfit
        {1,i}],'LineWidth',2,'EdgeColor','flat', 'FaceColor','
        none');
```

```
end
hold off
col = colorbar;
colormap jet
ylabel(col,'Radial Velocity Magnitude (m/s)','FontSize',18);
caxis([-0.1,0.1])
xlabel('X (mm)','FontSize',18);
ylabel('Y (mm)','FontSize',18);
zlabel('Z (mm)','FontSize',18);
axis equal
axis([Xmin Xmax Ymin Ymax Zmin Zmax])
grid on
set(gca,'FontSize',18)
AZ=0;
EL=90;
view(AZ,EL);
camorbit(225,22.5,'camera')

%DISPLAY 3D LOCATIONS COLORED BY INITIAL RADIAL POSITION
%------------------------------------------------------------%
figure(052)

for n=1:length(R)-1
    [x1 z1 y1]=pol2cart((0+pi/2:maxA/nbp:maxA+pi/2),R(n),
        Zfull(:,n)');
    [x2 z2 y2]=pol2cart((0+pi/2:maxA/nbp:maxA+pi/2),R(n+1),
        Zfull(:,n+1)');
    surface([x1;x2],[y1;y2],[z1;z2],'FaceColor',[0.6 0.6
        0.6],'FaceAlpha',0.3,'EdgeColor',[0.4 0.4 0.4],'
        EdgeAlpha',0.7);
```

```
end

pRifit=pRfit;

for i=1:pcount
    hold on
    pRifit{1,i}(:)=pRfit{1,i}(1);
    h = surface([pXfit{1,i}, pXfit{1,i}], [pYfit{1,i}, pYfit
        {1,i}], [pZfit{1,i}, pZfit{1,i}],[pRifit{1,i}, pRifit
        {1,i}],'LineWidth',2,'EdgeColor','flat', 'FaceColor','
        none');
end
hold off
col = colorbar;
colormap jet
ylabel(col,'Initial Radial Position (mm)','FontSize',18);
caxis([90,150])
xlabel('X (mm)','FontSize',18);
ylabel('Y (mm)','FontSize',18);
zlabel('Z (mm)','FontSize',18);
axis equal
axis([Xmin Xmax Ymin Ymax Zmin Zmax])
grid on
set(gca,'FontSize',18)
AZ=0;
EL=90;
view(AZ,EL);
camorbit(225,22.5,'camera')

%DISPLAY 3D LOCATIONS COLORED BY ANGULAR POSITION
```

```
%——————————————————————————————————————————%
figure(051)

for n=1:length(R)-1
    [x1 z1 y1]=pol2cart((0+pi/2:maxA/nbp:maxA+pi/2),R(n),
       Zfull(:,n)');
    [x2 z2 y2]=pol2cart((0+pi/2:maxA/nbp:maxA+pi/2),R(n+1),
       Zfull(:,n+1)');
    surface([x1;x2],[y1;y2],[z1;z2],'FaceColor','[0.6 0.6
       0.6]','FaceAlpha',0.3,'EdgeColor','[0.4 0.4 0.4]','
       EdgeAlpha',0.7);
end
for i=1:pcount
    hold on
    h = surface([pXfit{1,i}, pXfit{1,i}], [pYfit{1,i}, pYfit
       {1,i}], [pZfit{1,i}, pZfit{1,i}],[pAfit{1,i}, pAfit{1,
       i}],'LineWidth',2,'EdgeColor','flat', 'FaceColor','
       none');
end
hold off
col = colorbar;
colormap jet
ylabel(col,'Angular position (rad)','FontSize',18);
caxis([0,6])
xlabel('X (mm)','FontSize',18);
ylabel('Y (mm)','FontSize',18);
zlabel('Z (mm)','FontSize',18);
axis equal
axis([Xmin Xmax Ymin Ymax Zmin Zmax])
grid on
```

```
set(gca,'FontSize',18)
AZ=0;
EL=90;
view(AZ,EL);
camorbit(225,22.5,'camera')


% %DISPLAY SECONDARY FLOW (and make video)
% %-----------------------------------------------------------------------%
%
% for i=2:pcount
%
%       Asf=pAfit{1,i};
%       Rsf=pRfit{1,i};
%       Xsf=pXfit{1,i};
%       Ysf=pYfit{1,i};
%       Zsf=pZfit{1,i};
%       vYsf=pvYfit{1,i};
%       vRsf=pvRfit{1,i};
%
%       test=(Asf>=(4*pi()/16) & Asf<(9*pi()/16));
%
%       Asf=Asf(test);
%       Rsf=Rsf(test);
%       Xsf=Xsf(test);
%       Ysf=Ysf(test);
%       Zsf=Zsf(test);
%       vYsf=vYsf(test);
%       vRsf=vRsf(test);
%
```

```
%       delY=pitch*((Asf-Asf(1))/(2*pi()));
%
%       SFpAfit{1,i}=Asf; %Angular position between pi()/4 and
    pi()/2
%       SFpRfit{1,i}=Rsf+1;
%       SFpXfit{1,i}=Xsf;
%       SFpYfit{1,i}=Ysf+delY+40; %y without downward, y
    adjustement
%       SFpZfit{1,i}=Zsf;
%       SFpvYfit{1,i}=vYsf;
%       SFpvRfit{1,i}=vRsf;
%
% end
%
% RRR=[];
% YYY=[];
% vRRR=[];
% vYYY=[];
%
% for i=1:pcount
% RRR=[RRR;SFpRfit{1,i}];
% YYY=[YYY;SFpYfit{1,i}];
% vRRR=[vRRR;SFpvRfit{1,i}];
% vYYY=[vYYY;SFpvYfit{1,i}];
% end
%
% nbtot=length(RRR);
% nbparticle=15;
% nbfr=floor(nbtot/nbparticle);
% maxc=max(vRRR);
```

```
% minc=min(vRRR);
%
% for ffi=1:nbfr
%     h=figure('position', [0, 0, 800, 360]);
%
%     %Get only point for current frame
%     fri=1:nbfr:(nbtot-nbfr);
%     pii=fri+ffi-1;
%     vRRRfr=vRRR(pii);
%     RRRfr=RRR(pii);
%     YYYfr=YYY(pii);
%
%     %Plot
%     plot(R,P,'k','LineWidth',2); %profil
%     hold on
%     c=vRRRfr;
%     scatter(RRRfr,YYYfr,40,c,'filled'); %point
%     axis equal
%     axis([0 170 -5 60])
%     xlabel('Radial Position (mm)','FontSize',20);
%     ylabel('Profile Height (mm)','FontSize',20);
%     grid on
%     col = colorbar;
%     colormap jet
%     ylabel(col,'Radial Velocity (m/s)','FontSize',18);
%     caxis([-0.2,0.2])
%     set(gca,'FontSize',20)
%
% %     %Save pdf
% %     set(h,'Units','Inches');
```

```
% %       pos = get(h,'Position');
% %       set(h,'PaperPositionMode','Auto','PaperUnits','Inches
    ','PaperSize',[pos(3), pos(4)])
% %       print(h,'FigName','-dpdf','-r0')
%
%       %Save image
%       I=getframe(gcf);
%       imwrite(I.cdata,sprintf('FIG%d.png',ffi));
%       close all;
%
% end
%
%
%COMBINE FRAME INTO VIDEO
%-------------------------------------------------------------%

% writerObj = VideoWriter('Secondary_flow.avi');
% writerObj.FrameRate=10;
% %writerObj.Quality=100;
% open(writerObj);
% for iloop=1:5
% for K = 1:ffi
%       filename = sprintf('FIG%d.png', K);
%       thisimage = imread(filename);
%       writeVideo(writerObj, thisimage);
% end
% end
% close(writerObj);
%
%
```

```
%
% figure(101)
%
% for n=1:length(R)-1
%     [x1 z1 y1]=pol2cart((0+pi/2:maxA/nbp:maxA+pi/2),R(n),
  Zfull(:,n)');
%     [x2 z2 y2]=pol2cart((0+pi/2:maxA/nbp:maxA+pi/2),R(n+1),
  Zfull(:,n+1)');
%     surface([x1;x2],[y1;y2],[z1;z2],'FaceColor','[0.6 0.6
  0.6]','FaceAlpha',0.3,'EdgeColor','[0.4 0.4 0.4]','
  EdgeAlpha',0.7);
% end
% for i=1:pcount
%     hold on
%     h = surface([SFpXfit{1,i}, SFpXfit{1,i}], [SFpYfit{1,i
  }, SFpYfit{1,i}], [SFpZfit{1,i}, SFpZfit{1,i}],[SFpvRfit
  {1,i}, SFpvRfit{1,i}],'LineWidth',2,'EdgeColor','flat', '
  FaceColor','none');
% end
%
%
% hold off
% col = colorbar;
% colormap jet
% ylabel(col,'Radial Velocity (m/s)','FontSize',18);
% caxis([-0.1,0.1])
% xlabel('X (mm)','FontSize',18);
% ylabel('Y (mm)','FontSize',18);
% zlabel('Z (mm)','FontSize',18);
% axis equal
```

```
% axis([Xmin Xmax Ymin Ymax Zmin Zmax])
% grid on
% set(gca,'FontSize',18)
% AZ=0;
% EL=90;
% view(AZ,EL);
% camorbit(225,22.5,'camera')


%CUBIC BINNING (For volume averaging of quantities)
%-----------------------------------------------------%
 binsize=5; % Edge length of the cubic occupancy bin (mm)

EdgesX=[Xmin:binsize:Xmax]; % Creating the bins boundaries
EdgesY=[Ymin:binsize:Ymax];
EdgesZ=[Zmin:binsize:Zmax];

nbbinX=(length(EdgesX)-1); % Counting the bins
nbbinY=(length(EdgesY)-1);
nbbinZ=(length(EdgesZ)-1);
nbbin=nbbinX*nbbinY*nbbinZ;
bincount=0;

MatCount=zeros(nbbinX,nbbinY,nbbinZ); %Initialisation of a 3D
    matrix to count location in the bins.

MatCenterX=MatCount; %Initialisation of a 3D matrix to store
   X location of the center of the bins.
MatCenterY=MatCount;
MatCenterZ=MatCount;
```

```
MatTime=MatCount; %Initialisation of a 3D matrix to store the
    Time in the bin.
% MatX=MatCount; %Initialisation of a 3D matrix to store the
    X axis travel distance in the bin.
% MatY=MatCount;
% MatZ=MatCount;
MatvX=MatCount; %Initialisation of a 3D matrix to store X
    speed in the bin.
MatvY=MatCount;
MatvZ=MatCount;
%MatR=MatCount;
MatvR=MatCount;
MatvA=MatCount;

for kk=1:nbbinZ
    ET=T3; %Reset the matrix of locations
    EX=X3;
    EY=Y3;
    EZ=Z3;
    Eid=id3;

    EZmin=EdgesZ(kk); %Selecting the bin Z lower boundary
    EZmax=EdgesZ(kk+1); %Selecting the bin Z upper boundary
    EtZ=EZ>=EZmin & EZ<EZmax; %Filtering the data to keep
        only data point found into the Z Edges of the bin

    ET=ET(EtZ);
    EX=EX(EtZ);
    EY=EY(EtZ);
```

```
    EZ=EZ(EtZ);
    Eid=Eid(EtZ);

    for jj=1:nbbinY
        EET=ET; %Reset the matrix of locations
        EEX=EX;
        EEY=EY;
        EEZ=EZ;
        EEid=Eid;

        EEYmin=EdgesY(jj); %Selecting the bin Y lower
           boundary
        EEYmax=EdgesY(jj+1); %Selecting the bin Y upper
           boundary
        EEtY=EEY>=EEYmin & EEY<EEYmax; %Filtering the data to
            keep only data point found into the Y Edges of
           the bin

        EET=EET(EEtY);
        EEX=EEX(EEtY);
        EEY=EEY(EEtY);
        EEZ=EEZ(EEtY);
        EEid=EEid(EEtY);

        for ii=1:nbbinX
            EEET=EET; %Reset the matrix of locations
            EEEX=EEX;
            EEEY=EEY;
            EEEZ=EEZ;
            EEEid=EEid;
```

```

            EEEXmin=EdgesX(ii); %Selecting the bin X lower
               boundary
            EEEXmax=EdgesX(ii+1); %Selecting the bin X upper
               boundary
            EEEtX=EEEX>=EEEXmin & EEEX<EEEXmax; %Filtering
               the data to keep only data point found into
               the X Edges of the bin

            EEET=EEET(EEEtX);
            EEEX=EEEX(EEEtX);
            EEEY=EEEY(EEEtX);
            EEEZ=EEEZ(EEEtX);
            EEEid=EEEid(EEEtX);

            nbpoints=length(EEET); % Counting how many
               locations
            MatCount(ii,jj,kk)=nbpoints; % Writting the
               number of location in the bin
            MatCenterX(ii,jj,kk)=EdgesX(ii)+binsize/2; %
               Writting the bin center X coordinate
            MatCenterY(ii,jj,kk)=EdgesY(jj)+binsize/2;
            MatCenterZ(ii,jj,kk)=EdgesZ(kk)+binsize/2;

            id1=EEEid; % Getting the id of each location in
               the bin
            Tbin=0; % Initialisation of time count
            Xbin=0; % Initialisation of distance count
            Ybin=0;
            Zbin=0;
```

```
            Rbin=0;
            Abin=0;
            vXbin=0;
            vYbin=0;
            vZbin=0;
            vRbin=0;
            vAbin=0;


            bincount=bincount+1;

            if length(id1)>1
                for iT=1:nbpoints
                    Tbin=Tbin+T3(id1(iT));

                    Xbin=Xbin+X3(id1(iT));
                    Ybin=Ybin+Y3(id1(iT));
                    Zbin=Zbin+Z3(id1(iT));
                    Rbin=Rbin+R3(id1(iT));
                    Abin=Abin+A3(id1(iT));
                    vXbin=vXbin+vX3(id1(iT));
                    vYbin=vYbin+vY3(id1(iT));
                    vZbin=vZbin+vZ3(id1(iT));
                    vRbin=vRbin+vR3(id1(iT));
                    vAbin=vAbin+vA3(id1(iT));

                end
                MatTime(ii,jj,kk)=Tbin;
                MatvX(ii,jj,kk)=vXbin/nbpoints;
                MatvY(ii,jj,kk)=vYbin/nbpoints;
```

```
                    MatvZ(ii,jj,kk)=vZbin/nbpoints;
                    MatvR(ii,jj,kk)=vRbin/nbpoints;
                    MatvA(ii,jj,kk)=vAbin/nbpoints;
                else
                end
            end
        end
        %clc;
        %percent_bin=bincount/nbbin*100
end


%DISPLAY BIN COUNT SLICE BY SLICE
%-----------------------------------------------------------%
figure(06)

for i=1:length(EdgesY)-1
    C=squeeze(MatCount(:,i,:));
    surf(squeeze(MatCenterX(:,i,:)),squeeze(MatCenterY(:,i,:)
        ),squeeze(MatCenterZ(:,i,:)),C); hold on
end
col = colorbar;
ylabel(col,'Number of locations per bin','FontSize',20);
axis equal
xlabel('X (mm)','FontSize',20);
ylabel('Y (mm)','FontSize',20);
zlabel('Z (mm)','FontSize',20);
set(gca,'FontSize',20)
AZ=-37.5;
EL=37.5;
```

```
view(AZ,EL);


%DISPLAY BIN COUNT SUMMED ON Z AXIS IN % OF TOTAL NUMBER OF
    LOCATIONS
%-----------------------------------------------------------%
figure(07)

MatCountSum=squeeze(sum(MatCount,2));
MatCountSumPercent=MatCountSum/nbLocFit*100;
C=MatCountSumPercent;
SX=squeeze(MatCenterX(:,1,:));
SY=squeeze(MatCenterY(:,1,:));
SZ=squeeze(MatCenterZ(:,1,:));

surf(SX,SY,SZ,C); hold on
col = colorbar;
ylabel(col,'Percent of locations (summed on Y axis)','
    FontSize',20);
colormap hot
caxis([0,0.05])
axis equal
xlabel('X (mm)','FontSize',20);
ylabel('Y (mm)','FontSize',20);
zlabel('Z (mm)','FontSize',20);
set(gca,'FontSize',20)
AZ=-37.5;
EL=37.5;
view(AZ,EL);

```

```

%DISPLAY BIN TIME SUMMED ON Z AXIS IN % OF LONGEST TIME
%---------------------------------------------------------------%
figure(08)

MatTimeSum=squeeze(sum(MatTime,2));
MatTimeSumPercent=MatTimeSum/(sampleT)*100;
C=MatTimeSumPercent;
SX=squeeze(MatCenterX(:,1,:));
SY=squeeze(MatCenterY(:,1,:));
SZ=squeeze(MatCenterZ(:,1,:));

surf(SX,SY,SZ,C); hold on
col = colorbar;
ylabel(col,'% time in bin (summed on Y axis)','FontSize',20);
caxis([0,1])
axis equal
xlabel('X (mm)','FontSize',20);
ylabel('Y (mm)','FontSize',20);
zlabel('Z (mm)','FontSize',20);
set(gca,'FontSize',20)
AZ=-37.5;
EL=37.5;
view(AZ,EL);


% %DISPLAY 3D VELOCITY FIELD (heavy on GPU)
% %---------------------------------------------------------------%
% figure (09)
%
```

```
% quiver3(MatCenterX,MatCenterY,MatCenterZ,MatvX,MatvY,MatvZ
    ,10,'linewidth',1,'color','r')
% axis equal
% xlabel('X (mm)','FontSize',20);
% ylabel('Y (mm)','FontSize',20);
% zlabel('Z (mm)','FontSize',20);
% set(gca,'FontSize',20)
% AZ=-37.5;
% EL=37.5;
% view(AZ,EL);


%TOROID BINNING
%---------------------------------------------------------------%
 binsize=binsize; %Spacing of the square grid defining bins (
    mm) (same as cubic bin)

Rmin=0;
Rmax=Xmax;

EdgesR=[Rmin:binsize:Rmax]; % Creating the bins boundaries
EdgesY=[Ymin:binsize:Ymax];

nbbinR=(length(EdgesR)-1); % Counting the bins
nbbinY=(length(EdgesY)-1);

MatRCount=zeros(nbbinR,nbbinY); %Initialisation of a 2D (R, Y
    ) matrix to count location in the bins.
MatRCenterR=MatRCount; %Initialisation of a 2D matrix to
    store R location of the center of the bins.
```

```
MatRCenterY=MatRCount;
MatRT=MatRCount; %Initialisation of a 2D matrix to store Time
    in the bins.
MatRVol=MatRCount; %Volume of the bin
MatRvM=MatRCount; %Velocity Magnitude of the bin
MatRvR=MatRCount;
MatRvY=MatRCount;
MatRvA=MatRCount;
MatRaM=MatRCount; %Acceleration magnitude of the bin
MatRaR=MatRCount;
MatRaY=MatRCount;
MatRaA=MatRCount;
MatRFpM=MatRCount; %Force magnitude of the bin
MatRFpR=MatRCount;
MatRFpY=MatRCount;

for jj=1:nbbinY
    ET=T3; %Set the matrix of locations
    ER=R3;
    EY=Y3;
    Eid=id3;

    EYmin=EdgesY(jj); %Selecting the bin Y lower boundary
    EYmax=EdgesY(jj+1); %Selecting the bin Y upper boundary
    EtY=EY>=EYmin & EY<EYmax; %Filtering the data to keep
        only data point found into the Y Edges of the bin

    ET=ET(EtY);
    ER=ER(EtY);
    EY=EY(EtY);
```

```
    Eid=Eid(EtY);

    for rr=1:nbbinR
        EET=ET; %Set the matrix of locations
        EER=ER;
        EEY=EY;
        EEid=Eid;

        EERmin=EdgesR(rr); %Selecting the bin R lower
           boundary
        EERmax=EdgesR(rr+1); %Selecting the bin R upper
           boundary
        EEtR=EER>=EERmin & EER<EERmax; %Filtering the data to
            keep only data point found into the R Edges of
           the bin

        EET=EET(EEtR);
        EER=EER(EEtR);
        EEY=EEY(EEtR);
        EEid=EEid(EEtR);

        nbpoints=length(EET); % Counting how many locations
           remains in the Y and R boundaries
        MatRCount(rr,jj)=nbpoints;% Writting the number of
           location in the bin
        MatRVol(rr,jj)=pi()*((EdgesR(rr)+binsize)^2-EdgesR(rr
           )^2)*binsize; %Writting the volume of the bin (mm3
           )
        MatRCenterR(rr,jj)=EdgesR(rr)+binsize/2; %Writting
           the bin center R coordinate
```

```
        MatRCenterY(rr,jj)=EdgesY(jj)+binsize/2;

        id1=EEid; % Getting the id of each location in the
            bin

        Tbin=0; % Initialisation of time count
        Ybin=0;
        Rbin=0;
        Abin=0;
        vYbin=0;
        vMbin=0;
        vRbin=0;
        vAbin=0;
        aYbin=0;
        aMbin=0;
        aRbin=0;
        aAbin=0;
        FpYbin=0;
        FpMbin=0;
        FpRbin=0;

        if nbpoints>1;%Min number of point in the bin
            for iT=1:nbpoints
                if id1(iT)-1<1
                    Tbin=Tbin+0;
                else
                    Tbin=Tbin+(T3(id1(iT))-T3(id1(iT)-1));
                end
                Ybin=Ybin+Y3(id1(iT));
                Rbin=Rbin+R3(id1(iT));
```

```
                    Abin=Abin+A3(id1(iT));
                    vYbin=vYbin+vY3(id1(iT));
                    vMbin=vMbin+vM3(id1(iT));
                    vRbin=vRbin+vR3(id1(iT));
                    vAbin=vAbin+vA3(id1(iT));
                    aYbin=aYbin+aY3(id1(iT));
                    aMbin=aMbin+aM3(id1(iT));
                    aRbin=aRbin+aR3(id1(iT));
                    aAbin=aAbin+aA3(id1(iT));
                    FpYbin=FpYbin+FpY3(id1(iT));
                    FpMbin=FpMbin+FpM3(id1(iT));
                    FpRbin=FpRbin+FpR3(id1(iT));
                end
                MatRT(rr,jj)=Tbin; % Attribute the value to the
                    bin
                MatRvM(rr,jj)=vMbin/nbpoints; % average on the
                    number of location in this bin
                MatRvR(rr,jj)=vRbin/nbpoints;
                MatRvY(rr,jj)=vYbin/nbpoints;
                MatRvA(rr,jj)=vAbin/nbpoints;
                MatRaY(rr,jj)=aYbin/nbpoints;
                MatRaM(rr,jj)=aMbin/nbpoints;
                MatRaR(rr,jj)=aRbin/nbpoints;
                MatRaA(rr,jj)=aAbin/nbpoints;
                MatRFpY(rr,jj)=FpYbin/nbpoints;
                MatRFpM(rr,jj)=FpMbin/nbpoints;
                MatRFpR(rr,jj)=FpRbin/nbpoints;
            else
            end
        end
```

```
end

maxspeed=100; %Limit the max speed value m/s
MatRCount(MatRCount==0)=NaN; %Put NaN when no location in
    bins
MatRT(MatRT==0)=NaN;
MatRVol(MatRVol==0)=NaN;
MatRvM(MatRvM==0)=NaN;
MatRvR(MatRvR==0)=NaN;
MatRvR(MatRvR>maxspeed)=maxspeed;
MatRvR(MatRvR<(-maxspeed))=-maxspeed;
MatRvY(MatRvY==0)=NaN;
MatRvY(MatRvY>maxspeed)=maxspeed;
MatRvY(MatRvY<(-maxspeed))=-maxspeed;
MatRvA(MatRvA==0)=NaN;
MatRaM(MatRaM==0)=NaN;
MatRaR(MatRaR==0)=NaN;
MatRaY(MatRaY==0)=NaN;
MatRaA(MatRaA==0)=NaN;
MatRFpM(MatRFpM==0)=NaN;
MatRFpR(MatRFpR==0)=NaN;
MatRFpY(MatRFpY==0)=NaN;

%DISPLAY RADIAL LOCATION
%-----------------------------------------------------------%
figure(10)

C=MatRCount;
C(:)=NaN;
h=pcolor(MatRCenterR-binsize/2,MatRCenterY-binsize/2,C);
```

```
set(h,'EdgeColor','k','edgealpha',0.15)
hold on
plot(R3,Y3,'bo','LineWidth',1,'MarkerSize',5)
hold off
axis equal
axis([Rmin Rmax-binsize Ymin Ymax-binsize])
grid on
xlabel('Radius (mm)','FontSize',20);
ylabel('Elevation (mm)','FontSize',20);
set(gca,'FontSize',20)


%DISPLAY VELOCITY FIELD (TOROID BINS)
%---------------------------------------------------------%
figure (11)

C=MatRCount;
C(:)=NaN;
h=pcolor(MatRCenterR-binsize/2,MatRCenterY-binsize/2,C);
set(h,'EdgeColor','k','edgealpha',0.15)
hold on
quiver(MatRCenterR, MatRCenterY, MatRvR, MatRvY,1.5,'color','
    k') %Be carefull with scale
hold off
axis equal
grid on
axis([Rmin Rmax-binsize Ymin Ymax-binsize])
box on
xlabel('Radius (mm)','FontSize',20)
ylabel('Elevation (mm)','FontSize',20)
```

```
set(gca,'FontSize',20)


%DISPLAY OCCUPANCY (TOROID BINS)
%------------------------------------------------------------%
figure(12)

C=MatRCount;
h=pcolor(MatRCenterR-binsize/2,MatRCenterY-binsize/2,C);
set(h,'EdgeColor','k','edgealpha',0.15)
col = colorbar;
ylabel(col,'Occupancy (Location per bin)','FontSize',20);
caxis([0,1000])
colormap(cool)
axis equal
axis([Rmin Rmax-binsize Ymin Ymax-binsize])
xlabel('Radius (mm)','FontSize',20);
ylabel('Elevation (mm)','FontSize',20);
set(gca,'FontSize',20)


%DISPLAY OCCUPANCY (VOLUME NORMALISED) (TOROID BINS)
%------------------------------------------------------------%
figure(121)

MatROccV=MatRCount./MatRVol; %Occupancy count per unit volume
    (count/mm3)

C=MatROccV;
h=pcolor(MatRCenterR-binsize/2,MatRCenterY-binsize/2,C);
```

```
set(h,'EdgeColor','k','edgealpha',0.15)
col = colorbar;
ylabel(col,'Occupancy (Location/mm^{3})','FontSize',20);
caxis([0,0.05])
colormap(cool)
axis equal
axis([Rmin Rmax-binsize Ymin Ymax-binsize])
xlabel('Radius (mm)','FontSize',20);
ylabel('Elevation (mm)','FontSize',20);
set(gca,'FontSize',20)


%DISPLAY FRACTIONNAL OCCUPANCY (TOROID BINS)
%------------------------------------------------------------%
figure(13)

FracOccV=MatROccV/(sum(sum(MatRCount,'omitnan'),'omitnan'));
    %Fractionnal occupancy (number of time particle located in
     bin)/(volume)/(total number of location)

C=FracOccV;
h=pcolor(MatRCenterR-binsize/2,MatRCenterY-binsize/2,C);
set(h,'EdgeColor','k','edgealpha',0.15)
col = colorbar;
ylabel(col,'Occupancy (fraction of location/mm^{3})','
    FontSize',20);
caxis([0,0.00000025])
colormap(cool)
axis equal
axis([Rmin Rmax-binsize Ymin Ymax-binsize])
```

```
xlabel('Radius (mm)','FontSize',20);
ylabel('Elevation (mm)','FontSize',20);
set(gca,'FontSize',20)


%DISPLAY RESIDUALS (TOROID BINS)
%------------------------------------------------------------%
figure(131)

subplot(2,2,1)
plot(X,XRes,'ro','LineWidth',2,'MarkerSize',5);
axis([Xmin Xmax -25 25])
xlabel('X (mm)','FontSize',20);
ylabel('X Residual (mm)','FontSize',20);
grid on
set(gca,'FontSize',20)

subplot(2,2,[2,4])
plot(YRes,Y,'ro','LineWidth',2,'MarkerSize',5);
axis([-25 25 Ymin Ymax])
xlabel('Y Residuals(mm)','FontSize',20);
ylabel('Y (mm)','FontSize',20);
grid on
set(gca,'FontSize',20)

subplot(2,2,3)
plot(Z,ZRes,'ro','LineWidth',2,'MarkerSize',5);
axis([Zmin Zmax -25 25])
xlabel('Z (mm)','FontSize',20);
ylabel('Z Residual (mm)','FontSize',20);
```

```
grid on
set(gca,'FontSize',20)


%DISPLAY VELOCITY MAGNITUDE (TOROID BINS)
%------------------------------------------------------------%
figure(14)

C=MatRvM;
h=pcolor(MatRCenterR-binsize/2,MatRCenterY-binsize/2,C);
set(h,'EdgeColor','k','edgealpha',0.15)
col = colorbar;
ylabel(col,'Velocity magnitude (m/s)','FontSize',20);
caxis([0,1.2])
colormap(jet)
axis equal
axis([Rmin Rmax-binsize Ymin Ymax-binsize])
xlabel('Radius (mm)','FontSize',20);
ylabel('Elevation (mm)','FontSize',20);
set(gca,'FontSize',20)


%DISPLAY VELOCITY MAGNITUDE/Vtip (TOROID BINS)
%------------------------------------------------------------%
figure(141)

C=MatRvM/vTip;
h=pcolor(MatRCenterR-binsize/2,MatRCenterY-binsize/2,C);
set(h,'EdgeColor','k','edgealpha',0.15)
col = colorbar;
```

```
ylabel(col,'Velocity magnitude (m/s)','FontSize',20);
caxis([0,1])
colormap(hot)
axis equal
axis([Rmin Rmax-binsize Ymin Ymax-binsize])
xlabel('Radius (mm)','FontSize',20);
ylabel('Elevation (mm)','FontSize',20);
set(gca,'FontSize',20)


%DISPLAY VERTICAL VELOCITY (TOROID BINS)
%----------------------------------------------------%
figure(15)

C=MatRvY;
h=pcolor(MatRCenterR-binsize/2,MatRCenterY-binsize/2,C);
set(h,'EdgeColor','k','edgealpha',0.15)
col = colorbar;
ylabel(col,'Vertical velocity (m/s)','FontSize',20);
caxis([-0.5,0])
colormap(gray)
axis equal
axis([Rmin Rmax-binsize Ymin Ymax-binsize])
xlabel('Radius (mm)','FontSize',20);
ylabel('Elevation (mm)','FontSize',20);
set(gca,'FontSize',20)


%DISPLAY RADIAL VELOCITY (TOROID BINS)
%----------------------------------------------------%
```

```
figure(16)

C=MatRvR;
h=pcolor(MatRCenterR-binsize/2,MatRCenterY-binsize/2,C);
set(h,'EdgeColor','k','edgealpha',0.15)
col = colorbar;
ylabel(col,'Radial velocity (m/s)','FontSize',20);
caxis([-0.35,0.35])
colormap(jet)
axis equal
axis([Rmin Rmax-binsize Ymin Ymax-binsize])
xlabel('Radius (mm)','FontSize',20);
ylabel('Elevation (mm)','FontSize',20);
set(gca,'FontSize',20)


%DISPLAY ANGULAR VELOCITY (TOROID BINS)
%------------------------------------------------%
figure(17)

C=MatRvA;
h=pcolor(MatRCenterR-binsize/2,MatRCenterY-binsize/2,C);
set(h,'EdgeColor','k','edgealpha',0.15)
col = colorbar;
ylabel(col,'Angular velocity (rad/s)','FontSize',20);
caxis([0,4*pi()])
colormap(flipud(hot))
axis equal
axis([Rmin Rmax-binsize Ymin Ymax-binsize])
xlabel('Radius (mm)','FontSize',20);
```

```
ylabel('Elevation (mm)','FontSize',20);
set(gca,'FontSize',20)


% %DISPLAY MULTIPLE FIGURE TO SAVE PDF
% %------------------------------------------------%
%
%
% h1777=figure('position', [0, 0, 990, 590]);
%
% ha=subplot(1,3,1,'position',[0.07 0.11 0.28 0.87]);
%
% C=MatRvM;
% h=pcolor(MatRCenterR-binsize/2,MatRCenterY-binsize/2,C);
% set(h,'EdgeColor','k','edgealpha',0.15)
% col = colorbar;
% ylabel(col,'Velocity magnitude (m/s)','FontSize',14);
% caxis([0,1.2])
% colormap(ha, jet)
% axis equal
% axis([Rmin Rmax-binsize Ymin Ymax-binsize])
% xlabel('Radius (mm)','FontSize',16);
% ylabel('Elevation (mm)','FontSize',16);
% set(gca,'FontSize',16)
%
% xa = [0.105 0.13];
% ya = [0.38 0.51];
% ht=annotation('textarrow',xa,ya,'String','WW ')
% set(ht,'FontSize',16);
%
```

```
%
%
%
% hb=subplot(1,3,2,'position',[0.38 0.11 0.28 0.87]);
%
% C=MatRvR;
% h=pcolor(MatRCenterR-binsize/2,MatRCenterY-binsize/2,C);
% set(h,'EdgeColor','k','edgealpha',0.15)
% col = colorbar;
% ylabel(col,'Radial velocity (m/s)','FontSize',14);
% caxis([-0.35,0.35])
% colormap(hb, jet)
% axis equal
% axis([Rmin Rmax-binsize Ymin Ymax-binsize])
% xlabel('Radius (mm)','FontSize',16);
% set(gca,'YTick',[]);
% %ylabel('Elevation (mm)','FontSize',16);
% set(gca,'FontSize',16)
%
%
% hc=subplot(1,3,3,'position',[0.69 0.11 0.28 0.87]);
%
% C=MatRvA;
% h=pcolor(MatRCenterR-binsize/2,MatRCenterY-binsize/2,C);
% set(h,'EdgeColor','k','edgealpha',0.15)
% col = colorbar;
% ylabel(col,'Angular velocity (rad/s)','FontSize',14);
% caxis([0,4*pi()])
% colormap(hc, flipud(hot))
% axis equal
```

```
% axis([Rmin Rmax-binsize Ymin Ymax-binsize])
% xlabel('Radius (mm)','FontSize',16);
% set(gca,'YTick',[]);
% %ylabel('Elevation (mm)','FontSize',16);
% set(gca,'FontSize',16)
%
%
% set(h1777,'PaperUnits','inches');
% set(h1777,'papersize',[10 6]);
% set(h1777,'PaperPosition', [0.05 0.05 9.95 5.95]);
% print(h1777, '0300_0355_Hematite_WWON_Vel', '-dpdf');
%


%DISPLAY ANGULAR VELOCITY VS ELEVATION VS RADIUS (TOROID BINS
    )
%------------------------------------------------------------%
figure(18)

for i=1:nbpass
    hold on
    h = surface([PlibR(:,i), PlibR(:,i)], [PlibY(:,i), PlibY
        (:,i)], [PlibZ(:,i), PlibZ(:,i)],[PlibvA(:,i), PlibvA
        (:,i)],'LineWidth',2,'EdgeColor','flat', 'FaceColor','
        none');
end
hold off
col = colorbar;
ylabel(col,'Angular velocity (rad/s)','FontSize',20);
caxis([-4*pi(),0])
```

```
xlabel('Radius (mm)','FontSize',20);
ylabel('Elevation (mm)','FontSize',20);
zlabel('Z (mm)','FontSize',20);
axis([0 180 Ymin Ymax Zmin Zmax])
%axis equal
grid on
set(gca,'FontSize',20)
AZ=0;
EL=90;
view(2);


%DISPLAY VELOCITY MAGNITUDE VS ELEVATION VS RADIUS (TOROID
    BINS)
%--------------------------------------------------------%
figure(19)

for i=1:nbpass
    hold on
    h = surface([PlibR(:,i), PlibR(:,i)], [PlibY(:,i), PlibY
        (:,i)], [PlibZ(:,i), PlibZ(:,i)],[PlibvM(:,i), PlibvM
        (:,i)],'LineWidth',2,'EdgeColor','flat', 'FaceColor','
        none');
end
hold off
col = colorbar;
ylabel(col,'Velocity Magnitude (m/s)','FontSize',20);
caxis([0,1.75])
xlabel('Radius (mm)','FontSize',20);
ylabel('Elevation (mm)','FontSize',20);
```

```
zlabel('Z (mm)','FontSize',20);
axis([0 180 Ymin Ymax Zmin Zmax])
%axis equal
grid on
set(gca,'FontSize',20)
AZ=0;
EL=90;
view(2);


%DISPLAY ANGULAR POSITION VS ELEVATION (TOROID BINS)
%-----------------------------------------------------------%
figure(20)

plot(Afit, Yfit,'bo','LineWidth',1,'MarkerSize',5)
%axis equal
grid on
%axis([-20 20 -10 10])
xlabel('Angle (rad)','FontSize',20);
ylabel('Elevation (mm)','FontSize',20);
set(gca,'FontSize',20)


%DISPLAY ANGULAR VELOCITY VS RADIUS (TOROID BINS)
%-----------------------------------------------------------%
figure(21)

plot(Rfit, vAfit,'bo','LineWidth',1,'MarkerSize',5)
%axis equal
grid on
```

```
axis([0 180 -4*pi() 0])
xlabel('Radius(mm)','FontSize',20);
ylabel('Angular Velocity (rad/s)','FontSize',20);
set(gca,'FontSize',20)


%DISPLAY ANGULAR VELOCITY VS RADIAL VELOCITY (TOROID BINS)
%-----------------------------------------------------------%
figure(22)

plot(vRfit, vAfit,'bo','LineWidth',1,'MarkerSize',5)
%axis equal
grid on
axis([-0.5 0.5 -4*pi() 0])
xlabel('Radial velocity (m/s)','FontSize',20);
ylabel('Angular Velocity (rad/s)','FontSize',20);
set(gca,'FontSize',20)


%DISPLAY VELOCITY MAGNITUDE VS RADIUS (TOROID BINS)
%-----------------------------------------------------------%
figure(23)

plot(Rfit, vMfit,'bo','LineWidth',1,'MarkerSize',5)
%axis equal
grid on
axis([0 180 0 2])
xlabel('Radius (mm)','FontSize',20);
ylabel('Velocity Magnitude (m/s)','FontSize',20);
set(gca,'FontSize',20)
```

```
%DISPLAY HISTOGRAM OF RESIDUAL BETWEEN LOCATIONS AND FIT
%--------------------------------------------------------%
figure(24)

edges=[0:0.2:15];
histogram(abs(XRes),edges,'Normalization','probability','
    facecolor',[0 0 1],'facealpha',1,'edgecolor','none');
hold on
histogram(abs(YRes),edges,'Normalization','probability','
    facecolor',[0 1 0],'facealpha',0.5,'edgecolor','none');
hold on
histogram(abs(ZRes),edges,'Normalization','probability','
    facecolor',[1 0 0],'facealpha',1,'edgecolor','none');
xlabel('Residuals between tracked and fitted locations (mm)',
    'FontSize',24);
ylabel('Fraction of total locations','FontSize',24);
set(gca,'FontSize',24)
legend1=sprintf('X Residuals, Mean = %.1f, Median = %.1f, Std
     = %.1f',mean(abs(XRes)),median(abs(XRes)),std(XRes));
legend2=sprintf('Y Residuals, Mean = %.1f, Median = %.1f, Std
     = %.1f',mean(abs(YRes)),median(abs(YRes)),std(YRes));
legend3=sprintf('Z Residuals, Mean = %.1f, Median = %.1f, Std
     = %.1f',mean(abs(ZRes)),median(abs(ZRes)),std(ZRes));
legend({legend1, legend2, legend3},'FontSize',20);


figure(25)
%edges=[0:0.2:15];
```

```
histogram(NRes,edges,'facecolor',[0 0 1],'facealpha',1,'edgecolor','none');
xlabel('Residuals between tracked and fitted locations (mm)','FontSize',20);
ylabel('Number of locations','FontSize',20);
legend1=sprintf('STD Residuals = %.2f',std(NRes));
legend({legend1});
set(gca,'FontSize',20)

figure(26)
edges=[0:0.01:1];
histogram(vMfit/Vtip,edges,'Normalization','probability','facecolor',[0 0 1],'facealpha',1,'edgecolor','none','Normalization','probability');
xlabel('Normalised velocity (vM/vtip)','FontSize',20);
ylabel('Fraction of total locations','FontSize',20);
legend1=sprintf('Normalised velocity, Mean = %.2f, Median = %.2f, Std = %.2f',mean(abs(vMfit/Vtip)),median(abs(vMfit/Vtip)),std(vMfit/Vtip));
legend({legend1});
set(gca,'FontSize',20)


%DISPLAY ACCELERATION MAGNITUDE (TOROID BINS)
%-------------------------------------------------------------%
figure(27)

C=MatRaM;
h=pcolor(MatRCenterR-binsize/2,MatRCenterY-binsize/2,C);
set(h,'EdgeColor','k','edgealpha',0.15)
```

```
col = colorbar;
ylabel(col,'Acceleration magnitude (m/s^2)','FontSize',20);
caxis([0,6])
colormap(jet)
axis equal
axis([Rmin Rmax-binsize Ymin Ymax-binsize])
xlabel('Radius (mm)','FontSize',20);
ylabel('Elevation (mm)','FontSize',20);
set(gca,'FontSize',20)

%DISPLAY VERTICAL ACCELERATION (TOROID BINS)
%------------------------------------------------------------------%
figure(28)

C=MatRaY;
h=pcolor(MatRCenterR-binsize/2,MatRCenterY-binsize/2,C);
set(h,'EdgeColor','k','edgealpha',0.15)
col = colorbar;
ylabel(col,'Vertical acceleration (m/s^2)','FontSize',20);
caxis([-4,4])
colormap(jet)
axis equal
axis([Rmin Rmax-binsize Ymin Ymax-binsize])
xlabel('Radius (mm)','FontSize',20);
ylabel('Elevation (mm)','FontSize',20);
set(gca,'FontSize',20)

%DISPLAY RADIAL ACCELERATION (TOROID BINS)
%------------------------------------------------------------------%
figure(29)
```

```

C=MatRaR;
h=pcolor(MatRCenterR-binsize/2,MatRCenterY-binsize/2,C);
set(h,'EdgeColor','k','edgealpha',0.15)
col = colorbar;
ylabel(col,'Radial acceleration (m/s^2)','FontSize',20);
caxis([-6,6])
colormap(jet)
axis equal
axis([Rmin Rmax-binsize Ymin Ymax-binsize])
xlabel('Radius (mm)','FontSize',20);
ylabel('Elevation (mm)','FontSize',20);
set(gca,'FontSize',20)

%DISPLAY ANGULAR ACCELERATION (TOROID BINS)
%--------------------------------------------------------%
figure(30)

C=MatRaA;
h=pcolor(MatRCenterR-binsize/2,MatRCenterY-binsize/2,C);
set(h,'EdgeColor','k','edgealpha',0.15)
col = colorbar;
ylabel(col,'Angular acceleration (rad/s^2)','FontSize',20);
caxis([-75,75])
colormap(jet)
axis equal
axis([Rmin Rmax-binsize Ymin Ymax-binsize])
xlabel('Radius (mm)','FontSize',20);
ylabel('Elevation (mm)','FontSize',20);
set(gca,'FontSize',20)
```

```
%DISPLAY FORCE MAGNITUDE (TOROID BINS)
%--------------------------------------------------------%
figure(31)

C=MatRFpM*1000000;
h=pcolor(MatRCenterR-binsize/2,MatRCenterY-binsize/2,C);
set(h,'EdgeColor','k','edgealpha',0.15)
col = colorbar;
ylabel(col,'Force magnitude (\muN)','FontSize',20);
caxis([0,0.5])
colormap(jet)
axis equal
axis([Rmin Rmax-binsize Ymin Ymax-binsize])
xlabel('Radius (mm)','FontSize',20);
ylabel('Elevation (mm)','FontSize',20);
set(gca,'FontSize',20)

%DISPLAY FORCE IN Y AXIS (TOROID BINS)
%--------------------------------------------------------%
figure(32)

C=MatRFpY*1000000;
h=pcolor(MatRCenterR-binsize/2,MatRCenterY-binsize/2,C);
set(h,'EdgeColor','k','edgealpha',0.15)
col = colorbar;
ylabel(col,'Vertical force (\muN)','FontSize',20);
caxis([-0.5,0.5])
colormap(jet)
```

```
axis equal
axis([Rmin Rmax-binsize Ymin Ymax-binsize])
xlabel('Radius (mm)','FontSize',20);
ylabel('Elevation (mm)','FontSize',20);
set(gca,'FontSize',20)

%DISPLAY FORCE IN R AXIS (TOROID BINS)
%----------------------------------------------------------------%
figure(33)

C=MatRFpR*1000000;
h=pcolor(MatRCenterR-binsize/2,MatRCenterY-binsize/2,C);
set(h,'EdgeColor','k','edgealpha',0.15)
col = colorbar;
ylabel(col,'Radial force (\muN)','FontSize',20);
caxis([-0.5,0.5])
colormap(jet)
axis equal
axis([Rmin Rmax-binsize Ymin Ymax-binsize])
xlabel('Radius (mm)','FontSize',20);
ylabel('Elevation (mm)','FontSize',20);
set(gca,'FontSize',20)

%DISPLAY FORCE FIELD (TOROID BINS)
%----------------------------------------------------------------%
figure (34)

C=MatRCount;
C(:)=NaN;
h=pcolor(MatRCenterR-binsize/2,MatRCenterY-binsize/2,C);
```

```
set(h,'EdgeColor','k','edgealpha',0.15)
hold on
quiver(MatRCenterR, MatRCenterY, MatRFpR, MatRFpY,2.0,'color'
    ,'k') %Be carefull with scale
% hold on
% quiver(5,-10,10,0,'autoscale','off','color','k','
    MaxHeadSize',1);
% text(5,-13,'0.1 \muN','color','k','FontSize',12)
hold off
axis equal
grid on
axis([Rmin Rmax-binsize Ymin Ymax-binsize])
box on
xlabel('Radius (mm)','FontSize',20)
ylabel('Elevation (mm)','FontSize',20)
set(gca,'FontSize',20)


% %WRITE SELECTED DATA IN A FILE (for future processing)
% %--------------------------------------------------%
Datafit=[T3,R3,A3,X3,Y3,Z3,vR3,vA3,vX3,vY3,vZ3,vM3,aR3,aA3,
    aX3,aY3,aZ3,aM3];
formatSpec = '%8.5f %5.5f %5.5f %5.5f %5.5f %5.5f %5.5f %5.5f
     %5.5f %5.5f %5.5f %5.5f %5.5f %5.5f %5.5f %5.5f %5.5f
    %5.5f\n';

fileID = fopen('Datafit_test.txt','wt');
for i=1:length(T3)
    fprintf(fileID,formatSpec,Datafit(i,:));
end
```

```
fclose(fileID);
```